

¹ Observation of the Higgs boson in the WW^*
² channel and search for Higgs boson pair
³ production in the $b\bar{b}b\bar{b}$ channel with the
⁴ ATLAS detector

⁵ A DISSERTATION PRESENTED
⁶ BY
⁷ TOMO LAZOVICH
⁸ TO
⁹ THE DEPARTMENT OF PHYSICS

¹⁰ IN PARTIAL FULFILLMENT OF THE REQUIREMENTS
¹¹ FOR THE DEGREE OF
¹² DOCTOR OF PHILOSOPHY
¹³ IN THE SUBJECT OF
¹⁴ PHYSICS

¹⁵ HARVARD UNIVERSITY
¹⁶ CAMBRIDGE, MASSACHUSETTS
¹⁷ MAY 2016

¹⁸ ©2016 – TOMO LAZOVICH

¹⁹ ALL RIGHTS RESERVED.

20 **Observation of the Higgs boson in the WW^* channel and search
21 for Higgs boson pair production in the $b\bar{b}b\bar{b}$ channel with the
22 ATLAS detector**

23 **ABSTRACT**

24 This dissertation presents two studies: the observation and measurement of the Higgs boson in the
25 $H \rightarrow WW^* \rightarrow \ell\nu\ell\nu$ channel at $\sqrt{s} = 7$ TeV and $\sqrt{s} = 8$ TeV and a search for Higgs pair pro-
26 duction in the $HH \rightarrow b\bar{b}b\bar{b}$ channel at $\sqrt{s} = 13$ TeV with the ATLAS detector in pp collisions at the
27 Large Hadron Collider.

28 First, the discovery of a particle consistent with the Higgs in 4.8 fb^{-1} at $\sqrt{s} = 7$ TeV and 5.8 fb^{-1} at
29 $\sqrt{s} = 8$ TeV is discussed. Then, the measurement of the Higgs boson signal strength and cross section
30 in both the gluon fusion and vector boson fusion (VBF) production modes using 20.3 fb^{-1} of $\sqrt{s} =$
31 8 TeV data combined with 4.8 fb^{-1} of 7 TeV data is shown. The combined signal strength is measured
32 to be $\mu = 1.09^{+0.23}_{-0.21}$. The total observed significance of the $H \rightarrow WW^*$ process is observed to be
33 6.1σ (with 5.8σ expected). Advanced methods for background reduction and estimation, particularly in
34 same-flavor lepton final states, are shown. The VBF signal strength is measured to be $\mu_{\text{VBF}} = 1.27^{+0.53}_{-0.45}$
35 with an observed significance of 3.2σ (with 2.7σ expected). In the VBF channel, a selection requirement
36 based method, the precursor to the final multivariate technique used for the result, is detailed.

37 Finally, a search for Higgs pair production in the $b\bar{b}b\bar{b}$ final state with 3.2 fb^{-1} at $\sqrt{s} = 13$ TeV
38 is presented. A particular focus is placed on a tailored signal region for resonant production of Higgs
39 pairs at high masses, utilizing novel techniques in object reconstruction to increase signal acceptance in
40 boosted final state topologies. No significant excesses are observed, and upper limits on cross sections are
41 placed for spin-2 Randall Sundrum gravitons (RSG) and narrow spin-0 resonances. The cross section of
42 $\sigma(pp \rightarrow G_{\text{KK}}^* \rightarrow hh \rightarrow b\bar{b}b\bar{b})$ with $k/\bar{M}_{\text{Pl}} = 1$ is constrained to be less than 70 fb for masses in the
43 range $600 < m_{G_{\text{KK}}^*} < 3000 \text{ GeV}$. For the RSG model with $k/\bar{M}_{\text{Pl}} = 2$, cross sections limits between

Dissertation advisors: Professors João Guimarães da Costa
and Melissa Franklin

Tomo Lazovich

- ⁴⁴ 40 fb and 200 fb are set for the mass range of $500 < m_{G_{\text{KK}}^*} < 3000$ GeV. The cross section upper
⁴⁵ limits for $\sigma(pp \rightarrow H \rightarrow hh \rightarrow b\bar{b}b\bar{b})$ ranges from 30 to 300 fb in the mass range of $500 < m_H <$
⁴⁶ 3000 GeV.

Contents

47

48	o INTRODUCTION	I
49	I Theoretical and Experimental Background	5
50	I.1 THE PHYSICS OF THE HIGGS BOSON	6
51	1.1 The Standard Model of Particle Physics	6
52	1.2 Electroweak Symmetry Breaking and the Higgs	8
53	1.3 Higgs Boson Production and Decay	II
54	1.4 Higgs Pair Production in the Standard Model	15
55	1.5 Higgs Pair Production in Theories Beyond the Standard Model	16
56	1.6 Conclusion	21
57	2 THE ATLAS DETECTOR AND THE LARGE HADRON COLLIDER	22
58	2.1 The Large Hadron Collider	23
59	2.2 The ATLAS Detector	25
60	2.3 The ATLAS Muon New Small Wheel Upgrade	36
61	2.4 Object Reconstruction in ATLAS	40
62	II Observation and measurement of Higgs boson decays to WW^* in LHC	
63	Run 1 at $\sqrt{s} = 7$ and 8 TeV	49
64	3 $H \rightarrow WW^* \rightarrow \ell\nu\ell\nu$ ANALYSIS STRATEGY	50
65	3.1 Introduction	50
66	3.2 The $H \rightarrow WW^* \rightarrow \ell\nu\ell\nu$ signal in ATLAS	51
67	3.3 Background processes	52
68	3.4 Shared signal region selection requirements	55
69	3.5 Background reduction in same-flavor final states	58
70	3.6 Parameters of interest and statistical treatment	63
71	4 THE DISCOVERY OF THE HIGGS BOSON AND THE ROLE OF THE $H \rightarrow WW^* \rightarrow \ell\nu\ell\nu$	
72	CHANNEL	69
73	4.1 Introduction	69

74	4.2	Data and simulation samples	70
75	4.3	$H \rightarrow WW \rightarrow e\nu\mu\nu$ search	70
76	4.4	$H \rightarrow \gamma\gamma$ search	75
77	4.5	$H \rightarrow ZZ \rightarrow 4\ell$ search	76
78	4.6	Combined results	77
79	4.7	Conclusion	79
80	5	OBSERVATION OF VECTOR BOSON FUSION PRODUCTION OF $H \rightarrow WW^* \rightarrow \ell\nu\ell\nu$	82
81	5.1	Introduction	82
82	5.2	Data and simulation samples	83
83	5.3	Object selection	87
84	5.4	Analysis selection	90
85	5.5	Background estimation	98
86	5.6	Systematic uncertainties	109
87	5.7	Results	113
88	6	COMBINED RUN I $H \rightarrow WW^* \rightarrow \ell\nu\ell\nu$ RESULTS	118
89	6.1	Introduction	118
90	6.2	Results of gluon fusion $H \rightarrow WW^* \rightarrow \ell\nu\ell\nu$ search	119
91	6.3	Signal strength measurements in ggF and VBF production	121
92	6.4	Measurement of Higgs couplings to vector bosons and fermions	124
93	6.5	Higgs production cross section measurement	125
94	6.6	Conclusion	126
95	III	Search for Higgs pair production in the $HH \rightarrow b\bar{b}b\bar{b}$ channel in LHC	
96		Run 2 at $\sqrt{s} = 13$ TeV	128
97	7	SEARCH FOR HIGGS PAIR PRODUCTION IN BOOSTED $b\bar{b}b\bar{b}$ FINAL STATES	129
98	7.1	Introduction	129
99	7.2	Motivation	130
100	7.3	Data and simulation samples	132
101	7.4	Event reconstruction and object selection	134
102	7.5	Event selection	137
103	7.6	Data-driven background estimation	140
104	7.7	Systematic uncertainties	146
105	7.8	Results	149

106	8 COMBINED LIMITS FROM BOOSTED AND RESOLVED SEARCHES	151
107	8.1 Introduction	151
108	8.2 Resolved results	152
109	8.3 Search technique and results	152
110	8.4 Limit setting	153
111	IV Looking ahead	157
112	9 CONCLUSION	158
113	APPENDIX A OPTIMIZATION OF b-TAGGING WORKING POINT IN $X \rightarrow HH \rightarrow b\bar{b}b\bar{b}$	
114	SEARCH	162
115	APPENDIX B b-TAGGING PERFORMANCE AT HIGH p_T	164
116	B.1 MV2 algorithm overview	164
117	B.2 Changes in MV2 score at high p_T	165
118	B.3 Tagging efficiency by individual jet	168
119	B.4 Effect of multiple b -quarks inside one jet	169
120	B.5 Changes in track quality at high p_T	170
121	REFERENCES	172

Listing of figures

123	1.1	The particles of the Standard Model and their properties [6].	7
124	1.2	The four most common Higgs boson production modes at the LHC: (a) gluon-gluon fu-	
125		sion, (b) vector boson fusion, (c) $W/Z + H$ production, (d) $t\bar{t}H$ production	11
126	1.3	Higgs production cross sections as a function of center of mass energy (\sqrt{s}) at a pp collider [18]. .	12
127	1.4	Higgs boson branching ratios as a function of m_H [18].	14
128	1.5	The two leading diagrams for Standard Model di-Higgs production at the LHC: (a) box di-	
129		agram, (b) Higgs self coupling	16
130	1.6	Diagrams with new vertices for non-resonant Higgs pair production arising in composite	
131		Higgs models	17
132	1.7	Generic Feynman diagram for resonant Higgs pair production in BSM theories	18
133	1.8	Branching ratios for a spin-2 Randall-Sundrum graviton as a function of mass computed in	
134		MadGraph with the CP3-Origins implementation [24, 30]	18
135	1.9	$\sigma \times BR(HH)$ for RSG as a function of mass computed in MadGraph with the CP3-Origins	
136		implementation [24, 30]	19
137	1.10	RSG width as a function of mass computed in MadGraph with the CP3-Origins implemen-	
138		tation [24, 30]	20
139	1.11	Branching ratios for heavy Higgs H in Type I (left) and Type II (right) 2HDM models with	
140		$\tan \beta = 1.5$ and $\cos(\beta - \alpha) = 0.1(0.01)$ for Type I (Type II). [28]	21
141	2.1	A schematic view of the LHC ring [36]	23
142	2.2	A full diagram of the ATLAS detector [32]	26
143	2.3	The ATLAS coordinate system	27
144	2.4	Layout of the ATLAS Inner Detector system [40]	28
145	2.5	Layout of the ATLAS calorimeter system [32]	30
146	2.6	Layout of the ATLAS muon system [32]	32
147	2.7	Predicted field integral as a function of $ \eta $ for the ATLAS magnet system [32]	34
148	2.8	ATLAS trigger rates for Level-1 triggers as a function of instantaneous luminosity in 2012	
149		and 2015 operation. These are single object triggers for electromagnetic clusters (EM), muons	
150		(MU), jets (J), missing energy (XE), and τ leptons (TAU). The threshold of the trigger is given	
151		in the name in GeV. [42]	35
152	2.9	Instantaneous luminosity as a function of time for data recorded by ATLAS at different cen-	
153		ter of mass energies [43, 44]	36

154	2.10	MDT tube hit (solid) and segment (dashed) efficiency as a function of hit rate per tube [45]	37
155	2.11	Trigger rate as a function of p_T threshold with and without the NSW upgrade [45]	38
156	2.12	Illustrations of the geometry (left) and operating principle (right) of the micromegas detector [45]	39
158	2.13	Geometry of the sTGC detector [45]	40
159	2.14	Illustration of particle interactions in ATLAS [48]	41
160	2.15	Electron performance: (a) reconstruction efficiency as a function of electron E_T [50] (b) energy resolution in simulation as a function of $ \eta $ for different energy electrons [51]	42
162	2.16	Muon performance: (a) reconstruction efficiency as a function of muon p_T (b) dimuon mass resolution as a function of average p_T [52]	44
164	2.17	Jet energy response after calibration as a function of true p_T in simulation [56]	45
165	2.18	Light jet rejection (1/efficiency) vs. b -jet efficiency for MV1 and its input algorithms (a) [57] and MV2 (b) [58] in simulated $t\bar{t}$ events. The numbers in the algorithm names in (b) refer to the fraction of charm events used in the MV2 training.	46
168	2.19	Resolution of E_T^{miss} components as a function of $\sum E_T$ before pileup suppression with different pileup techniques [60]	48
170	3.1	Branching ratios for a WW system. q refers to quarks. ℓ can be either an electron or muon, and the leptonic branching ratios of the τ are included. For example, the $\ell\nu qq$ final state includes one W decaying to $e\nu$, $\mu\nu$, or $\tau\nu$. τ_h refer to hadronic decays of the τ .	52
172	3.2	Feynman diagram for Standard Model WW production	53
174	3.3	Feynman diagrams for top pair production (left) and Wt production (right)	53
175	3.4	An example Feynman diagram of W +jets production	54
176	3.5	An example Feynman diagram of Z +jets production	55
177	3.6	An illustration of the unique analysis signal regions [61]. The most sensitive regions for both gluon fusion and vector boson fusion production are underlined.	56
179	3.7	A graphical illustration of the $E_{T,\text{rel}}^{\text{miss}}$ calculation	57
180	3.8	Predicted backgrounds (compared with data) as a function of n_j (a and b) and n_b (c) after pre-selection requirements	59
182	3.9	An event display of a Z/γ^* + jets event illustrating the effect of pileup interactions	60
183	3.10	The RMS of different missing transverse momentum definitions as a function of the average number of interactions per bunch crossing	60
184	3.11	The difference between the true and reconstructed values of the missing transverse momentum (a) and m_T (b) in a gluon fusion signal sample	62
186	3.12	Comparison of f_{recoil} distributions for Z/γ^* +jets, $H \rightarrow WW^*$, and other backgrounds with real neutrinos.	63
188	3.13	Signal significance as a function of required value for f_{recoil} and $p_{T,\text{rel}}^{\text{miss}(\text{trk})}$ in the ggF $H \rightarrow WW^*$ with $n_j = 0$	64

191	4.1	Jet multiplicity distribution in data and MC after applying lepton, jet, and $E_{\text{T},\text{rel}}^{\text{miss}}$ selections. The WW and top backgrounds have been normalized using control samples, and the hashed band indicates the total uncertainty on the prediction. [1]	71
192			
193	4.2	Comparison of m_{T} between data and simulation in the $n_j = 0$ WW (a) and $n_j = 1$ top (b) control samples [1]	73
194			
195	4.3	m_{T} distribution in the $H \rightarrow WW \rightarrow e\nu\mu\nu$ $n_j \leq 1$ channels for 8 TeV data [1].	75
196			
197	4.4	Diphoton mass spectrum in 7 and 8 TeV data. Panel a) shows the unweighted data distri- bution superimposed on the background fit, while panel c) shows the data where each event category is weighted by its signal to background ratio. Panels b) and d) show the respective distributions with background subtracted [1].	76
198			
199	4.5	Four lepton invariant mass spectrum ($m_{4\ell}$) in 7 and 8 TeV data compared to background estimate. A 125 GeV SM Higgs signal is shown in blue [1].	77
200			
201	4.6	Local p_0 distribution as a function of hypothesized Higgs mass for the $H \rightarrow ZZ^* \rightarrow 4\ell$ (a), $H \rightarrow \gamma\gamma$ (b), and $H \rightarrow WW^* \rightarrow \ell\nu\ell\nu$ (c) channels. Dashed curves show expected results, while solid curves show observed. Red curves are from 7 TeV data, blue curves from 8 TeV, and black curved combined [1].	79
202			
203	4.7	Combined 95% CL limits (a), local p_0 values (b), and signal strength measurement (c) as a function of Higgs mass [1].	80
204			
205	4.8	Comparison of measured signal strength μ for a 126 GeV Higgs in the 7 and 8 TeV datasets [1].	81
206			
207	4.9	Two dimensional likelihood as a function of signal strength μ and Higgs mass m_H [1].	81
208			
209	5.1	A comparison of the subleading lepton p_{T} spectrum between VBF $H \rightarrow WW^*$ production and $t\bar{t}$ background	84
210			
211	5.2	Leading jet η in VBF $H \rightarrow WW^*$ (red) and $t\bar{t}$ (black)	92
212			
213	5.3	Distributions of (a) m_{jj} , (b) Δy_{jj} , (c) $C_{\ell 1}$, and (d) $\sum m_{\ell j}$, for the VBF analysis. The top panels compare simulation and data, while the bottom panels show normalized distributions for all background processes and signal [61].	94
214			
215	5.4	A cartoon of the WW final state. Momenta are represented with thin arrows, spins with thick arrows. [61]	95
216			
217	5.5	Event display of a VBF candidate event [61].	96
218			
219	5.6	Distributions of $m_{\ell\ell}$ (top left), $\Delta\phi_{\ell\ell}$ (top right), and m_{T} (bottom), Higgs topology vari- ables used in the selection requirements of the cut-based signal region and as inputs to the BDT result. These are plotted after all of the BDT pre-training selection cuts [61].	99
220			
221	5.7	Distributions of m_{jj} (top left), Δy_{jj} (top right), $\sum C_{\ell}$ (bottom), VBF topology variables used in the selection requirements of the cut-based signal region and as inputs to the BDT result. These are plotted after all of the BDT pre-training selection cuts [61].	100
222			
223	5.8	Distributions of m_{jj} (a) and O_{BDT} (b) in the VBF $n_b = 1$ top CR [61].	102
224			

227	5.9	Comparison of m_{jj} shape in a same flavor $Z \rightarrow \ell\ell$ control region and the VBF cut-based signal region.	104
228	5.10	General illustration of the ABCD region definitions for $Z/\gamma^* \rightarrow \ell\ell$ background estimation.	105
231	5.11	Distribution of m_{T2} in the WW validation region of the VBF analysis [61].	106
232	5.12	Extrapolation factors for the $W + \text{jets}$ estimate derived for muons (a) and electrons (b) as a function of lepton p_T [61].	108
234	5.13	Background composition in final VBF signal region [61].	109
235	5.14	Variations in the top background extrapolation factor in the cut-based analysis due to PDF uncertainties, binned in m_T	III
237	5.15	Variations in the top background extrapolation factor in the cut-based analysis due to QCD scale uncertainties, binned in m_T	II2
239	5.16	Post-fit distributions in the cut-based VBF analysis. Panel (a) shows the one-dimensional m_T distribution, while (b) shows the data candidates split into the bins of m_T and m_{jj} used in the final fit [61].	II5
242	5.17	Postfit distributions in the BDT VBF analysis [61].	II6
243	5.18	Overlap between cut-based and BDT VBF signal region candidates in the m_{jj} - m_T plane. .	II6
244	6.1	Post-fit m_T distribution in the $n_j \leq 1$ regions [61].	120
245	6.2	Best fit signal strength $\hat{\mu}$ as a function of hypothesized m_H [61].	122
246	6.3	Local p_0 as a function of m_H [61].	122
247	6.4	Likelihood as a function of $\mu_{\text{VBF}}/\mu_{\text{ggF}}$ [61].	123
248	6.5	Likelihood scan as a function of μ_{VBF} and μ_{ggF} [61].	124
249	6.6	Likelihood scan as a function of κ_F and κ_V [61].	125
250	6.7	Comparison of signal strength measurements in different Higgs decay channels on ATLAS [90].	127
251	7.1	Parton luminosity ratios as a function of resonance mass M_X for 13/8 TeV and 7/8 TeV [91].	130
252	7.2	Summary of HH branching ratios [92].	131
253	7.3	Minimum ΔR between B decay vertices for different RSG masses in a $G_{\text{KK}}^* \rightarrow HH \rightarrow 4b$ sample with $c = 1$	132
255	7.4	Trigger efficiency for events passing all signal region selections as a function of mass in $G_{\text{KK}}^* \rightarrow HH \rightarrow 4b$ samples with $c = 1$ [101]. In the trigger names, “j” refers to a jet or jets. “ht” refers to H_T , the scalar sum of transverse momenta in the event. “bloose” refers to a loose b-tagging requirement applied to the jet. “aor” refers to anti- k_T jets with $R = 1.0$. The numbers at the end are the thresholds on the given quantity in GeV.	134
258	7.5	Comparison of untrimmed and trimmed jet masses for large radius jets in a RSG sample with $m_{G_{\text{KK}}^*} = 1$ TeV. JES (JMS) refers to the standard jet energy (mass) scale calibration for ATLAS [56].	135

262	7.6 Efficiency of finding two b -jets from each Higgs in an RSG event using calorimeter jets with $R = 0.3$ or different track jet radii [105]	136
263		
264	7.7 Illustration of the boosted selection requirements on Higgs candidates. Each large-radius calorime- ter jet (Higgs candidate) must contain two track jets	138
265		
266	7.8 Acceptance \times efficiency as a function of mass for (a) RSG and (b) narrow heavy scalar sig- nal models [107].	139
267		
268	7.9 Efficiency of requiring 3 or 4 b -tagged track jets vs. RSG mass. The efficiency quoted is rel- ative to the previous selection requirements (rather than an absolute efficiency).	140
269		
270	7.10 M_J^{sublead} vs. M_J^{lead} in a 2 b -tag data sample. The signal region is defined by the inner black contour ($X_{hh} < 1.6$) and the sideband region is defined by the outer contour ($R_{hh} >$ 35.8 GeV). The region between the black contours is the control region. The mass region which is enriched in $t\bar{t}$ background is also shown for illustration. [107]	142
271		
272		
273		
274	7.11 An illustration of the data-driven background estimation technique for the boosted anal- ysis	143
275		
276	7.12 Leading large-R jet mass in the 3 b (a) and 4 b (b) sideband regions. The multijet and $t\bar{t}$ back- grounds are estimated using the data-driven methods described above. Because their normal- izations are derived in the sideband region, the total background normalization is constrained by default to match the normalization of the data [107].	144
277		
278		
279		
280	7.13 Di-jet invariant mass ($M_{2,J}$) in the 3 b (a) and 4 b (b) control regions. The multijet and $t\bar{t}$ back- grounds are estimated using the data-driven methods described above [107].	145
281		
282	7.14 Di-jet invariant mass ($M_{2,J}$) in the 3 b (a) and 4 b (b) signal regions. The multijet and $t\bar{t}$ back- grounds are estimated using the data-driven methods described above. In the 3 b region, a graviton signal with $m_{G_{KK}^*} = 1.8$ TeV and $c = 1$ is overlaid, with the cross section mul- tiplied by a factor of 50 so that the signal is visible. In the 4 b region, signals with $m_{G_{KK}^*} =$ 1.0 TeV and $m_{G_{KK}^*} = 1.5$ TeV are overlaid, both with $c = 1$ and the yields multiplied by factors of 2 and 5 respectively [107].	150
283		
284		
285		
286		
287		
288	8.1 Di-jet invariant mass ($M_{2,J}$) in the resolved signal region. A graviton signal with $m_{G_{KK}^*} =$ 800 GeV and $c = 1$ is overlaid. [107].	153
289		
290	8.2 Expected and observed upper limit as a function of mass for G_{KK}^* in the RSG model with (a) $c = 1$ and (b) $c = 2$, as well as (c) H with fixed $\Gamma_H = 1$ GeV, at the 95% confidence	
291		
292	level in the CL_s method. [107]	156
293		
294	9.1 Combined ATLAS and CMS measurements in Run 1 for (a) Higgs signal strength in gluon fusion and VBF and (b) Higgs couplings normalized to their SM predictions	160
295	9.2 Discovery significance for RSG models at the HL-LHC in three different budget scenarios [114]. Systematic uncertainties on the background prediction (σ_B) of 2.5% and 5.0% are both tested.	161
296		

297	A.1	Estimated significance as a function of signal mass for RSG $c = 1$ models in the $3b$ (a) and 298 $4b$ (b) regions for different b -tagging efficiency working points	163
299	B.1	Summary of the inputs to the MV2 b -tagging algorithm	165
300	B.2	p_T of the leading track jet in the leading calorimeter jet for different signal masses in RSG $c =$ 301 1 models	166
302	B.3	MV2c2o score for the leading track jet (a) and subleading track jet (b) of the leading calorime- 303 ter jet for different signal masses in RSG $c = 1$ models	166
304	B.4	IP3D log-likelihood ratio ($\log(p_b/p_u)$) of the leading track jet in the leading calorimeter jet 305 for different signal masses in RSG $c = 1$ models	167
306	B.5	Mass (a) and number of tracks (b) for the secondary vertices computed with the SV1 algo- 307 rithm. When no secondary vertex is found, the quantities are assigned to default negative val- 308 ues.	167
309	B.6	Mass (a) and number of tracks (b) for vertices computed with the JetFitter algorithm. When 310 no vertices are found, the quantities are assigned to default negative values.	168
311	B.7	MV2c2o b -tagging efficiency for each of the four track jets in the boosted $4b$ selection as a func- 312 tion of RSG mass for $c = 1$ models.	169
313	B.8	MV2c2o score (a) and SV1 mass (b) for leading track jets with two truth b quarks ($n_{tb,lead} =$ 314 2) compared to those with only one truth b ($n_{tb,lead} = 1$).	170
315	B.9	Track fit χ^2/n_{DOF} (a) and number of pixel detector hits (b) for the leading track of the lead- 316 ing track jet in different mass RSG $c = 1$ samples	171
317	B.10	MV2c2o score (a) and SV1 mass (b) for leading track jets whose leading track jet has at least 318 four pixel hits ($N_{pix} \geq 4$) compared to those which do not ($N_{pix} < 4$).	171

Listing of tables

319

320	1.1	Production cross sections for a 125 GeV Higgs boson at $\sqrt{s} = 8$ TeV with scale and PDF		13
321	uncertainties [18].			
322	1.2	Branching ratios for a 125 GeV Higgs boson [18].		15
323	1.3	Possible channels for Higgs searches. Checkmarks denote the most sensitive production modes [5].		15
324			
325	1.4	Production cross sections for pair production of a 125 GeV Higgs boson at $\sqrt{s} = 14$ TeV with total uncertainty [19]. The uncertainties include QCD scale and PDF variations as well		16
326	as uncertainties on α_S			
327				
328	2.1	Evolution of LHC machine conditions [38, 39]		25
329	2.2	Performance requirements for the ATLAS detector [32].		37
330	2.3	Signal efficiencies for WH production with $H \rightarrow b\bar{b}$ and $H \rightarrow WW^* \rightarrow \mu\nu qq$ under different trigger configurations [45].		40
331				
332	3.1	A summary of backgrounds to the $H \rightarrow WW^* \rightarrow \ell\nu\ell\nu$ signal		55
333				
334	4.1	Monte carlo generators used to model signal and background for the Higgs search [1]. . . .		70
335	4.2	Normalization factors (ratio of data and MC yields in a control sample) for the Standard Model WW and top backgrounds in the $H \rightarrow WW^* \rightarrow \ell\nu\ell\nu$ analysis [1]. Only statistical un-		
336	certainties are shown.			73
337				
338	4.3	Data and expected yields for signal and background in the final $H \rightarrow WW^* \rightarrow \ell\nu\ell\nu$ signal region. Uncertainties shown are both statistical and systematic. [1]		74
339	4.4	Summary of the expected and observed significance and measured signal strengths in the com-		
340	bined 7 and 8 TeV datasets for the Higgs discovery analysis [1].			78
341				
342	5.1	Single lepton triggers used for electrons and muons. A logical “or” of the triggers listed for each lepton type is taken. Units are in GeV, and the i denotes an isolation requirement in the trigger.		84
343				
344	5.2	Di-lepton triggers used for different flavor combinations. The two thresholds listed refer to leading and sub-leading leptons, respectively. The di-muon trigger only requires a single lep-		
345	ton at level-1.			84
346				

347	5.3	Trigger efficiency for signal events and relative gain of adding a dilepton trigger on top of the single lepton trigger selection. The first lepton is the leading, while the second is the sub-leading. Efficiencies shown here are for the ggF signal in the $n_j = 0$ category but are comparable for the VBF signal.	85
348			
349	5.4	Monte Carlo samples used to model the signal and background processes [61].	86
350			
351	5.5	p_T dependent isolation requirements for muons. Muons are required to have the amount of calorimeter or track based cone sums be less than this fraction of their p_T	88
352			
353	5.6	p_T dependent requirements for electrons. Electrons are required to have the amount of calorimeter or track based cone sums be less than this fraction of their E_T	89
354			
355	5.7	Event selection for the $n_j \geq 2$ VBF analysis in the 8 TeV cut-based analysis [61].	97
356			
357	5.8	Top normalization factors computed at each stage of the cut-based selection. Uncertainties are statistical only.	101
358			
359	5.9	Top normalization factors computed for each bin of O_{BDT} . Uncertainties are statistical only.	101
360	5.10	$Z/\gamma^* \rightarrow \tau\tau$ correction factors for the VBF cut-based analysis. Uncertainties are statistical only.	104
361			
362	5.11	$Z/\gamma^* \rightarrow \ell\ell$ normalization factors for cut-based and BDT analyses. Uncertainties are statistical only.	106
363			
364	5.12	Systematic uncertainties for various processes in the cut-based VBF analysis, given in units of % change in yield. Values are given for the low m_{jj} signal region.	110
365			
366	5.13	Composition of the post-fit uncertainties (in %) on the total signal (N_{sig}), total background (N_{bkg}), and individual background yields in the VBF analysis [61].	113
367			
368	5.14	Event selection for the VBF BDT analysis. The event yields in (a) are shown after the pre-selection and the additional requirements applied before the BDT classification (see text). The event yields in (b) are given in bins in O_{BDT} after the classification [61].	114
369			
370			
371	6.1	All signal regions definitions input into final statistical fit [61].	119
372	6.2	Post-fit yields in the different ggF and VBF dedicated signal regions [61].	120
373	7.1	Summary of requirements on objects used in the $X \rightarrow HH \rightarrow b\bar{b}b\bar{b}$ search	137
374	7.2	Effect of boosted selection on data, RSG signal models, $t\bar{t}$, and $Z + \text{jets}$. The numbers from simulation are normalized with the MC generator cross section and do not take into account the data driven estimates described in section 7.6 [108].	141
375			
376	7.3	Mass region definitions used for background estimation	142
377			
378	7.4	Parameters derived for exponential fit to background M_{2J} shape in the 3 b and 4 b signal regions [108]	145
379			
380	7.5	The number of events in data and predicted background events in the boosted 3-tag and 4-tag sideband and control regions. The uncertainties shown are statistical only. [107]	146
381			

382	7.6 Summary of systematic uncertainties in the total background and signal event yields (expressed in %) in the boosted 3-tag and 4-tag signal regions. Systematic uncertainties on the signal normalization are shown for models with $m_{G_{KK}^*} = 1.5$ TeV and both $c = 1$ and $c = 2$ as well as a narrow width heavy scalar.	148
383		
384		
385		
386	7.7 Alternate fit functions used to model the M_{JJ} distribution in the QCD multijet background. In the equations, $x = M_{JJ}/\sqrt{s}$	149
387		
388		
389		
390	7.8 Observed yields in the 3-tag and 4-tag signal regions for the boosted analysis compared to the predicted number of background events Errors correspond to the total uncertainties in the predicted event yields. The yields for a graviton with $m_{G_{KK}^*} = 1$ TeV and $c = 1$ are also shown. [107]	150
391		
392	8.1 Observed yields in the resolve selection 4-tag signal region compared to the predicted num- ber of background events Errors correspond to the total uncertainties in the predicted event yields. The yields for a graviton with $m_{G_{KK}^*} = 800$ GeV and $c = 1$ are also shown. [107] .	152
393		
394		

Acknowledgments

397 I have been a member of the Harvard ATLAS group for many years now, first as an undergraduate and
 398 then as a graduate student. As a result, I have had the privilege of interacting with many amazing people
 399 there over the years and have accumulated a large list of folks to thank.

400 First and foremost, I must thank the two people who have effectively been my academic parents since
 401 I started in the Harvard group: João Guimarães da Costa and Melissa Franklin. Melissa Franklin and
 402 João Guimarães da Costa. They have both been so important to both my academic and personal devel-
 403 opment that I can't even put one before the other. João has been an excellent PhD advisor, showing me
 404 how to look at the big picture and helping me navigate the sometimes complicated politics of ATLAS.
 405 He got me started on my first projects with ATLAS as a young college sophomore before there was even
 406 beam in the LHC (go cosmic ray muons!). He has also been a constant source of advice and support,
 407 even when we have been on different continents. Melissa gave me my start in HEP as a summer student
 408 on CDF and has been an unbelievable mentor throughout my time at Harvard. I still remember our
 409 weekly chalkboard particle physics lessons after that first summer. She also graciously took me on as a
 410 co-advisee after João moved on to his new position at IHEP. I am incredibly lucky to have had both of
 411 them as advisors.

412 Another mentor who was essential to my development as a graduate student is Paolo Giromini. His
 413 uncanny knowledge and intuition about detectors is unmatched and I am very grateful to have had the
 414 chance to work with him on the micromegas for the ATLAS New Small Wheel upgrade project. I owe
 415 essentially all my practical knowledge about detectors (and building things in general) to him. I also
 416 appreciated his unique sense of humor which made sometimes difficult tasks much easier to get through.

417 I am grateful to John Huth and Masahiro Morii for their helpful advice as the other professors in the
 418 Harvard ATLAS group as well. I especially thank John for helping me get started on the micromegas
 419 trigger project and being a great professor to TF particle physics for. Additionally I thank Howard

420 Georgi for serving as my third committee member and offering me feedback throughout my graduate
421 career.

422 I also owe enormous thanks to Hugh Skottowe, the postdoc that I worked most closely with in my
423 early years as a graduate student. He was always able to help me through complicated tasks in everything
424 from writing code to understanding difficult physics concepts. I particularly enjoyed walking down to
425 his office in Palfrey at random times and talking through whatever problem I was tackling on that day.

426 Alex Tuna, the second postdoc that I worked closely with at Harvard, deserves great thanks as well.
427 He helped me push through to the end of my graduate career and offered great advice along the way.

428 Being at Harvard, I have seen an incredible array of graduate students graduate before me: Ben Smith,
429 Verena Martinez Outschoorn, Srivas Prasad, Michael Kagan, Giovanni Zevi Della Porta, Laura Jeanty,
430 Kevin Mercurio, William Spearman, and Andy Yen. I want to thank them all for showing me what a
431 good physicist looks like and for patiently answering my questions and offering insightful advice about
432 physics and life.

433 Getting through graduate school would not have been possible without the support and friendship
434 of the other students in our group. Thanks to Emma Tolley for geeking out with me about cool com-
435 puting stuff, going to taste delicious beers with me, and helping start the Palfrey tradition of Taco Tues-
436 days. Thanks to Brian Clark for being a great friend and housing companion both in Kirkland House
437 and in our tiny summer apartment in Geneva (and thanks to his partner Allison Goff for the same rea-
438 sons!). Thanks to Siyuan Sun for giving me my first aikido lesson and always being there for great con-
439 versations, big and small. Tony (Baojia) Tong deserves special recognition for working with me on the
440 4b analysis and putting up with my sometimes strange requests (and giving me rides to the Val Thoiry
441 Migros so I wouldn't have to pay exorbitant Geneva grocery prices!). Stephen Chan is probably the only
442 student in the group who both understands my references to the Sopranos and makes some of his own.
443 To the younger graduate students - Karri Di Petrillo, Jennifer Roloff, Julia Gonski, and Ann Wang - I
444 want to say thank you for making the group a fun and lively place to be and giving all of us energy that
445 the older graduate students like myself can sometimes lack.

446 I'd like to thank Annie Wei and Gray Putnam, the two undergraduates I have worked with as a gradu-

447 ate student. Their unbelievable intuition and quickness in picking up difficult particle physics concepts
448 is inspiring.

449 I would also like to thank all of the postdocs that I have interacted with in my time in the Harvard
450 group: Kevin Black, Alberto Belloni (who would always ask me “Do you have it?”...I can now say that
451 I do!), Shulamit Moed, Corrinne Mills, Geraldine Conti, David Lopez Mateos, Chris Rogan, Valerio
452 Ippolito, and Stefano Zambito.

453 There are many people on ATLAS who have helped me get to this point as well. In the *WW* group,
454 I have to thank Jonathan Long, Joana Machado Miguens, Ben Cerio, Philip Chang, Bonnie Chow,
455 Richard Polifka, Heberth Torres, Tae Min Hong, and Jennifer Hsu for being wonderful colleagues and
456 making the entire analysis run smoothly. In the *4b* group, I have to thank Qi Zeng, Tony Tong, Alex
457 Tuna, Michael Kagan, Max Bellomo, John Alison, and Patrick Bryant.

458 Kirkland House was my home for the last three years of graduate school and was an wonderful envi-
459 ronment and support system. I want to thank my fellow tutors, especially Brian Clark and Allison Goff
460 (again), Zach Abel, Kelly Bodwin, Alex Lupsasca, John and Pam Park, Luke and Erin Walczewski, and
461 Philip Gant for their friendship and support. I also want to thank Kate Drizos Cavell, Bob Butler, and
462 the Faculty Deans Tom and Verena Conley.

463 There are still a few friends that haven’t been covered yet and deserve great thanks. Jake Connors and
464 Meredith MacGregor have been absolutely wonderful friends and I thank them in particular for the
465 many home-cooked meals and great conversations we’ve had in their apartment. Nihar Shah has been
466 my friend and confidant since we were both wee freshmen in Harvard Yard. Gareth Kafka, though he
467 sits on the “neutrino” side of Palfrey House, has made days there more fun and has also been an enthusi-
468 astic participant in the Palfrey Taco Tuesdays.

469 Being at Harvard necessarily means having to navigate through bureaucracy at some point or another.
470 I thank Lisa Cacciabuado, Carol Davis, and Jacob Barandes for always having open doors and being the
471 most kind, helpful people in the Physics department.

472 I thank Venky Narayananamurti for putting on a great SPU course that I was proud to be a part of and
473 TF for. I’d also like to thank Jim Waldo for offering me much advice about working in Computer Science

474 and giving me a fun data project to be a part of in my free time.

475 I grew up in a very tight knit Serbian community on the south side of Chicago which helped make
476 me the person I am today. I would like to thank all of the people at St. Simeon Mirotochivi Serbian
477 Orthodox Church who have always been sources of enthusiasm and support in my life.

478 I would not be here without the unconditional love and constant support and encouragement of my
479 family. To my pokojni Dedas Branko and Miloje, my pokojni Baba Milka, and my Baba Desa, I want to
480 say thank you for instilling in me at an early age the love of curiosity and storytelling that I have carried
481 throughout my life. To my sister Angelina, I want to say thank you for always loving me and being my
482 partner in crime throughout our childhoods. To my parents, Miroljub and Nada, Tata and Mama, I
483 really cannot express how grateful I am to you and how much I owe you. As I look back now I see how
484 I am a combination of both of your best qualities and every day I am in situations where I understand
485 more and more the lessons you made sure to teach me and the sacrifices you made to make sure I got the
486 best possible education. I love you all.

487 Finally, I have to thank my soul mate, the one person in my life who understands me more than any-
488 one else, my fiancée Kelly Brock. You are my sounding board, my support system, my cheerleader (fig-
489 uratively and literally!), my best friend, my role model, and my everything. I would not have gotten
490 through graduate school without you and my life would not be the same without you. I cannot wait to
491 start our new lives together as the married doctors, tackling whatever comes our way with the same zeal
492 with which we tackled graduate school. I love you with all my heart and soul.

0

493

494

Introduction

495 The Higgs boson is often described as one of the cornerstones of the Standard Model. Since the concep-
496 tion of the Higgs mechanism as the source of electroweak symmetry breaking in the early 1960s, count-
497 less collider experiments have searched for this elusive particle. This dissertation presents the story of the
498 Higgs boson from its discovery to its use as a tool in the search for physics beyond the Standard Model
499 with the ATLAS detector at the Large Hadron Collider (LHC).

500 One of the first priorities of the early LHC was the search for the Higgs boson. This search was first
501 tackled in three main channels: $H \rightarrow \gamma\gamma$, $H \rightarrow ZZ^*$, and $H \rightarrow WW^*$. Each channel has its own
502 merits, but the WW^* is particularly suited to searching over a wide range of masses. The $H \rightarrow WW^*$
503 branching ratio is large and it is the primary decay channel above the $2m_W$ mass threshold.

504 While the rate of events produced in $H \rightarrow WW^*$ is large, the channel poses some challenges. First,
505 the most common mode of study for this channel is $H \rightarrow WW^* \rightarrow \ell\nu\ell\nu$. With neutrinos in the
506 final state, it is not possible to fully reconstruct the invariant mass of the parent Higgs like the $\gamma\gamma$ and

507 $ZZ \rightarrow 4\ell$ channels. Second, the final state topology is mimicked by a wide variety of backgrounds that
508 need to be properly estimated. This means tailored selection requirements for background reduction
509 and robust background estimation techniques must both be developed.

510 In 2012, the ATLAS and CMS experiments announced the discovery of a new particle consistent with
511 the Higgs boson [1, 2]. In ATLAS, this discovery was made with 4.8 fb^{-1} collected at $\sqrt{s} = 7 \text{ TeV}$ and
512 5.8 fb^{-1} at $\sqrt{s} = 8 \text{ TeV}$. The $H \rightarrow WW^* \rightarrow \ell\nu\ell\nu$ analysis played an important role in this discovery.
513 After the discovery, measurement of the properties of the newly discovered particle and confirmation
514 of its consistency with the Standard Model Higgs were the main priorities. The WW^* channel is also
515 uniquely suited to these types of measurements. Because of its good rate, it offers some of the best cross
516 section measurements available among the various Higgs decay modes. It is also suited for measurement
517 of multiple Higgs production modes, like the vector boson fusion (VBF) mode, where incoming quarks
518 radiate W/Z bosons which fuse to make a Higgs. In VBF production with the WW^* decay channel,
519 the coupling of the Higgs to the W boson is present in both the production and decay which allows for
520 more precise measurements of this coupling than other channels which rely on gluon fusion production
521 (where gluons couple to the Higgs through a top loop in the production). The measurement of VBF
522 carries the additional challenge that its cross section is an order of magnitude smaller than that of gluon
523 fusion, meaning that the large branching ratio to WW^* offers an additional advantage in isolating this
524 production mode. In the final ATLAS Run 1 results, combining 20.3 fb^{-1} taken at $\sqrt{s} = 8 \text{ TeV}$ with
525 the 4.8 fb^{-1} collected at $\sqrt{s} = 7 \text{ TeV}$, the WW^* channel achieved its first observation of VBF produc-
526 tion of the Higgs.

527 After Run 1 of the LHC, with the existence of the Higgs now firmly established, the focus shifted to
528 searches for physics beyond the Standard Model. In particular, searches for high mass resonances bene-
529 fit from the LHC's increase to $\sqrt{s} = 13 \text{ TeV}$ in Run 2. The cross section for a generic gluon-initiated
530 resonance with a mass of 2 TeV increases tenfold in Run 2, making searches for high mass resonances a
531 high priority. The newly discovered Higgs can be used as a tool in these searches. After the discovery,
532 the Higgs boson provides a large swath of unmeasured phase space where new physics could be discov-
533 ered. Higgs pair production in the Standard Model has a low cross section that requires large datasets

534 (on the order of the LHC’s lifetime) for full measurement. However, new physics can modify this cross
535 section, especially through new resonances which decay to two Higgs bosons. Such high mass resonances
536 also produce difficult to recognize final state topologies due to the merging of decay products from high
537 momentum Higgs bosons. A search for Higgs pair production in the $HH \rightarrow b\bar{b}b\bar{b}$ final state was per-
538 formed with 3.2 fb^{-1} collected with ATLAS at $\sqrt{s} = 13 \text{ TeV}$ in 2015. The results are presented in this
539 dissertation with a focus on a dedicated signal region for boosted final states. This signal region uses new
540 techniques for recognizing jet substructure and b -tagging to the improve signal acceptance of high mass
541 resonances.

542 This dissertation begins by discussing the discovery of the Higgs and the role of the $H \rightarrow WW^* \rightarrow$
543 $\ell\nu\ell\nu$ channel. It then discusses the first observation of the VBF production mode in $H \rightarrow WW^* \rightarrow$
544 $\ell\nu\ell\nu$ with the full ATLAS Run 1 dataset, as well as the final combined Run 1 measurements from this
545 channel. Finally, it presents a search for Higgs pair production in the $HH \rightarrow b\bar{b}b\bar{b}$ channel. It is orga-
546 nized into four parts.

547 Part 1 presents the theoretical and experimental background required for the subsequent parts. Chap-
548 ter 1 gives an overview of Higgs physics, particularly single and double Higgs production in the Standard
549 Model and beyond. Chapter 2 presents details regarding the Large Hadron Collider and the ATLAS
550 experiment. The evolution of machine conditions, descriptions of the ATLAS sub-detectors, and an
551 overview of object reconstruction in ATLAS are all shown. A brief interlude on the ATLAS Muon New
552 Small Wheel upgrade is also given, as this upgrade has been a focus of my graduate work and will have
553 important impact on ATLAS’ ability to study the Higgs at the High Luminosity LHC.

554 Part 2 discusses the observation and measurement of the Higgs in the $H \rightarrow WW^* \rightarrow \ell\nu\ell\nu$
555 channel in the ATLAS Run 1 dataset at $\sqrt{s} = 7$ and 8 TeV . Because I worked in this channel from
556 before the discovery through to the final analysis of the Run 1 dataset, Part 2 is organized in such a way
557 to allow easy presentation of multiple analyses on different subsets of the full Run 1 dataset. Chapter 3
558 presents a general overview of the $H \rightarrow WW^*$ analysis strategy and defines many of the variables and
559 common elements used in the rest of Part 2. Chapter 4 presents the discovery of the Higgs boson, fo-
560 cusing on the role of the WW^* channel in this discovery. Chapter 5 presents the first observation of the

561 VBF production mode of the Higgs in the WW^* channel, a study which was done on the full Run 1
562 ATLAS dataset. In this chapter, the focus is mainly on the selection cut-based VBF analysis. The cut-
563 based analysis was an important first step to the final VBF result which used a Boosted Decision Tree
564 (BDT). Where appropriate, connections between the cut-based and BDT analyses are shown and their
565 compatibility is discussed. Finally, the VBF analysis was an important input into the combined Run 1
566 $H \rightarrow WW^* \rightarrow \ell\nu\ell\nu$ result, which used both the gluon fusion and VBF channels in a combined
567 fit to infer properties of the Higgs, including its couplings to the gauge bosons and its production cross
568 section. This is the topic of Chapter 6.

569 Part 3 presents a search for Higgs pair production in the $HH \rightarrow b\bar{b}b\bar{b}$ channel. Chapter 7 presents
570 an overview of this search in the boosted regime, where the Higgs pairs are the result of the decay of a
571 heavy resonance. Chapter 8 shows the combined results between the boosted regime and the resolved
572 regime, which is sensitive to lower mass resonances and non-resonant Higgs pair production. Finally,
573 Part 4 presents a conclusion and brief outlook of future Higgs physics with ATLAS.

574

Part I

575

Theoretical and Experimental Background

In modern physics, there is no such thing as “nothing.”

Richard Morris

1

576

577

The Physics of the Higgs Boson

578 This chapter presents an overview of the Standard Model of Particle Physics and in particular the physics
579 of the Higgs boson. First, a brief overview of the Standard Model and its history are presented. Then, a
580 description of the Higgs mechanism of electroweak symmetry breaking is given. Next, the physics of sin-
581 gle Higgs boson production and decay is described. The Standard Model also allows for production of
582 two Higgs bosons and this is detailed as well. Finally, di-Higgs production in two beyond the Standard
583 Model (BSM) theories - Randall-Sundrum gravitons (RSG) and Two Higgs Doublet Models (2HDM) -
584 is shown.

585 I.I THE STANDARD MODEL OF PARTICLE PHYSICS

586 The Standard Model (SM) of Particle Physics is a quantum field theory describing the fundamental
587 particles of nature and the forces that govern their interactions. Several comprehensive treatments of
588 the SM already exist in the literature [3–8] and this section will not rehash those. Rather, this section

589 presents a brief overview of the SM particles and forces in order to define them for subsequent discussions.
 590

591 The Standard Model consists of two primary categories of fundamental particles: fermions (spin 1/2
 592 particles) and bosons (integer spin particles). The SM also describes three forces: electromagnetism, the
 593 weak nuclear force, and the strong nuclear force. Gravity is not included in the theory and is largely irrelevant
 594 at the scales currently probed by collider experiments. Within the fermions, there are both quarks
 595 (which interact via all three forces) and the leptons. The charged leptons interact via electromagnetic and
 596 weak interactions, while neutrinos (neutral leptons) interact only via the weak force. Within the bosons,
 597 there are the W^\pm and Z bosons (the mediators of the weak force), the gluon (g , the mediator of the
 598 strong force), and the photon (γ), the mediator of the electromagnetic force. Finally, there is the Higgs
 599 boson, a fundamental spin-0 particle resulting from the Higgs mechanism of electroweak symmetry
 600 breaking. Figure 1.1 summarizes the fermions and bosons of the SM.

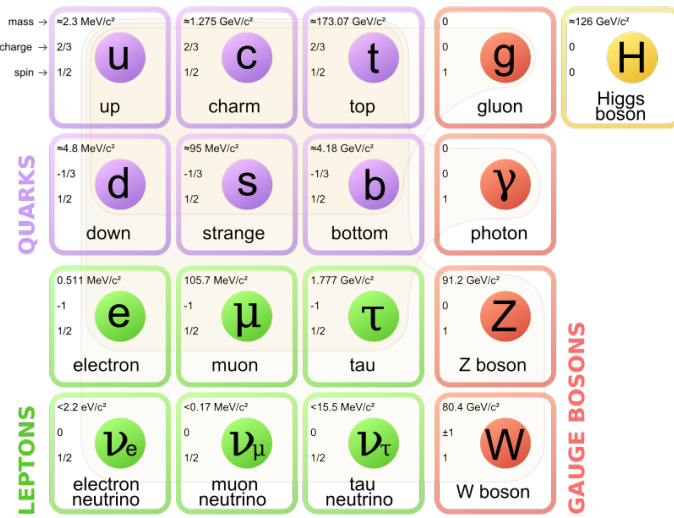


Figure 1.1: The particles of the Standard Model and their properties [6].

601 The Standard Model coalesced into a unified theoretical framework in the 1960s through the work
 602 of Glashow, Weinberg, Salam, and others on the theory of electroweak interactions [9–12]. This theory
 603 characterized both the electromagnetic and weak interactions as unified under a single gauge symmetry
 604 group, namely $SU(2) \times U(1)$. At low enough energy scales (on the order of the W and Z masses,
 605 the electroweak symmetry is broken, as evidenced by the fact that the weak bosons have mass while the

606 photon does not. The discovery of the Higgs boson in 2012 confirmed the Higgs mechanism as the most
 607 likely candidate for this electroweak symmetry breaking [1, 2]. The electroweak theory is then combined
 608 with the theory of quantum chromodynamics (which models the strong sector as a non-Abelian $SU(3)$
 609 gauge group) to form the complete SM [13].

610 1.2 ELECTROWEAK SYMMETRY BREAKING AND THE HIGGS

611 In the Standard Model Lagrangian, it is difficult to include mass terms for the W and Z bosons without
 612 breaking the fundamental gauge symmetry of the Lagrangian. A traditional mass term does not preserve
 613 the $SU(2) \times U(1)$ symmetry. Additionally, scattering of massive W and Z bosons violate unitarity
 614 and these diagrams diverge at high energy scales. In the 1960s, Higgs, Brout, Englert, Guralnik, Kibble,
 615 and Hagen developed a mechanism for spontaneous symmetry breaking via the addition of a complex
 616 scalar doublet to the SM. Three of the four real degrees of freedom of this complex field would go to the
 617 longitudinal modes of the W^\pm and Z , thus allowing them to have mass [14–17]. The remaining degree
 618 of freedom would manifest as an additional scalar, known now as the Higgs boson.

619 The mechanism works by introducing a Lagrangian for the newly introduced field that still respects
 620 the symmetry of the Standard Model inherently, but with a minimum at a non-zero vacuum expectation
 621 value for the field. In this minimum of the potential, the electroweak symmetry is broken. Specifically,
 622 consider a complex scalar doublet Φ with four degrees of freedom, as shown in equation 1.1.

$$\Phi = \begin{pmatrix} \phi^+ \\ \phi^0 \end{pmatrix} = \frac{1}{\sqrt{2}} \begin{pmatrix} \phi_1^+ + i\phi_2^+ \\ \phi_1^0 + i\phi_2^0 \end{pmatrix} \quad (1.1)$$

623 The minimal potential of a self-interacting Higgs that still respects the SM symmetry is given in equa-
 624 tion 1.2.

$$V(\Phi) = \mu^2 \Phi^\dagger \Phi + \lambda (\Phi^\dagger \Phi)^2 \quad (1.2)$$

625 If the μ^2 term of this potential is positive, then the potential has a minimum at $\Phi = 0$ and the SM

626 symmetry is preserved. However, if instead $\mu^2 < 0$, then the minimum is at a finite value of Φ , namely

$$\Phi_{\min} = \frac{1}{\sqrt{2}} \begin{pmatrix} 0 \\ v \end{pmatrix} \quad (1.3)$$

627 where $v = \sqrt{\mu^2/\lambda}$. Because this is the location of the minimum, it corresponds to the vacuum expecta-
628 tion value for the field ($\langle \Phi \rangle = \Phi_{\min}$). The excitations of the Higgs can then be parameterized as

$$\Phi = \frac{1}{\sqrt{2}} \begin{pmatrix} 0 \\ v + H \end{pmatrix} \quad (1.4)$$

629 The full scalar Lagrangian, including the kinetic term, is then given as

$$\mathcal{L}_s = (D^\mu \Phi)^\dagger (D_\mu \Phi) - V(\Phi) \quad (1.5)$$

630 where the covariant derivative is defined as

$$D_\mu = \partial_\mu + \frac{ig}{2} \tau^a W_\mu^a + ig' Y B_\mu \quad (1.6)$$

631 and W^1, W^2, W^3 and B are the $SU(2)$ and $U(1)$ gauge fields of the electroweak theory, respectively. g
632 and g' are the corresponding coupling constants. With the scalar Lagrangian in place, the physical gauge
633 fields can then be written as

$$W_\mu^\pm = \frac{1}{\sqrt{2}} (W_\mu^1 \mp i W_\mu^2) \quad (1.7)$$

634

$$Z_\mu = \frac{-g' B_\mu + g W_\mu^3}{\sqrt{g^2 + g'^2}} \quad (1.8)$$

635

$$A_\mu = \frac{g B_\mu + g' W_\mu^3}{\sqrt{g^2 + g'^2}} \quad (1.9)$$

636 Equation 1.7 corresponds to the charged W^+ and W^- bosons, equation 1.8 corresponds to the neutral

637 Z boson, and equation 1.9 corresponds to the neutral photon. The masses of the particles also arise from
 638 the Lagrangian. The photon has zero mass, while the masses of the W and Z bosons are given in equa-
 639 tion 1.10.

$$\begin{aligned} M_W^2 &= \frac{1}{4}g^2v^2 \\ M_Z^2 &= \frac{1}{4}(g^2 + g'^2)v^2 \end{aligned} \quad (1.10)$$

640 The fermion masses also arise through a coupling with the Higgs via the Yukawa interaction (for a de-
 641 tailed description, see [8]). In this case the coupling between the Higgs and the fermions goes as

$$g_{Hf\bar{f}} = \frac{m_f}{v} \quad (1.11)$$

642 The full Lagrangian of Higgs interactions can be written as

$$\mathcal{L}_{\text{Higgs}} = -g_{Hf\bar{f}}\bar{f}fH + \frac{g_{HHH}}{6}H^3 + \frac{g_{HHHH}}{24}H^4 + \delta_V V_\mu V^\mu \left(g_{HV}VH + \frac{g_{HVV}}{2}H^2 \right) \quad (1.12)$$

643 with

$$\begin{aligned} g_{HV} &= \frac{2m_V^2}{v} & g_{HVV} &= \frac{2m_V^2}{v^2} \\ g_{HHH} &= \frac{3m_H^2}{v} & g_{HHHH} &= \frac{3m_H^2}{v^2} \end{aligned} \quad (1.13)$$

644 Here, V refers to the W^\pm and Z , and $\delta_W = 1$ while $\delta_Z = 1/2$. Phenomenologically, there are a few
 645 features of this Lagrangian that are useful to note. First, note that the Higgs mass is a free parameter
 646 of the theory that must be determined experimentally. Second, note that the coupling of the Higgs to
 647 the vector bosons and fermions scales with the masses of these particles, a fact that is important when
 648 considering both the production and decays of the particle. Also note that the branching ratio of the
 649 Higgs to W bosons will be twice that of the branching ratio to Z if the Higgs mass is large enough to
 650 produce the particles on shell because of the extra symmetry factor associated with the W coupling.
 651 Finally, note the presence of the cubic and quartic Higgs self interaction terms, which can lead to final
 652 states with multiple Higgs bosons produced.

653 1.3 HIGGS BOSON PRODUCTION AND DECAY

654 This section discusses the properties of Higgs production and decay mechanisms. The details presented
655 here will focus on the properties of a 125 GeV Higgs boson, as this is the mass closest to that of the
656 newly discovered Higgs.

657 1.3.1 HIGGS PRODUCTION

658 The Higgs is produced by four main production modes at the Large Hadron Collider - gluon-gluon
659 fusion (ggF), vector boson fusion (VBF), associated production with a W or Z boson, or associated
660 production with top quarks ($t\bar{t}H$). Figure 1.2 shows the Feynman diagrams for these four modes.

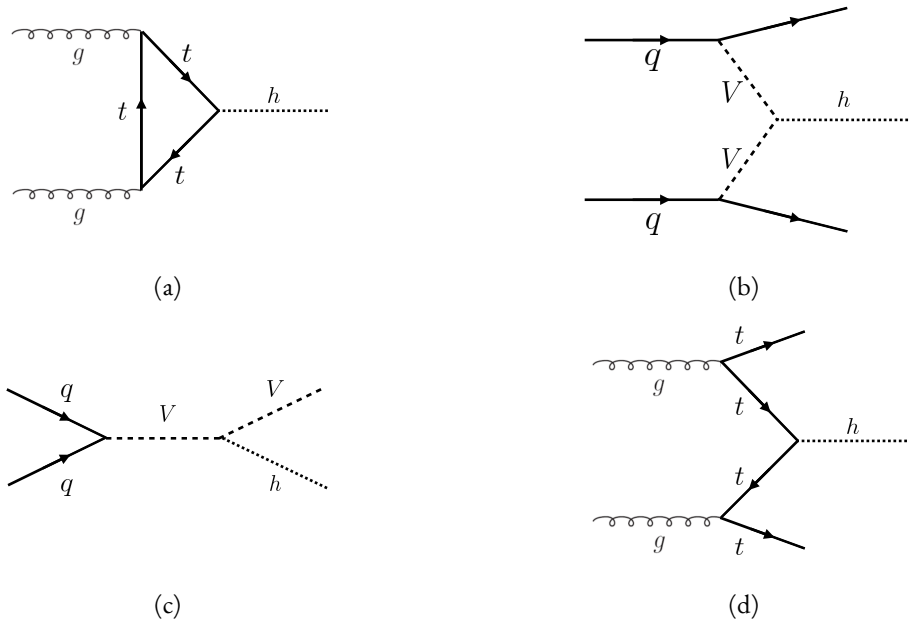


Figure 1.2: The four most common Higgs boson production modes at the LHC: (a) gluon-gluon fusion, (b) vector boson fusion, (c) $W/Z + H$ production, (d) $t\bar{t}H$ production

661 In gluon-gluon fusion, gluons from the incoming protons fuse via a top-quark loop to produce a
662 Higgs. The top quark is the dominant contribution in the loop due to its heavy mass and the fact that
663 the Higgs-fermion coupling constant scales with fermion mass. In vector boson fusion, the incoming
664 quarks each radiate a W or Z boson which fuse to produce the Higgs. This production mode results in
665 a final state with a Higgs boson and two additional jets which tend to be forward because they carry the

666 longitudinal momentum of the incoming partons. The Higgs can also be produced in association with a
 667 W or Z boson. The W/Z is produced normally and then radiates a Higgs (this mode is also sometimes
 668 known as “Higgs-strahlung”). Finally, the Higgs can be produced in association with two top quarks.
 669 Each incoming gluon splits into a $t\bar{t}$ pair, and one of the top pairs combines to create a Higgs. Figure 1.3
 670 shows the production cross section for a 125 GeV Higgs boson in each of these modes at a pp collider as
 671 a function of center of mass energy.

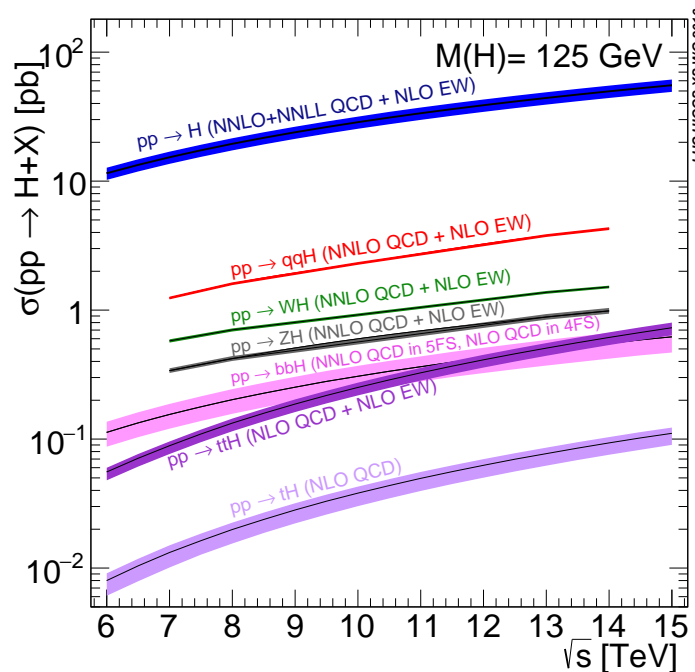


Figure 1.3: Higgs production cross sections as a function of center of mass energy (\sqrt{s}) at a pp collider [18].

672 In figure 1.3, note that gluon fusion has the largest cross section, while VBF is the second largest at
 673 approximately a factor of 10 smaller. The figure also includes the less commonly studied $b\bar{b}H$ and tH
 674 modes. The $b\bar{b}H$ and tH modes are not studied as commonly as $t\bar{t}H$ due to the larger background con-
 675 tributions and lower cross sections, respectively. At $\sqrt{s} = 8$ TeV, ggF production of a 125 GeV Higgs
 676 has a cross section of 19.47 pb, while VBF has a cross section of 1.601 pb [18]. The cross sections of all
 677 of the main Higgs production modes at this center of mass energy, as well as their uncertainties from
 678 varying the renormalization and factorization scales and PDFs, are summarized in table 1.1 for a 125 GeV
 679 Higgs.

Production mode	σ (pb)	QCD scale uncert. (%)	PDF + α_s uncert. (%)
Gluon fusion	19.47	+7.3/ - 8.0	3.1
Vector boson fusion	1.601	+0.3/ - 0.2	2.2
WH	0.7026	+0.6/ - 0.9	2.0
ZH	0.4208	+2.9/ - 2.4	1.7
$t\bar{t}H$	0.1330	+4.1/ - 9.2	4.3
bbH	0.2021	+20.7/ - 22.3	
$t\bar{H}$ (t -channel)	0.01869	+7.3/ - 16.5	4.6
$t\bar{H}$ (s -channel)	1.214×10^{-3}	+2.8/ - 2.4	2.8

Table 1.1: Production cross sections for a 125 GeV Higgs boson at $\sqrt{s} = 8$ TeV with scale and PDF uncertainties [18].

680 1.3.2 HIGGS BRANCHING RATIOS

681 The fact that the Higgs couples more strongly to more massive particles is crucial for understanding its
 682 branching ratios. The width for Higgs decays to fermions is given in equation 1.14 [5].

$$\Gamma(H \rightarrow f\bar{f}) = \frac{N_c \sqrt{2} G_F m_f^2 m_H}{8\pi} \quad (1.14)$$

683 In this case, N_c is the number of colors, G_F is the Fermi constant, m_f is the mass of the fermion, and
 684 m_H is the mass of the Higgs. Note that the width scales with the square of the fermion mass. (This also
 685 assumes that the Higgs mass is large enough to decay with both the fermions on shell.)

686 The decay width to WW is given in equation 1.15 [5].

$$\Gamma(H \rightarrow W^+W^-) = \frac{\sqrt{2} G_F M_W^2 m_H}{16\pi} \frac{\sqrt{1-x_W}}{x_W} (3x_W^2 - 4x_W + 4) \quad (1.15)$$

687 where m_W is the mass of the W and $x_W = 4M_W^2/m_H^2$. To get the branching ratio to ZZ , the equa-
 688 tion is divided by 2 to account for identical particles in the final state, and x_W is replaced with $x_Z =$
 689 $4M_Z^2/m_H^2$. This is shown in equation 1.16 [5].

$$\Gamma(H \rightarrow ZZ) = \frac{\sqrt{2} G_F M_Z^2 m_H}{32\pi} \frac{\sqrt{1-x_Z}}{x_Z} (3x_Z^2 - 4x_Z + 4) \quad (1.16)$$

690 These formulas can also be visualized as a function of Higgs mass. Figure 1.4 shows the branching ratios
as a function of the Higgs mass. There are a few interesting features to note in this figure. First, note that

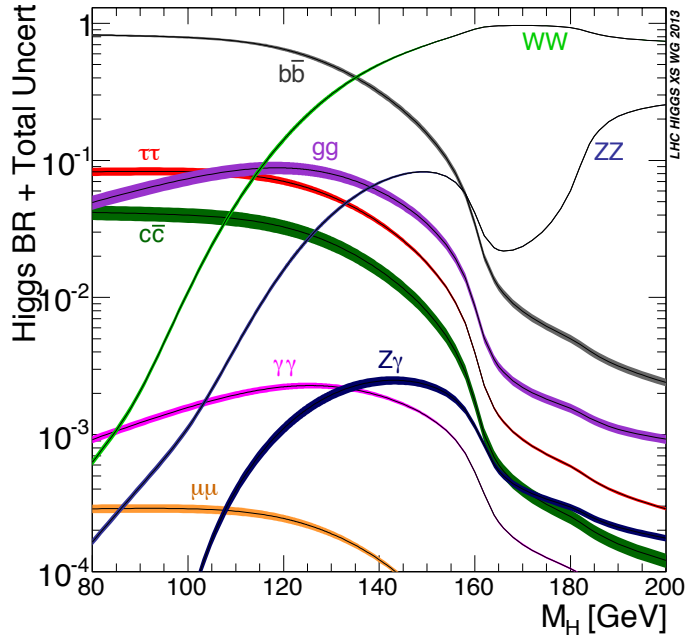


Figure 1.4: Higgs boson branching ratios as a function of m_H [18].

691
692 at high Higgs masses, once on-shell production of both W and Z bosons is possible, these two decays
693 are the dominant ones due to the large masses of the W/Z . Also note that the branching ratio to W s
694 is twice that of Z s at these large masses due to the δ_V symmetry factor noted previously. At 125 GeV,
695 the Higgs is accessible through many different decay modes. The largest branching ratio is the decay
696 $H \rightarrow b\bar{b}$ at 58.24% [18]. This branching is larger than the WW/ZZ decays because one of the two
697 bosons must be produced off-shell for $m_H = 125$ GeV. The second largest branching ratio is to WW^*
698 at 21.37 % (before taking into account the branching ratios of the W). Table 1.2 summarizes the branch-
699 ing ratios for a 125 GeV Higgs. Note that there is in fact a Higgs branching ratio to $\gamma\gamma$ even though
700 photons are massless. This decay happens through a loop (the largest contributions to the loop are top
701 and W) which suppresses the branching ratio.

702 Note that the branching ratios alone do not tell the full story of which Higgs channels are the most
703 sensitive. For example, a $H \rightarrow b\bar{b}$ search in gluon fusion production is incredibly difficult due to the

Decay	Branching ratio (%)
$b\bar{b}$	58.24
WW^*	21.37
gg	8.187
$\tau\tau$	6.272
$c\bar{c}$	2.891
ZZ^*	2.619
$\gamma\gamma$	0.2270
$Z\gamma$	0.1533
$\mu\mu$	0.02176

Table 1.2: Branching ratios for a 125 GeV Higgs boson [18].

704 large QCD dijet background at the LHC. However, in associated production of the Higgs, where a W
 705 or Z gives additional final state particles that can be used to reduce background, a search for $H \rightarrow b\bar{b}$
 706 can be sensitive. The combinations of production and decay modes that are most commonly studied are
 707 summarized in table 1.3 [5].

Decay	Inclusive (incl. ggF)	VBF	WH/ZH	$t\bar{t}H$
$H \rightarrow \gamma\gamma$	✓	✓	✓	✓
$H \rightarrow b\bar{b}$			✓	✓
$H \rightarrow \tau^+\tau^-$		✓		
$H \rightarrow WW^* \rightarrow \ell\nu\ell\nu$	✓	✓	✓	
$H \rightarrow ZZ \rightarrow 4\ell$	✓			
$H \rightarrow Z\gamma \rightarrow \ell\ell\gamma$	very low			

Table 1.3: Possible channels for Higgs searches. Checkmarks denote the most sensitive production modes [5].

708 1.4 HIGGS PAIR PRODUCTION IN THE STANDARD MODEL

709 The Standard Model also allows for processes that produce two Higgs bosons in the final state, known
 710 as Higgs pair production or di-Higgs production. The two main production mechanisms are shown
 711 in figure 1.5. The two diagrams in figure 1.5 interfere destructively with one another, resulting in a low
 712 overall cross section for di-Higgs production at the LHC. Nevertheless, Higgs pair production is quite
 713 interesting to study because it gives direct access to the λ parameter of the Higgs potential, also known as
 714 the Higgs self coupling. The diagram in figure 1.5(b) is sensitive to this coupling through the triple Higgs

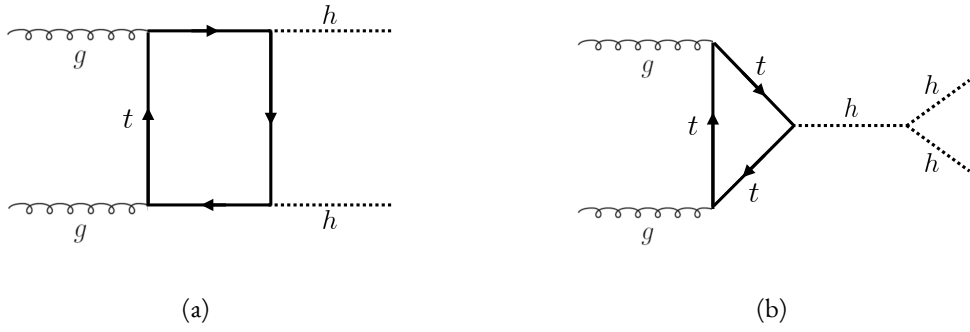


Figure 1.5: The two leading diagrams for Standard Model di-Higgs production at the LHC: (a) box diagram, (b) Higgs self coupling

715 vertex.

716 One can substitute the gluon fusion production of diagram 1.5(b) with any of the other production
717 modes previously discussed. These other modes do not suffer from interference with the box diagram
718 in figure 1.5(a) due to the presence of additional particles in the final state. They still have a lower cross
719 section than the gluon fusion mode, however. The cross sections for di-Higgs production in the differ-
720 ent modes, as well as their uncertainties, are shown in table 1.4 [19]. These are shown for $\sqrt{s} = 14$ TeV
721 as the higher center of mass energy is more sensitive to this process. Note that the scale of cross section
722 quoted is now in fb rather than pb.

Production mode	σ (fb)	Total uncert. (%)
Gluon fusion	33.89	+37.2/ - 27.8
Vector boson fusion	2.01	+7.6/ - 5.1
$W H H$	0.57	+3.7/ - 3.3
$Z H H$	0.42	+7.0/ - 5.5
$t \bar{t} H$	1.02	-

Table 1.4: Production cross sections for pair production of a 125 GeV Higgs boson at $\sqrt{s} = 14$ TeV with total uncertainty [19]. The uncertainties include QCD scale and PDF variations as well as uncertainties on α_S .

722

723 1.5 HIGGS PAIR PRODUCTION IN THEORIES BEYOND THE STANDARD MODEL

724 The Standard Model Higgs pair production cross section is rather small, and datasets on the scale of the
725 full lifetime of the LHC will be required to obtain sensitive measurements of the Higgs self-coupling.

726 However, the discovery of the Higgs also gives particle physicists a new tool that can be exploited in the
 727 search for new physics beyond the Standard Model. In particular, Higgs pair production is a promising
 728 channel in the search for new physics. The cross section for di-Higgs production can be altered through
 729 both resonant and non-resonant production of Higgs pairs. In non-resonant production, di-Higgs pro-
 730 duction vertices can arise from the presence of a new strong sector and additional colored particles [20–
 731 22]. Figure 1.6 shows examples of the types of vertices that can arise. In the resonant case, new heavy par-
 732 ticle can decay to Higgs pairs. Such new particles can include heavy Higgs bosons arising in two Higgs
 733 doublet models (2HDM) or Higgs portal models as well as heavy gravitons in Randall-Sundrum theo-
 734 ries [20, 23–29]. Figure 1.7 shows a generic diagram for a heavy resonance decaying to two Higgs bosons.
 735 In the 2HDM, X corresponds to the heavy CP-even scalar H . In the Randall-Sundrum model, X cor-
 736 responds to a heavy spin-2 graviton G . The next sections provide more detail on the phenomenology of

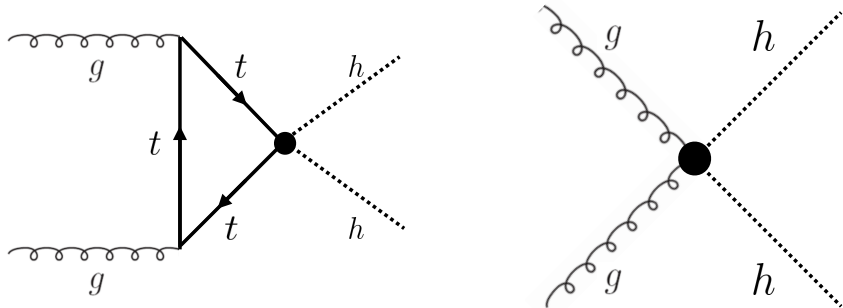


Figure 1.6: Diagrams with new vertices for non-resonant Higgs pair production arising in composite Higgs models

736
 737 resonant Higgs production in Randall-Sundrum and 2HDM models, as these models will later be tested
 738 in a dedicated search for resonant production of boosted Higgs pairs.

739 1.5.1 RANDALL-SUNDRUM GRAVITONS

740 The Randall-Sundrum model is a proposed solution to the hierarchy problem that posits a five-dimensional
 741 warped spacetime that contains two branes: one where the force of gravity is very strong and a second
 742 brane at the TeV scale corresponding to the known Standard Model sector [23]. In the theory, the
 743 branes are weakly coupled and the graviton probability function drops exponentially going from the
 744 gravity brane to the SM brane, rendering gravity weak on the SM brane. The experimental consequence

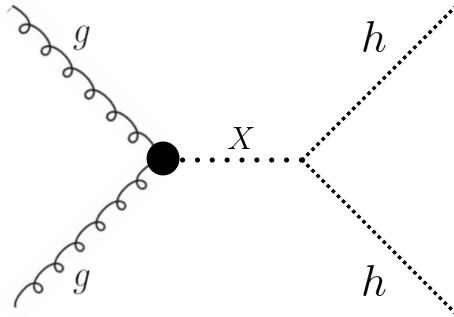


Figure 1.7: Generic Feynman diagram for resonant Higgs pair production in BSM theories

of this theory is a tower of widely spaced (in mass) Kaluza-Klein graviton resonances. In theories where the fermions are localized to the SM brane, production of gravitons from fermion pairs is suppressed and the primary mode of production is gluon fusion [24]. These gravitons have a substantial branching fraction to Higgs pairs, ranging from 6.43% for gravitons with a mass of 500 GeV to 7.66% at 3 TeV. Figure 1.8 shows the branching ratios of the spin-2 Randall Sundrum graviton (RSG) as a function of its mass. The predominant decays are to $t\bar{t}$ above the mass threshold for that channel.

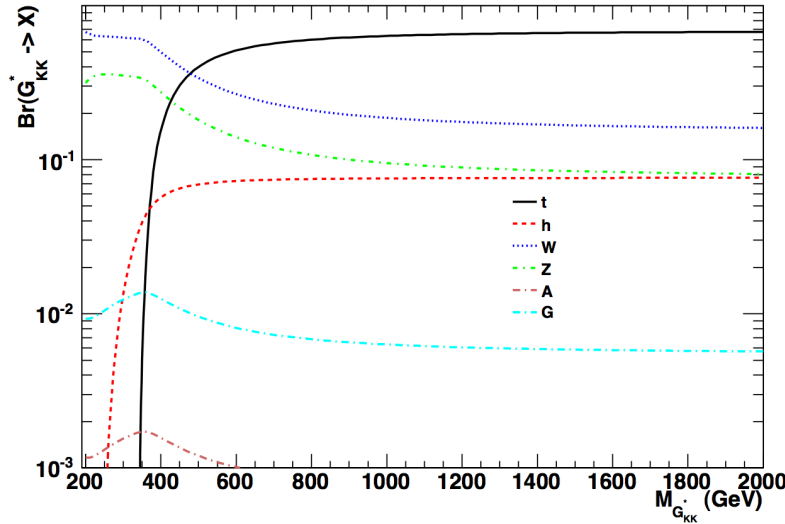


Figure 1.8: Branching ratios for a spin-2 Randall-Sundrum graviton as a function of mass computed in MadGraph with the CP3-Origins implementation [24, 30]

These models have two free parameters - the mass of the graviton and a curvature parameter k . Typically, rather than k , the theory is parameterized using $c \equiv k/\bar{M}_{\text{pl}}$, where \bar{M}_{pl} is the reduced Planck

mass. The cross section for production of the RSG decreases as a function of mass and is strongly dependent on the gluon PDF. The increase in center of mass energy from 8 to 13 TeV in LHC Run 2 greatly increases the cross section at higher mass. Figure 1.9 shows the cross section as a function of graviton mass at $\sqrt{s} = 13$ TeV for RSG models with $c = 1.0$ and $c = 2.0$.

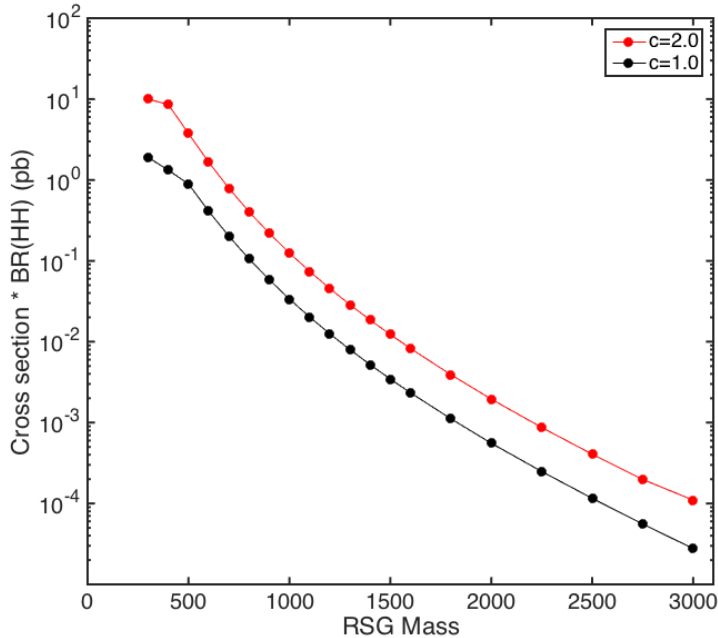


Figure 1.9: $\sigma \times \text{BR}(HH)$ for RSG as a function of mass computed in MadGraph with the CP3-Origins implementation [24, 30]

Another interesting feature of the theory is that the width of the graviton increases with both c and m_G . Figure 1.10 shows the graviton width for both $c = 1.0$ and $c = 2.0$ as a function of mass. In $c = 1.0$, the width starts at 8.365 GeV for a mass of 300 GeV and increases to 187.2 GeV at a mass of 3 TeV. Similarly, with $c = 2.0$, the width starts at 33.46 GeV for $m_G = 300$ GeV and increases to 748.8 GeV at a mass of 3 TeV.

1.5.2 TWO HIGGS DOUBLET MODELS

In Two Higgs Doublet Models (2HDM), a second complex scalar doublet is added to SM [26–28]. In this case, all four degrees of freedom in the second doublet correspond to new particles, meaning that

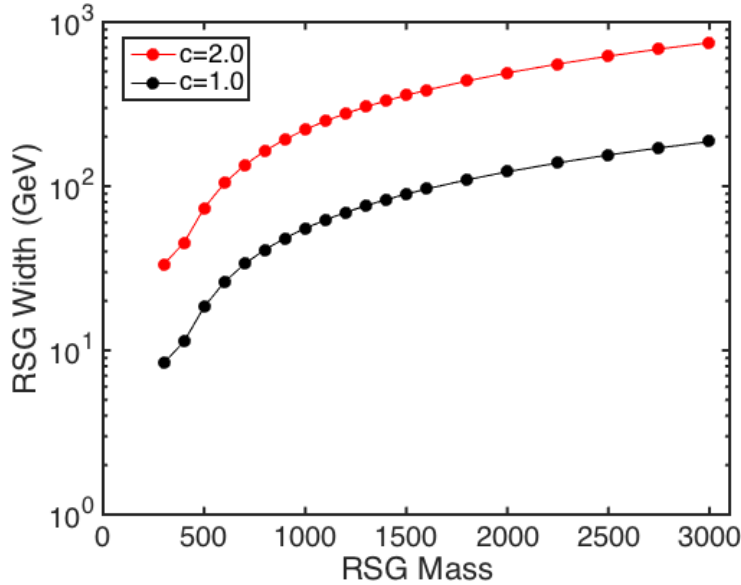


Figure 1.10: RSG width as a function of mass computed in MadGraph with the CP3-Origins implementation [24, 30]

765 there are five total scalars from the two Higgs doublets - h (light CP-even Higgs), H (heavy CP-even
 766 Higgs), A (heavy CP-odd Higgs), and H^\pm (charged Higgs). The model is parameterized by two main
 767 parameters. The first, $\tan \beta \equiv \frac{v_2}{v_1}$, is the ratio of the vacuum expectation values of the two Higgs dou-
 768 blets (where v_1 corresponds to the v in the SM Higgs model described above). The second parameter
 769 is α , a mixing angle between the heavy and light Higgs fields. Models are also often parameterized with
 770 $\cos(\beta - \alpha)$ rather than α directly. The limit where $\cos(\beta - \alpha) = 0$ is called the alignment limit, and it
 771 is in this limit that the light Higgs h has the same couplings as a Standard Model Higgs.

772 2HDM models are usually separated into two main types - Type I and Type II. In Type I models, the
 773 charged fermions only couple to the second Higgs doublet, leading to a fermiophobic light Higgs. In
 774 Type II models, up-type quarks couple to the first doublet while down-type quarks couple to the second
 775 doublet. One specific realization of a Type II 2HDM is the Minimal Supersymmetric Standard Model
 776 (MSSM).

777 Resonant di-Higgs production in this model can proceed through decays of the heavy CP-even Higgs
 778 $H \rightarrow hh$. The branching ratio for $H \rightarrow hh$ depends on the model type as well as the values of $\tan \beta$
 779 and $\cos \beta - \alpha$. Figure 1.11 shows the branching ratios as a function of the mass of the heavy scalar H for

780 both Type I and Type II models. Depending on the type of model hh can be a substantial fraction of the
 781 decays of H .

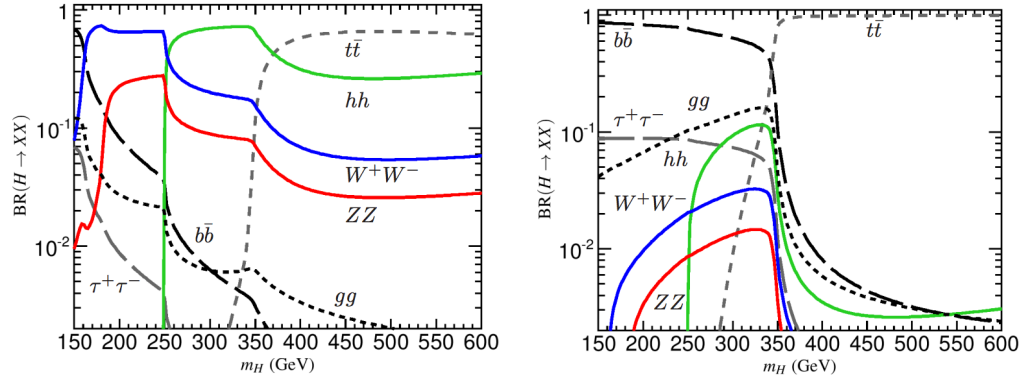


Figure 1.II: Branching ratios for heavy Higgs H in Type I (left) and Type II (right) 2HDM models with $\tan \beta = 1.5$ and $\cos(\beta - \alpha) = 0.1(0.01)$ for Type I (Type II). [28]

782 1.6 CONCLUSION

783 Studying the Higgs sector is essential for understanding the details of how mass arises in the Standard
 784 Model and how the electroweak symmetry is broken. The discovery of the Higgs boson also opens the
 785 door for its use as a tool to search for new physics, and Higgs pair production is an ideal candidate for
 786 this study. Even if no BSM physics is found in Higgs pair production, searches for Higgs pairs will put
 787 constraints on the Higgs self coupling and thus further knowledge of the Standard Model and the details
 788 of the Higgs potential.

*The enthusiasm and motivation to explore particle
physics at the high-energy frontier knows no borders
between the nations and regions of the planet.*

Peter Jenni

2

789

790

The ATLAS detector and the Large Hadron 791 Collider

792 This chapter presents an overview of the experimental systems used to conduct the measurements pre-
793 sented in this thesis. First, a brief overview of the accelerator, the Large Hadron Collider, will be given.
794 In this section, the accelerator conditions relevant to data-taking are presented as well. Next, an overview
795 of the ATLAS experiment is given. The basics of each sub-detector's role are summarized, as well as the
796 details of the datasets accumulated. Then, a brief interlude on the ATLAS Muon New Small Wheel up-
797 grade is presented. While this new detector does not have a direct impact on any of the datasets taken
798 so far, it will have an impact on future analyses and the work done on it is briefly summarized here. Fi-
799 nally, an overview of object reconstruction in ATLAS is given. While the details of all of the algorithms
800 will not be presented in detail, aspects of the reconstruction performance such as object resolutions are
801 shown as these are relevant to the two studies presented later in this thesis.

802 2.1 THE LARGE HADRON COLLIDER

803 The Large Hadron Collider (LHC) is a proton-proton collider at the CERN laboratory in Geneva,
804 Switzerland [31]. It is designed for a maximum collision center of mass energy of $\sqrt{s} = 14 \text{ TeV}$ and
805 has a circumference of 26.7 kilometers. Four main experiments are located at the interaction points (IP)
806 of the accelerator: ATLAS (A Toroidal LHC ApparatuS), CMS (the Compact Muon Solenoid), AL-
807 ICE (A Large Ion Collider Experiment), and LHCb [32–35]. The studies performed in this thesis were
808 all completed with the ATLAS detector. Figure 2.1 shows a schematic of the LHC ring and the various
809 experiments.

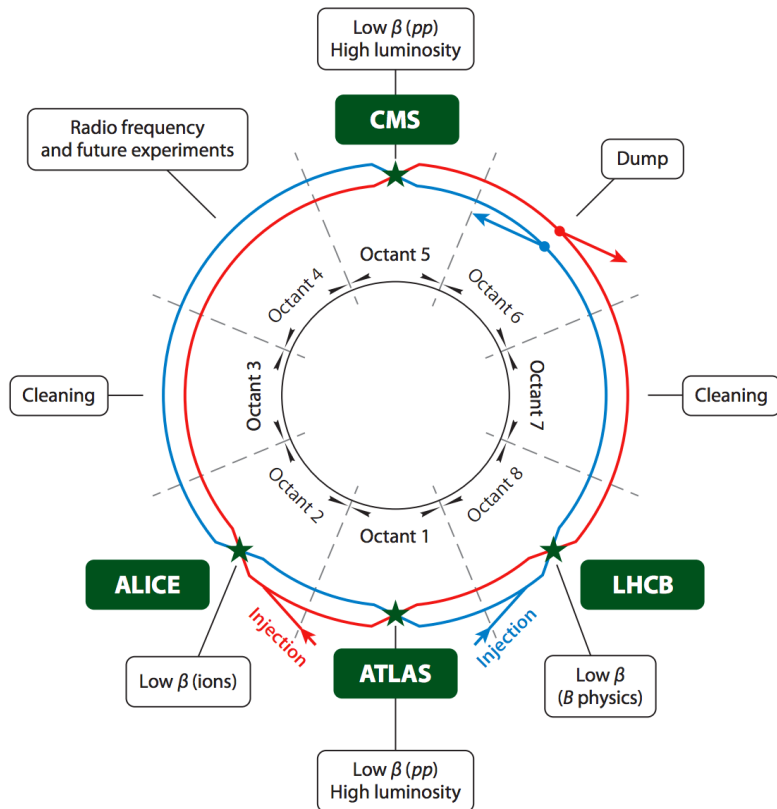


Figure 2.1: A schematic view of the LHC ring [36]

810 One of the most interesting features of the LHC is in its magnet design. Because the tunnel does not
811 have room for separate superconducting magnets for each of the beam pipes, the LHC employs a twin-
812 bore magnet design. Each magnet must hold an 8.3 Tesla magnetic field in order to bend the proton

813 beams at $\sqrt{s} = 14$ TeV. The superconducting magnets are cooled to a temperature of 1.9 Kelvin with
814 superfluid helium.

815 2.I.I INSTANTANEOUS LUMINOSITY

816 The rate of physics events expected from the accelerator is dependent on the instantaneous luminosity
817 of the machine and the cross section of the physics process, $R_{\text{events}} = L\sigma$. Here, R_{events} is the number
818 of events per second, L is the instantaneous luminosity of the machine, and σ is the cross section for the
819 physics process being measured. The instantaneous luminosity of the LHC is determined by numerous
820 factors related to machine conditions. Equation 2.1 gives the equation for instantaneous luminosity of
821 Gaussian beam profile [36].

$$L = \frac{N_b^2 n_b f_{\text{rev}} \gamma_r}{4\pi \epsilon_n \beta^*} F \quad (2.1)$$

822 The LHC collides protons in bunches, and in the above equation N_b is the number of protons per
823 bunch while n_b is the number of bunches per beam. Nominally, the LHC can hold up to 2808 pro-
824 ton bunches. f_{rev} is the revolution frequency. ϵ_n is the normalized transverse beam emittance, a mea-
825 surement of the average spread of the particles position-momentum space which has the dimension of
826 length. β^* is the value of the *beta* function for the beam at the interaction point. It relates the emittance
827 to the Gaussian width of the beam with $\sigma_{\text{beam}} = \sqrt{\epsilon \cdot \beta}$. F is a reduction factor that corrects for the
828 fact that the beams are colliding at an angle at the IP.

829 Another way of writing the instantaneous luminosity is shown in equation 2.2. In this case, the in-
830 stantaneous luminosity is written as the ratio of the rate of inelastic collisions with the inelastic cross
831 section [37].

$$L = \frac{R_{\text{inel}}}{\sigma_{\text{inel}}} = \frac{\mu n_b f_{\text{rev}}}{\sigma_{\text{inel}}} \quad (2.2)$$

832 In this case, μ is the average number of interactions per bunch crossing in the accelerator. μ is a useful
833 parameter for characterizing the amount of activity recorded in an experiment. As the instantaneous
834 luminosity and thus μ increase, there are more interactions per bunch crossing and more activity in the
835 detector. This is often characterized with $\langle \mu \rangle$, the measured per bunch crossing μ value averaged over

836 all bunch crossings. The interactions inside each bunch crossing that are not the main physics process of
 837 interest are often referred to as “pileup” interactions, and $\langle \mu \rangle$ is a measurement of the level of pileup in
 838 the detector.

839 **2.1.2 EVOLUTION OF MACHINE CONDITIONS**

840 This thesis uses datasets taken at three different center of mass energies: $\sqrt{s} = 7\text{ TeV}$ data taken in
 841 the year 2011, $\sqrt{s} = 8\text{ TeV}$ data taken in the year 2012, and $\sqrt{s} = 13\text{ TeV}$ data taken in the year
 842 2015. In addition to increasing center of mass energy, the instantaneous luminosity and parameters that
 843 determine it were evolving. Table 2.1 summarizes that machine conditions in each of these datasets.

	2011	2012	2015	Design
$\sqrt{s} [\text{TeV}]$	7	8	13	14
Number of bunches	1380	1380	1825	2808
Max. protons per bunch	1.45×10^{11}	1.7×10^{11}	1.2×10^{11}	1.15×10^{11}
Bunch spacing [ns]	50	50	25	25
Max. instantaneous luminosity [$\text{cm}^{-2}\text{s}^{-1}$]	3.7×10^{33}	7.7×10^{33}	5×10^{33}	10^{34}
$\beta^* [\text{m}]$	1.0	0.6	0.8	0.55
$\langle \mu \rangle$	11.6	20.7	13.7	-

Table 2.1: Evolution of LHC machine conditions [38, 39]

844 **2.2 THE ATLAS DETECTOR**

845 The ATLAS detector is a multi-purpose particle detector experiment at the LHC’s Point 1 [32]. It has
 846 nearly 4π coverage in solid angle around the interaction point. It consists of an inner detector for mea-
 847 suring charged particles, electromagnetic and hadronic calorimeters, and a muon spectrometer. Fig-
 848 ure 2.2 gives an overview of the detector.

849 **2.2.1 COORDINATE SYSTEM**

850 Before defining the properties of the individual detectors, it is important to establish the coordinate
 851 system used. Figure 2.3 shows a schematic of the coordinate system. The azimuthal plane (perpendicular



Figure 2.2: A full diagram of the ATLAS detector [32]

852 to the beam line) is defined as the x - y plane. The angle in this plane is referred to as ϕ . The angle relative
 853 to the beam axis is referred to as θ . Rather than using θ directly as a coordinate, the experiment often
 854 uses the pseudorapidity η . η is defined in equation 2.3.

$$\eta = \ln \left(\tan \left(\frac{\theta}{2} \right) \right) \quad (2.3)$$

855 Pseudorapidity is the massless approximation of rapidity, the angle used to parameterize boosts in
 856 special relativity. This is important for two reasons. First, it means that differences in η are Lorentz in-
 857 variant. Second, particle production is roughly constant in pseudorapidity. Particles with η close to zero
 858 are referred to as “central”, while those at high $|\eta|$ are called “forward”. In general, two main detector
 859 topologies can be seen in figure 2.2. There are “barrel” elements, which surround the beam line cylin-
 860 drically and are in the central region of the detector. In the forward region, there are “endcap” regions
 861 which are arranged as disks perpendicular to the beam line.

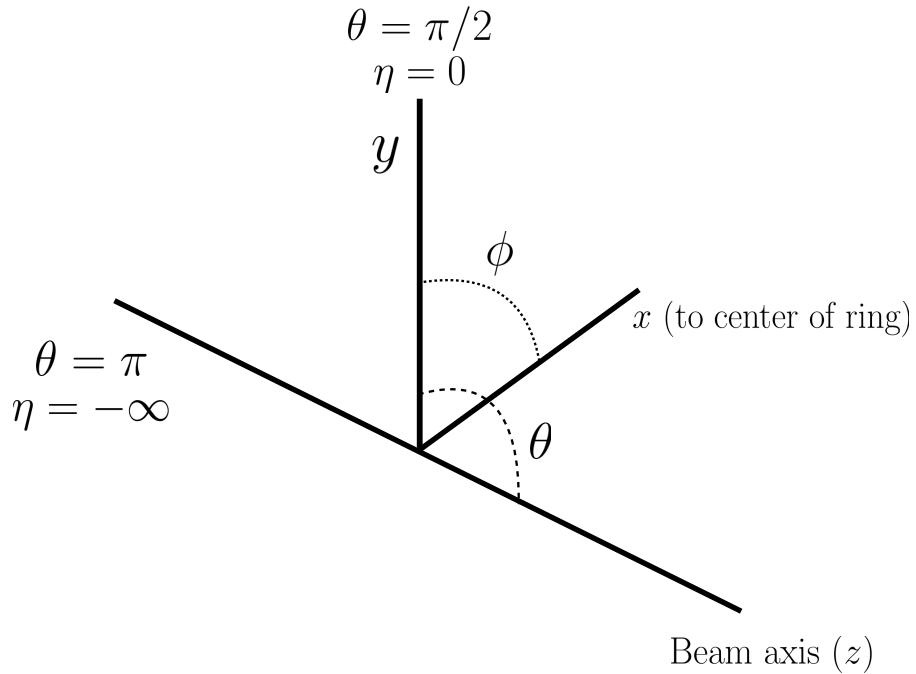


Figure 2.3: The ATLAS coordinate system

862 2.2.2 INNER DETECTOR

863 The ATLAS Inner Detector (ID) system is built for precision tracking of charged particles. It covers the
 864 range $|\eta| < 2.5$. In this range, approximately 1000 particles are generated every bunch crossing in the
 865 detector. This requires having fine granularity to achieve the resolutions required for good momentum
 866 measurement and vertex reconstruction.

867 The ID consists of three sub-components: the pixel detector, semiconductor tracker (SCT), and trans-
 868 sition radiation tracker (TRT). It is surrounded by a solenoid providing a 2 T axial magnetic field which
 869 bends particles in the transverse plane to allow for momentum measurement. Figure 2.4 shows the layout
 870 of each of these components.

871 PIXEL DETECTOR

872 The pixel detector is the first detector particles traverse after being generated in proton collisions and is
 873 the most granular detector. Its operation is crucial for precision tracking and vertex reconstruction as



Figure 2.4: Layout of the ATLAS Inner Detector system [40]

well as higher level object reconstruction like tagging of jets from b -quarks. The basic sensing element in this subdetector is a silicon pixel detector. The operating principle for the silicon pixels is that of a $p-n$ junction. When a charged particle passes through, it creates electron-hole pairs that are then separated by the electric field. The sensors are $250\ \mu\text{m}$ thick and use oxygenated n -type wafers with readout pixels on the n^+ side of the detector [32]. Overall, the pixel detector has 1744 sensors and 80.4 million readout channels.

In the barrel region, the pixel detector has three concentric layers of sensors surrounding the beam-line. In the endcap region, it consists of disks perpendicular to the beam axis. The detector is segmented in the R - ϕ plane and in z . Usually, three pixel layers are crossed by a charged particle track. The intrinsic accuracies of the sensors are $10\ \mu\text{m}$ in R - ϕ and $115\ \mu\text{m}$ in z (or R for the endcap).

884 INSERTABLE B-LAYER

885 In Run 2, a new innermost pixel layer, known as the insertable B-layer (IBL), was added to the Inner
886 Detector [41]. This layer was added to cope with the higher luminosities planned in LHC Run 2 and

887 at the high luminosity HL-LHC. Additionally it improves tracking position resolution which in turn
888 improves the vertexing and b -tagging capabilities in ATLAS. The detector sits directly on a new beam
889 pipe, only 33.25 mm away from the collision points in the azimuthal plane.

890 SEMICONDUCTOR TRACKER (SCT)

891 The semiconductor tracker (SCT) consists of silicon microstrips and comprises the next four layers of
892 the ID. This sub-detector has 6.4cm long sensors that are daisy-chained into strips with a strip pitch
893 of $80\ \mu\text{m}$ [32]. Some of the strips have a small stereo angle to allow for measurement of both angular
894 coordinates. In total there are 6.3 million readout channels. The intrinsic accuracies are $17\ \mu\text{m}$ in $R\phi$
895 and $580\ \mu\text{m}$ in z (or R in the endcap).

896 TRANSITION RADIATION TRACKER (TRT)

897 The transition radiation tracker (TRT) serves two purposes. First, it consists of 4mm diameter straw
898 tubes filled with a 70/27/3% gas mixture of xenon, carbon dioxide, and oxygen to provide tracking of
899 charged particles. Particles typically have 36 TRT straw tube hits per track. The material in between
900 the straws is designed to induce transition radiation which can be useful for particle identification. As
901 particles pass between media with different dielectric constants, they emit transition radiation that can
902 cause additional showers in the TRT. In particular it is useful for discrimination between electrons and
903 pions or other charged hadrons, as the amount of transition radiation is proportional to the Lorentz
904 factor of the particle.

905 2.2.3 CALORIMETERS

906 The calorimeter system consists of two main sub-components: a fine granularity electromagnetic calorime-
907 ter tailored for the measurement of photons and electrons and multiple coarser hadronic calorimeters
908 dedicated to the measurement of hadronic showers [32]. The calorimeter system has broader cover-
909 age than the inner detector, covering the region out to $|\eta| < 4.9$. It is also designed to deliver good
910 containment of showers so as to limit leakage into the muon system. Figure 2.5 shows the layout of the
911 calorimeter system.

912 Both the electromagnetic and hadronic calorimeters are sampling calorimeters. They alternate active
 913 material for energy measurement with passive material for energy absorption. The materials used for
 914 each purpose vary based on the type of calorimeter and its location in the detector.

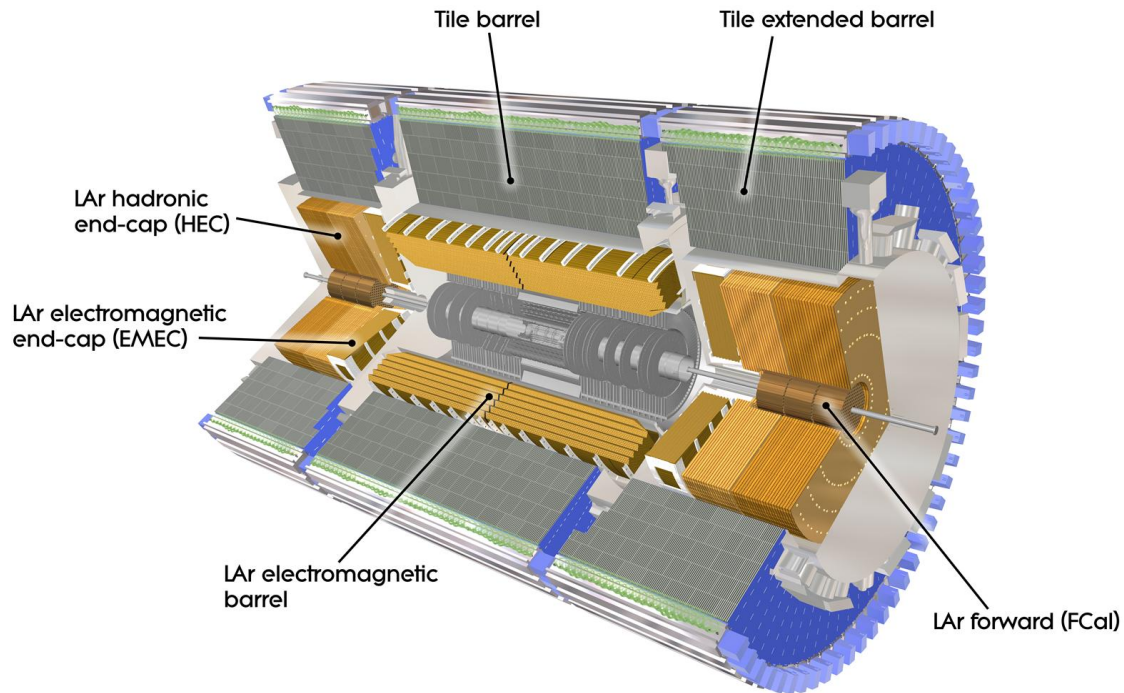


Figure 2.5: Layout of the ATLAS calorimeter system [32]

915 ELECTROMAGNETIC CALORIMETER

916 The electromagnetic calorimeter (EM calorimeter) use liquid Argon (LAr) as its active material and lead
 917 as its passive material. It is arrange in an accordion geometry to increase the absorption area while still
 918 allowing it to have no azimuthal cracks (complete symmetry in ϕ). The EM calorimeter is divided into a
 919 barrel portion that extends to $|\eta| < 1.475$ and an endcap portion going from $1.375 < |\eta| < 3.2$. The
 920 region where these two units overlap is called the “transition region”.

921 In order to provide good containment the calorimeter depth must be optimized. Typically, for elec-
 922 tromagnetic calorimeters the depth is measured in radiation lengths. In general, the intensity of a par-
 923 ticle beam attenuates exponentially in distance with a constant equal to the radiation length. That is,

924 $I(x) = I_0 e^{-x/X_0}$, where I is the intensity, x is the distance traveled, and X_0 is the radiation length.

925 The ATLAS EM calorimeter is designed to have > 22 radiation lengths in the barrel and > 24 in the
926 endcap [32].

927 **HADRONIC CALORIMETERS**

928 There are three types of hadronic calorimeters present in ATLAS: the tile calorimeter (TileCal), hadronic
929 endcap (HEC), and forward calorimeter (FCal). Each one is optimized for stopping of hadronic showers
930 and the materials chosen are specific to their placement in the detector.

931 The TileCal is a scintillating tile calorimeter placed directly outside the EM calorimeter. It uses steel as
932 the absorber and plastic scintillator tiles as the active material. It has coverage in the barrel at $|\eta| < 1.0$
933 and in the “extended barrel” region of $0.8 < |\eta| < 1.7$.

934 The HEC had two wheels perpendicular to the beam line per endcap and is located directly behind
935 the EM calorimeter endcap modules. The HEC covers the region from $1.5 < |\eta| < 3.2$, overlapping
936 slightly with both the tile calorimeter and the forward calorimeter. Like the EM calorimeter, it uses liq-
937 uid Argon as the active material, but it uses copper as the absorber.

938 The FCal covers the most forward regions of the calorimeter system, extending to the region of $3.1 <$
939 $|\eta| < 4.9$. It again uses liquid argon as its active material. For absorber, it consists of an innermost
940 module made of copper followed by a module made of tungsten.

941 The hadronic equivalent of radiation length is called the interaction length and is denoted as λ . In the
942 barrel, the hadronic calorimeter depth is approximately 9.7λ , while in the endcap is is 10λ . The outer
943 supports contribute an additional 1.3λ . This is been shown to be sufficient to limit punch-through of
944 showers to the muon system [32].

945 **2.2.4 MUON SPECTROMETER**

946 The muon spectrometer is dedicated to measuring the momentum and position of muons. It consists
947 of tracking and trigger chambers which are unique in the barrel and endcap regions. The magnetic field
948 for bending of muons is provided by a system of three large air-core toroid magnets (from which ATLAS

949 derives its name.) These magnets provide 1.5 to 5.5 Tm of bending power at $0 < |\eta| < 1.4$ and approx-
 950 imately 1 to 7.5 Tm in the endcap region of $1.6 < |\eta| < 2.7$. The entire muon system covers the range
 951 $0 < |\eta| < 2.7$. Monitored drift tubes (MDTs) are used for tracking in the barrel and the two outer
 952 layers of the endcap, while cathode strip chambers (CSCs) are used to provide tracking in the innermost
 953 endcap wheel. In the barrel, resistive plate chambers (RPCs) are used as trigger chambers while thin gap
 954 chambers (TGCs) are used in the endcap. Figure 2.6 shows the layout of the ATLAS muon system. The
 955 entire muon system is designed with the specification of providing a 10% momentum resolution for a
 956 1 TeV muon.

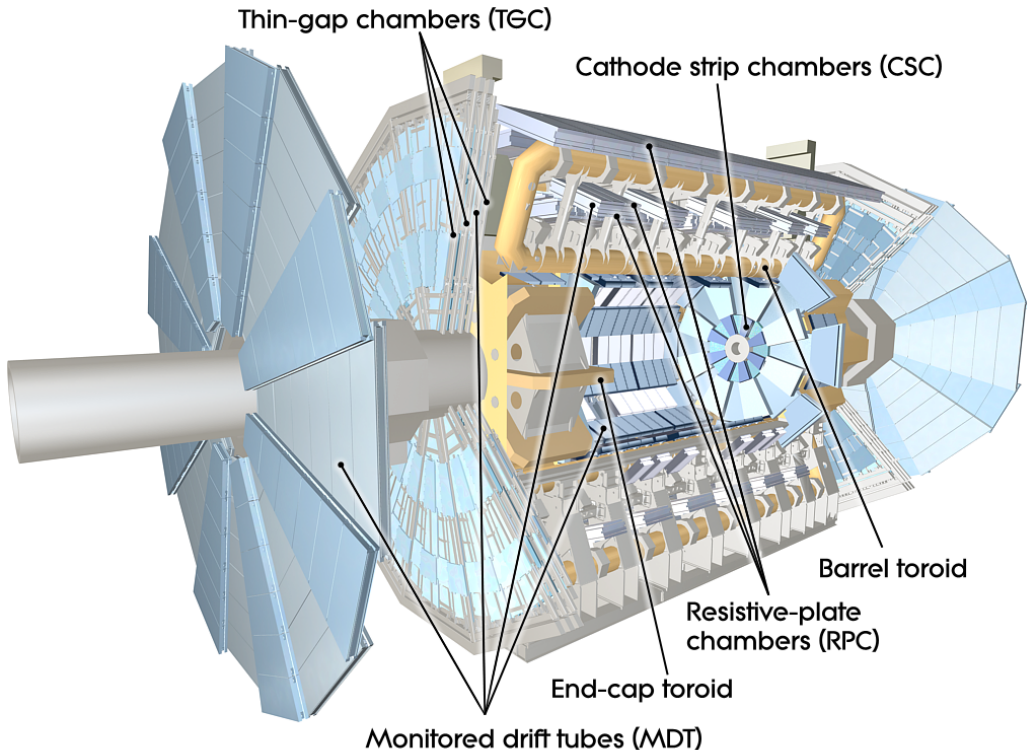


Figure 2.6: Layout of the ATLAS muon system [32]

957 MONITORED DRIFT TUBES (MDTs)

958 The monitored drift tubes (MDTs) are aluminum 3cm diameter tubes filled with a 93/7 % mixture of
 959 Argon and CO₂, with trace amounts of water. As a charged particle traverses the tube, it ionizes the gas

and the ions drift to a wire at the center of the tube. The radial distance of traversal of the particle in the tube is determined by the drift time of the electrons, allowing for fine position resolution. The tubes have an average resolution of $80\ \mu\text{m}$ per tube and a maximum drift time of approximately 700ns. The tubes are oriented so that they give precision measurement in η and run along ϕ . They cover $|\eta| < 2.7$, except in the innermost layer of the endcap where they only go to $|\eta| < 2.0$ [32].

965 CATHODE STRIP CHAMBERS (CSCs)

966 The cathode strip chambers cover a narrow window of the innermost endcap region at $2.0 < |\eta| <$
967 2.7. In this region the background rates in the cavern are particularly high and the CSCs are designed
968 to handle these higher rates. The CSCs are multiwire proportional chambers with wires pointing in
969 the radial direction (away from the beam pipe). The wire serves as an anode and there are two types of
970 segmented cathode strip, one perpendicular to the wires which gives the precision measurement and one
971 parallel which provides the transverse coordinate. It has an 80/20 gas mixture of Argon and CO₂ [32].

972 RESISTIVE PLATE CHAMBERS (RPCs)

973 The resistive plate chambers (RPCs) are gaseous electrode-plate detectors covering the region $|\eta| <$
974 1.05. They consist of two resistive plates separated by a distance of 2 mm. The gas mixture used is a
975 94.7/5/0.3% mixture of C₂H₂F₄, Iso-C₄H₁₀, and SF₆. It has readout strips with a pitch of 23-35 mm
976 for both η and ϕ measurement and thus provides measurement of the azimuthal coordinate in the barrel
977 that the MDTs do not. The thin gas gap allows for a quick response time which makes it ideal for use in
978 the trigger. There are three layers of RPCs which are referred to as the three trigger stations. They allow
979 for both a low p_T and high p_T trigger. The coincidence of hits in the innermost chambers allows for
980 triggering of muons between 6 and 9 GeV, while the outermost layer allows the trigger to select high
981 momentum tracks in the range of 9 to 35 GeV [32].

982 THIN GAP CHAMBERS (TGCs)

983 The thin gap chambers (TGCs) are multiwire proportional chambers where the wire to cathode distance
984 (1.4mm) is smaller than the wire-to-wire distance (1.8 mm). They contain a gas mixture of CO₂ and

985 *n*-pentane and use a high electric field to gain good time resolution. They serve two functions in the
 986 end-cap system. First, they serve as the trigger chambers. Second, they also provide azimuthal coordi-
 987 nate measurement which the MDTs do not. They sit on the inner and middle layers of the endcap. The
 988 outermost layer's azimuthal coordinate is determined by extrapolation [32].

989 2.2.5 MAGNET SYSTEM

990 As mentioned previously, there are two independent magnet systems in ATLAS. The first is a 2 T solenoid
 991 field in the inner detector which provides bending in the azimuthal plane. The second is an approxi-
 992 mately 0.5 T toroidal field in the muon system which provides bending in η . Figure 2.7 shows the pre-
 993 dicted field integral as a function of $|\eta|$ [32].

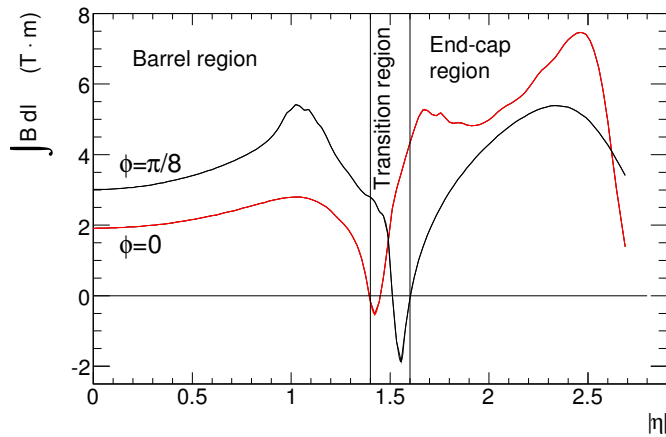


Figure 2.7: Predicted field integral as a function of $|\eta|$ for the ATLAS magnet system [32]

994 2.2.6 TRIGGER SYSTEM

995 The ATLAS trigger system searches for signatures of muons, electrons, photons, hadronically decay-
 996 ing τ leptons, and jets in order to save these events for further analysis. The trigger system in ATLAS
 997 is designed to reduce the maximum LHC event rate of 40 MHz to a more reasonable rate that can be
 998 recorded. The trigger first consists of a fast, hardware based system called the Level-1 (L1) trigger. The
 999 L1 trigger consists of independent dedicated detector sub-components that can seed regions of inter-
 1000 est (RoIs) for further analysis downstream. For muons, the RPCs and TGCs are used, while in the

1001 calorimeter coarsely grained sections of calorimeter cells called towers are used. Once regions of inter-
 1002 est are seeded, a software based system called the High Level Trigger (HLT) is used to reconstruct objects
 1003 and integrate information from different parts of the detector. In Run 1 of ATLAS, the HLT consisted
 1004 of two separate stages: the level 2 (L2) trigger and the event filter (EF).

1005 The maximum trigger rate that the L1 trigger can handle is 75 kHz. In the HLT, the rate of events
 1006 written to disk is approximately 200 Hz. Figure 2.8 shows the trigger rates for different L1 triggers in
 1007 2012 and 2015 for ATLAS [42].

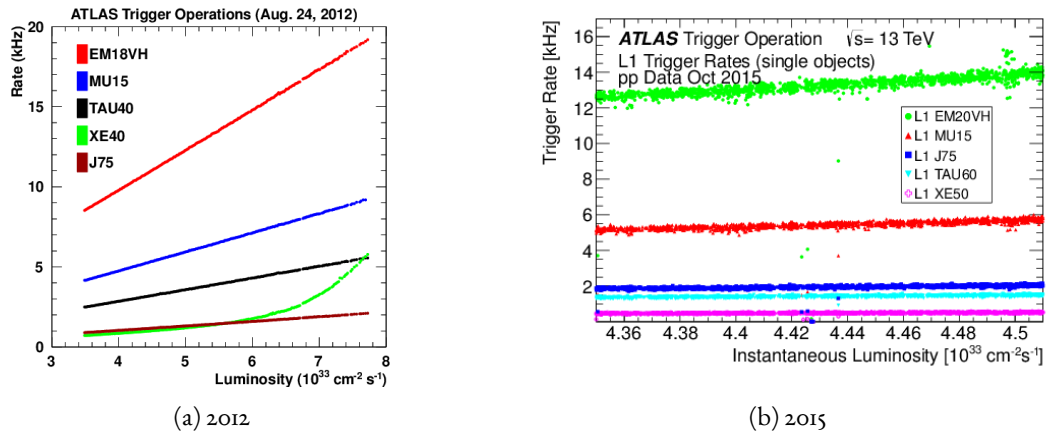


Figure 2.8: ATLAS trigger rates for Level-1 triggers as a function of instantaneous luminosity in 2012 and 2015 operation. These are single object triggers for electromagnetic clusters (EM), muons (MU), jets (J), missing energy (XE), and τ leptons (TAU). The threshold of the trigger is given in the name in GeV. [42]

1008 2.2.7 ATLAS DATASETS

1009 ATLAS has collected data at center of mass energies of 7, 8, and 13 TeV. Figure 2.9 shows the integrated
 1010 luminosity as a function of time for each of the three collected datasets. At $\sqrt{s} = 7 \text{ TeV}$, ATLAS
 1011 recorded 5.08 fb^{-1} . Increased instantaneous luminosity in 2012 led to a larger dataset of 21.3 fb^{-1}
 1012 recorded at $\sqrt{s} = 8 \text{ TeV}$. After Long Shutdown 1 (LS1) of the LHC and a restart in 2015, ATLAS
 1013 recorded 3.9 fb^{-1} of data at $\sqrt{s} = 13 \text{ TeV}$. [43, 44]

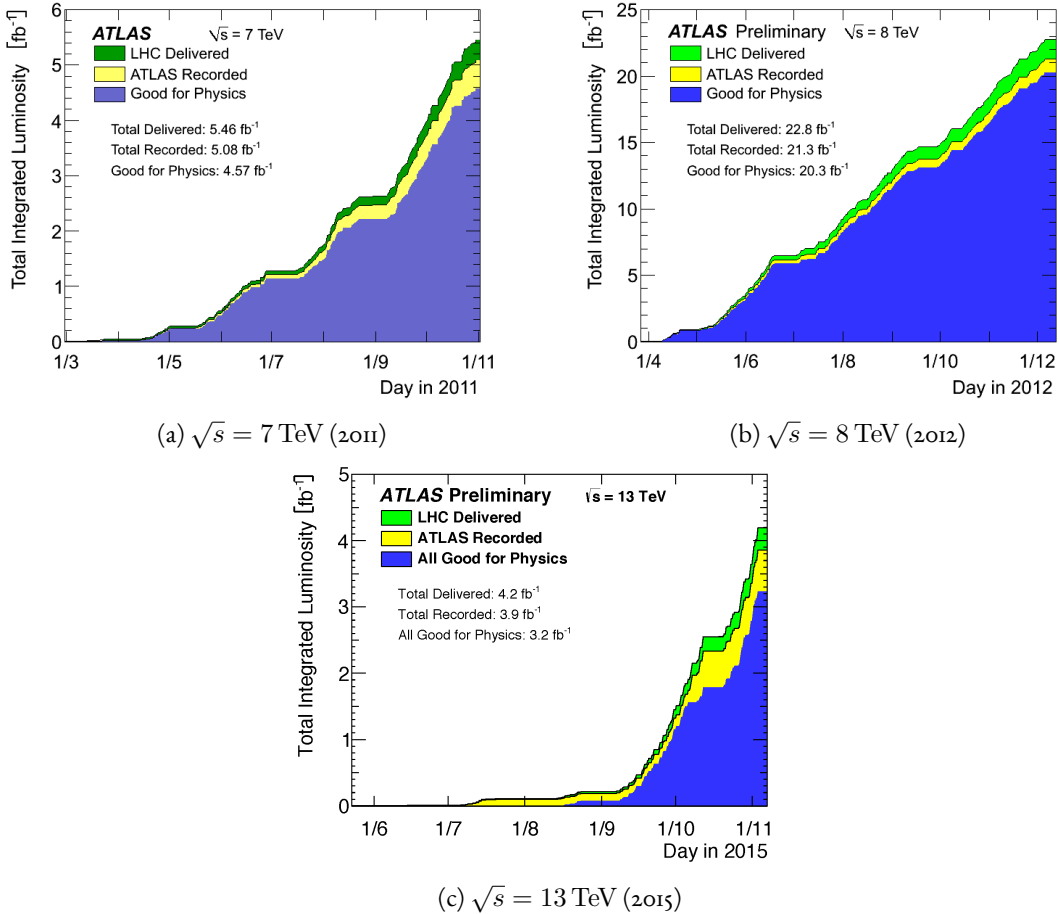


Figure 2.9: Instantaneous luminosity as a function of time for data recorded by ATLAS at different center of mass energies [43, 44]

2.2.8 DETECTOR PERFORMANCE

Table 2.2 summarizes the design requirements for each of the different sub-detectors. This table shows the energy and momentum resolution of each tracking, calorimetry, and muon measurements.

2.3 THE ATLAS MUON NEW SMALL WHEEL UPGRADE

As the LHC continues operation, it is scheduled to be upgraded in several phases to allow it to reach higher instantaneous luminosities and thus collect larger datasets. These conditions will open new doors for study of rare physics processes but will also present interesting challenges that must be faced. ATLAS will require new detector technologies to cope with the increased background rates in the cavern in these

	Required resolution
Tracking	$\sigma_{p_T}/p_T = 0.05\% p_T \oplus 1\%$
EM calorimetry	$\sigma_E/E = 10\%/\sqrt{E} \oplus 0.7\%$
Hadronic calorimetry	
Barrel and end-cap	$\sigma_E/E = 50\%/\sqrt{E} \oplus 3\%$
Forward	$\sigma_E/E = 100\%/\sqrt{E} \oplus 10\%$
Muon spectrometer	σ_{p_T}/p_T at $p_T = 1$ TeV

Table 2.2: Performance requirements for the ATLAS detector [32].

1022 high luminosity conditions. One such upgrade, scheduled to be installed during Long Shutdown 2
 1023 (LS2) of the LHC in 2018, is the ATLAS Muon New Small Wheel (NSW) upgrade [45]. The NSW will
 1024 replace the innermost end-cap wheel of the muon system with new technologies, as this is the part of the
 1025 muon detector closest to the beam and thus suffers from the highest rates.

1026 **2.3.1 MOTIVATION**

1027 The motivation of the NSW is two-fold. First, the objective is to alleviate the decreased tracking effi-
 1028 ciency that comes in a high rate environment. As figure 2.10, at the LHC design luminosity both the
 1029 efficiency of recording hits and reconstructing track segments in the MDTs decreases at the LHC design
 1030 luminosity.

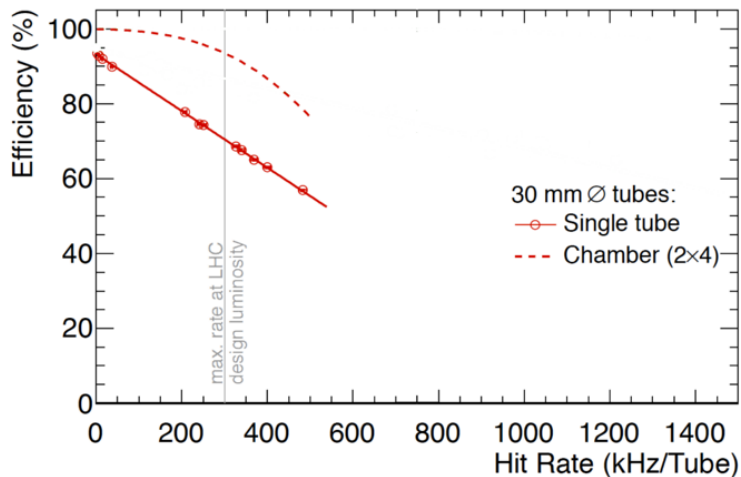


Figure 2.10: MDT tube hit (solid) and segment (dashed) efficiency as a function of hit rate per tube [45]

1031 Second, the NSW will work to alleviate the rate of fake triggers arising in the endcap. Figure 2.II
 1032 shows the extrapolated trigger rates as a function of the p_T threshold with and without the NSW up-
 1033 grade. As the figure shows, the NSW upgrade will reduce the trigger rate by an order of magnitude com-
 1034 pared to the current endcap trigger system.

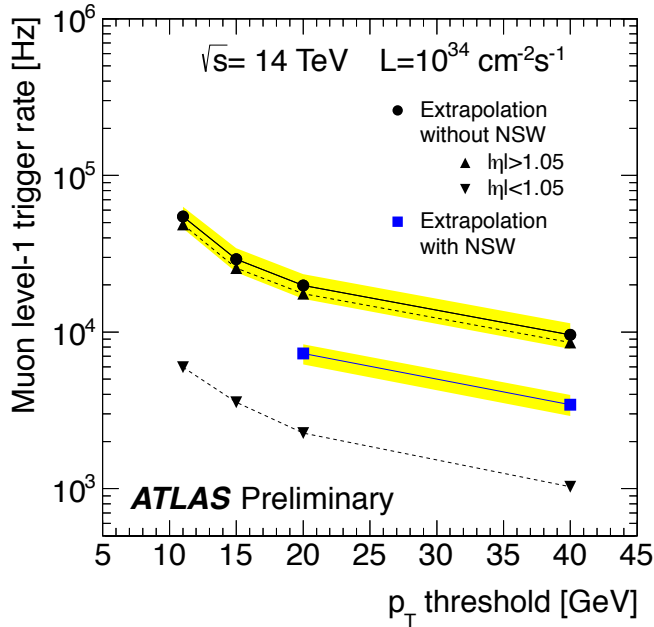


Figure 2.II: Trigger rate as a function of p_T threshold with and without the NSW upgrade [45]

1035 2.3.2 NSW DETECTOR TECHNOLOGIES

1036 The NSW will use two new detector technologies - micromesh gaseous structure detectors (micromegas)
 1037 and small-strip thin gap chambers (sTGCs) [45, 46]. Unlike the previous detectors, both of these detec-
 1038 tor technologies can be used for tracking or trigger. However, the micromegas is more suited to tracking
 1039 because of its good spatial resolution, while the sTGCs have better time resolution and are more suited
 1040 for the trigger. To maintain a fully redundant system, both technologies are used for both purposes.

1041 **MICROMEGAS**

1042 Micromegas detectors operate using a thin metallic mesh that sits approximately $100\ \mu\text{m}$ away from
1043 the readout electrodes to create the amplification region. Above this mesh, there is a drift region on the
1044 order of a few mm in length capped by a drift electrode. As a charged particle traverses the detector, it
1045 ionizes gas and the electrons drift down towards readout strips. The timing of the drift can be used to
1046 reconstruct the angle of traversal of the particle. This is illustrated in figure 2.12. The micromegas used in
1047 ATLAS will be resistive micromegas, where the readout electrodes are topped with resistive strips [47].
1048 This alleviates the risk of sparking in the large area detectors that ATLAS will use.

1049 In ATLAS, the micromegas drift gap will be 5 mm and the amplification gap will be $128\ \mu\text{m}$. They
1050 are filled with the same gas mixture as the MDTs. They will be stacked in an octuplet in an XXUV-
1051 UVXX geometry, where X refers to straight strips and U and V refer to stereo strips at an angle of $\pm 1.5^\circ$.
1052 This arrangement allows for measurement of the azimuthal coordinate and gives a large lever arm be-
1053 tween the straight strips for triggering purposes. Figure 2.12 shows the geometry of a single micromegas
1054 detector as well as its operating principle [45].

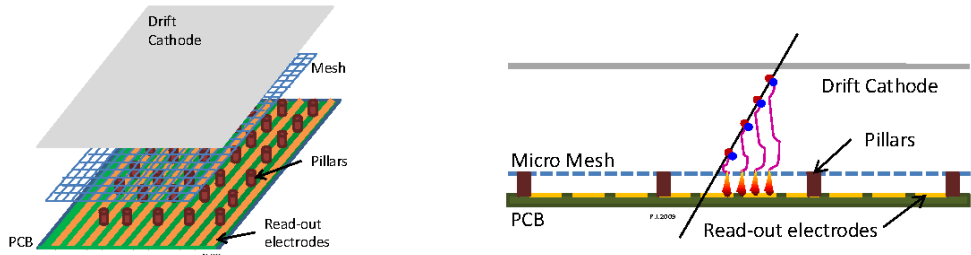


Figure 2.12: Illustrations of the geometry (left) and operating principle (right) of the micromegas detector [45]

1055 **sTGCs**

1056 The sTGCs are similar to the TGCs already described. They consist of gold-plated tungsten wires with
1057 a 1.8 mm pitch between two cathode planes 1.4 mm away from the wire plane. One cathode plane
1058 consists of strips with a 3.2 mm pitch (much smaller pitch than the TGCs), while the other consists
1059 of coarser pads that are used for defining regions of interest in the sTGC trigger algorithm. Figure 2.13
1060 shows the basic detector geometry.

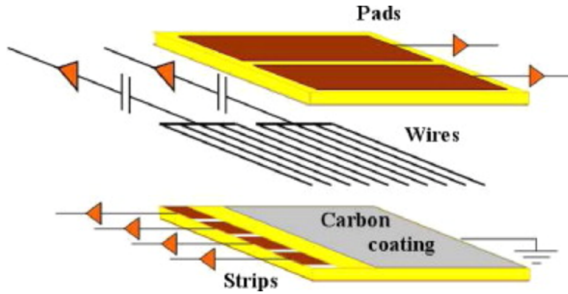


Figure 2.13: Geometry of the sTGC detector [45]

1061 2.3.3 PHYSICS IMPACT

1062 Maintaining low p_T thresholds for muons while still staying within the trigger rate budget at Level 1
 1063 (20 kHz) for the muon system is crucial for physics analyses to be successful in high luminosity condi-
 1064 tions. One realm where the lepton trigger threshold is especially important is in Higgs physics. In the
 1065 $H \rightarrow WW^*$ analysis, one of the W bosons is off shell and tends to decay to soft leptons. In associated
 1066 production of a Higgs with a W , the lepton is also important because the lepton provides the main han-
 1067 dle which allows the event to be triggered. Table 2.3 shows the impact of increasing the trigger thresholds
 1068 on these analyses. It shows that either raising the threshold or using only the barrel both have signifi-
 1069 cant impacts on the signal efficiency. With the NSW, the signal efficiency is largely maintained and the
 1070 triggers can be unprescaled.

Threshold	$H \rightarrow bb$ (%)	$H \rightarrow WW^*$ (%)
$p_T > 20$ GeV	93	94
$p_T > 40$ GeV	61	75
$p_T > 20$ GeV (barrel only)	43	72
$p_T > 20$ GeV (with NSW)	90	92

Table 2.3: Signal efficiencies for WH production with $H \rightarrow b\bar{b}$ and $H \rightarrow WW^* \rightarrow \mu\nu qq$ under different trigger configurations [45].

1071 2.4 OBJECT RECONSTRUCTION IN ATLAS

1072 ATLAS analyses first start by requiring the presence of certain reconstructed physics objects in the event.
 1073 This section will present a brief overview of the algorithms used to reconstruct electrons, muons, jets

1074 (including b -jets), and missing energy*. The performance of object reconstruction and measurement will
 1075 also be discussed as these are relevant to the analyses presented later. Figure 2.14 gives an overview of the
 1076 different sub-detectors that each type of particle will interact with in ATLAS.

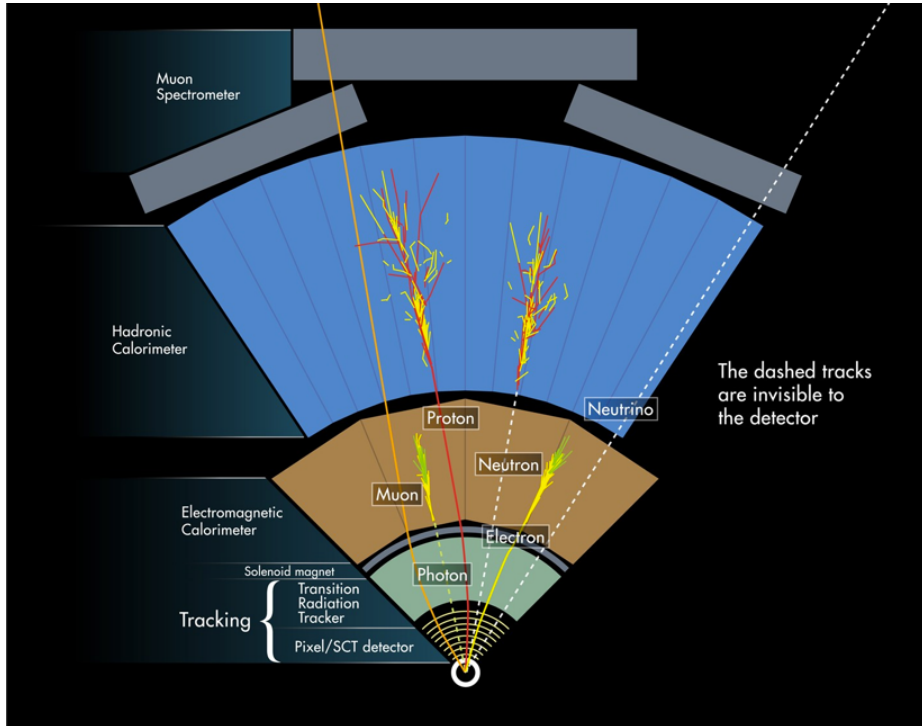


Figure 2.14: Illustration of particle interactions in ATLAS [48]

1077 2.4.I ELECTRONS

1078 Electrons in ATLAS will leave tracks in the inner detector and energy deposits in the electromagnetic
 1079 calorimeter. The algorithm for recognizing the signature of electrons proceeds in two steps: reconstruc-
 1080 tion and identification.

1081 In reconstruction, an electron candidate is formed by matching EM calorimeter deposits with ID
 1082 tracks. The algorithm first chooses seed clusters in the EM calorimeter by using a sliding window algo-
 1083 rithm that searches for towers with transverse energy larger than 2.5 GeV. In addition to seed clusters,
 1084 track candidates must be identified in the ID. The algorithm selects seed tracks with $p_T > 1$ GeV that

*Reconstruction algorithms for other objects, such as photons and τ leptons, are not detailed here as these objects are not used in the presented studies.

1085 do not fit well with a pion hypothesis. Once candidate tracks are selected, they are re-fit with a Gaussian
 1086 Sum Filter (GSF) algorithm to estimate electron parameters [49]. Finally, an electron candidate is
 1087 formed if at least one track matches to a seed cluster in the calorimeter. The full details of the reconstruc-
 1088 tion algorithm can be found in reference [50].

1089 Once an electron candidate is present, identification criteria must be applied in order to reject fake
 1090 electrons from background. Many different variables are used for this identification, most of them re-
 1091 lated to the shower shape in the EM calorimeter and the amount of leakage into the hadronic calorime-
 1092 ter, as well as information from the ID and in particular the TRT. There are both cut-based and likelihood-
 1093 based criteria that range from “loose” to “very tight”. For details, see reference [50].

1094 Figure 2.15 shows the algorithm’s reconstruction efficiency of true electrons for different identification
 1095 criteria as well as the electron energy resolution in simulation [50, 51]. The reconstruction efficiency is
 1096 measured using both Z and J/ψ tag and probe techniques.

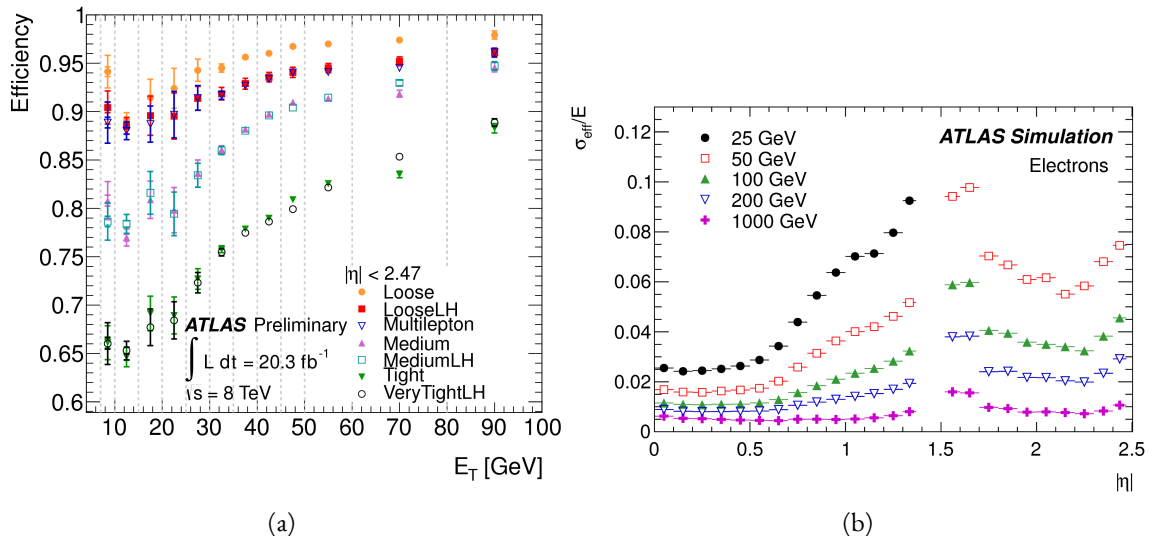


Figure 2.15: Electron performance: (a) reconstruction efficiency as a function of electron E_T [50] (b) energy resolution in simulation as a function of $|\eta|$ for different energy electrons [51]

1097 2.4.2 MUONS

1098 The ATLAS detector is designed to stop most particles before they reach the muon spectrometer. Muons,
 1099 however, are minimum ionizing particles, meaning that they will not lose a significant amount of energy

1100 through interactions with the detector and will thus pass through. Therefore, the muon reconstruction
1101 works to match tracks in the muon spectrometer with tracks in the inner detector.

1102 The first step of reconstruction is to reconstruct local straight line tracks, called segments, in each
1103 muon chamber. Segments are then fit to larger tracks that traverse the entire muon spectrometer. Such
1104 muon tracks are referred to as “standalone” tracks (SA) as they only use information from the muon
1105 spectrometer. The standalone tracks are then matched to tracks in the inner detector to form “com-
1106 bined” (CB) muons, where the combined ID and MS fit are used to determine the momentum and di-
1107 rection of the muon. To improve acceptance, segment-tagged and calorimeter-tagged muons are also
1108 reconstructed. In these cases, ID tracks are matched to segments in the MS and calorimeter deposits con-
1109 sistent with a minimum ionizing particle, respectively. The details of the reconstruction can be found in
1110 reference [52].

1111 As with electrons, once muon candidates are reconstructed they have identification criteria applied to
1112 reduce background. These criteria include the χ^2 match between the ID and MS tracks, the number of
1113 hits in the ID, overall ID and MS track fit quality, and additional variables [52]. The criteria range from
1114 “loose” to “tight” as with electrons.

1115 Figure 2.16 shows the muon reconstruction efficiency (measured with Z and J/ψ tag and probe) and
1116 invariant mass resolution [52].

1117 2.4.3 JETS

1118 When a quark or gluon is produced in collisions, it is not measured directly in ATLAS. Rather, due to
1119 QCD effects, it produces a collimated spray of hadrons in the direction of the original parton, which is
1120 known as a jet. Jets are reconstructed in ATLAS using energy deposits in the hadronic calorimeter. The
1121 first step is build “topological clusters” out of energy deposits in calorimeter cells [53, 54]. This is done
1122 using strategy where seed cells are chosen by picking cells whose energy measurements are four times the
1123 amount of noise expected for that cell. Adjacent cells with at least 2σ energy measurements are added
1124 to the cluster, then a final layer of clusters with energy above 0σ are added. Once calorimeter clusters
1125 are formed, they are clustered further into jet candidates using the anti- k_T jet clustering algorithm [55].

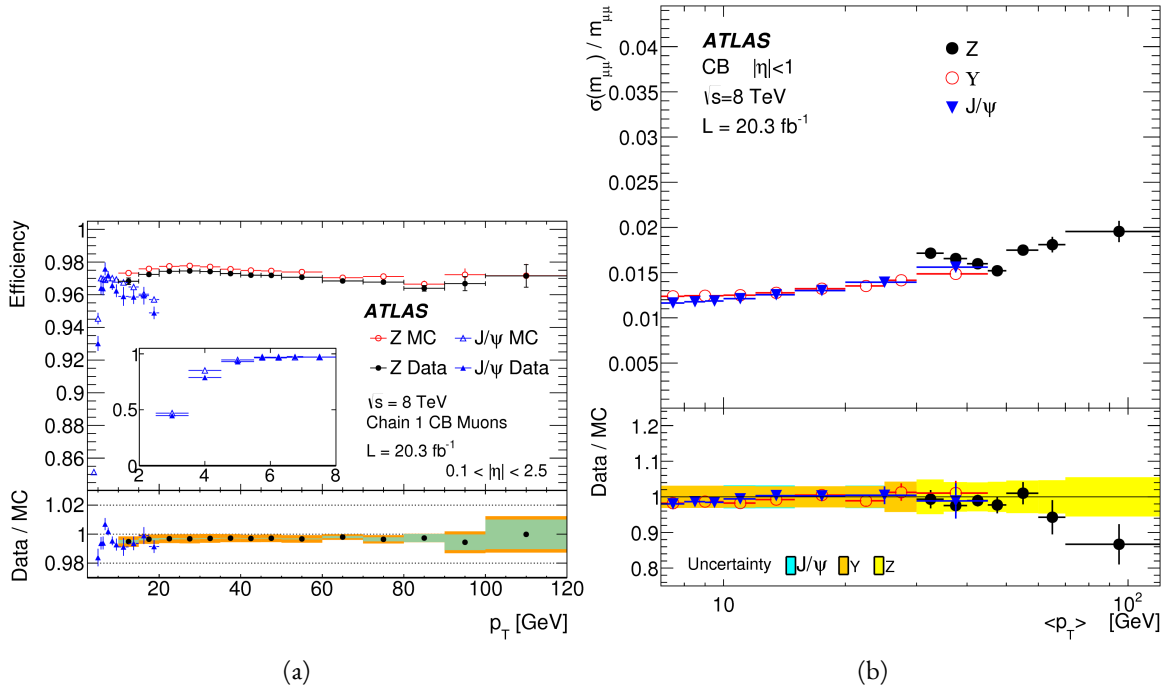


Figure 2.16: Muon performance: (a) reconstruction efficiency as a function of muon p_T (b) dimuon mass resolution as a function of average p_T [52]

1126 This algorithm uses a parameter R that appears in the denominator of the clustering distance metric and
 1127 defines the radial size of the jet in η - ϕ space.

1128 The energy response of the calorimeter must be properly characterized in order to reconstruct jet en-
 1129 ergy. Calorimeter clusters can be calibrated either with the EM calibration, where each cluster is assumed
 1130 to have come from the energy deposit of an electron or photon, or the LCW calibration, where local
 1131 cluster weights are computed to allow for local calibration of clusters as hadronic or electromagnetic.

1132 The details of the jet energy calibration are not detailed here and are discussed in reference [56].

1133 Figure 2.17 shows the jet energy response after calibration in Monte Carlo as a function of the true p_T
 1134 of the jet [56].

1135 2.4.4 b -TAGGING

1136 One important aspect of jet physics is the task of identifying the flavor of parton that produced the mea-
 1137 sured jet. While in general this is very difficult, jets from b -quarks offer an interesting case where such
 1138 identification is possible. B mesons have a lifetime on the order of 10^{-12} seconds, which makes a $c\tau$

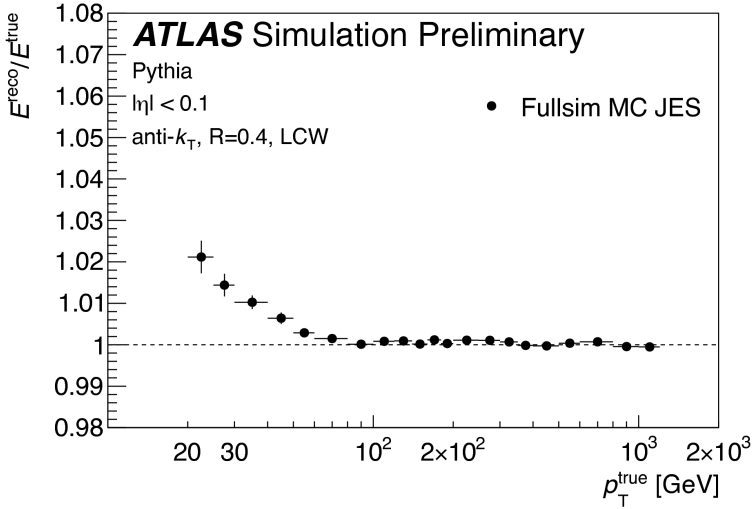


Figure 2.17: Jet energy response after calibration as a function of true p_T in simulation [56]

on the order of millimeters [6]. This type of displaced decay vertex can be identified in detectors like ATLAS and allows b -jets to be distinguished from other flavors of jets[†].

ATLAS uses a multivariate machine learning algorithm to identify jets from b -quarks. The inputs to this algorithm are determined from lower level reconstruction algorithms. There are three distinct algorithms that reconstruct variables which are used as input to the multivariate technique.

The first family is referred to as IPxD (where the x can either be 2 or 3). These algorithms use the transverse and longitudinal impact parameters d_0 and z_0 of the tracks inside a jet to determine their consistency with the primary vertex. They two or three dimensional (hence the x) templates for light flavor, charm, and bottom jets and then evaluate the likelihood of the jet coming from each of these types. The likelihood ratios are used as inputs to the multivariate algorithm.

The next two algorithms used as input are referred to as the secondary vertex (SV) and JetFitter (JF) algorithms. The SV algorithm uses tracks inside the jet to fit for vertices that are displaced from the primary vertex. The JF algorithm attempts to reconstruct the full flight path of the b by looking for multiple displaced vertices along the same line (as B decays often result in subsequent c decays).

In Run 1, the multivariate b -tagging algorithm used a neural network and was referred to as MV1.

[†]Jets from charm quarks can also be detected in this way but they do not live quite as long so the displacement of the vertex is harder to distinguish

1154 The details of this algorithm and its inputs are given in reference [57]. In Run 2, the number of inputs
 1155 was simplified and a boosted decision tree with 24 input variables was used, referred to as MV2. The
 1156 details of this algorithm are in reference [58]. Figure 2.18 shows the performance of each of these algo-
 1157 rithms.

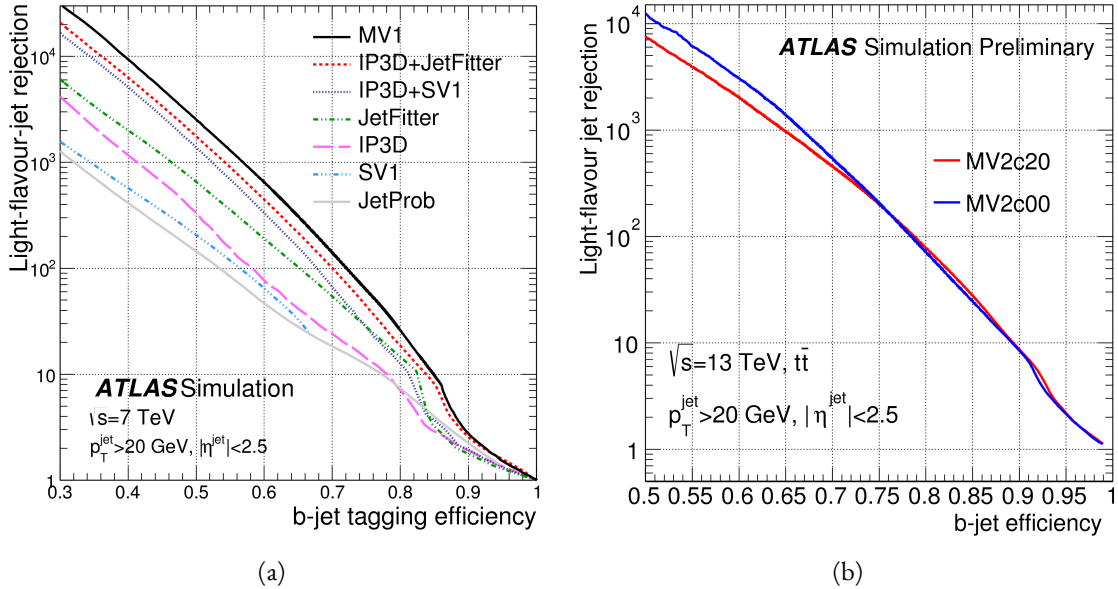


Figure 2.18: Light jet rejection (1/efficiency) vs. b-jet efficiency for MV1 and its input algorithms (a) [57] and MV2 (b) [58] in simulated $t\bar{t}$ events. The numbers in the algorithm names in (b) refer to the fraction of charm events used in the MV2 training.

1158 2.4.5 MISSING TRANSVERSE ENERGY

1159 As noted in figure 2.14, neutrinos produced in ATLAS will pass through the detector without inter-
 1160 acting. The only way of detecting the presence of particles like neutrinos (or BSM particles that are
 1161 long-lived) is to use missing transverse momentum. The basic principle of missing transverse energy is
 1162 to use the momentum balance of the incoming protons to infer the presence of missing particles. The
 1163 net longitudinal momentum of the incoming partons that collide is not known (since each carries an un-
 1164 known fraction of the proton's momentum). However, the protons (and thus incoming partons) have
 1165 no net momentum in the plane transverse to the beam line (the x - y plane). Therefore, if there are no
 1166 un-measured particles in the final state, the transverse momenta of all of the final state particles should

1167 balance. The magnitude of this imbalance is known as missing transverse momentum (E_T^{miss}).

1168 The basic calculation of missing transverse momentum from calorimeter cells is given in equation 2.4 [59].

1169

$$\begin{aligned} E_x^{\text{miss}} &= -\sum_{i=1}^{N_{\text{cell}}} E_i \sin \theta_i \cos \phi_i \\ E_y^{\text{miss}} &= -\sum_{i=1}^{N_{\text{cell}}} E_i \sin \theta_i \sin \phi_i \end{aligned} \quad (2.4)$$

1170 The E_T^{miss} calculation is separated into different terms based on the objects that the calorimeter clusters
1171 are associated with. This way, each cell's contribution is calibrated appropriately according to the object.

1172 This separation of terms is shown in equation 2.5 [59].

$$\begin{aligned} E_{x(y)}^{\text{miss,calo}} &= E_{x(y)}^{\text{miss},e} + E_{x(y)}^{\text{miss},\gamma} + E_{x(y)}^{\text{miss},\tau} + E_{x(y)}^{\text{miss,jets}} \\ &\quad + E_{x(y)}^{\text{miss,softjets}} + E_{x(y)}^{\text{miss},\mu} + E_{x(y)}^{\text{miss,CellOut}} \end{aligned} \quad (2.5)$$

1173 The CellOut term of the above equation corresponds to calorimeter cells with energy deposits that are
1174 not associated with other objects. The soft jets term comes from cells associated to jets with p_T between
1175 7 and 20 GeV, while the jets term comes from jets with $p_T > 20$ GeV. Because muons do not deposit
1176 significant energy in the calorimeter, the muon momentum is used for the muon term [59]. The final
1177 E_T^{miss} is calculated using equation 2.6.

$$E_T^{\text{miss}} = \sqrt{(E_x^{\text{miss}})^2 + (E_y^{\text{miss}})^2} \quad (2.6)$$

1178 Figure 2.19 shows the resolution of the components of the E_T^{miss} under different pileup suppression
1179 techniques [60].

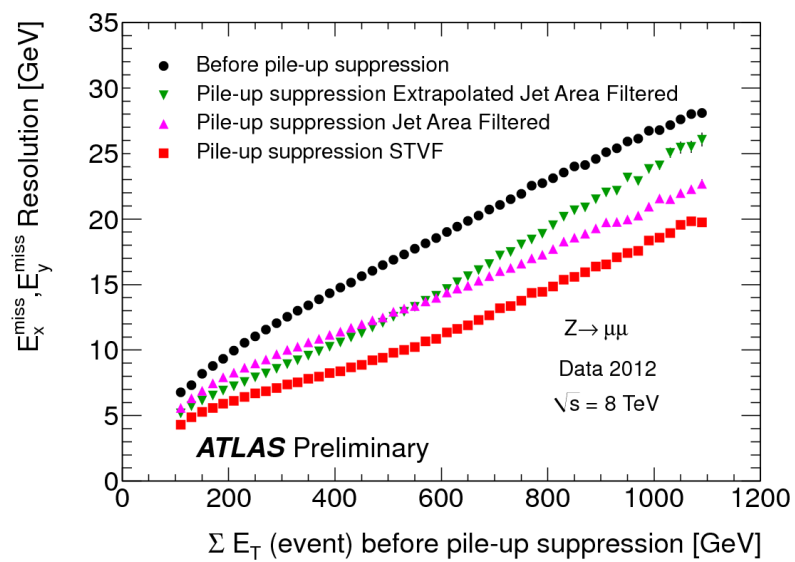


Figure 2.19: Resolution of E_T^{miss} components as a function of $\sum E_T$ before pileup suppression with different pileup techniques [60]

1180

Part II

1181

Observation and measurement of Higgs

1182

boson decays to WW^* in LHC Run I at

1183

$\sqrt{s} = 7$ and 8 TeV

*Basic research is what I am doing when I don't know
what I am doing.*

Wernher von Braun

3

1184

1185

$H \rightarrow WW^* \rightarrow \ell\nu\ell\nu$ Analysis Strategy

1186 3.1 INTRODUCTION

1187 This chapter presents an overview of the strategy for searching for a Higgs boson in the $H \rightarrow WW^* \rightarrow$
1188 $\ell\nu\ell\nu$ decay topology. Its purpose is to define in broad terms how the search and measurement are un-
1189 dertaken, before going into details on the specific sub-categories within the larger analysis. First, the
1190 properties of the Higgs signal are discussed and the associated backgrounds are presented. Next, the ob-
1191 servables used to enhance the signal to background ratio are defined. Finally, the parameters of interest
1192 in the search and measurement will be shown, along with a brief overview of the statistical treatment of
1193 the final Higgs candidates.

1194 Following this chapter, the results of three different studies within the $H \rightarrow WW^* \rightarrow \ell\nu\ell\nu$ channel
1195 are shown. Chapter 4 presents a search for Higgs boson production in gluon fusion mode and the role
1196 of the $H \rightarrow WW^*$ channel in its discovery. Chapter 5 shows the search and first observation in ATLAS
1197 of the Vector Boson Fusion (VBF) production mode of the Higgs in the $H \rightarrow WW^*$ decay channel.

1198 Finally, chapter 6 shows the combined Run 1 $H \rightarrow WW^*$ results for the measurement of the Higgs
1199 cross section and relative coupling strengths to other SM particles.

1200 3.2 THE $H \rightarrow WW^* \rightarrow \ell\nu\ell\nu$ SIGNAL IN ATLAS

1201 The signal studied in this and subsequent chapters is the Higgs boson in the WW^* final state, where
1202 each W boson subsequently decays into a charged lepton and a neutrino. In the simplest decay path,
1203 the final state consists of two neutrinos and two charged leptons, each of which can be either an electron
1204 or a muon. If a W decays to a τ lepton, only leptonic decays of the τ are considered. The τ lepton pro-
1205 duce additional neutrinos in the final state but still yield two charged leptons (where each lepton is an
1206 electron or muon). Neutrinos are not detected in ATLAS, so the final state ultimately consists of two
1207 reconstructed leptons and missing transverse momentum (denoted as E_T^{miss}). Final states where both of
1208 the charged leptons are electrons or muons are referred to as the “same flavor” ($ee/\mu\mu$) final states, while
1209 those with one electron and one muon are referred to as “different flavor” ($e\mu$ or μe).

1210 There can be additional jets produced in association with the Higgs boson. As described in detail
1211 in Chapter 1, if the Higgs is produced via vector boson fusion production, there will be two additional
1212 forward jets in the event. In gluon fusion, one or more jets can be produced through initial state radi-
1213 ation from the incoming gluons. Because of the varying background composition as a function of jet
1214 multiplicity, each bin in this variable has its own dedicated requirements applied in the search and mea-
1215 surement. The $n_j = 0$ and $n_j = 1$ bins are dedicated to gluon fusion production, while the $n_j \geq 2$ bin
1216 has separate dedicated searches for ggF and VBF production.

1217 Figure 3.1 shows the relative branching fractions for the $H \rightarrow WW^*$ process, calculated from the Par-
1218 ticle Data Group values for the W and τ branching ratios [6]. The largest branching ratio corresponds
1219 to both W bosons decaying to quark pairs at 45.44%. The second largest ratio is for one W decaying lep-
1220 tonically and the other decaying to quarks, a branching ratio of 34.18%. In all cases, ℓ denotes either an
1221 electron or muon, and the leptonic branching ratios of the τ are included. For example, the $\ell\nu qq$ final
1222 state includes one W decaying to $e\nu$, $\mu\nu$, or $\tau\nu$. In the case of the $W \rightarrow \tau\nu$ decay, the τ lepton then
1223 decays to an electron or muon via $\tau \rightarrow \nu_\tau \ell \nu_\ell$. Final states with a τ_h refer to hadronic decays of the τ .

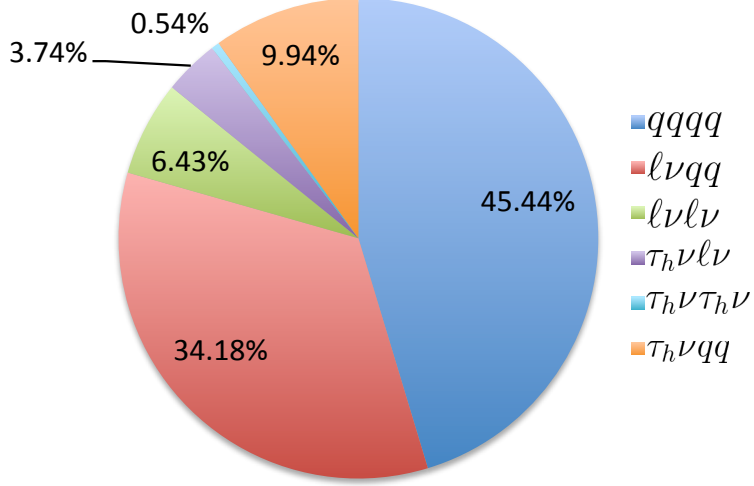


Figure 3.1: Branching ratios for a WW system. q refers to quarks. ℓ can be either an electron or muon, and the leptonic branching ratios of the τ are included. For example, the $\ell\nu qq$ final state includes one W decaying to $e\nu$, $\mu\nu$, or $\tau\nu$. τ_h refer to hadronic decays of the τ .

1224 The branching ratio of the $\ell\nu\ell\nu$ final state is 6.43%.

1225 While the $\ell\nu\ell\nu$ final state is not a large fraction of the branching ratio, there are significant advantages
 1226 to using this channel in an analysis. First, both the $qqqq$ and $\ell\nu qq$ channels suffer from a large QCD
 1227 multijet background, which is often difficult to model. Second, events in the the $\ell\nu\ell\nu$ channel in data
 1228 can be triggered more efficiently due to the presence of two leptons.

1229 3.3 BACKGROUND PROCESSES

1230 Many processes from the Standard Model can also produce a final state with two leptons and missing
 1231 transverse momentum. This section describes the dominant backgrounds to Higgs production and fur-
 1232 ther explains how they can be reduced. Table 3.1 summarizes the different background processes.

1233 3.3.1 STANDARD MODEL WW PRODUCTION

1234 Non-resonant Standard Model diboson production, as shown in figure 3.2, is an irreducible background
 1235 to Higgs boson production in the WW final state. It produces the same exact final state objects, namely

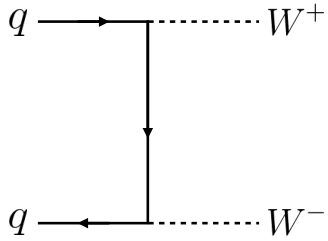


Figure 3.2: Feynman diagram for Standard Model WW production

1236 leptonically decaying W bosons. There are no additional objects in the final state that allow for back-
1237 ground reduction. Therefore the analysis solely relies on the correlations between the leptons to reduce
1238 this background.

1239 **3.3.2 TOP QUARK PRODUCTION**

1240 Top quark production can mimic the Higgs in the WW^* final state as well. Top quarks can be produced
1241 either in pairs ($t\bar{t}$ production) or singly (s -channel, t -channel, or associated production Wt). The domi-
1242 nant top background are $t\bar{t}$ and Wt production.

1243 Because top quarks decay via $t \rightarrow Wb$, top pair production can produce a final state with two W
1244 bosons that then decay leptonically. In Wt production, there are two real W bosons produced, as with
1245 $t\bar{t}$. In both cases, there is at least one b -jet in the final state. By vetoing on the presence of b -jets, these top
1246 quark backgrounds can be reduced. Figure 3.3 shows the Feynman diagrams for $t\bar{t}$ and Wt production.

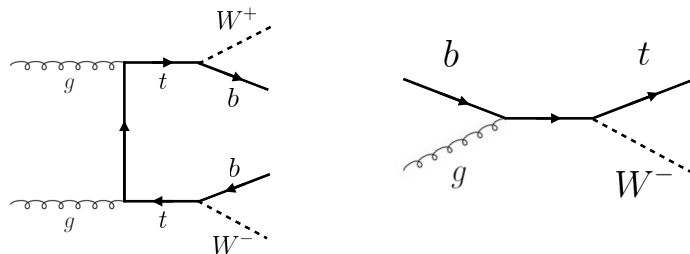


Figure 3.3: Feynman diagrams for top pair production (left) and Wt production (right)

1247 3.3.3 W +JETS BACKGROUND

1248 Single W boson production in association with jets is a unique background to Higgs production. The
1249 other backgrounds considered thus far have all included two prompt leptons, each decaying from a W
1250 boson, in the final state. In W +jets production, however, only one reconstructed lepton originates from
1251 a W . The second reconstructed lepton is either an algorithmic “fake” or the result of non-prompt de-
1252 cays. In the first case, the lepton is a jet misidentified as a lepton by either the electron or muon recon-
1253 struction algorithms. In the second case, the lepton may be a real lepton but coming from semi-leptonic
1254 decays of particles inside the shower of the jet. This background can be reduced by requiring that the
1255 reconstructed lepton have little activity in the surrounding region of the calorimeter (also known as an
1256 “isolation”). Figure 3.4 shows the Feynman diagram for W +jets production.

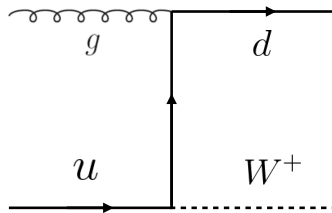


Figure 3.4: An example Feynman diagram of W +jets production

1257 3.3.4 Z/γ^* +JETS BACKGROUND

1258 Production of a Z boson or virtual photon (also known as Drell-Yan and denoted with Z/γ^*) in associa-
1259 tion with jets is also a background to Higgs production. The Z boson decays to two leptons of the same
1260 flavor. When the Z/γ^* decays directly to electrons or muons, the background enters the same flavor fi-
1261 nal state. When the Z decays to two τ leptons the background can enter the different flavor final state as
1262 well. Figure 3.5 shows the production of a Z in association with one jet. Because there are no neutrinos
1263 in this final state, variables like E_T^{miss} can be used to reduce the background*.

The E_T^{miss} cut is much more effective for the reduction of Z/γ^ production in the same flavor final state. If the background enters the different flavor final state through τ decays, there will be neutrinos present. Other requirements on the lepton invariant mass are made to reduce the $Z/\gamma^* \rightarrow \tau\tau$ background.



Figure 3.5: An example Feynman diagram of Z +jets production

1264 3.3.5 SUBDOMINANT BACKGROUNDS

1265 There are additional processes which contribute to the background composition. These backgrounds are
 1266 subdominant and contribute less to the total background estimate than those discussed previously. The
 1267 first process is referred to as VV or “Other diboson” processes and includes multiple Standard Model
 1268 diboson processes, including WZ , ZZ , $W\gamma$, $W\gamma^*$, and $Z\gamma$ production. Additionally, there is a back-
 1269 ground contribution from QCD multijet production. While the cross section for this process is large, its
 1270 contribution to the WW^* final state is small because two jets must be misidentified as leptons.

Category	Process	Description
SM WW	$WW \rightarrow \ell\nu\ell\nu$	Real leptons and neutrinos
Top quark production	$t\bar{t} \rightarrow WbWb \rightarrow \ell\nu b\bar{\nu}b$	Real leptons, untagged b s
	$tW \rightarrow WbW \rightarrow \ell\nu\ell\nu b$	Real leptons, untagged b
	$t\bar{b}, t q \bar{b}$	Untagged b , jet misidentified as lepton
Drell-Yan	$Z/\gamma^* \rightarrow ee, \mu\mu$	“Fake” E_T^{miss}
	$Z/\gamma^* \rightarrow \tau\tau \rightarrow \ell\nu\ell\nu\nu$	Real leptons and neutrinos
Other dibosons	$ZZ \rightarrow \ell\ell\nu\nu$	Real leptons and neutrinos
	$W\gamma^*, WZ \rightarrow \ell\nu\ell\ell, ZZ \rightarrow \ell\ell\ell\ell$	Unreconstructed leptons
	$W\gamma, Z\gamma$	γ reconstructed as e , unreconstructed lepton
W +jets	$Wj \rightarrow \ell\nu j$	Jet reconstructed as lepton
QCD multijet	jj	Jets reconstructed as leptons

Table 3.1: A summary of backgrounds to the $H \rightarrow WW^* \rightarrow \ell\nu\ell\nu$ signal

1271 3.4 SHARED SIGNAL REGION SELECTION REQUIREMENTS

1272 As presented in section 3.2, there are many different combinations of physics objects that can define a
 1273 $H \rightarrow WW^* \rightarrow \ell\nu\ell\nu$ final state. The multiplicity of jets and the flavor combinations of the leptons

1274 both lead to many potential signal regions. Additionally, signal regions can be optimized separately to
 1275 be sensitive to the distinct production modes of the Higgs. Gluon fusion, vector boson fusion, and asso-
 1276 ciated production of a Higgs all lead to unique final state topologies. Figure 3.6 delineates the different
 1277 signal regions used in the gluon fusion and vector boson fusion $H \rightarrow WW^*$ analyses. While there are
 1278 different optimizations possible in each signal region, there are also some commonly shared selections
 1279 that will be described here.

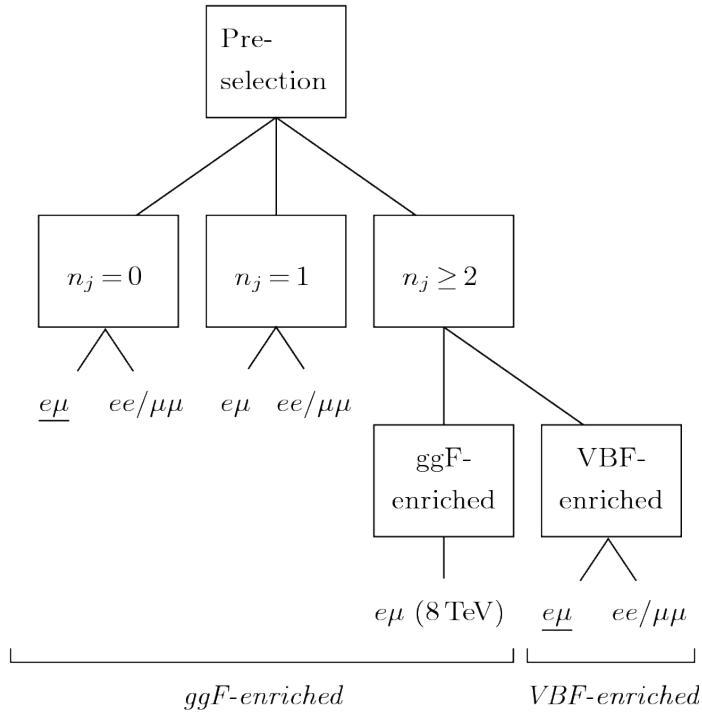


Figure 3.6: An illustration of the unique analysis signal regions [61]. The most sensitive regions for both gluon fusion and vector boson fusion production are underlined.

1280 3.4.I EVENT PRE-SELECTION

1281 Before being sorted into the distinct signal regions, basic requirements are applied to the reconstructed
 1282 objects in the event to select Higgs-like event candidates. First, two oppositely charged leptons are re-
 1283 quired. Once the leptons are selected, the last requirement for event pre-selection is the presence of
 1284 neutrinos. As neutrinos cannot be detected directly in ATLAS, E_T^{miss} can be used as a proxy for the
 1285 combined neutrino momentum in the transverse plane.

1286 In general, it is expected that the signal should have a harder E_T^{miss} spectrum than backgrounds, espe-
 1287 cially if these backgrounds do not contain neutrinos in the final state. When using E_T^{miss} , it is possible
 1288 mis-measurements of objects in the detector can lead to imbalances in the transverse plane. When such
 1289 a mis-measurement occurs, the E_T^{miss} vector in the transverse plane will often point in the same direc-
 1290 tion as the mis-measured object. Therefore, a new variable, $E_{T,\text{rel}}^{\text{miss}}$, is used in the pre-selection. $E_{T,\text{rel}}^{\text{miss}}$ is
 1291 defined in equation 3.1.

$$E_{T,\text{rel}}^{\text{miss}} = \begin{cases} E_T^{\text{miss}} \sin \Delta\phi_{\text{near}} & \text{if } \Delta\phi_{\text{near}} < \pi/2 \\ E_T^{\text{miss}} & \text{otherwise,} \end{cases} \quad (3.1)$$

1292 If the closest object to the E_T^{miss} vector is within $\pi/2$ radians in the transverse plane, the E_T^{miss} is pro-
 1293 jected away from this object. Otherwise, the normal E_T^{miss} vector is used. Figure 3.7 shows a graphical
 illustration of this concept.

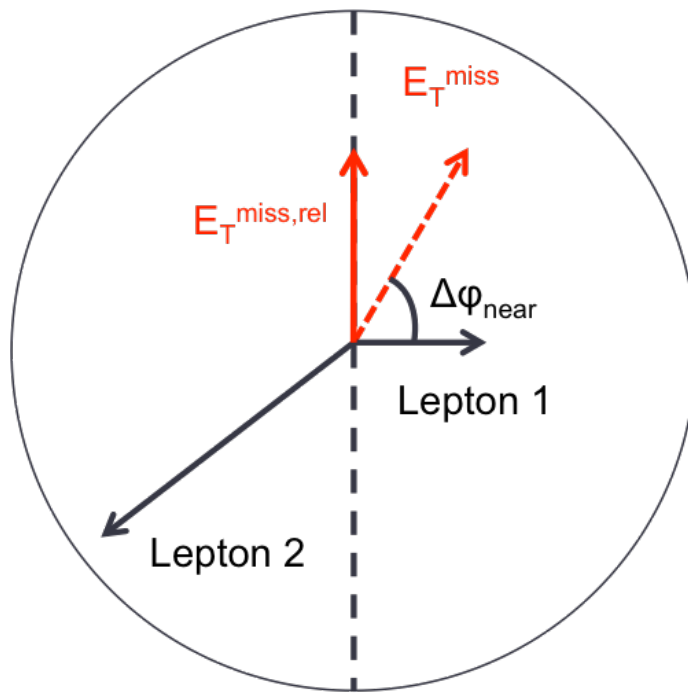


Figure 3.7: A graphical illustration of the $E_{T,\text{rel}}^{\text{miss}}$ calculation

1294
 1295 Once the lepton and E_T^{miss} pre-selections are made, the analysis is divided into different regions ac-
 1296 cording to jet multiplicity.

1297 3.4.2 JET MULTIPLICITY

1298 Jet multiplicity, denoted as n_j , is used to sub-divide the analysis into distinct signal regions. By creating
1299 separate signal regions, each bin in jet multiplicity becomes sensitive to different modes of Higgs produc-
1300 tion and different backgrounds.

1301 For example, the $n_j \geq 2$ region is more sensitive to VBF production because of the two high momen-
1302 tum jets produced at matrix element level. For gluon fusion production to enter this bin, two initial state
1303 radiation jets must be emitted.

1304 Figure 3.8 shows the jet multiplicity in both the different flavor and same flavor regions after the pre-
1305 selection. It also shows the background composition in the bins of n_b . A few trends from this distribu-
1306 tion are worth noting. The first is that the Drell-Yan background dominates in the same flavor chan-
1307 nels for $n_j \leq 1$. Second, the top background becomes a clear contributor to the total background for
1308 $n_j \geq 1$. Lastly, the SM WW production dominates in the $n_j = 0$ bin, as it is an irreducible back-
1309 ground to $H \rightarrow WW^*$ production. Because of these distinct features, each jet multiplicity bin is treated
1310 separately.

1311 3.5 BACKGROUND REDUCTION IN SAME-FLAVOR FINAL STATES

1312 As described in section 3.4.2, the background composition of the same flavor final states is different from
1313 that of the different flavor states. In particular, Drell Yan processes play a much larger role because the
1314 Z/γ^* decays to same flavor leptons. Because real neutrinos are absent in the Z/γ^* decays to ee and $\mu\mu$,
1315 a requirement on E_T^{miss} should largely reduce the background. However, as this section will demon-
1316 strate, with increasing pileup conditions the resolution of the calorimeter-based E_T^{miss} degrades greatly.
1317 Therefore, two new variables for Z/γ^* background reduction are constructed and described in this sec-
1318 tion.

1319 3.5.1 PILEUP AND E_T^{miss} RESOLUTION

1320 Secondary interactions of protons in the colliding bunches of the LHC (known as pileup interactions,
1321 described in detail in Chapter 2) deposit energy into the ATLAS calorimeter in addition to the energy

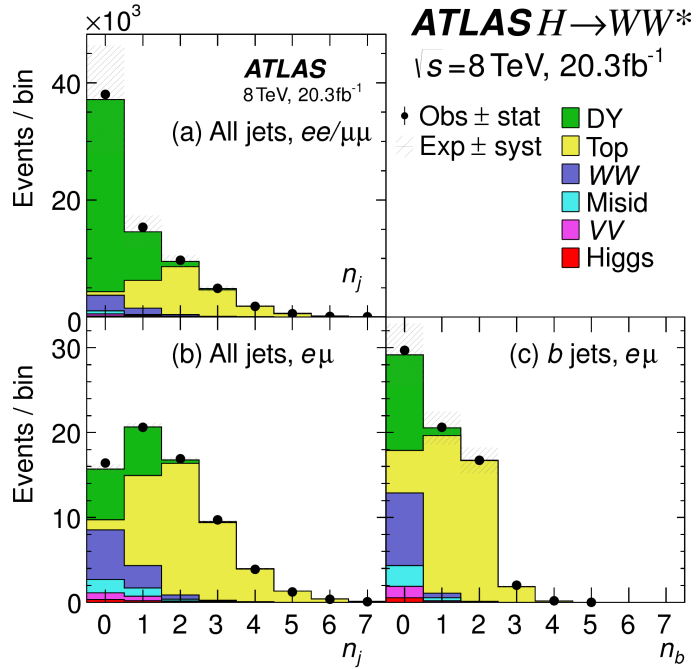


Figure 3.8: Predicted backgrounds (compared with data) as a function of n_j (a and b) and n_b (c) after pre-selection requirements

that comes from the hard scatter process of interest. The calculation of E_T^{miss} is fundamentally Poissonian. Summing up all of the energy deposits in individual calorimeter cells or clusters is similar to a counting experiment. The error on a mean of N in a Poisson distribution is \sqrt{N} , so the energy resolution scales as \sqrt{E} . As more energy is deposited in the calorimeter, the E_T^{miss} resolution degrades, meaning that the E_T^{miss} resolution is particularly sensitive to LHC instantaneous luminosity conditions.

Figure 3.9 shows an event display of a $Z/\gamma^* + \text{jets}$ event candidate with the twenty-five reconstructed primary vertices. This display illustrates that while the interaction of interest only has tracks coming from the hardest primary vertex, all of the secondary interactions deposit energy in the calorimeter as well.

Figure 3.10 shows the RMS of the E_T^{miss} distribution in $Z \rightarrow \mu\mu$ events (where there are no real neutrinos) as a function of the number of the average number of interactions. Under 2011 LHC conditions, this RMS was approximately 9 GeV, while under 2012 running conditions the resolution worsened to 12 GeV. The increase in pileup dilutes the E_T^{miss} variable's ability to reduce the Z/γ^* background.

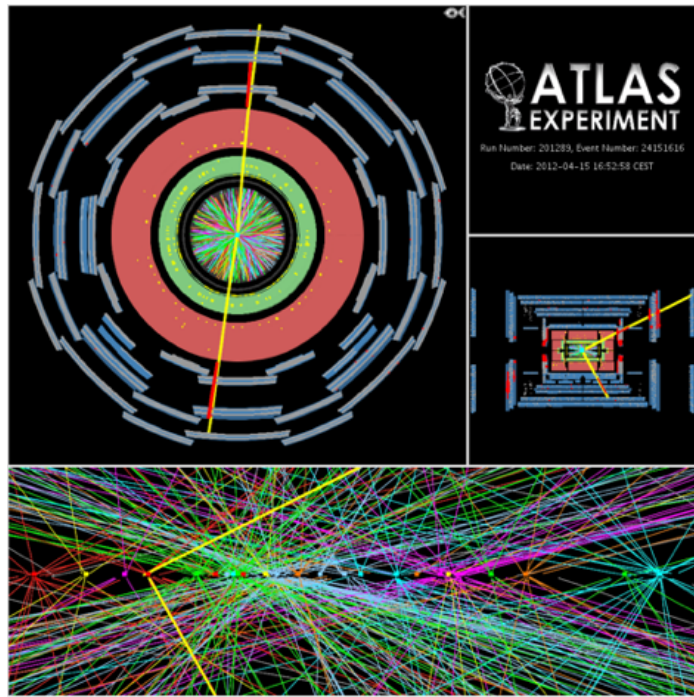


Figure 3.9: An event display of a $Z/\gamma^* + \text{jets}$ event illustrating the effect of pileup interactions

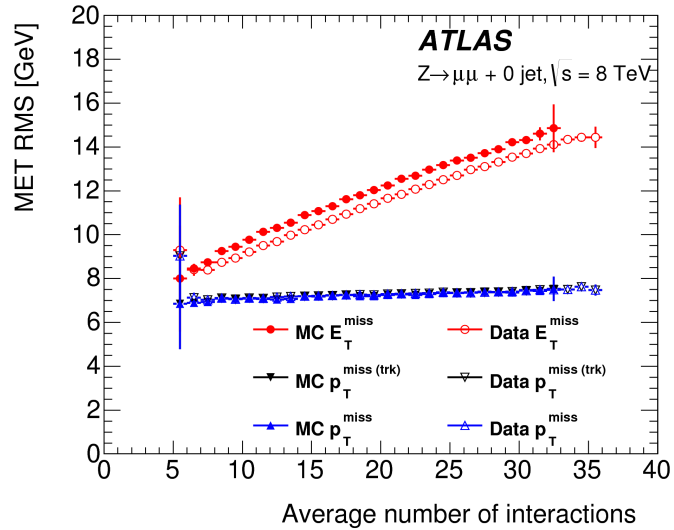


Figure 3.10: The RMS of different missing transverse momentum definitions as a function of the average number of interactions per bunch crossing

1335 3.5.2 TRACK-BASED DEFINITIONS OF MISSING TRANSVERSE MOMENTUM

1336 Because the increasing number of secondary proton-proton interactions degrades calorimeter-based
 1337 E_T^{miss} resolution, a new variable using only contributions from the primary interaction vertex is nec-

1338 essary to further reduce the Z/γ^* background. While it is not possible to associate calorimeter energy
 1339 deposits with a particular vertex, individual charged particle tracks in the Inner Detector are associated to
 1340 unique vertices. Thus, two track-based definitions of missing transverse momentum , using only tracks
 1341 coming from the primary vertex in the event, are used in the analysis. The simplest variable, $p_T^{\text{miss}(\text{trk})}$,
 1342 is the vectorial sum of the p_T of all of the tracks from the primary vertex and the selected leptons (ex-
 1343 cluding the tracks associated with the selected leptons to avoid double counting). Equation 3.2 defines
 1344 $p_T^{\text{miss}(\text{trk})}$.

$$p_T^{\text{miss}(\text{trk})} = - \left(\sum_{\text{selected leptons}} p_T + \sum_{\text{other tracks}} p_T \right), \quad (3.2)$$

1345 To further improve the resolution on the missing transverse momentum, the variable p_T^{miss} is used as
 1346 defined in equation 3.3. For selected leptons and jets, the nominal p_T measurements are used. Tracks
 1347 are used to estimate the soft component of the missing transverse momentum instead of calorimeter
 1348 measurements.

$$p_T^{\text{miss}} = - \left(\sum_{\text{selected leptons}} p_T + \sum_{\text{selected jets}} p_T + \sum_{\text{other tracks}} p_T \right), \quad (3.3)$$

1349 Figure 3.10 illustrates that these two new variables accomplish their intended purpose. The resolution as
 1350 a function of mean number of interactions for both $p_T^{\text{miss}(\text{trk})}$ and p_T^{miss} is much flatter than the depen-
 1351 dence for E_T^{miss} . Figure 3.11a shows the difference between the true and reconstructed values of missing
 1352 transverse momentum using both the track-based p_T^{miss} and calorimeter based E_T^{miss} . The RMS of the
 1353 distribution improves by 3.5 GeV when using p_T^{miss} .

1354 3.5.3 DISTINGUISHING Z/γ^* +JETS AND $H \rightarrow WW^*$ TOPOLOGIES

1355 In addition to measuring missing transverse momentum, another variable can be constructed to exploit
 1356 kinematic and topological differences between the Z/γ^* background and $H \rightarrow WW^*$ signal. Because
 1357 there are no real neutrinos in the final state (in the case of $Z/\gamma^* \rightarrow ee, \mu\mu$ decays), the dilepton system
 1358 will be balanced with the jets produced in the hard scatter. A new variable, f_{recoil} , is constructed to es-
 1359 timate the balance between the dilepton system and recoiling jets and is defined in equation 3.4. The
 1360 transverse plane is divided into four sections, or quadrants, with one quadrant centered on the dilepton

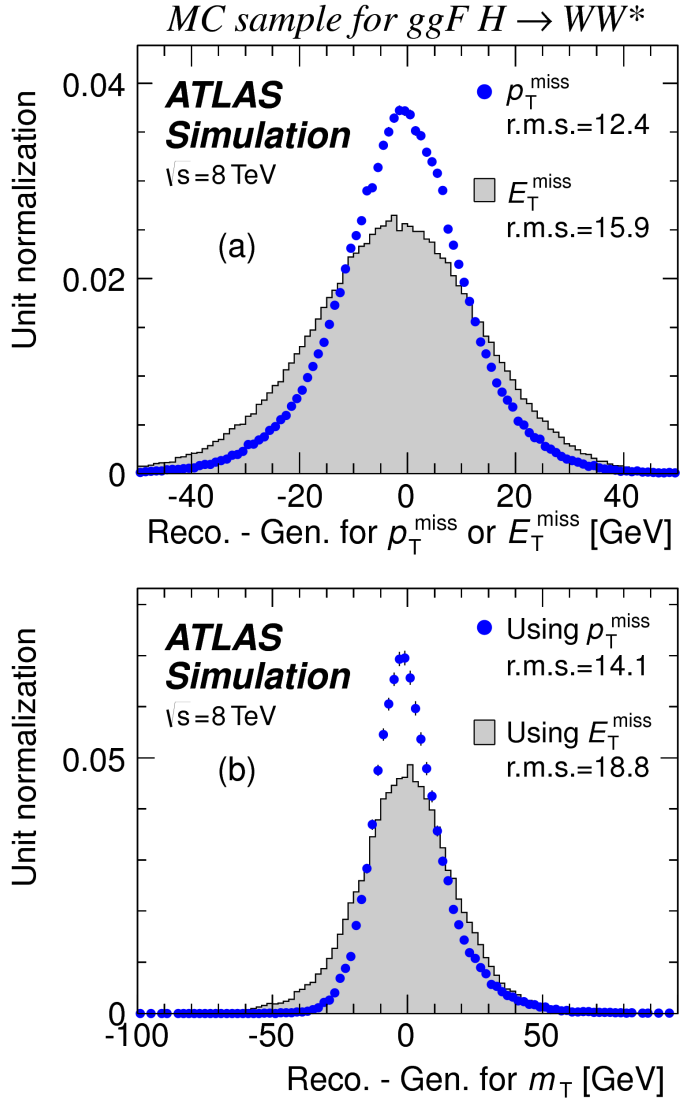


Figure 3.11: The difference between the true and reconstructed values of the missing transverse momentum (a) and m_T (b) in a gluon fusion signal sample

¹³⁶¹ vector. The numerator of f_{recoil} is the magnitude of the vectorial sum of the p_T of jets in the quadrant
¹³⁶² opposite the dilepton system, weighted by each jet's Jet Vertex Fraction (JVF, described in chapter 2).
¹³⁶³ The denominator is the magnitude of the dilepton p_T .

$$f_{\text{recoil}} = \left| \sum_{\text{jets } j \text{ in } \wedge} \text{JVF}_j \cdot \mathbf{p}_T^j \right| / p_T^{\ell\ell}. \quad (3.4)$$

1364 Figure 3.12 shows a shape comparison of the f_{recoil} distribution in a simulated $Z/\gamma^* + \text{jets}$ sample, a
 1365 $H \rightarrow WW^*$ signal sample, and other backgrounds that contain real neutrinos. The $Z/\gamma^* + \text{jets}$ events
 1366 tend to be more balanced between the dilepton system and recoiling jets, while the processes containing
 1367 real neutrinos are less balanced in the transverse plane. Thus, a requirement on f_{recoil} will reduce the
 1368 $Z/\gamma^* + \text{jets}$ background while maintaining a good signal efficiency.

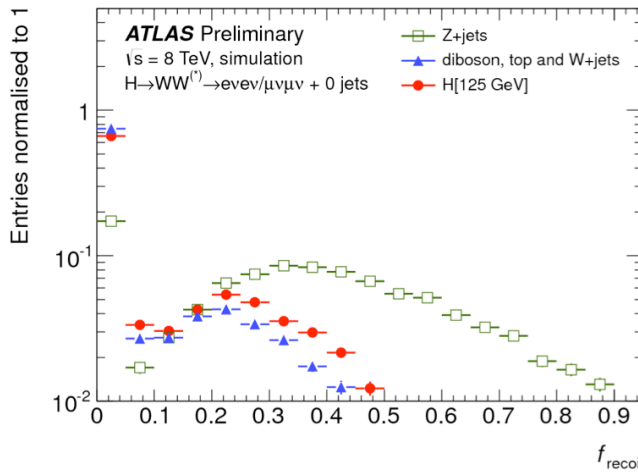


Figure 3.12: Comparison of f_{recoil} distributions for $Z/\gamma^* + \text{jets}$, $H \rightarrow WW^*$, and other backgrounds with real neutrinos.

1369 3.5.4 OPTIMIZING BACKGROUND REDUCTION SELECTION REQUIREMENTS

1370 The requirements on $p_T^{\text{miss}(\text{trk})}$ and f_{recoil} used to reduce the $Z + \text{jets}$ background must be optimized to
 1371 maximize expected signal significance in the same flavor channels. Figure 3.13 shows an optimization of
 1372 the combination of the two requirements in the gluon fusion zero jet bin. Each bin shows the expected
 1373 signal significance if the $p_{T,\text{rel}}^{\text{miss}(\text{trk})}$ is required to be greater than the left edge of the bin and the f_{recoil} is
 1374 required to be less than the top edge of the bin. The figure shows that the best signal significance comes
 1375 from requiring low values of f_{recoil} (< 0.05) and $p_{T,\text{rel}}^{\text{miss}(\text{trk})}$ values greater than 45 GeV.

1376 3.6 PARAMETERS OF INTEREST AND STATISTICAL TREATMENT

1377 As with any search or measurement, there are particular parameters of the Higgs that the $H \rightarrow WW^*$
 1378 analysis is interested in measuring. In this case, the parameters of interest are the mass of the Higgs bo-

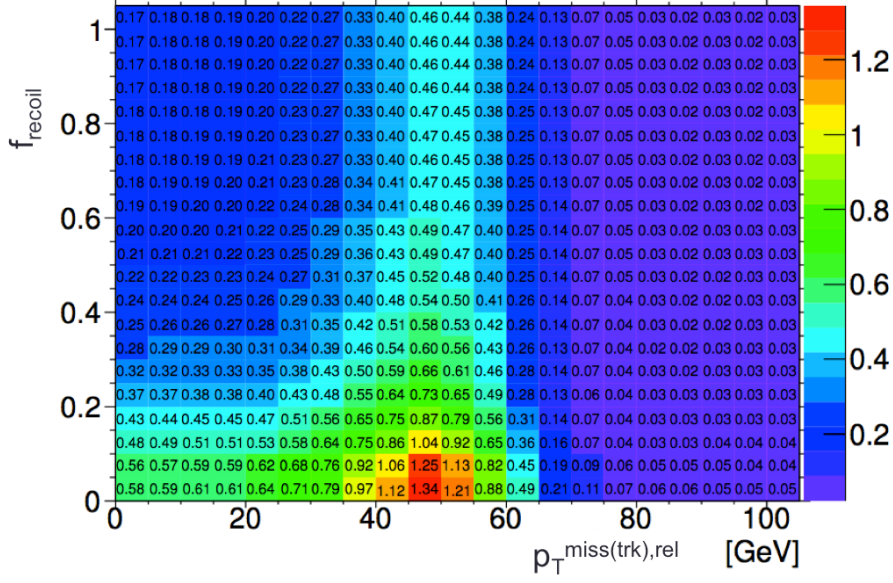


Figure 3.13: Signal significance as a function of required value for f_{recoil} and $p_{T,\text{rel}}^{\text{miss}(\text{trk})}$ in the ggF $H \rightarrow WW^*$ with $n_j = 0$

son and its production cross section. Because the $H \rightarrow WW^* \rightarrow \ell\nu\ell\nu$ process does not have a closed final state, it is not possible to measure the full invariant mass of the particle that may have produced the final state. However, a proxy for the invariant mass is defined using transverse plane information and detailed in section 3.6.1. The second parameter of interest is the ratio of the measured cross section to that expected from the Standard Model Higgs, which is denoted a μ . This is defined in equation 3.5.

$$\mu = \frac{\sigma}{\sigma_{\text{SM}}} \quad (3.5)$$

All of the likelihoods used in the statistical analysis of the final signal region events are parameterized as a function of μ . μ is a natural variable for hypothesis testing, as $\mu = 0$ corresponds to a background only hypothesis and $\mu = 1$ corresponds exactly to a Standard Model Higgs.

3.6.1 TRANSVERSE MASS

The $H \rightarrow WW^* \rightarrow \ell\nu\ell\nu$ analysis cannot reconstruct the full invariant mass of the Higgs because of the neutrinos in the final state. The transverse mass serves as a proxy for the full invariant mass by

1390 exploiting information from the transverse plane. The transverse mass is defined in equation 3.6.

$$m_T = \sqrt{(E_T^{\ell\ell} + p_T^{\text{miss}})^2 - |\vec{p}_T^{\ell\ell} + \vec{p}_T^{\text{miss}}|^2}, \quad (3.6)$$

1391 Here the $E_T^{\ell\ell}$ and $p_T^{\ell\ell}$ are the transverse energy and momentum of the dilepton system, while p_T^{miss} is a
1392 proxy for the transverse momentum of the di-neutrino system. The track-based p_T^{miss} is used in the m_T
1393 rather than the calorimeter based E_T^{miss} because it has a better resolution on the true transverse mass.
1394 Figure 3.11b shows the improvement in the RMS of the difference between the true and reconstructed
1395 transverse mass in a ggF signal sample. The RMS improves by 4.7 GeV using p_T^{miss} in the m_T calcula-
1396 tion.

1397 3.6.2 STATISTICAL TREATMENT[†]

1398 LIKELIHOOD FUNCTION

1399 The statistical analysis of final event candidates is framed as a hypothesis test, where the null hypothe-
1400 sis is background-only (no Standard Model Higgs). The first step in the analysis is to form a likelihood
1401 function for the data. In its simplest form, this likelihood is the probability of observing the number
1402 of events seen in the final signal region given knowledge of the signal strength. Because observation of
1403 events is fundamentally a Poisson counting experiment, this simple likelihood can be expressed as a Pois-
1404 son probability of observing N events given a total number of predicted signal and background events.
1405 This basic likelihood is shown in equation 3.7.

$$\mathcal{L}(\mu) = P(N|\mu S + B) \quad (3.7)$$

1406 Here, P is the Poisson probability density function, N is the total number of observed events, μ is the
1407 signal strength, S is the predicted number of signal events, and B is the predicted number of back-
1408 ground events.

1409 In particle physics, certain background estimates are commonly normalized in so-called “control” re-

[†]Many thanks to Aaron Armbruster, whose thesis [62] inspired parts of this section.

1410 gions and those predictions are scaled by the same normalization factor in the signal region. This leads
1411 to a slightly more complicated likelihood, which is a function of both the signal strength and the back-
1412 ground normalization. This is shown in equation 3.8.

$$\mathcal{L}(\mu, \theta) = P(N|\mu S + \theta B) P(N_{\text{CR}}|\theta B_{\text{CR}}) \quad (3.8)$$

1413 Here, θ serves as a “nuisance parameter”, or a parameter that is not of primary interest but still enters the
1414 likelihood. The second Poisson term enforces that the background normalization be consistent with the
1415 number of observed events in data in the control region, N_{CR} .

1416 So far, these two formulations of likelihoods have assumed a single signal region and do not take into
1417 account any shape information of potential discriminating variables. The $H \rightarrow WW^*$ analysis is di-
1418 vided into many different categories, the counting experiment described above can be performed in each
1419 individual category. As mentioned in section 3.6.1, the transverse mass is used as the primary discriminat-
1420 ing variable in many of the $H \rightarrow WW^*$ sub-analyses. The same counting experiment can be performed
1421 in each bin of the m_T distribution to incorporate some shape information. Thus, the total likelihood
1422 becomes a product over signal regions and bins of the m_T distribution. Finally, there are usually many
1423 backgrounds that are normalized in control regions. The new formulation of the likelihood takes this
1424 into account by including a product over control regions in the second Poisson term. All of these modi-
1425 fications are shown in equation 3.9.

$$\mathcal{L}(\mu, \theta) = \prod_{\substack{\text{SRs } i \\ \text{bins } b}} P\left(N_{ib} \middle| \mu S_{ib} + \sum_{\text{bkg k}} \theta_k B_{kib}\right) \prod_{\text{CRs } l} P\left(N_l \middle| \sum_{\text{bkg k}} \theta_k B_{kl}\right) \quad (3.9)$$

1426 The final step to obtain the full likelihood used in the analysis is to add nuisance parameters for the
1427 systematic uncertainties. In cases where the uncertainty does not affect the shape of m_T bin-by-bin, each
1428 systematic uncertainty ϵ is allowed to affect the expected event yields through a linear response function
1429 of the nuisance parameter, namely $\nu(\theta) = (1 + \epsilon)\theta$. If instead the uncertainty does affect the shape,
1430 the effect is instead parameterized by $\nu_b(\theta) = 1 + \epsilon_b\theta$. The value of the nuisance parameters for the
1431 systematic uncertainty are constrained with a Gaussian term that is added to the likelihood as well. This

¹⁴³² is of the form $g(\delta|\theta) = e^{-(\delta-\theta)^2/2}/\sqrt{2\pi}$, where δ is the central value and θ is a nuisance parameter.

¹⁴³³ Finally, a last term is added to account for the statistical uncertainty in the Monte Carlo samples used,
¹⁴³⁴ which adds an additional poisson term. The full likelihood used in the final statistical analysis is defined
¹⁴³⁵ in equation 3.10.

$$\begin{aligned} \mathcal{L}(\mu, \boldsymbol{\theta}) = & \prod_{\substack{\text{SRs i} \\ \text{bins b}}} P \left(N_{ib} \left| \mu S_{ib} \cdot \prod_{\substack{\text{sig.} \\ r}} \nu_{br}(\theta_r) + \sum_{\text{bkg k}} \theta_k B_{kib} \cdot \prod_{\substack{\text{bkg.} \\ \text{syst.} \\ s}} \nu_{bs}(\theta_s) \right. \right) \\ & \cdot \prod_{\text{CRs l}} P \left(N_l \left| \sum_{\text{bkg k}} \theta_k B_{kl} \right. \right) \\ & \cdot \prod_{\substack{\text{syst} \\ t}} g(\delta_t|\theta_t) \cdot \prod_{\text{bkg k}} P(\xi_k|\zeta_k \theta_k) \end{aligned} \quad (3.10)$$

¹⁴³⁶ The fourth term of the equation quantifies the uncertainty due to finite Monte Carlo sample size.

¹⁴³⁷ Here, ξ represents the central value of the background prediction, θ is the associated nuisance parameter,
¹⁴³⁸ $\zeta = (B/\delta B)^2$, where δB is the statistical uncertainty of B .

¹⁴³⁹ The best fit value of the signal strength μ is determined by finding the values of μ and $\boldsymbol{\theta}$ that maximize
¹⁴⁴⁰ the likelihood, while setting $\delta = 0$ and $\xi = \zeta$. Once the likelihood is defined, a test statistic must
¹⁴⁴¹ be built for use in hypothesis testing.

¹⁴⁴² TEST STATISTIC

¹⁴⁴³ To distinguish whether the data match a background only or background and signal hypothesis, a test
¹⁴⁴⁴ statistic must be used. The $H \rightarrow WW^*$ analysis uses the profile likelihood technique [63]. The first step
¹⁴⁴⁵ in formulating this test statistic is to define the profile likelihood ratio, shown in equation 3.11.

$$\lambda(\mu) = \frac{\mathcal{L}(\mu, \hat{\theta}_\mu)}{\mathcal{L}(\hat{\mu}, \hat{\theta})} \quad (3.11)$$

1446 Here $\hat{\theta}_\mu$ is the value of θ that maximizes the likelihood for the choice of μ being tested. Additionally, $\hat{\theta}$
1447 and $\hat{\mu}$ represent the values of θ and μ that gives the overall maximum value of the likelihood.

1448 Once this is defined, a test statistic q_μ is constructed. This is shown in equation 3.12.

$$q_\mu = -2 \ln \lambda(\mu) \quad (3.12)$$

1449 A higher value of q_μ indicates that the data are more incompatible with the hypothesized value of μ , and
1450 q_0 then corresponds to the value of the test statistic for the background only hypothesis. A p_0 value is
1451 then defined to quantify the compatibility between the data and the null hypothesis. The p_0 value is the
1452 probability of obtaining a value of q_0 larger than the observed value, and this is shown in equation 3.13.

$$p_0 = \int_{q_0^{\text{obs}}}^{\infty} f(q_\mu | \mu = 0) dq_\mu \quad (3.13)$$

1453 Here $f(q_\mu)$ is the probability distribution function of the test statistic. Finally, the p_0 value can be con-
1454 verted into a signal significance, using the formula in equation 3.14, or the one-sided tail of the Gaussian
1455 distribution.

$$Z_0 = \sqrt{2} \operatorname{erf}^{-1}(1 - 2p_0) \quad (3.14)$$

1456 The threshold for discovery used in particle physics is $Z_0 \geq 5$, more commonly known as a value of 5σ .

The real voyage of discovery consists not in seeking new landscapes, but in having new eyes.

Marcel Proust

4

1457

1458

The discovery of the Higgs boson and the 1459 role of the $H \rightarrow WW^* \rightarrow \ell\nu\ell\nu$ channel

1460

4.1 INTRODUCTION

1461 This chapter presents the results of the search for the Higgs boson in 4.8 fb^{-1} collected at $\sqrt{s} = 7 \text{ TeV}$
1462 and 5.8 fb^{-1} at $\sqrt{s} = 8 \text{ TeV}$. The results of three searches at $\sqrt{s} = 8 \text{ TeV}$ in the $H \rightarrow WW^* \rightarrow \ell\nu\ell\nu$
1463 , $H \rightarrow \gamma\gamma$, and $H \rightarrow ZZ \rightarrow 4\ell$ channels are combined with results of searches at $\sqrt{s} = 7 \text{ TeV}$
1464 in the same search channels (as well as the $H \rightarrow \tau\tau$ production and associated production searches for
1465 $H \rightarrow b\bar{b}$). The results of this combination are a 5.9σ detection of a new particle consistent with a Higgs
1466 boson. Rather than going into detail for all of the different Higgs decay searches, this chapter will discuss
1467 the three most sensitive channels and in particular focus on $H \rightarrow WW^* \rightarrow \ell\nu\ell\nu$. While the focus is
1468 on WW^* , some of the ZZ^* and $\gamma\gamma$ results are shown for completeness. The results not discussed here

¹⁴⁶⁹ can be found in the ATLAS Higgs discovery publication [1].

¹⁴⁷⁰ 4.2 DATA AND SIMULATION SAMPLES

¹⁴⁷¹ The data sample used for the following results was taken in 2011 and 2012 at center of mass energies of 7
¹⁴⁷² and 8 TeV, respectively, with 4.8 fb^{-1} collected at 7 TeV and 5.8 fb^{-1} collected at 8 TeV. Higgs pro-
¹⁴⁷³ duction in the gluon fusion and vector boson fusion modes is modeled with **POWHEG** for the hard scat-
¹⁴⁷⁴ tering event and **PYTHIA** for the showing and hadronization. Associated production of a Higgs with a
¹⁴⁷⁵ vector boson or top quarks is modeled via **PYTHIA**. Table 4.1 shows the Monte Carlo generators used for
¹⁴⁷⁶ modeling the signal and background processes relevant for the three analyses to be discussed.

Process	Generator
ggF, VBF H	POWHEG + PYTHIA
$WH, ZH, t\bar{t}H$	PYTHIA
$W + \text{jets}, Z/\gamma^* + \text{jets}$	ALPGEN + HERWIG
$t\bar{t}, tW, tb$	MC@NLO + HERWIG
tqb	ACERMC + PYTHIA
$q\bar{q} \rightarrow WW$	MC@NLO + HERWIG
$gg \rightarrow WW$	GG2WW+ HERWIG
$q\bar{q} \rightarrow ZZ$	POWHEG + PYTHIA
$gg \rightarrow ZZ$	GG2ZZ+ HERWIG
WZ	MADGRAPH+ PYTHIA , HERWIG
$W\gamma + \text{jets}$	ALPGEN + HERWIG
$W\gamma^*$	MADGRAPH+ PYTHIA
$q\bar{q}/gg \rightarrow \gamma\gamma$	SHERPA

Table 4.1: Monte carlo generators used to model signal and background for the Higgs search [1].

¹⁴⁷⁷ 4.3 $H \rightarrow WW \rightarrow e\nu\mu\nu$ SEARCH

¹⁴⁷⁸ The $H \rightarrow WW \rightarrow e\nu\mu\nu$ search is unique compared to the ZZ and $\gamma\gamma$ channels. The Higgs mass can-
¹⁴⁷⁹ not be fully reconstructed due to the presence of neutrinos in the final state, so the transverse mass m_T
¹⁴⁸⁰ is used as the final discriminating variable. Compared to the other channels, there are more backgrounds
¹⁴⁸¹ here as well, as discussed in chapter 3. The same flavor final states are excluded from this search due to
¹⁴⁸² high pileup in the 8 TeV dataset.

1483 4.3.I EVENT SELECTION

1484 The analysis requires two opposite charge isolated leptons, with the leading (sub-leading) lepton required
 1485 to have $p_T > 25(15)$ GeV. The events are separated into different signal regions depending on which
 1486 flavor of lepton is leading ($e\mu$ for leading electron, μe for leading muon). Strict lepton quality cuts are
 1487 applied to the sample to reduce backgrounds from fake leptons.

1488 Jets are reconstructed with the anti- k_T algorithm with a radius parameter $R = 0.4$. The jets are
 1489 required to have $p_T > 25$ GeV and $|eta| < 4.5$, with jets in the tracking volume required to have a
 1490 jet vertex fraction of 0.5 and jets in the forward region required to have $p_T > 30$ GeV. The analysis is
 1491 separated into three different signal regions based on jet multiplicity: $n_j = 0, 1, \geq 2$.

1492 To indicate the presence of neutrinos in the event, a requirement of $E_{T,\text{rel}}^{\text{miss}} > 25$ GeV is made*. This
 1493 requirement significantly reduces the QCD multijet and Z/γ^* + jets backgrounds. Figure 4.1 shows the
 1494 distribution of n_j in data and simulation after applying these “pre-selection” requirements.

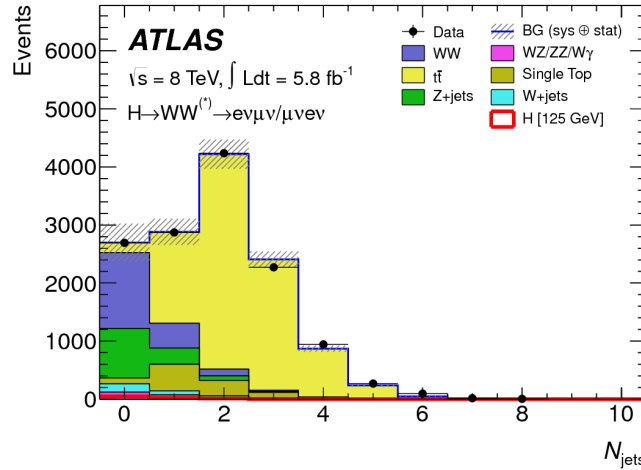


Figure 4.1: Jet multiplicity distribution in data and MC after applying lepton, jet, and $E_{T,\text{rel}}^{\text{miss}}$ selections. The WW and top backgrounds have been normalized using control samples, and the hashed band indicates the total uncertainty on the prediction. [1]

1495 Additional selections are applied to require the dilepton topology to correspond to that of a SM
 1496 Higgs. The requirements are presented here - more detailed discussion on the motivation for each re-
 1497 quirement is saved for Chapter 5. In all of the jet multiplicity channels, the dilepton system is required to

*For the definition of $E_{T,\text{rel}}^{\text{miss}}$, see chapter 3

1498 have a small gap in azimuthal angle, $\Delta\phi_{\ell\ell} < 1.8$. Similarly, the $m_{\ell\ell}$ is required to be less than 50 GeV
1499 in the lower jet multiplicity channels and less than 80 GeV in the $n_j \geq 2$ channel. In the $n_j = 0$ chan-
1500 nel, the magnitude of the dilepton p_T , $p_T^{\ell\ell}$, is required to be greater than 30 GeV.

1501 In the higher jet multiplicity channels ($n_j \geq 1$), the top background is a more important component
1502 and must be reduced. The total transverse momentum p_T^{sum} is thus required to be less than 30 GeV.
1503 Additionally, the di- τ invariant mass $m_{\tau\tau}$ (dilepton mass computed under the assumption that the neu-
1504 trinos from the τ decay are emitted collinear to the charged leptons) is used to reject $Z \rightarrow \tau\tau$ events by
1505 requiring $|m_{\tau\tau} - m_Z| > 25$ GeV. These variables are also discussed in more detail in Chapter 5.

1506 In the $n_j \geq 2$ channel, requirements are made to isolate the VBF contribution to Higgs production.
1507 The kinematics of the two leading jets are used to make these requirements. In particular, the event must
1508 have $\Delta y_{jj} > 3.8$ and $m_{jj} > 500$ GeV, along with a veto on having any additional jets with rapidity
1509 between the two leading jets.

1510 4.3.2 BACKGROUND ESTIMATION

1511 The details of the background estimation techniques used in the $H \rightarrow WW^* \rightarrow \ell\nu\ell\nu$ analysis are dis-
1512 cussed in section 5.5. As that section refers to a later iteration of the analysis, a general discussion is given
1513 here for completeness. The dominant backgrounds are SM WW production and top (both pair and
1514 single) production, and these backgrounds have their normalizations estimated from dedicated control
1515 regions while their shapes are taken from simulation.

1516 The control sample for the Standard Model WW background is defined by making the same require-
1517 ments as the signal region with the $m_{\ell\ell}$ requirement inverted (now requiring $m_{\ell\ell} > 80$ GeV) and
1518 removing the $\Delta\phi_{\ell\ell}$ requirement. This creates a control sample that is 70% (40%) pure in the 0(1)-jet
1519 region. The correction to the pure MC-based background estimate is quantified by defining a normal-
1520 ization factor β which is the ratio of the data yield to the MC yield ($N_{\text{data}}/N_{\text{MC}}$) in this control sample.
1521 Table 4.2 shows the WW normalization factors in the $n_j = 0$ and $n_j = 1$ bins (the $n_j \geq 2$ estimate is
1522 taken directly from MC).

1523 The top background estimate is also computed separately in each jet multiplicity bin. In the $n_j = 0$

n_j	β_{WW}	β_t
= 0	1.06 ± 0.06	1.11 ± 0.06
= 1	0.99 ± 0.15	1.11 ± 0.05
≥ 2	-	1.01 ± 0.26

Table 4.2: Normalization factors (ratio of data and MC yields in a control sample) for the Standard Model WW and top backgrounds in the $H \rightarrow WW^* \rightarrow \ell\nu\ell\nu$ analysis [1]. Only statistical uncertainties are shown.

channel, the background is first normalized using data after pre-selection requirements with no selection on n_j . Then, a dedicated b -tagged control sample is used to evaluate the ratio of one-jet to two-jet events in data. The details of this technique are shown in reference [64]. In the $n_j = 1$ and the $n_j \geq 2$ regions, the top background is normalized in a control sample where the signal region selections are applied, but the b -jet veto is reversed and the Higgs topology requirements on $m_{\ell\ell}$ and $\Delta\phi_{\ell\ell}$ are removed. The resulting normalization factors for these techniques are shown in table 4.2.

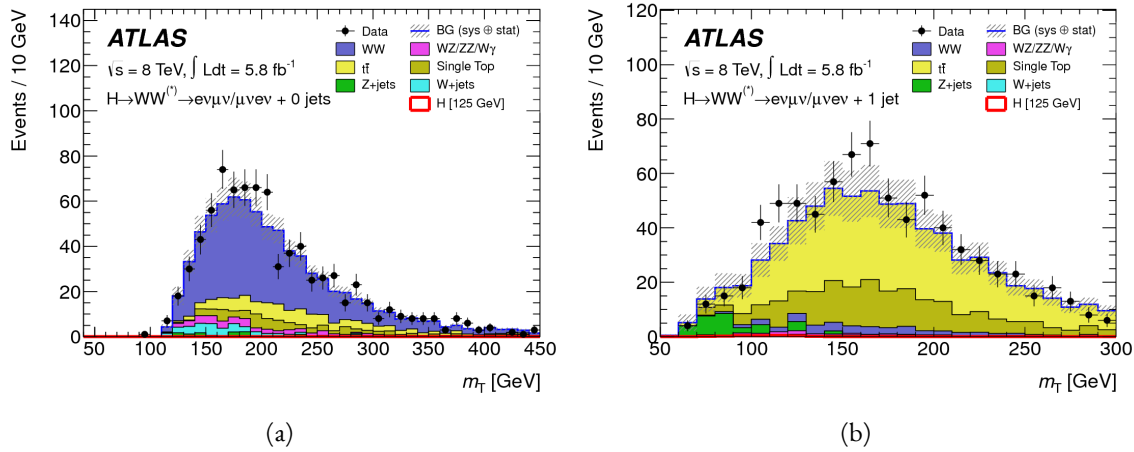


Figure 4.2: Comparison of m_T between data and simulation in the $n_j = 0$ WW (a) and $n_j = 1$ top (b) control samples [1]

The control samples which are used for background normalization can also be used to validate the modeling of the m_T distribution for each background. Figure 4.2 shows the comparison between data and MC for the m_T distribution after correcting the normalization of the backgrounds in the WW and top control regions. Good agreement between data and simulation is seen in both cases.

The $W+jets$ background estimate is taken entirely from data using a control sample with one well reconstructed lepton and one anti-identified lepton. All other backgrounds are taken purely from simu-

1536 lation.

1537 **4.3.3 SYSTEMATIC UNCERTAINTIES**

1538 The systematic uncertainties that have the largest impact on the analysis are the theoretical uncertainties
1539 associated with the signal cross section, and these are shared with the ZZ^* and $\gamma\gamma$ channels. The un-
1540 certainties resulting from variations of the QCD scale are $+7\% / -8\%$ on the final singal yield. Those
1541 coming from variations of the parton distribution function (PDF) used in the simulation add a $\pm 8\%$
1542 uncertainty on the yield. The uncertainties on the branching ratios of the Higgs are $\pm 5\%$.

1543 The main experimental uncertainties come from variations of the jet energy scale (JES), jet energy
1544 resolution, pile-up, E_T^{miss} , b -tagging efficiency, $W + \text{jets}$ background estimate, and integrated luminosity.
1545 For more details, see reference [1].

1546 **4.3.4 RESULTS**

1547 Table 4.3 shows the signal and background yields in the final signal region after normalizing the back-
1548 grounds according to the methods described above.

	$n_j = 0$	$n_j = 1$	$n_j \geq 2$
Signal	20 ± 4	5 ± 2	0.34 ± 0.07
WW	101 ± 13	12 ± 5	0.10 ± 0.14
Other dibosons	12 ± 3	1.9 ± 1.1	0.10 ± 0.10
$t\bar{t}$	8 ± 2	6 ± 2	0.15 ± 0.10
Single top	3.4 ± 1.5	3.7 ± 1.6	-
$Z/\gamma^* + \text{jets}$	1.9 ± 1.3	0.10 ± 0.10	-
$W + \text{jets}$	15 ± 7	2 ± 1	-
Total background	142 ± 16	26 ± 6	0.35 ± 0.18
Observed in data	185	38	0

Table 4.3: Data and expected yields for signal and background in the final $H \rightarrow WW^* \rightarrow \ell\nu\ell\nu$ signal region.
Uncertainties shown are both statistical and systematic. [1]

1549 Figure 4.3 shows the m_T distribution in the $n_j \leq 1$ channels for 8 TeV data. (No events are observed
1550 in data in the $n_j \geq 2$ channels in this dataset). The excess shown here relatively flat as a function of
1551 hypothesized Higgs mass. The combined 7 and 8 TeV data gives an excess with local significance of 2.8σ
1552 with an expected significance of 2.3σ , corresponding to a μ measurement of 1.3 ± 0.5 .

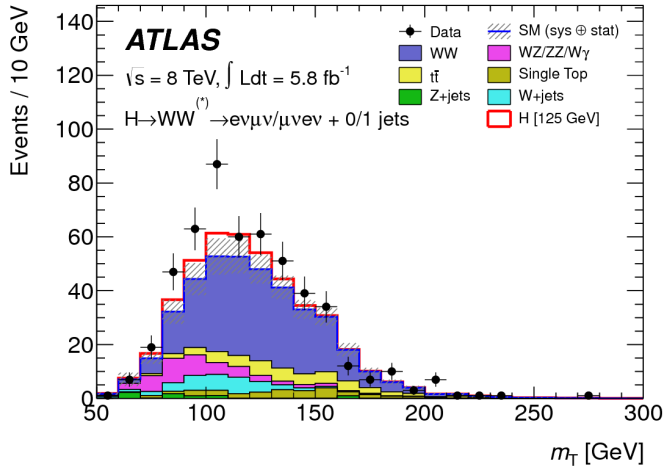


Figure 4.3: m_T distribution in the $H \rightarrow WW \rightarrow e\nu\mu\nu n_j \leq 1$ channels for 8 TeV data [1].

1553 4.4 $H \rightarrow \gamma\gamma$ SEARCH

1554 The $H \rightarrow \gamma\gamma$ search is in essence a search for a peaked excess above the falling SM diphoton mass spec-
 1555 trum, with $m_{\gamma\gamma}$ as the ultimate discriminating variable. Events are selected by requiring two isolated
 1556 photons, with the leading (sub-leading) photon required to have $E_T > 40(30)$ GeV. In the 8 TeV
 1557 data, the photons are required to pass cut-based identification criteria consistent with a photon in the
 1558 electromagnetic calorimeter and little leakage in the hadronic calorimeter.

1559 The main challenges for this analysis are accurate mass reconstruction and background estimation.
 1560 In order to accurately reconstruct the invariant mass of the di-photon system, both the energy and di-
 1561 rection of the photons must be measured well. Therefore, the identification of the primary vertex of the
 1562 hard interaction is particularly important, and is done using a multivariate likelihood which combines
 1563 information about the photon direction and vertex position. The background is modeled with a falling
 1564 spectrum in $m_{\gamma\gamma}$ that is parameterized by different functions depending on the category of the event.

1565 4.4.1 RESULTS

1566 The resulting diphoton mass spectrum is shown in figure 4.4. The best fit mass value in the $\gamma\gamma$ channel
 1567 alone in the combined 7 and 8 TeV data is 126.5 GeV. The local significance at this point is 4.5σ , with
 1568 an expected significance of 2.5σ . Therefore, the measured signal strength μ is 1.8 ± 0.5 in this channel.

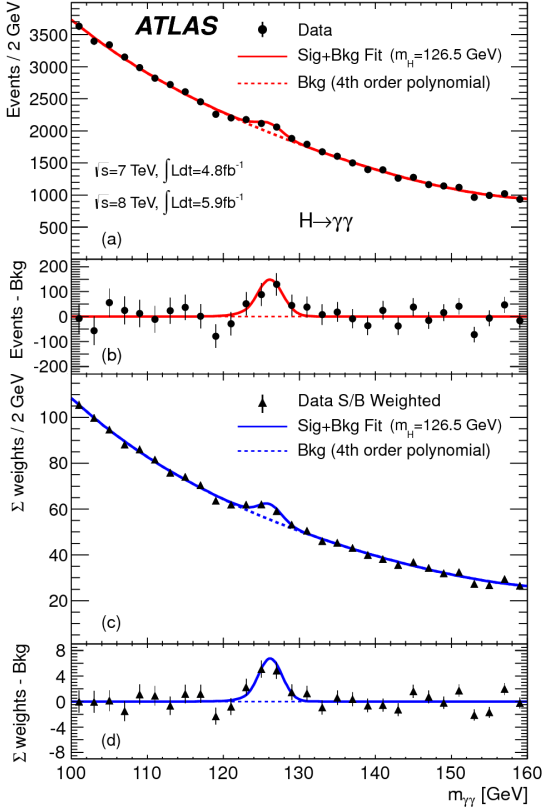


Figure 4.4: Diphoton mass spectrum in 7 and 8 TeV data. Panel a) shows the unweighted data distribution superimposed on the background fit, while panel c) shows the data where each event category is weighted by its signal to background ratio. Panels b) and d) show the respective distributions with background subtracted [1].

1569 4.5 $H \rightarrow ZZ \rightarrow 4\ell$ SEARCH

1570 The $H \rightarrow ZZ \rightarrow 4\ell$ analysis searches for a Standard Model Higgs boson decaying to two Z bosons,
 1571 each of which decays to a pair of same flavor, opposite charge isolated leptons. The ultimate discriminat-
 1572 ing variable is $m_{4\ell}$, or the invariant mass of the four selected leptons. The ℓ denotes an e or μ as with the
 1573 $H \rightarrow WW^* \rightarrow \ell\nu\ell\nu$ analysis.

1574 Four distinct signal regions are constructed depending on the flavors of the final state, additionally
 1575 separated by the flavor of the leading lepton pair. These are referred to as $4e$, $2e2\mu$, $2\mu2e$, 4μ .

1576 The main backgrounds in the $H \rightarrow ZZ \rightarrow 4\ell$ search are continuum ZZ^* production, $Z +$ jets pro-
 1577 duction, and $t\bar{t}$. The $m_{4\ell}$ distribution for background is estimated from simulation. The normalization
 1578 of the SM ZZ^* background is also taken from MC simulation, while the $Z +$ jets and $t\bar{t}$ normalizations

1579 are taken from data-driven methods.

1580 **4.5.1 RESULTS**

1581 Figure 4.5 shows the $m_{4\ell}$ spectrum measured in the 7 and 8 TeV datasets. The total number of events
1582 observed in the window between 120 and 130 GeV is 13, with 6 events in the 4μ channel, 2 events in
1583 the $4e$ channel, and 5 events in the $2e2\mu/2\mu2e$. The best fit μ value in the combined 7 and 8 TeV data
1584 occurs at 125 GeV and is measured to be 1.2 ± 0.6 . The observed significance at this mass is 3.6σ , with
1585 an expected significance of 2.7σ .

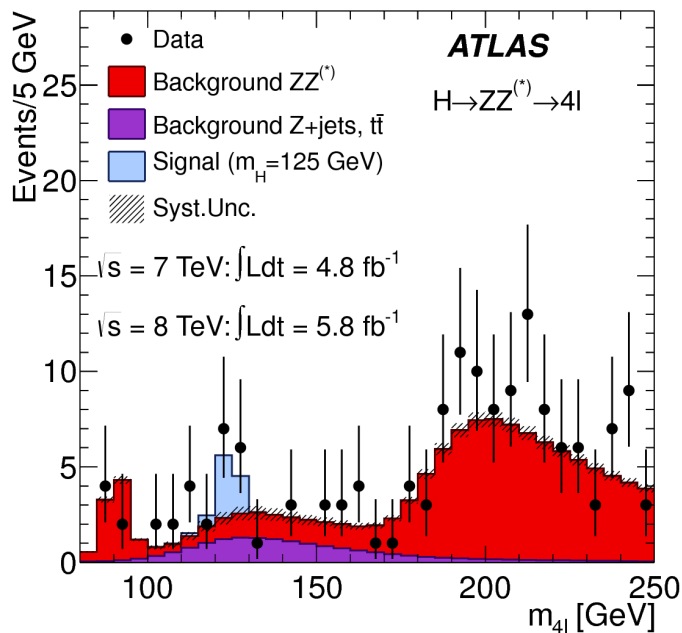


Figure 4.5: Four lepton invariant mass spectrum ($m_{4\ell}$) in 7 and 8 TeV data compared to background estimate. A 125 GeV SM Higgs signal is shown in blue [1].

1586 **4.6 COMBINED RESULTS**

1587 The statistical interpretation of the combined results is undertaken as described in section 3.6.2, with a
1588 hypothesis test based on a likelihood ratio parameterized by the Higgs signal strength μ . The null hy-
1589 pothesis corresponds to $\mu = 0$, while the SM Higgs corresponds to $\mu = 1$.

1590 Table 4.4 summarizes the properties of the individual channels as well as the significances of the ex-
 1591 cesses seen. The most significant observed local excess comes from the $\gamma\gamma$ channel. Figure 4.6 shows a
 1592 comparison of the observed local p_0 values as a function of hypothesized mass for the three different
 1593 search channels. Both the ZZ^* and $\gamma\gamma$ channels have very peaked excesses, while the WW^* excess can
 1594 be seen as very broad because the m_T distribution does not provide detailed information about the true
 1595 Higgs mass.

Channel	Fit var.	Observed Z_l	Expected Z_l	$\hat{\mu}$
$H \rightarrow ZZ^* \rightarrow 4\ell$	$m_{4\ell}$	3.6	2.7	1.2 ± 0.6
$H \rightarrow \gamma\gamma$	$m_{\gamma\gamma}$	4.5	2.5	1.8 ± 0.5
$H \rightarrow WW^* \rightarrow e\nu\mu\nu$	m_T	2.8	2.3	1.3 ± 0.5
Combined	-	6.0	4.9	1.4 ± 0.3

Table 4.4: Summary of the expected and observed significance and measured signal strengths in the combined 7 and 8 TeV datasets for the Higgs discovery analysis [1].

1596 Figure 4.7 shows the combined exclusion limit, p_0 , and signal strength. The highest local excess comes
 1597 at a value of 126.5 GeV and corresponds to a 6.0σ observed excess.

1598 Figure 4.8 shows a comparison of the measured signal strengths between the different Higgs search
 1599 channels. All measured μ are consistent with unity within their uncertainty, and the combined μ mea-
 1600 surement is 1.4 ± 0.3 .

1601 The likelihood can also be computed in a two-dimensional plane of m_H and μ , and this is shown in
 1602 figure 4.9. The figure shows that while the $\gamma\gamma$ and ZZ^* channels have very good mass resolution, the
 1603 excess in WW^* covers a broad mass range. The banana shape of the WW^* result is due to the fact that
 1604 the excess in this channel can either be explained by increasing the signal strength or by changing the
 1605 mass (and thus the cross section). The two parameters are correlated due to the lack of mass sensitivity in
 1606 this channel.

1607 Because multiple Higgs mass points are searched for, the local significance must be corrected for a
 1608 look-elsewhere effect to compute a true global significance. The global significance for finding a Higgs
 1609 anywhere in the mass range of 110 GeV to 600 GeV is 5.1σ . This increases slightly to 5.3σ if only mass
 1610 range from 110 to 150 GeV.

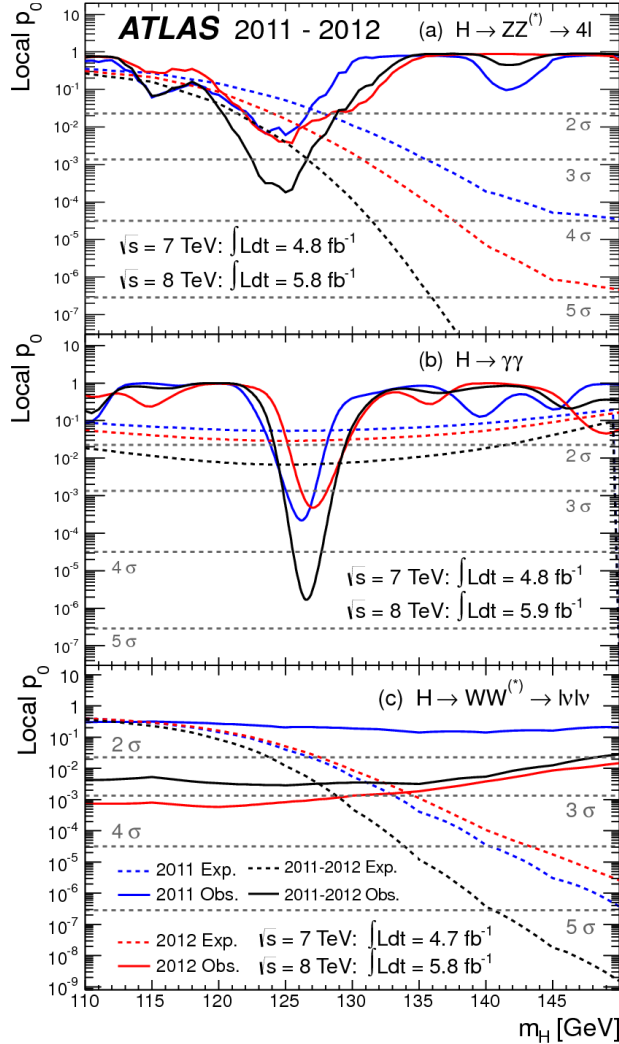


Figure 4.6: Local p_0 distribution as a function of hypothesized Higgs mass for the $H \rightarrow ZZ^* \rightarrow 4\ell$ (a), $H \rightarrow \gamma\gamma$ (b), and $H \rightarrow WW^* \rightarrow \ell\nu\ell\nu$ (c) channels. Dashed curves show expected results, while solid curves show observed. Red curves are from 7 TeV data, blue curves from 8 TeV, and black curved combined [1].

4.7 CONCLUSION

A search for the production of a Standard Model Higgs boson was conducted in 4.8 fb^{-1} collected at $\sqrt{s} = 7 \text{ TeV}$ and 5.8 fb^{-1} at $\sqrt{s} = 8 \text{ TeV}$. A new particle consistent with the Higgs boson was observed, with a mass of 126.5 GeV and a global (local) significance of $5.1(6.0)\sigma$. This is the first discovery level observation of a particle consistent with the Higgs.

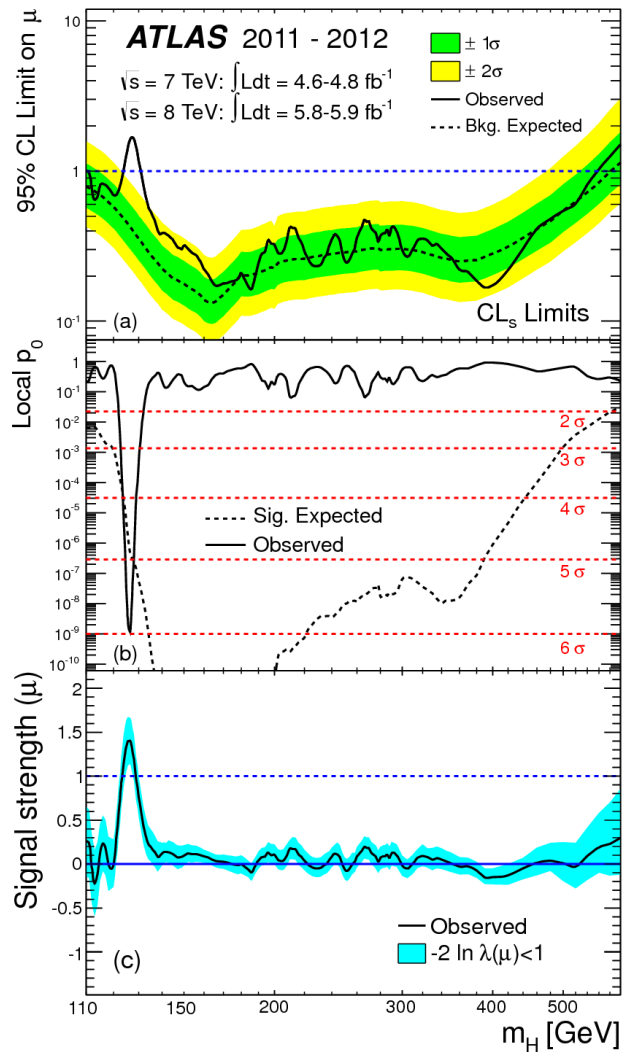


Figure 4.7: Combined 95% CL limits (a), local p_0 values (b), and signal strength measurement (c) as a function of Higgs mass [1].

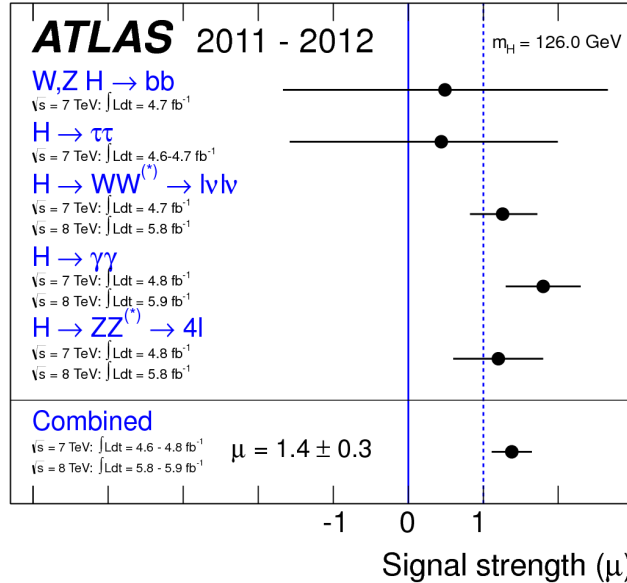


Figure 4.8: Comparison of measured signal strength μ for a 126 GeV Higgs in the 7 and 8 TeV datasets [1].

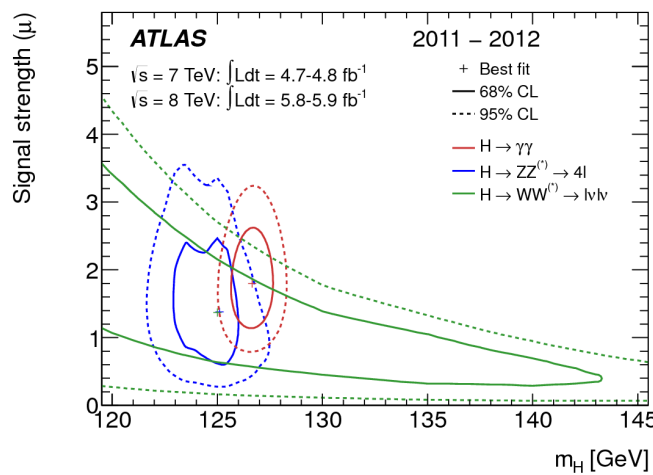


Figure 4.9: Two dimensional likelihood as a function of signal strength μ and Higgs mass m_H [1].

*The imagination of nature is far, far greater than the
imagination of man.*

Richard Feynman

5

1616

1617

Observation of Vector Boson Fusion

1618

production of $H \rightarrow WW^* \rightarrow \ell\nu\ell\nu$

1619

5.1 INTRODUCTION

1620 After the discovery of a particle consistent with the Higgs boson, the $H \rightarrow WW^*$ analysis had two main
1621 goals. The first goal was to increase the sensitivity of the analysis to fully confirm that the $H \rightarrow WW^*$
1622 process did indeed exist. The second goal was to characterize the particle as much as possible, including
1623 searching for the lower cross-section production modes, in order to confirm that it was indeed a Higgs
1624 boson. This chapter presents a dedicated search for Vector Boson Fusion (VBF) production of a Higgs
1625 boson decaying via the $H \rightarrow WW^* \rightarrow \ell\nu\ell\nu$ mode. First, basics of the topology of VBF production
1626 are presented. Then, the details of the analysis are shown, including signal region definition, background
1627 estimation techniques, and systematic uncertainties. Finally, the results of the analysis are presented. As

1628 will be shown, this analysis is the first and most sensitive observation of the VBF production mode of the
1629 Higgs on ATLAS.

1630 In the VBF channel, there are both a selection requirement based signal region analysis (known as the
1631 “cut-based”) and a multivariate analysis which uses a boosted decision tree (known as the BDT analysis).
1632 The focus of this chapter will be on the cut-based signal region, as this is an important component of the
1633 VBF analysis and in particular acts as strong validation for the final BDT result. Connections between
1634 the cut-based and BDT analyses will be discussed where appropriate.

1635 5.2 DATA AND SIMULATION SAMPLES

1636 The results presented here are with 20.3 fb^{-1} taken at $\sqrt{s} = 8 \text{ TeV}$ and 4.5 fb^{-1} taken at $\sqrt{s} = 7 \text{ TeV}$.
1637 The details of the LHC and detector conditions during this period are given in Chapter 2. The trigger
1638 selection defining the dataset is discussed in section 5.2.1. The simulation samples used for signal and
1639 background modeling are given in section 5.2.2.

1640 5.2.1 TRIGGERS

1641 The analysis uses a combination of single lepton and dilepton triggers to allow lowering of the p_T thresh-
1642 olds and increased signal acceptance. The p_T threshold on the leptons is a particularly important consid-
1643 eration for this signal. Because the second W produced in the decay can be off-shell, it tends to pro-
1644 duce lower momentum leptons. Thus, being able to lower the p_T threshold while still maintaining
1645 a low background rate is critical. Figure 5.1 shows an example of the subleading lepton p_T for a VBF
1646 $H \rightarrow WW^*$ signal compared to the corresponding $t\bar{t}$ background. Note that the lepton p_T spectrum is
1647 considerably softer in the signal sample.

1648 As discussed in Chapter 2, there are multiple levels in the ATLAS trigger system, and there are differ-
1649 ent p_T thresholds imposed for the leptons at each level. Additionally, some triggers have a loose selection
1650 on the isolation of the lepton (looser than that applied offline in the analysis object selection). Table 5.1
1651 shows the thresholds used for single lepton triggers, while table 5.2 shows the thresholds coming from
1652 di-lepton triggers. The single lepton trigger efficiency for muons that pass the analysis object selection is



Figure 5.1: A comparison of the subleading lepton p_T spectrum between VBF $H \rightarrow WW^*$ production and $t\bar{t}$ background

1653 70% for muons in the barrel region ($|\eta| < 1.05$) and 90% in the endcap region. The electron trigger ef-
 1654 ficiency increases with electron p_T but the average is approximately 90%. These efficiencies are measured
 1655 by combined performance and trigger signature groups [65, 66].

	Level-1 threshold	High-level threshold
Electron	18	$24i$
	30	60
Muon	15	$24i$
		36

Table 5.1: Single lepton triggers used for electrons and muons. A logical “or” of the triggers listed for each lepton type is taken. Units are in GeV, and the i denotes an isolation requirement in the trigger.

	Level-1 threshold	High-level threshold
ee	10 and 10	12 and 12
$\mu\mu$	15	18 and 8
$e\mu$	10 and 6	12 and 8

Table 5.2: Di-lepton triggers used for different flavor combinations. The two thresholds listed refer to leading and sub-leading leptons, respectively. The di-muon trigger only requires a single lepton at level-1.

1656 The combination of all triggers shown gives good efficiency for signal events. This efficiency is sum-
 1657 marized in table 5.3. The relative improvement in efficiency by adding the dilepton triggers is also shown

1658 in the same table. The largest gain comes in the $\mu\mu$ channel. Overall the trigger selection shows a good
1659 efficiency for $H \rightarrow WW^*$ signal events.

Channel	Trigger efficiency	Gain from 2ℓ trigger
ee	97%	9.1%
$\mu\mu$	89%	18.5%
$e\mu$	95%	8.3%
μe	81%	8.2%

Table 5.3: Trigger efficiency for signal events and relative gain of adding a dilepton trigger on top of the single lepton trigger selection. The first lepton is the leading, while the second is the sub-leading. Efficiencies shown here are for the ggF signal in the $n_j = 0$ category but are comparable for the VBF signal.

1660 5.2.2 MONTE CARLO SAMPLES

1661 Modeling of signal and background processes in the signal region, in particular for the m_T distribution,
1662 is an important consideration for the final interpretation of the analysis. Therefore, careful consideration
1663 must be paid to which Monte Carlo (MC) generators are used for specific processes. With the exception
1664 of the $W + \text{jet}$ and multijet backgrounds, the m_T shape used as the final discriminant is taken from simu-
1665 lation. (Many backgrounds are normalized from data, as described in section 5.5).

1666 Table 5.4 shows the MC generators used for the signal and background processes, as well as their cross
1667 sections. In order to include corrections up to next-to-leading order (NLO) in the QCD coupling con-
1668 stant α_s , the POWHEG [67] generator is often used. In some cases, only leading order generators like
1669 ACERMC [68] and GG2VV [69] are available for the process in question. If the process requires good
1670 modeling for very high parton multiplicities, the SHERPA [70] and ALPGEN [71] generators are used
1671 to provide merged calculations for five or fewer additional partons. These matrix element level calcula-
1672 tions must then be additionally matched to models of the underlying event, hadronization, and parton
1673 shower. There are four possible generators for this: SHERPA, PYTHIA 6 [72], PYTHIA 8 [73], or HERWIG
1674 [74] + JIMMY [75]. The simulation additionally requires an input parton distribution function (PDF).
1675 The CT10 [76] PDFs are used for SHERPA and POWHEG simulated samples, while CTEQ6L1 [77] is used
1676 for ALPGEN + HERWIG and ACERMC simulations. The Drell-Yan samples are reweighted to the MRST
1677 [78] PDFs, as these are found to give the best agreement between data and simulation.

Process	MC generator	$\sigma \cdot \mathcal{B}$ (pb)
Signal		
ggF $H \rightarrow WW^*$	POWHEG +PYTHIA 8	0.435
VBF $H \rightarrow WW^*$	POWHEG +PYTHIA 8	0.0356
VH $H \rightarrow WW^*$	PYTHIA 8	0.0253
WW		
$q\bar{q} \rightarrow WW$ and $qg \rightarrow WW$	POWHEG +PYTHIA 6	5.68
$gg \rightarrow WW$	GG2VV +HERWIG	0.196
$(q\bar{q} \rightarrow W) + (q\bar{q} \rightarrow W)$	PYTHIA 8	0.480
$q\bar{q} \rightarrow WW$	SHERPA	5.68
VBS $WW + 2$ jets	SHERPA	0.0397
Top quarks		
$t\bar{t}$	POWHEG +PYTHIA 6	26.6
Wt	POWHEG +PYTHIA 6	2.35
$t\bar{q}\bar{b}$	ACERMC +PYTHIA 6	28.4
$t\bar{b}$	POWHEG +PYTHIA 6	1.82
Other dibosons (VV)		
$W\gamma$ ($p_T^\gamma > 8$ GeV)	ALPGEN +HERWIG	369
$W\gamma^*$ ($m_{\ell\ell} \leq 7$ GeV)	SHERPA	12.2
WZ ($m_{\ell\ell} > 7$ GeV)	POWHEG +PYTHIA 8	12.7
VBS $WZ + 2$ jets	SHERPA	0.0126
($m_{\ell\ell} > 7$ GeV)		
$Z\gamma$ ($p_T^\gamma > 8$ GeV)	SHERPA	163
$Z\gamma^*$ (min. $m_{\ell\ell} \leq 4$ GeV)	SHERPA	7.31
ZZ ($m_{\ell\ell} > 4$ GeV)	POWHEG +PYTHIA 8	0.733
$ZZ \rightarrow \ell\ell\nu\nu$ ($m_{\ell\ell} > 4$ GeV)	POWHEG +PYTHIA 8	0.504
Drell-Yan		
Z ($m_{\ell\ell} > 10$ GeV)	ALPGEN +HERWIG	16500
VBF $Z + 2$ jets	SHERPA	5.36
($m_{\ell\ell} > 7$ GeV)		

Table 5.4: Monte Carlo samples used to model the signal and background processes [61].

Once the basic hard scattering process is simulated, it must be passed through a detector simulation and additional pile-up events must be overlaid. The pile-up events are modeled with PYTHIA 8, and the ATLAS detector is simulated with GEANT4 [79]. Because of the unique phase space of the $H \rightarrow WW^*$

1681 analysis, events are sometimes filtered at generator level to allow for more efficient generation of relevant
1682 events. The efficiency of the trigger in MC simulation does not always match the measured efficiency in
1683 data, so trigger scale factors are applied to correct the MC efficiency to the data. These are derived by the
1684 combined performance groups [65, 66].

1685 5.3 OBJECT SELECTION

1686 In order to define the signal region, the analysis must first select the objects to be considered. The de-
1687 tails of the object reconstruction algorithms are discussed in Chapter 2, while this section gives specific
1688 selection cuts used in the $H \rightarrow WW^*$ analysis.

1689 The first step in this process is to select a primary vertex candidates. The event's primary vertex is the
1690 vertex with the largest sum of p_T^2 for associated tracks and is required to have at least three tracks with
1691 $p_T > 450$ MeV. Many of the object selection cuts are then made relative to this chosen primary vertex.

1692 5.3.1 MUONS

1693 The analysis uses combined muon candidates, where a track in the Inner Detector has been matched
1694 to a standalone track in the Muon Spectrometer. The track parameters are combined statistically in the
1695 muon reconstruction algorithm [52]. The muons are required to be within $|\eta| < 2.5$ and have a $p_T >$
1696 10 GeV. To reduce backgrounds coming from mis-reconstructed leptons, there are requirements on
1697 the impact parameter of the muon relative to the primary vertex. The transverse impact parameter d_0
1698 is required to be small relative to its estimated uncertainty, the exact cut value being $d_0/\sigma_{d_0} < 3$. The
1699 longitudinal impact parameter z_0 must satisfy $|z_0 \sin \theta| < 1$ mm.

1700 As discussed previously, the muons must also be isolated. There are two types of lepton isolations
1701 that are calculated: track-based and calorimeter-based. For muons, the track-based isolation is defined
1702 using the scalar sum $\sum p_T$ for tracks with $p_T > 1$ GeV (excluding the muon's track) within a cone of
1703 $\Delta R = 0.3$ (0.4) for muon with $p_T > 15$ GeV ($10 < p_T < 15$ GeV). The final isolation requirement
1704 is made my requiring that this scalar sum be no more than a certain fraction of the muon's p_T . This re-
1705 quirement varies with muon p_T and the exact cuts are defined in table 5.5.

1706 The calorimeter-based muon isolation is defined using as a $\sum E_T$ calculated from calorimeter cells
 1707 using the same cone size as the track-based isolation but excluding cells with $\Delta R < 0.05$ around the
 1708 muon. This requirement is also defined as a cut on the ratio of the sum to the muon p_T and varies with
 1709 muon p_T . The cut values are also given in table 5.5.

1710 The isolation requirements loosen as a function of p_T to allow for larger signal acceptance. At low p_T ,
 1711 the isolation is tightened to reduce the $W + \text{jets}$ background which arises from a misidentified lepton.

p_T range (GeV)	Calorimeter isolation	Track isolation
10 – 15	0.06	0.06
15 – 20	0.12	0.08
20 – 25	0.18	0.12
> 25	0.30	0.12

Table 5.5: p_T dependent isolation requirements for muons. Muons are required to have the amount of calorimeter or track based cone sums be less than this fraction of their p_T .

1712 5.3.2 ELECTRONS

1713 Electrons are identified by matching reconstructed clusters in the electromagnetic calorimeter with tracks
 1714 in the inner detector. The electrons are identified using a likelihood based method [49, 50] which takes
 1715 into account the shower shapes in the calorimeter, the matching of tracks to clusters, and the amount of
 1716 transition radiation in the TRT. The electrons are required to have $|\eta| < 2.47$, and candidates in the
 1717 transition region between the barrel and endcap ($1.37 < |\eta| < 1.52$) are excluded. As the muons, the
 1718 electrons are required to have transverse impact parameter significance < 3 , while in the longitudinal
 1719 direction they must have $|z_0 \sin \theta| < 0.4$ mm. Some electron requirements also vary with electron E_T ,
 1720 and these requirements are summarized in table 5.6.

1721 The isolation for electrons are defined similarly to the muons but with unique cuts on the objects in-
 1722 cluded. The track-based isolation is defined using tracks with $p_T > 400$ MeV with cone sizes as defined
 1723 previously. The calorimeter-based isolation also uses the same cone size as the muon, but here the cells
 1724 within a 0.125×0.175 area in $\eta \times \phi$ around the electron cluster's barycenter are excluded. The other
 1725 difference with respect to muons is that the denominator of the isolation ratio is the electron's E_T rather
 1726 than p_T . The isolation cuts very with electron E_T and are defined in table 5.6.

1727 The electron is also required to not be consistent with a vertex coming from a photon conversion.

p_T range (GeV)	Quality cut	Calorimeter isolation	Track isolation
10 – 15	Very tight LH	0.20	0.06
15 – 20	Very tight LH	0.24	0.08
20 – 25	Very tight LH	0.28	0.10
> 25	Medium	0.28	0.10

Table 5.6: p_T dependent requirements for electrons. Electrons are required to have the amount of calorimeter or track based cone sums be less than this fraction of their E_T .

1728 5.3.3 JETS

1729 Jets are clustered with the anti- k_T reconstruction algorithm using a radius parameter of $R = 0.4$. They
1730 are required to have a jet vertex fraction (JVF) of at least 50%, meaning that half of the tracks associated
1731 with the jet originated from the primary vertex. Jets with no tracks associated (i.e. those outside the ac-
1732 ceptance of the ID) do not have this requirement applied. Jets are required to have $p_T > 25$ GeV if
1733 they are within the tracking acceptance ($|\eta| < 2.4$). Jets with $2.4 < |\eta| < 4.5$ are required to have
1734 $p_T > 30$ GeV. This tighter requirement reduces jets from pileup in the region where JVF requirements
1735 cannot be applied. The two highest p_T jets in the event are referred to as the “VBF” jets and used to com-
1736 pute various analysis selections later.

1737 Identification of b -jets is done using the MV1 algorithm and is limited to the acceptance of the ID
1738 ($|\eta| < 2.5$). The operating point of MV1 that is used is the one that is 85% efficient for identifying true
1739 b -jets. This operating point has a 10.3% of mis-tagging a light quark jet as a b -jet. In order to improve
1740 the rejection of b -jets, a lower threshold than the nominal p_T threshold described above is used. For the
1741 purposes of counting the number of b -jets, jets with p_T down to 20 GeV are used.

1742 5.3.4 OVERLAP REMOVAL

1743 There are some cases where certain reconstructed objects will overlap and one will have to be chosen
1744 (for example, an electron and a jet in the calorimeter). First, the case of lepton overlap is dealt with. If
1745 an electron candidate extends into the muon spectrometer, it is removed. If a muon or electron have a
1746 $\Delta R < 0.1$, the electron is removed and the muon is kept. If two electron candidates overlap within

1747 the same radius, then the higher E_T electron is kept. Next, the overlap between leptons and jets is con-
1748 sidered. If an electron and jet are within $\Delta R < 0.3$ of one another, the electron is kept and the jet is
1749 removed. However, if a muon and jet overlap within $\Delta R < 0.3$, the jet is kept (as it is likely that the
1750 muon is the result of a semileptonic decay inside the jet).

1751 Once the overlap removal is complete, the final set of objects used in the analysis is defined.

1752 5.4 ANALYSIS SELECTION

1753 The VBF analysis uses two distinct selections. The first is a more standard selection, referred to as “cut-
1754 based”, that applies requirements on the VBF variables and uses m_T as the final discriminating variable.
1755 The second is a looser selection that uses a Boosted Decision Tree (BDT) score as the final discriminator
1756 in order to take advantage of the detailed correlations between the VBF variables. While the BDT analy-
1757 sis is ultimately more sensitive, the cut-based serves as an important component of the analysis. First, the
1758 cut-based allows for confirming the modeling and validity of many variables used as input to the BDT.
1759 Second, because this is the first use of such an MVA technique in the $H \rightarrow WW^*$ analysis, the cut-based
1760 selection allows confirmation of the final BDT result with a more traditional analysis. The cut-based
1761 techniques are the focus of this chapter, but connections to the BDT result will be illustrated when ap-
1762 propriate.

1763 One important note is that because this analysis is dedicated to the measurement of the VBF pro-
1764 duction mode of the Higgs, events coming from gluon fusion production with the Higgs decaying via
1765 $H \rightarrow WW^* \rightarrow \ell\nu\ell\nu$ are treated as background events. This will be seen throughout the various
1766 predictions shown.

1767 5.4.1 COMMON PRE-SELECTION

1768 Both the cut-based and BDT analyses have a common pre-selection that is applied before the main signal
1769 region requirements. The requirements on leptons are common to all n_j bins. The analysis requires two
1770 oppositely charged leptons, with the leading lepton required to have $p_T > 22$ GeV while the subleading
1771 lepton must have $p_T > 10$ GeV. Next, to remove low mass Z/γ^* events, a cut on the dilepton mass

1772 $m_{\ell\ell} > 10$ (12) GeV is applied in the different (same) flavor channel. In the same flavor channels, there is
1773 an additional veto placed on the region around the Z peak, requiring that $|m_{\ell\ell} - m_Z| > 15$ GeV.

1774 There are also requirements on the amount of missing transverse momentum in the event. These
1775 are only applied in the same flavor channels, as in the different flavor channels $t\bar{t}$ is the dominant back-
1776 ground in $n_j \geq 2$. The BDT analysis requires $p_T^{\text{miss}} > 40$ GeV and $E_T^{\text{miss}} > 45$ GeV. The cut-
1777 based analysis must select more tightly on these variables to have maximal sensitivity and thus requires
1778 $p_T^{\text{miss}} > 50$ GeV and $E_T^{\text{miss}} > 55$ GeV.

1779 Finally, because this analysis is focused on VBF, a requirement on the jet multiplicity is placed, with
1780 $n_j \geq 2$. Additionally, the analysis requires that there are no jets identified as b-quarks in the event, or
1781 $n_b = 0$.

1782 5.4.2 CUT-BASED SELECTION

1783 The cut-based selection places sequential requirements on variables reconstructed from the VBF jets in
1784 order to increase the signal to background ratio.

1785 GENERAL BACKGROUND REDUCTION

1786 Top pair production is the primary background in the $n_j \geq 2$ bin. Even though $n_b = 0$ is required,
1787 an additional variable is constructed to further suppress the top background. There is often additional
1788 QCD radiation that accompanies the $t\bar{t}$ system when it is produced. Therefore, a variable which tests for
1789 the presence of this additional radiation, p_T^{sum} , is constructed. It is defined in equation 5.1.

$$p_T^{\text{sum}} = p_T^{\ell\ell} + p_T^{\text{miss}} + \sum p_T^j \quad (5.1)$$

1790 The first cut after pre-selection in the cut-based analysis requires $p_T^{\text{sum}} < 15$ GeV to further suppress $t\bar{t}$
1791 production.

1792 In the different flavor channels, a cut is made to reduce the contamination from $Z \rightarrow \tau\tau$ decays.
1793 The di- τ invariant mass, $m_{\tau\tau}$, is constructed by assuming that the neutrinos from the τ decays were
1794 collinear with the leptons [80]. The analysis requires that this mass not be consistent with a Z by requir-

1795 ing $m_{\tau\tau} < m_Z - 25$ GeV.

1796 VBF TOPOLOGICAL CUTS

1797 The characteristic feature of VBF production of the Higgs is the presence of two additional forward jets
1798 coming from the incoming partons which radiate the vector bosons that make the Higgs. These jets are
1799 forward because the outgoing partons still carry the longitudinal momentum of the incoming partons.
1800 Figure 5.2 shows the distribution of the η for the leading jet in a VBF event compared to a background
1801 top pair production event. As can be seen, the VBF jets tend to be more forward in η , while the $t\bar{t}$ jets are
1802 more central.

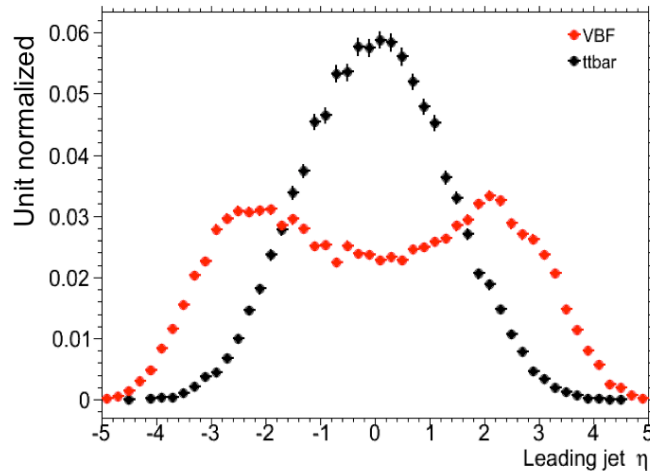


Figure 5.2: Leading jet η in VBF $H \rightarrow WW^*$ (red) and $t\bar{t}$ (black)

1803 Because the cross section for VBF production is an order of magnitude smaller than gluon fusion pro-
1804 duction, these forward jets must be used in order to better reduce background and achieve a good signal
1805 to background ratio. The dedicated VBF search selection requirements are constructed to maximally
1806 exploit the features of the unique VBF topology.

1807 Requirements on the VBF jets are collectively referred to as the “VBF topological cuts”. First, a re-
1808 quirement on the dijet invariant mass of the VBF jets, m_{jj} , is placed, requiring $m_{jj} > 600$ GeV. Next,
1809 the event is required to have a large gap in rapidity between the two VBF jets, or $\Delta y_{jj} > 3.6$. Both

1810 of these cuts put tight requirements on the presence of two forward, high p_T jets moving in opposite
1811 directions in the longitudinal plane.

1812 Beyond requiring the presence of the two forward VBF jets, the analysis also vetoes on the presence
1813 of any additional jets that fall between the two VBF jets. This cut is referred to as the central jet veto, or
1814 CJV. Any events with a third jet with $p_T > 20$ GeV whose rapidity is between the region defined by the
1815 two VBF jets are vetoed. This can be expressed in terms of a variable called the jet centrality, defined in
1816 equation 5.2.

$$C_{j3} = \left| \eta_{j3} - \frac{\eta_{j1} + \eta_{j2}}{2} \right| / \frac{|\eta_{j1} - \eta_{j2}|}{2}, \quad (5.2)$$

1817 Here, η_{j1} and η_{j2} are the pseudorapidities of the leading and subleading jets, respectively, while η_{j3} is
1818 the pseudorapidity of the extra jet in the event (if one exists). Intuitively, C_{j3} is zero when η_{j3} is directly
1819 centered between the two jets and unity when η_{j3} is aligned with either of the VBF jets. Thus, the CJV
1820 can be expressed as a requirement that $C_{j3} > 1$.

1821 The decay products of the Higgs tend to be central as well. Thus, the analysis also requires that both
1822 leptons in the analysis fall within the rapidity gap defined by the jets. This cut is referred to as the outside
1823 lepton veto, or OLV. A quantitative way to define the cut is to require that the centrality of each lepton
1824 (defined analogously to that of the third jet in equation 5.2) correspond to the lepton being within the jet
1825 rapidity gap, or $C_\ell < 1$ for both leptons.

1826 Figure 5.3a-c shows the m_{jj} , Δy_{jj} , and $C_{\ell 1}$ variables at the stage where all previous cuts in the se-
1827 quence have been made. The agreement between data and Monte Carlo is good, and the bottom panels
1828 show their power in discriminating the VBF signal from the background processes.

1829 The final signal region is also split into two bins of m_{jj} , with the first bin corresponding to $600 \text{ GeV} <$
1830 $m_{jj} < 1 \text{ TeV}$ and the second bin corresponding to $m_{jj} > 1 \text{ TeV}$. The first bin has more statistics but
1831 also a larger contribution from background, while the second bin has lower statistics but a 1:1 signal to
1832 background ratio.

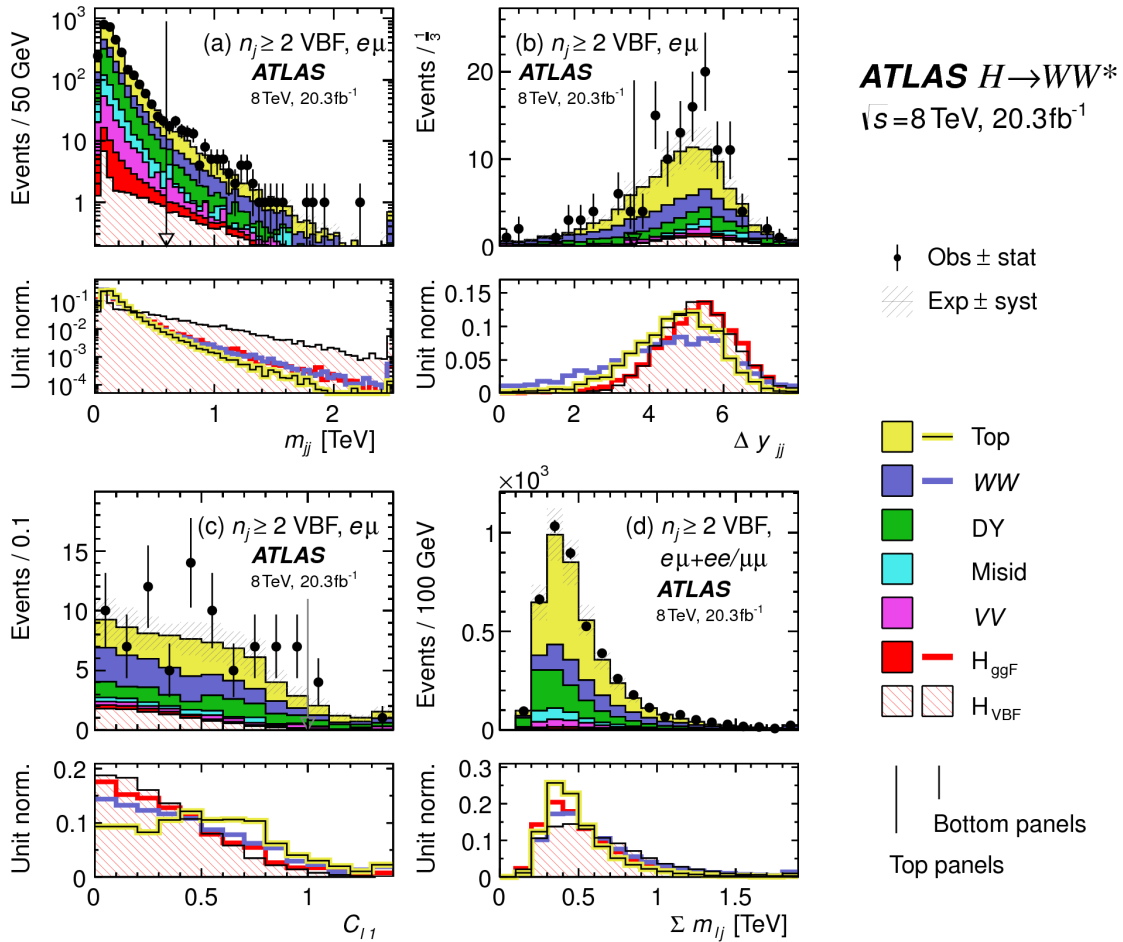


Figure 5.3: Distributions of (a) m_{jj} , (b) Δy_{jj} , (c) $C_{\ell 1}$, and (d) $\Sigma m_{\ell j}$, for the VBF analysis. The top panels compare simulation and data, while the bottom panels show normalized distributions for all background processes and signal [61].

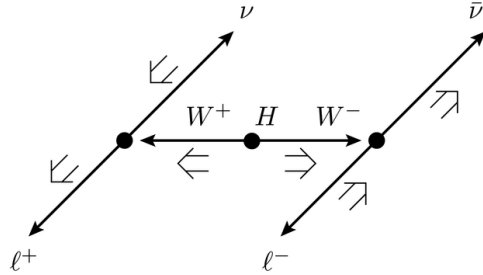


Figure 5.4: A cartoon of the WW final state. Momenta are represented with thin arrows, spins with thick arrows.
[61]

1833 HIGGS TOPOLOGICAL CUTS

1834 The final state leptons will exhibit unique correlations due to the fact that they are arising from the decay
 1835 of a spin zero resonance. In particular, the spins of the final state leptons and neutrinos must all cancel,
 1836 as shown in figure 5.4. Because the neutrino has a left handed chirality and the anti-neutrino has a right
 1837 handed chirality (in the massless neutrino approximation), the spin and momentum of the particles
 1838 will be anti-aligned and aligned, respectively. In the transverse plane, the momenta of all four final state
 1839 objects must cancel as well. With the constraint of having both the momenta and the spin alignments
 1840 cancel, the final state kinematics strongly prefer having a small angle between the leptons in the trans-
 1841 verse plane (low $\Delta\phi_{\ell\ell}$). This angular correlation will also lead to low values of the di-lepton invariant
 1842 mass $m_{\ell\ell}$. These unique signal final state kinematic correlations will be exploited to define the ultimate
 1843 signal region.

1844 The analysis places additional requirements on the final state leptons. Two requirements on dilepton
 1845 kinematics are made that are common with lower multiplicity jet bins as well. The angle between leptons
 1846 in the transverse plane, $\Delta\phi_{\ell\ell}$, is required to be less than 1.8 radians. Additionally, the dilepton mass $m_{\ell\ell}$
 1847 is required to be less than 50 GeV.

1848 The cut-based analysis uses m_T as the final discriminating variable as in the ggF focused analysis. The
 1849 optimal number of bins in m_T was found to be three bins, with the bin boundaries at 80 and 130 GeV.

1850 Table 5.7 shows the data and estimated signal and background yields from simulation as each cut de-
 1851 scribed above is made. The table shows how each cut reduces specific backgrounds and how the overall

1852 signal to background ratio grows through the various selection requirements.

1853 Figure 5.5 shows an ATLAS event display of a candidate event in the final signal region.

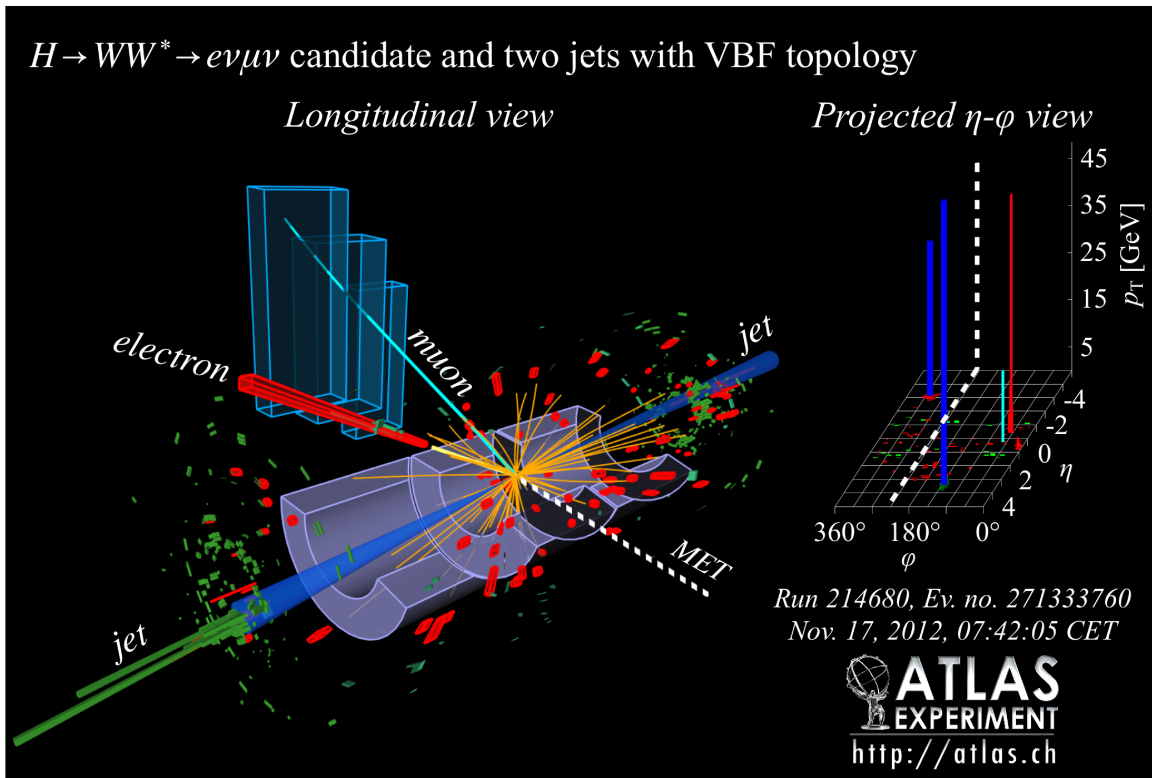


Figure 5.5: Event display of a VBF candidate event [61].

1854 5.4.3 BDT-BASED SELECTION

1855 The boosted decision tree based analysis takes a different philosophy compared to the cut-based. Rather
1856 than cutting sequentially on many variables, the BDT analysis uses many of these variables as inputs
1857 to the BDT and the output BDT score (O_{BDT}) as the final discriminant. The BDT is trained with the
1858 VBF $H \rightarrow WW^*$ simulation as the signal samples and all other processes as background, including ggF
1859 $H \rightarrow WW^*$ production. While the BDT based analysis is treated as a separate result, it has significant
1860 overlap with the cut-based selection.

Table 5.7: Event selection for the $n_j \geq 2$ VBF analysis in the 8 TeV cut-based analysis [61].

Selection	Summary						Composition of N_{bkg}									
	$N_{\text{obs}}/N_{\text{bkg}}$	N_{obs}	N_{bkg}	N_{ggF}	N_{VBF}	N_{signal}	N_{WW}	N_{WW}^{EW}	$N_{t\bar{t}}$	N_t	N_{Wj}	N_{jj}	N_{VV}	N_{misid}	$N_{Drell-Yan}$	$N_{ee/\mu\mu} N_{\tau\tau}^{\text{QCD}}$
$e\mu$ sample	1.00 ± 0.00	61434	61180	85	32	26	1350	68	51810	2970	847	308	380	51	3260	46
$n_b = 0$	1.02 ± 0.01	7818	7700	63	26	16	993	43	3000	367	313	193	273	35	2400	29
$p_T^{\text{sum}} < 15$	1.03 ± 0.01	5787	5630	46	23	13	781	38	1910	270	216	107	201	27	2010	23
$m_{\tau\tau} < m_Z - 25$	1.05 ± 0.02	3129	2970	40	20	9.9	484	22	1270	177	141	66	132	7.6	627	5.8
$m_{jj} > 600$	1.31 ± 0.12	131	100	2.3	8.2	—	18	8.9	40	5.3	1.8	2.4	5.1	0.1	15	1.0
$\Delta y_{jj} > 3.6$	1.33 ± 0.13	107	80	2.1	7.9	—	11.7	6.9	35	5.0	1.6	2.3	3.3	—	11.6	0.8
$C_{j3} > 1$	1.36 ± 0.18	58	43	1.3	6.6	—	6.9	5.6	14	3.0	1.3	1.3	2.0	—	6.8	0.6
$C_{l1} < 1, C_{l2} < 1$	1.42 ± 0.20	51	36	1.2	6.4	—	5.9	5.2	10.8	2.5	1.3	1.3	1.6	—	5.7	0.6
$m_{\ell\ell}, \Delta\phi_{\ell\ell}, m_{\text{T}}$	2.53 ± 0.71	14	5.5	0.8	4.7	—	1.0	0.5	1.1	0.3	0.3	0.3	0.6	—	0.5	0.2
$ee/\mu\mu$ sample	0.99 ± 0.01	26949	27190	31	14	10.1	594	37	23440	1320	230	8.6	137	690	679	16
$n_b, p_T^{\text{sum}}, m_{\tau\tau}$	1.03 ± 0.03	1344	1310	13	8.0	4.0	229	12.0	633	86	26	0.9	45	187	76	1.5
$m_{jj}, \Delta y_{jj}, C_{j3}, C_\ell$	1.39 ± 0.28	26	19	0.4	2.9	0.0	3.1	5.5	1.0	0.2	0.0	0.7	3.8	0.7	0.1	0.1
$m_{\ell\ell}, \Delta\phi_{\ell\ell}, m_{\text{T}}$	1.63 ± 0.69	6	3.7	0.3	2.2	0.0	0.4	0.2	0.6	0.2	0.0	0.1	1.5	0.3	0.1	0.1

1861 PRE-TRAINING SELECTION AND BDT INPUTS

1862 Before training, the common pre-selection cuts described in section 5.4.1 are applied. Additionally, the
1863 central jet veto and outside lepton veto described in section 5.4.2 are applied. The BDT has eight input
1864 variables, six of which are also variables that are used in the cut-based analysis. The six shared variables
1865 are p_T^{sum} , m_{jj} , Δy_{jj} , $m_{\ell\ell}$, $\Delta\phi_{\ell\ell}$, and m_T . The seventh variable input in the BDT is a combination of
1866 the variables used to do the OLV in the cut-based analysis. The BDT uses as input the sum of lepton
1867 centralities, or $\sum C_\ell = C_{\ell 1} + C_{\ell 2}$. The final BDT input variable, $\Sigma m_{\ell j}$, is constructed to account for
1868 the correlations between the jets and leptons in the event. It is the sum of the invariant masses of all four
1869 possible lepton-jet combinations.

1870 Figure 5.3d shows the agreement between data and simulation for the $\Sigma m_{\ell j}$ variable, as well as show-
1871 ing its discriminating power. Figure 5.6 shows the distributions of the Higgs topological variables that
1872 are shared between the cut-based and BDT analyses. Figure 5.7 shows the distributions of the VBF topo-
1873 logical variables shared between the cut-based and BDT analyses. In both cases, the VBF yield has been
1874 scaled by a factor of 50 to better show the shape difference compared to the backgrounds.

1875 Table ?? summarizes the cuts applied for the cut-based and analyses, as well as which variables are used
1876 as input to the BDT.

1877 5.5 BACKGROUND ESTIMATION

1878 This section describes the procedures used to estimate backgrounds for the VBF analysis in both the
1879 cut-based and BDT analyses.

1880 5.5.1 GENERAL STRATEGY

1881 Most of the backgrounds in the VBF analysis have shapes estimated from Monte Carlo simulation but
1882 normalizations derived from control regions in data. In essence, a normalization factor (denoted with
1883 β or abbreviated as NF) is derived by scaling the MC yield in the control region to the corresponding
1884 yield in data. Once this factor is derived, it can be used to scale the MC estimate of the background in the

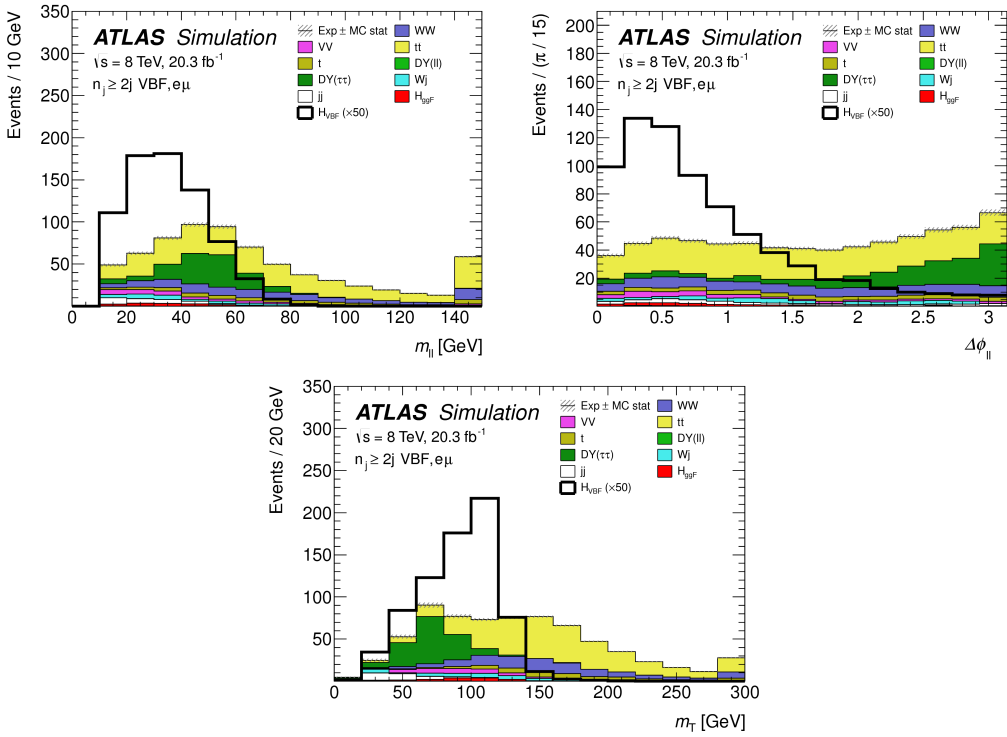


Figure 5.6: Distributions of m_{ll} (top left), $\Delta\phi_{ll}$ (top right), and m_T (bottom), Higgs topology variables used in the selection requirements of the cut-based signal region and as inputs to the BDT result. These are plotted after all of the BDT pre-training selection cuts [61].

1885 signal region. This is illustrated in equation 5.3.

$$B_{\text{SR}}^{\text{est}} = B_{\text{SR}} \times \frac{N_{\text{CR}}}{B_{\text{CR}}} \equiv B_{\text{SR}} \times \beta \quad (5.3)$$

1886 Here, B denotes the MC yield prediction in the denoted region, while N denotes the observed number
1887 of events in data in the denoted region.

1888 Another way of writing the same equation, in terms of an extrapolation factor α rather than a nor-
1889 malization factor β . The overall calculation is exactly the same. However, when phrased in this way, it
1890 shows how the uncertainty on the background estimation can be reduced. This is shown in equation 5.4.

1891

$$B_{\text{SR}}^{\text{est}} = N_{\text{CR}} \times \frac{B_{\text{SR}}}{B_{\text{CR}}} \equiv N_{\text{CR}} \times \alpha \quad (5.4)$$

1892 Phrased this way, the equation shows that with enough statistics in the control region, a large theoretical

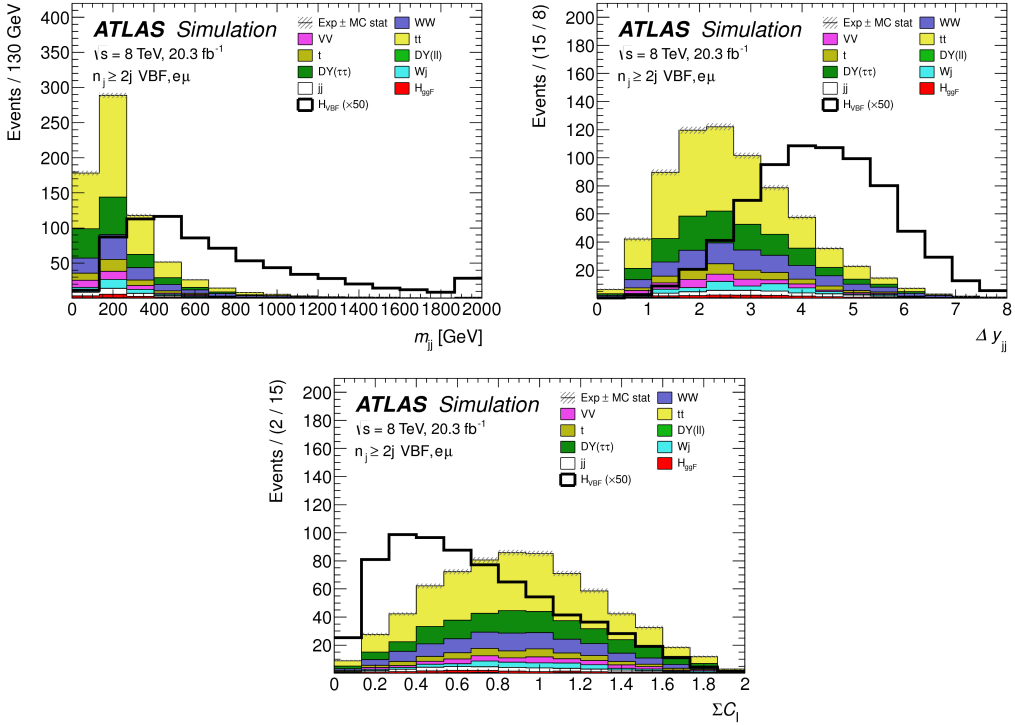


Figure 5.7: Distributions of m_{jj} (top left), Δy_{jj} (top right), $\sum C_\ell$ (bottom), VBF topology variables used in the selection requirements of the cut-based signal region and as inputs to the BDT result. These are plotted after all of the BDT pre-training selection cuts [61].

uncertainty on the overall background yield in the signal region can be replaced by a small statistical uncertainty coming from the number of data events in the CR and a smaller theoretical uncertainty on the extrapolation from the control region to the signal region.

5.5.2 TOP BACKGROUND

The normalization factor β_t for the top background in the VBF analysis is derived in a region required to have one b-tagged jet, or $n_b = 1$. In the cut-based analysis, normalization factors are computed at every stage of the cutflow by applying the appropriate cuts in the CR. These NF are then applied to the $t\bar{t}$ and single top event yields in the SR. In the BDT analysis, a single normalization factor is computed for each bin of O_{BDT} after applying the BDT pre-training cuts described previously. The computed normalization factors are derived with all flavor combinations combined in order to decrease statistical uncertainty. Additionally, in the BDT analysis, BDT bins 2 and 3 are merged for the same reason.

1904 Table 5.8 shows the evolution of the β_t through the cut-based selection. Table 5.9 shows the value
 1905 of the β_t in each bin of O_{BDT} . In all cases, the computed factors are relatively consistent with unity,
 1906 with the largest discrepancy coming in bin 1 of O_{BDT} . The normalization factors in the bins of O_{BDT}
 1907 are also consistent with those derived in the cut-based signal region, increasing confidence in the BDT
 1908 estimation.

Cut	β_t
$p_T^{\text{sum}} < 15 \text{ GeV}$	1.03 ± 0.01
$m_{\tau\tau} < m_Z - 25$	1.05 ± 0.01
$m_{jj} > 600 \text{ GeV}$	0.96 ± 0.06
$\Delta y_{jj} > 3.6$	1.02 ± 0.08
CJV	1.13 ± 0.16
OLV	1.01 ± 0.19
$m_{jj} < 1 \text{ TeV}$	0.94 ± 0.19
$m_{jj} > 1 \text{ TeV}$	1.48 ± 0.66

Table 5.8: Top normalization factors computed at each stage of the cut-based selection. Uncertainties are statistical only.

O_{BDT}	β_t
Bin0	1.09 ± 0.02
Bin1	1.58 ± 0.15
Bin2	0.95 ± 0.31
Bin3	0.95 ± 0.31

Table 5.9: Top normalization factors computed for each bin of O_{BDT} . Uncertainties are statistical only.

1909 Figure 5.8 shows the m_{jj} and O_{BDT} distributions in the top control region. Overall the modeling
 1910 looks consistent with the data.

1911 While these normalization factors can be computed and applied to the expected background yields
 1912 listed in tables like table 5.7, in the end the normalization of the top background is profiled (meaning
 1913 there is a dedicated Poisson constraint) and allowed to float in the final statistical fit.

1914 5.5.3 $Z/\gamma^* \rightarrow \tau\tau$ BACKGROUND

1915 In the different flavor channels, the $Z/\gamma^* \rightarrow \tau\tau$ background is an important one. Di-tau production
 1916 can produce an $e\mu$ final state if each τ lepton decays to a different flavor lepton.

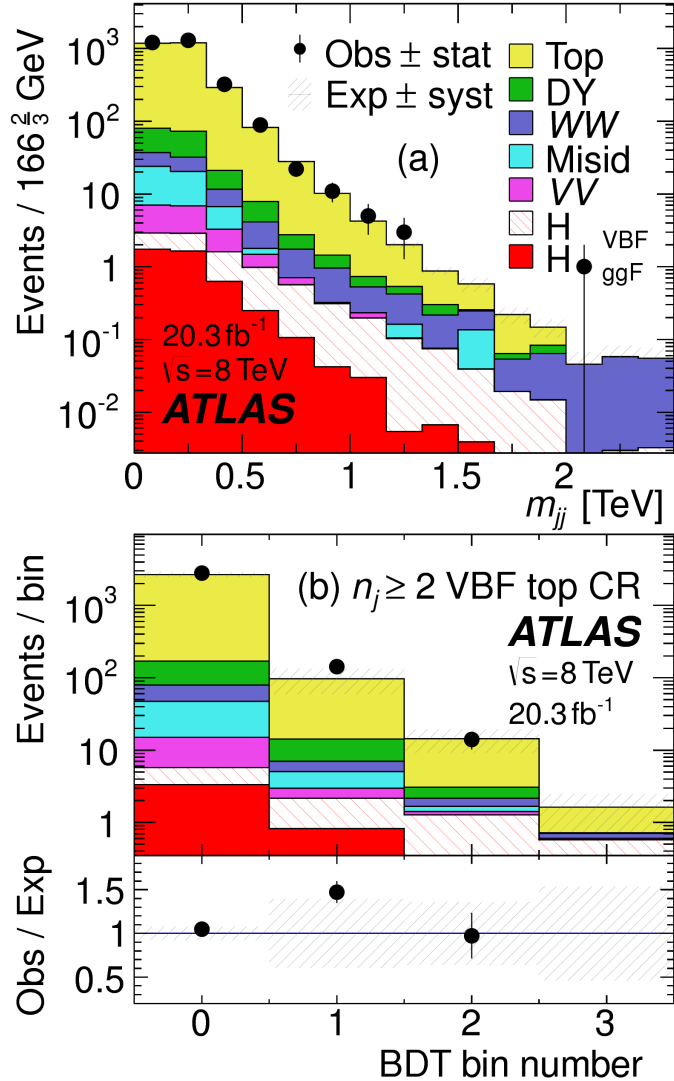


Figure 5.8: Distributions of m_{jj} (a) and O_{BDT} (b) in the VBF $n_b = 1$ top CR [61].

In the BDT analysis, a single normalization factor for the background is derived. A control region is defined using the pre-training selection cuts, except requiring that $|m_{\tau\tau} - m_Z| < 25 \text{ GeV}$ so that the region is enriched in $Z/\gamma^* \rightarrow \tau\tau$ background. Additional requirements of $m_{\ell\ell} < 80(75) \text{ GeV}$ in the different (same) flavor channel, as well as $O_{\text{BDT}} > -0.48$ are applied to increase the purity of the region. The final $\beta_{Z/\gamma^* \rightarrow \tau\tau}$ is calculated to be 0.9 ± 0.3 (statistical uncertainty only). Because of the small contribution of this background in the BDT analysis and the large statistical uncertainty, no additional systematics are calculated. The final SR estimate is scaled by this β and not allowed to float in

1924 the fit.

1925 The cut-based corrections are a bit more involved because they need to be applied selection by selec-
1926 tion, as well as in the final signal region for the fit. The region is defined including all SR cuts up to the
1927 $Z/\gamma^* \rightarrow \tau\tau$ veto, which is instead made into a Z mass peak requirement as for the BDT region. The
1928 $m_{\ell\ell}$ cut from the BDT region is included as well. The cut-based approach aims to correct the normal-
1929 ization of the $Z/\gamma^* \rightarrow \tau\tau$ background in two ways. First, an overall normalization factor is computed
1930 from the control region. However, the VBF topological cuts are not included in this region, and apply-
1931 ing them as is done in the top CR is not feasible due to limited statistics. So, instead, correction factors
1932 (CF) to the cut efficiencies of the VBF cuts are derived in a same flavor $Z \rightarrow \ell\ell$ control region, which has
1933 significantly more statistics. The CF is simply the ratio of the cut efficiencies in data and MC derived in
1934 this region. In the end, the overall background estimate is given by equation 5.5.

$$N_{Z/\gamma^* \rightarrow \tau\tau}^{\text{est}} = B_{Z/\gamma^* \rightarrow \tau\tau}^{\text{SR}} \times \beta_{\tau\tau} \times \frac{\epsilon_{\text{VBF cuts}}^{\text{data}}}{\epsilon_{\text{VBF cuts}}^{\text{MC}}} \quad (5.5)$$

1935 The hypothesis is that while the normalization correction must be derived in a dedicated region, the
1936 efficiency of the VBF cuts should not be sensitive to the type of Z/γ^* process and thus the larger control
1937 region can be exploited to derive the CF. Figure 5.9 shows a shape comparison for the m_{jj} variable in
1938 $Z \rightarrow \tau\tau$ events in the signal region and $Z \rightarrow \ell\ell$ events in the control region. The figure shows that the
1939 shapes are indeed comparable and thus any CF derived in the same flavor control region can reliably be
1940 applied in the signal region.

1941 Table 5.10 shows the overall normalization factor $\beta_{\tau\tau}$ and the efficiency correction factors for the var-
1942 ious VBF topological cuts. In general, the statistical uncertainties on the cut efficiency corrections are
1943 quite good, and the MC tends to underestimate the efficiency of the VBF cuts for the $Z/\gamma^* \rightarrow \tau\tau$ back-
1944 ground. The overall normalization factor is also consistent with that calculated for the BDT analysis.

1945 5.5.4 $Z/\gamma^* \rightarrow \ell\ell$ BACKGROUND

1946 In the same flavor channels, the $Z/\gamma^* \rightarrow \ell\ell$ background is dominant and thus must be estimated
1947 correctly. In both the BDT and cut-based analyses, the background is estimated using the so-called

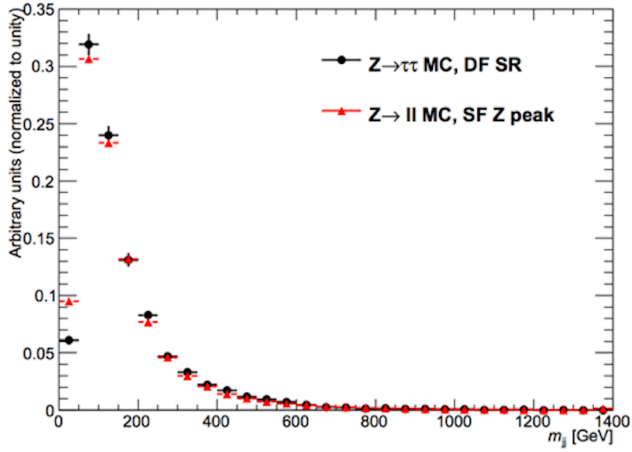


Figure 5.9: Comparison of m_{jj} shape in a same flavor $Z \rightarrow \ell\ell$ control region and the VBF cut-based signal region.

$\beta_{\tau\tau}$	0.97 ± 0.04
Cut	Correction factors
$m_{jj} > 600$ GeV	1.09 ± 0.01
$\Delta y_{jj} > 3.6$	1.14 ± 0.02
CJV	1.20 ± 0.02
OLV	1.17 ± 0.03
$m_{jj} < 1$ TeV	1.17 ± 0.06
$m_{jj} > 1$ TeV	1.18 ± 0.13

Table 5.10: $Z/\gamma^* \rightarrow \tau\tau$ correction factors for the VBF cut-based analysis. Uncertainties are statistical only.

1948 “ABCD” method. The ABCD method creates four different regions by defining cuts on two variables.
 1949 One of the regions (A) is the signal region, while the other regions are defined by inverting one of both
 1950 of the cuts. in this case, the two variables used are $m_{\ell\ell}$ and E_T^{miss} , because inverting either of the SR cuts
 1951 on these variables will give regions rich in the $Z/\gamma^* \rightarrow \ell\ell$ background. Figure 5.10 illustrates the general
 1952 strategy for each region.

1953 In both of the cut-based and BDT analyses, the Z peak region is defined with $|m_{\ell\ell} - m_Z| < 15$ GeV.
 1954 In the cut-based analysis, low $m_{\ell\ell}$ corresponds to $m_{\ell\ell} < 50$ GeV (this defines the cut-based SR) while
 1955 in the BDT it is $m_{\ell\ell} < 75$ GeV. In the cut-based, high and low E_T^{miss} are defined as opposite ends of
 1956 the 55 GeV cut applied for the signal region definition. The BDT low E_T^{miss} region is between 25 and
 1957 45 GeV, while the high E_T^{miss} region is $E_T^{\text{miss}} > 45$ GeV.

1958 Once the regions are defined, the final signal region background estimate is done by taking the esti-

Region A (SR)	Region C
High E_T^{miss}	High E_T^{miss}
Low $m_{\ell\ell}$	Z peak
Region B	Region D
Low E_T^{miss}	Low E_T^{miss}
Low $m_{\ell\ell}$	Z peak

Figure 5.10: General illustration of the ABCD region definitions for $Z/\gamma^* \rightarrow \ell\ell$ background estimation.

1959 mate in region B and extrapolating it to the signal region (A) by multiplying it by the ratio of regions
 1960 C and D. Effectively, the Z peak region is used to estimate the efficiency of the E_T^{miss} cut in data, and
 1961 then this efficiency is applied in the low $m_{\ell\ell}$ region. An additional correction is also applied for the non-
 1962 closure of the method in MC. This is summarized in equations 5.6 and 5.7.

$$N_{Z/\gamma^*\rightarrow\ell\ell}^{\text{SR}} = N_{Z/\gamma^*\rightarrow\ell\ell}^{\text{B}} \times \frac{N_{Z/\gamma^*\rightarrow\ell\ell}^{\text{C}}}{N_{Z/\gamma^*\rightarrow\ell\ell}^{\text{D}}} \times f_{\text{corr}} \quad (5.6)$$

$$f_{\text{corr}} = \frac{B_{\text{MC}}^{\text{A}}/B_{\text{MC}}^{\text{B}}}{B_{\text{MC}}^{\text{C}}/B_{\text{MC}}^{\text{D}}} \quad (5.7)$$

1963 Here, the N refer to data yields in each region with the non Z/γ^* backgrounds subtracted, while B
 1964 refer to the Z/γ^* yields in MC in each region.

1965 A normalization factor $\beta_{\ell\ell}$ is computed for each analysis as the ratio of the predicted data yield to
 1966 the MC yield in the SR. The shape of the BDT distribution is taken from data region B, while the shape
 1967 of the m_T distribution in the cut-based analysis is taken from Z/γ^* MC in the SR. The values of the
 1968 $\beta_{\ell\ell}$ in the cut-based and BDT analyses from this method are summarized in table 5.11. They are quite
 1969 consistent with one another within the statistical uncertainties. In the cut-based analysis, the same cut
 1970 efficiency correction factors shown in table 5.10 are also applied (in product with the $\beta_{\ell\ell}$) in the same
 1971 flavor channels to this background, as they were derived in the Z peak region.

	β_t
BDT Bin 1	1.01 ± 0.15
BDT Bin 2	0.89 ± 0.28
Cut-based	0.81 ± 0.21

Table 5.II: $Z/\gamma^* \rightarrow \ell\ell$ normalization factors for cut-based and BDT analyses. Uncertainties are statistical only.

1972 5.5.5 WW AND OTHER DIBOSON BACKGROUNDS

1973 The WW and other diboson backgrounds have both their shape and normalization taken from MC
 1974 simulation. They are validated in dedicated control regions and found to agree with data well.

1975 As WW is the largest of these backgrounds and is irreducible, validating the estimate is of particular
 1976 importance. The validation region is constructed by requiring the pre-selection cuts on leptons and $m_{\ell\ell}$,
 1977 $n_b = 0$, and $m_T > 100$ GeV. The m_{T2} variable [81] is an additional discriminant that will isolate
 1978 the WW background, and a requirement of $m_{T2} > 160$ GeV is placed to define the WW validation
 1979 region. This cut gives a 60% purity for the validation region. The derived normalization factor in the
 1980 region is 1.15 ± 0.19 and is thus consistent with unity. Figure 5.II shows the m_{T2} distribution and how
 1981 it distinguishes the WW background.

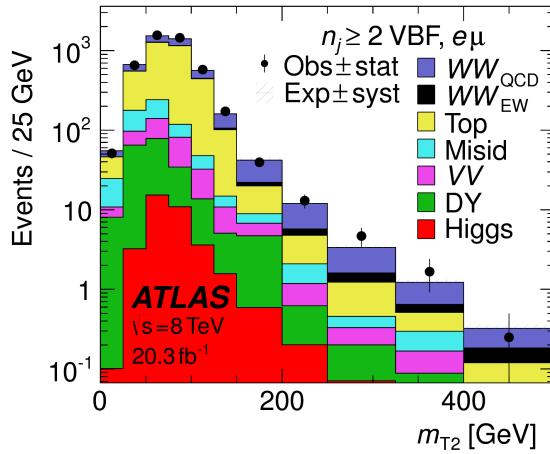


Figure 5.II: Distribution of m_{T2} in the WW validation region of the VBF analysis [61].

1982 5.5.6 HIGGS PRODUCTION VIA GLUON-GLUON FUSION

1983 Because this analysis is dedicated to measuring the VBF contribution to Higgs production, the com-
1984 ponent of Higgs production from gluon-gluon fusion is treated as a background. The shape is taken
1985 directly from simulation, using the generators described in table 5.4. In the final combined fit of all dif-
1986 ferent signal regions, the normalization is controlled by either a combined signal strength parameter μ ,
1987 which controls the normalization of both ggF and VBF production, or a separate parameter μ_{ggF} de-
1988 pending on the interpretation being presented in the final results.

1989 5.5.7 BACKGROUNDS WITH MISIDENTIFIED LEPTONS

1990 As discussed previously, the $W + \text{jets}$ and QCD multijet backgrounds are derived with fully data-driven
1991 methods. These backgrounds do not make a large contribution to the final VBF signal region but their
1992 estimation methods are discussed briefly here.

1993 $W + \text{jets}$ BACKGROUND

1994 The $W + \text{jets}$ background enters the signal region by having one of the jets mis-reconstructed as a lep-
1995 ton. The background is estimated by constructing a control sample with two leptons, where one lepton
1996 passes the usual lepton quality cuts but the second lepton fails one of those cuts (also known as the “anti-
1997 identified” lepton). This control region is rich in the $W + \text{jets}$ contribution because if a second lepton is
1998 reconstructed in a $W + \text{jets}$ event it is likely to be poor quality. The purity of this $W + \text{jets}$ control sample
1999 is 85% to 90% depending on the exact configuration of leptons in the final state.

2000 The signal region estimate of $W + \text{jets}$ is estimated by extrapolation from the control sample to the sig-
2001 nal region using extrapolation factors derived in a $Z + \text{jets}$ control sample in data. The extrapolation fac-
2002 tor is the ratio of the number of lepton candidates satisfying all quality criteria to the number of lepton
2003 candidates anti-identified. This ratio is measured in bins of p_T and η . Thus, the final signal region esti-
2004 mate (binned as the extrapolation factor is binned) is simply the number of events in the anti-identified
2005 lepton control sample multiplied by the extrapolation factor derived from the $Z + \text{jets}$ control sample.

2006 Figure 5.12 shows the extrapolation factors derived for electrons and muons.

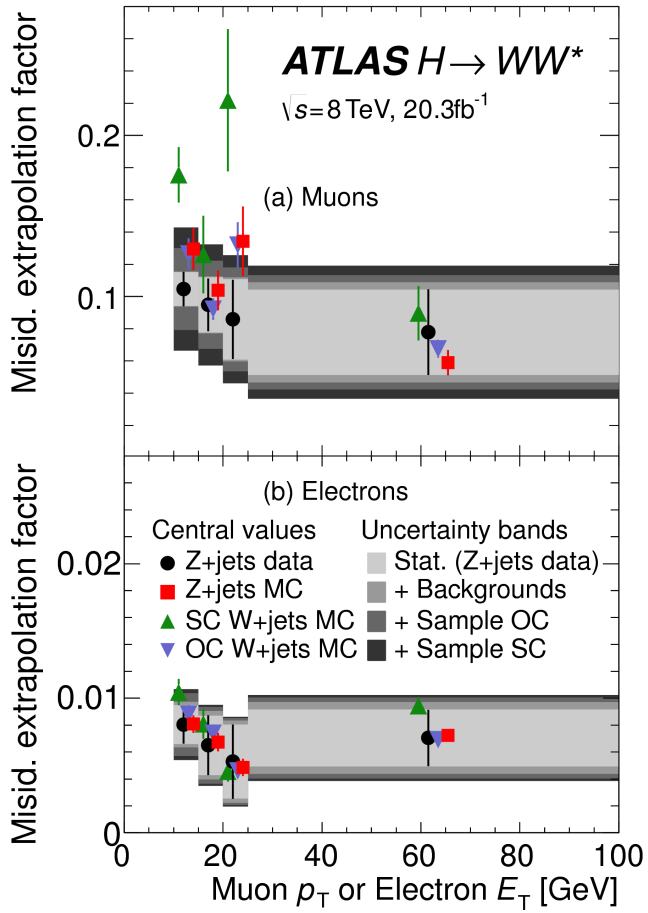


Figure 5.12: Extrapolation factors for the $W + \text{jets}$ estimate derived for muons (a) and electrons (b) as a function of lepton p_T [61].

2007 **QCD MULTIJET BACKGROUND**

2008 The method for estimating the multijet background is very similar to the $W + \text{jets}$ estimation method.
 2009 The control sample in this case has two anti-identified leptons but otherwise satisfies all signal region
 2010 requirements. The extrapolation factor is estimated from a multijet sample and applied twice to the
 2011 control sample.

2012 **5.5.8 BACKGROUND COMPOSITION IN FINAL SIGNAL REGION**

2013 After all of these estimation procedures, the final signal region composition can be calculated. The esti-
 2014 mated yields are all shown in table 5.7. Figure 5.13 shows the relative percentages of the different back-

2015 ground for the different flavor and same flavor final states. In $e\mu$, the leading backgrounds are top back-
 2016 grounds, ggF Higgs, and SM WW production. In $ee/\mu\mu$, the leading background is Drell-Yan, fol-
 2017 lowed by top and ggF Higgs.

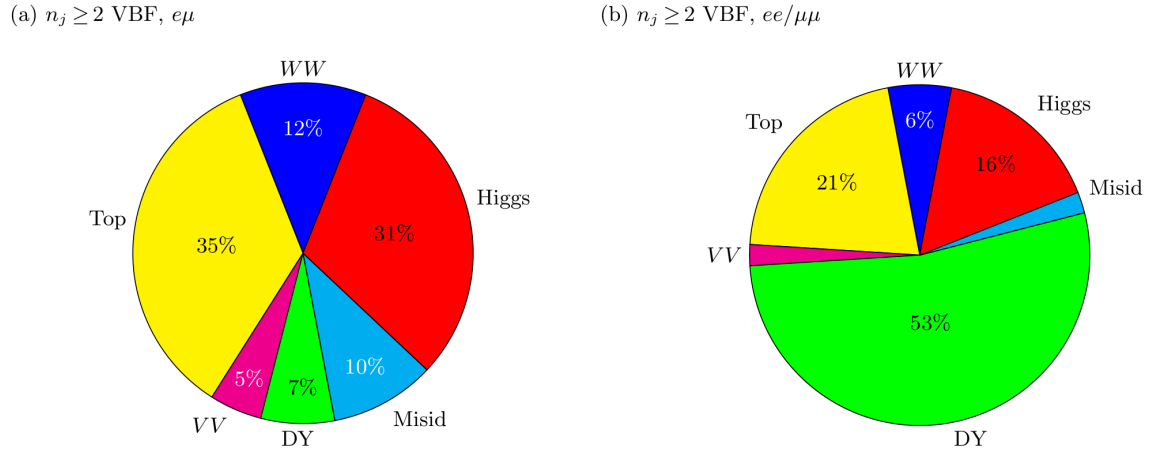


Figure 5.13: Background composition in final VBF signal region [61].

2018 5.6 SYSTEMATIC UNCERTAINTIES

2019 There are two main types of systematic uncertainties that are assessed for the analysis. First, theoreti-
 2020 cal uncertainties associated with the various signal and background yield estimates are discussed. Then,
 2021 experimental uncertainties due to detector effects are shown. Normalization uncertainties refer to uncer-
 2022 tainties that affect the cross section of the process in question in the signal region being probed. Shape
 2023 uncertainties refer to systematic uncertainties that affect the shape of the final discriminating variable
 2024 (either m_T or O_{BDT}).

2025 5.6.1 THEORETICAL UNCERTAINTIES

2026 There are four main components to theoretical uncertainties assigned to signal and background pro-
 2027 cesses taken from Monte Carlo. Each one is a different source of variation in the overall acceptance for
 2028 that process. The first involves variation of the QCD renormalization and factorization scales used in
 2029 the calculation. In this case, the two scales are varied independently and simultaneously by factors of
 2030 two high or low and quantifying the resulting variation in normalization and shape for the process. This

approximates the correction to the cross section that would come from including the next order of the QCD calculation (referred to as scale uncertainty). Next, there is an uncertainty associated with the PDF set used in generating the events. The uncertainty eigenvectors for the given PDF set are studied, and the envelope of maximal variation is taken as an uncertainty. Finally, there are two uncertainties associated with the choice of MC software (referred to as PDF uncertainty). An uncertainty associated with the generator chosen for the hard scattering process is evaluated by keeping the parton showering software constant but varying the matrix element generator and taking the maximal variation as an uncertainty (referred to as the generator uncertainty). The converse variation can also be done, where the matrix element generator remains constant and the generator used for the underlying event/parton shower modeling is varied (referred to as the UE/PS uncertainty). In cases where the background is normalized in a control region, the systematic uncertainty arises from variations of the extrapolation factor α between the CR and the SR, which can affect the normalization of the background in the SR.

There are two additional uncertainties that are applied to the Higgs processes as well. First, there are uncertainties assigned to the Higgs total production cross section. Then, there are uncertainties assigned based on the fact that the analysis is done in exclusive jet bins and it is possible for signal events to migrate from one bin to the next depending on the presence or absence of jets. These are assigned using the Jet Veto Efficiency (JVE) procedure [18, 82] for ggF events and the Stewart-Tackmann (ST) method [83] for VBF production.

Table 5.12 shows the total theory uncertainties on the backgrounds in the cut-based analysis. These are the sum in quadrature of the uncertainties from each of the variations described above.

Process	Theory syst. (%)
ggF H	48
Top	26
QCD WW	37
$Z/\gamma^* \rightarrow \tau\tau$	6.1

Table 5.12: Systematic uncertainties for various processes in the cut-based VBF analysis, given in units of % change in yield. Values are given for the low m_{jj} signal region.

Figures 5.14 and 5.15 show the variations in the extrapolation factor from the PDF and QCD uncertainties on the top background estimate, binned in m_T , for the cut-based analysis. In both cases, there

2053 was no significant shape uncertainty but normalization uncertainties were assigned according to the
 2054 maximal variation. These uncertainties enter into the 26% total uncertainty on top quoted in table 5.12
 2055 While the estimate for the same-flavor $Z/\gamma^* \rightarrow \ell\ell$ background is data-driven, there is still a sys-
 2056 tematic uncertainty taken for the non-closure of the method in Monte Carlo. This is taken as the max-
 2057 imum of the deviation of the non-closure factor f_{corr} from unity and its uncertainty, or $\max(|1 -$
 2058 $f_{\text{corr}}|, \delta f_{\text{corr}})$. For the cut-based analysis this non-closure uncertainty 23%, while for the BDT analy-
 2059 sis it is 17%.

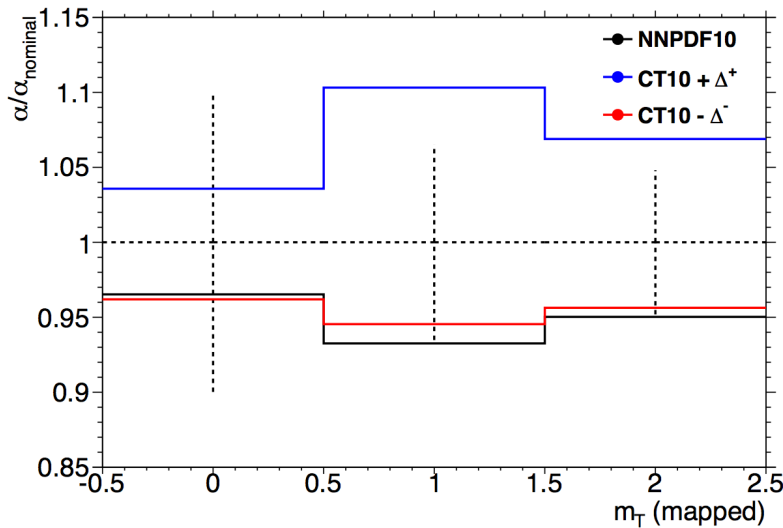


Figure 5.14: Variations in the top background extrapolation factor in the cut-based analysis due to PDF uncertainties, binned in m_T .

2060 5.6.2 EXPERIMENTAL UNCERTAINTIES

2061 In this analysis, the theoretical uncertainties end up being the most dominant, but there are some ex-
 2062 perimental uncertainties that make a contribution as well. The first is the uncertainty on the measured
 2063 integrated luminosity, which affects backgrounds whose normalization is taken from MC and is mea-
 2064 sured to be 2.8% in the 8 TeV dataset [84]. The dominant sources of uncertainty overall are uncertainties
 2065 on the jet energy scale and resolution and the b -tagging efficiency. Additional sources include lepton
 2066 uncertainties on identification, resolution, and trigger efficiency, as well as uncertainties on the missing
 2067 transverse momentum .

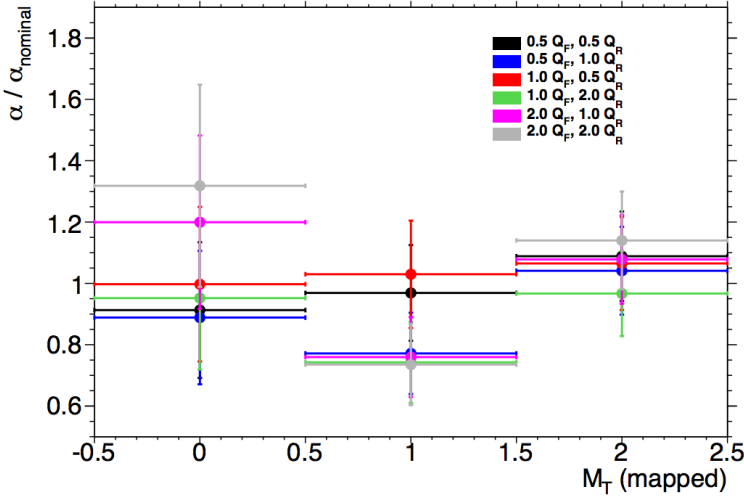


Figure 5.15: Variations in the top background extrapolation factor in the cut-based analysis due to QCD scale uncertainties, binned in m_T .

The jet energy scale uncertainty is split into several independent components, including jet-flavor dependent calorimeter response uncertainties, uncertainties on modeling of pile-up interactions, uncertainties on extrapolation from the central to forward detector regions, and MC non-closure [85]. The uncertainty on energy scale for jets used in this analysis ranges from 1% to 7% depending on the jet p_T and η . The jet energy resolution varies from 5% to 20%, with uncertainties ranging from 2% to 40% (the largest uncertainties occurring at the selection threshold).

The b-tagging efficiency is independently measured in data samples enriched in dileptonic decays of $t\bar{t}$ events or in events where a muon is reconstructed in the vicinity of a jet [86, 87]. The efficiencies and their uncertainties are binned in p_T and decomposed into uncorrelated components using an eigenvector method [88]. Uncertainties on the efficiency range from 1% to 7.8%. The uncertainty on the rate of misidentification of c -jets as b -jets ranges from 6-14%, while the uncertainty on the rate of light jet mis-tagging ranges from 9-19% depending on p_T and η .

The total experimental uncertainties on different signal and background components are summarized in table 5.13. They are compared to the level of other statistical and systematic uncertainties as well. Overall, the experimental uncertainties are sub-dominant compared to the statistical and theoretical uncertainties.

Sample	Total error	Stat. error	Expt. syst. err.	Theo. syst. err.
$n_j \geq 2$ VBF-enriched				
N_{sig}	13	-	6.8	12
N_{bkg}	9.2	4.7	6.4	4.5
N_{WW}	32	-	14	28
N_{top}	15	9.6	7.6	8.5
N_{misid}	22	-	12	19
N_{VV}	20	-	12	15
$N_{\tau\tau}$ (DY)	40	25	31	2.9
$N_{ee/\mu\mu}$ (DY)	19	11	15	-

Table 5.13: Composition of the post-fit uncertainties (in %) on the total signal (N_{sig}), total background (N_{bkg}), and individual background yields in the VBF analysis [61].

2084 5.7 RESULTS

2085 While the combined results of all the $H \rightarrow WW^*$ sub-analyses will be discussed in the next chapter, this
 2086 section presents the results of the VBF specific analysis and interpretations. As table 5.7 shows, the final
 2087 cut-based signal region contains 20 events in data with $m_T < 150$ GeV, 14 coming from the $e\mu$ channel
 2088 and 6 coming from the $ee + \mu\mu$ channel. The BDT analysis has many more candidates due to its looser
 2089 selection, and the yields in each bin of O_{BDT} are shown in table 5.14.

2090 Figure 5.16(a) shows the final distribution of data candidates compared to the expected m_T distri-
 2091 bution for signal and background. The data are very consistent with a VBF Higgs hypothesis. Fig-
 2092 ure 5.16(b) shows where the data candidates fall in the two-dimensional binning of m_T and m_{jj} used
 2093 in the fit for the cut-based analysis.

2094 Figure 5.17 shows the distributions of O_{BDT} and m_T in the VBF BDT analysis. Again the data are
 2095 quite consistent with a VBF Higgs hypothesis.

2096 Because the cut-based result is used as a validation for the BDT analysis and the two signal regions are
 2097 not fully orthogonal, it is interesting to explore which events overlap between the two analyses. Of the
 2098 twenty events in the cut-based signal region, only seven were not selected by the BDT analysis, while the
 2099 other thirteen also enter the BDT signal region. Figure 5.18 shows where the different analysis candidates
 2100 lie in the m_{jj} - m_T plane. This shows clearly that the advantage of the BDT analysis is that it can extract

(a) Before the BDT classification

Selection	Summary						Composition of N_{bkg}													
	$N_{\text{obs}}/N_{\text{bkg}}$	N_{bkg}	N_{obs}	N_{bkg}	N_{signal}	N_{eggF}	N_{VBF}	N_{VH}	N_{WW}^{SD}	N_{WW}^{EW}	$N_{t\bar{t}}$	N_t	N_{Wj}	N_{jj}	N_{VV}	N_{missid}	$N_{\text{Drell-Yan}}$	$N_{e/\mu}^{\text{SD}}$	$N_{e/\mu}^{\text{EW}}$	$N_{\tau\tau}^{\text{SD}}$
$e\mu$ sample	1.04 ± 0.04	718	689	13	15	2.0	90	II	327	42	29	23	31	2.2	130	2				
$ee/\mu\mu$ sample	1.18 ± 0.08	469	397	6.0	7.7	0.9	37	3	132	17	5.2	1.2	10.1	168	23	1				
(b) Bins in O_{BDT}																				
$e\mu$ sample																				
Bin 0 (not used)	1.02 ± 0.04	661	650	8.8	3.0	1.9	83	9	313	40	26	21	28	2.2	126	1				
Bin 1	0.99 ± 0.16	37	37	3.0	4.2	0.1	5.0	1.0	17	3.1	3.3	1.8	2.6	—	4.0	0.2				
Bin 2	2.26 ± 0.63	14	6.2	1.2	4.2	—	1.5	0.5	1.8	0.3	0.4	0.3	0.8	—	0.3	0.3				
Bin 3	5.41 ± 2.32	6	1.1	0.4	3.1	—	0.3	0.2	0.3	0.1	—	—	0.1	—	0.1	0.1				
$ee/\mu\mu$ sample																				
Bin 0 (not used)	1.91 ± 0.08	396	345	3.8	1.3	0.8	33	2	123	16	4.1	1.1	8.8	137	20.5	0.5				
Bin 1	0.82 ± 0.14	53	45	1.5	2.2	0.1	3.0	0.5	10.4	1.8	0.8	0.2	0.9	26	1.7	0.1				
Bin 2	1.77 ± 0.49	14	7.9	0.6	2.5	—	0.8	0.3	1.1	0.2	0.2	—	0.3	4.4	0.3	0.1				
Bin 3	6.32 ± 2.87	6	0.9	0.2	1.7	—	0.1	0.2	0.2	—	—	—	0.7	—	—	—				

Table 5.14: Event selection for the VBF BDT analysis. The event yields in (a) are shown after the pre-selection and the additional requirements applied before the BDT classification (see text). The event yields in (b) are given in bins in O_{BDT} after the classification [61].

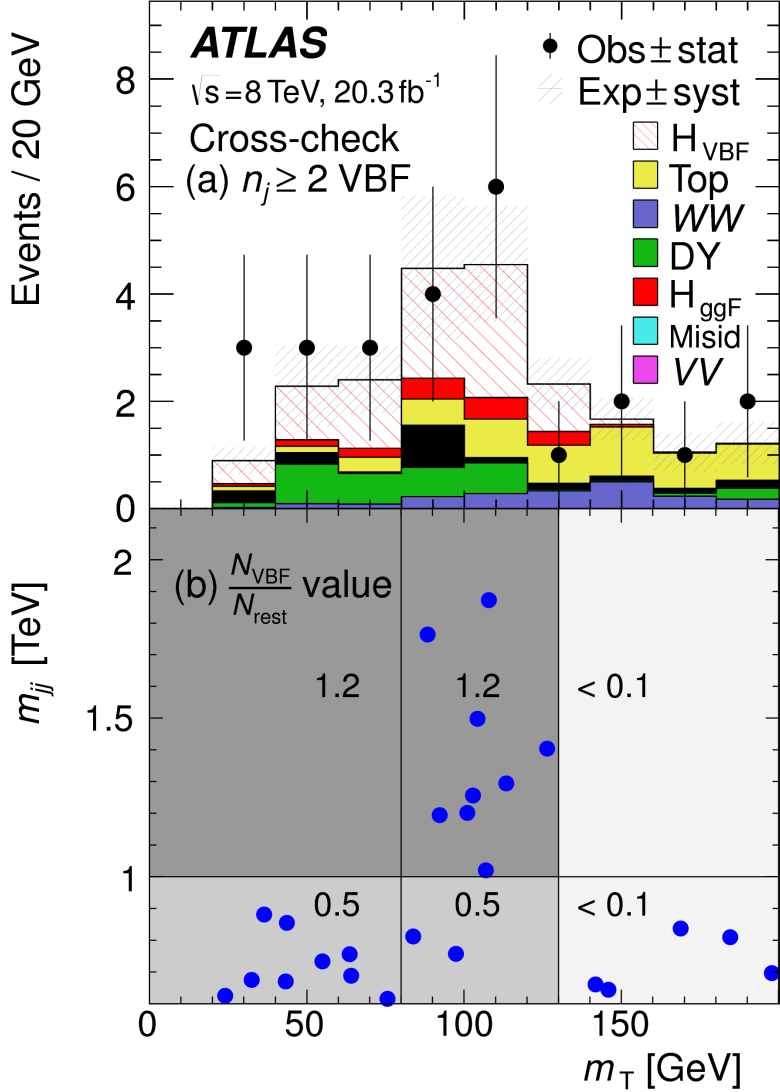


Figure 5.16: Post-fit distributions in the cut-based VBF analysis. Panel (a) shows the one-dimensional m_T distribution, while (b) shows the data candidates split into the bins of m_T and m_{jj} used in the final fit [61].

signal candidates lower m_{jj} region due to its ability to recognize correlations with other variables.
 While the context of these results in the broader $H \rightarrow WW^*$ statistical analysis will be presented in the next chapter, the significance of the VBF observation can be shown here. In the BDT analysis, the expected signal significance was 2.7σ , while the observed significance was 3.1σ . In the cut-based analysis, the expected significance was 2.1σ and the observed significance was 3.0σ . The compatibility between these two results can be evaluated by computing the probability of observing a larger difference

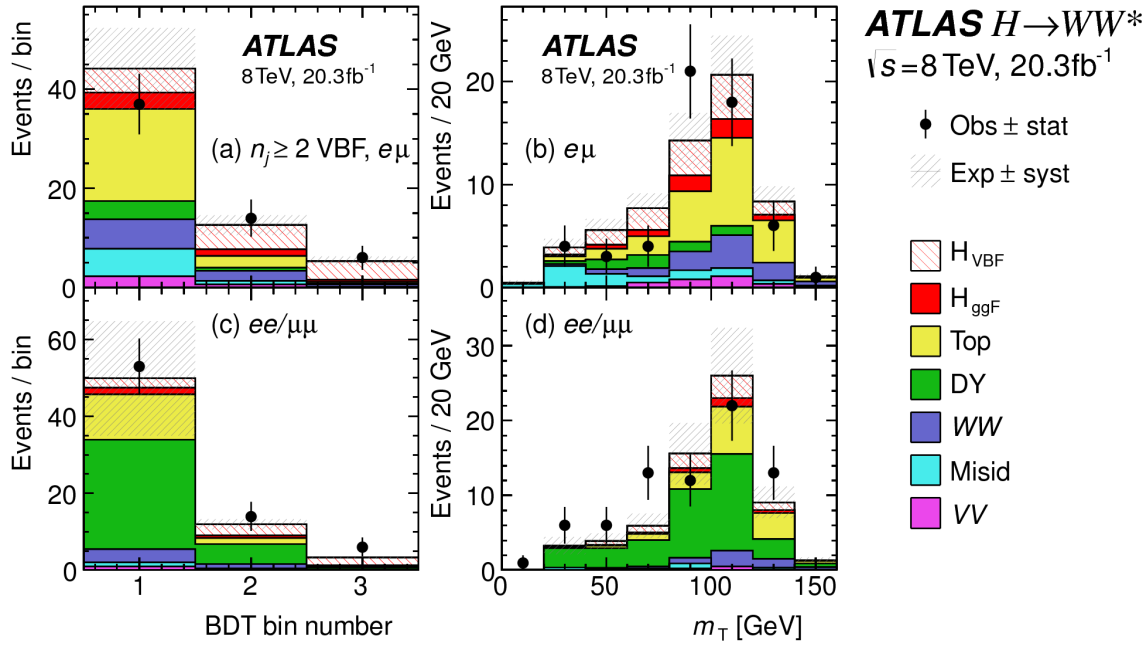


Figure 5.17: Postfit distributions in the BDT VBF analysis [61].

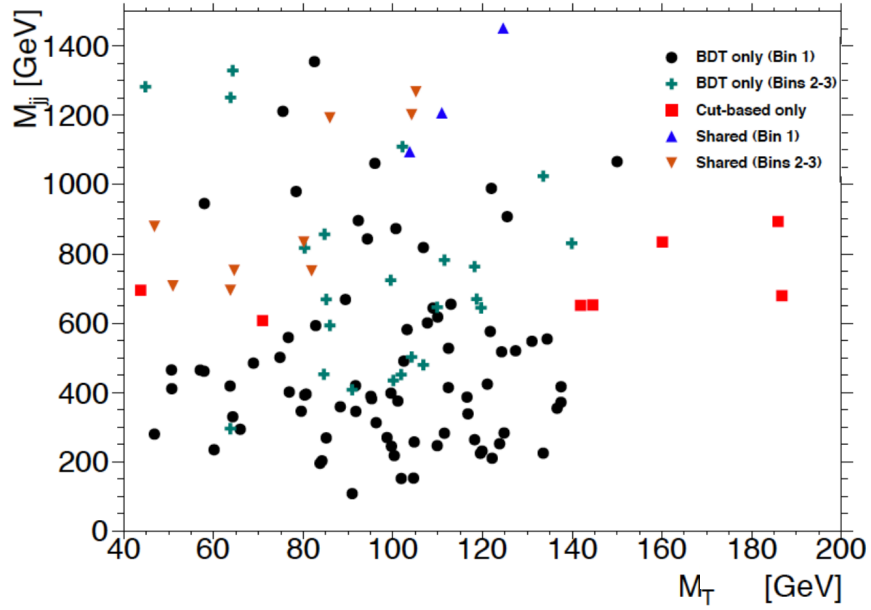


Figure 5.18: Overlap between cut-based and BDT VBF signal region candidates in the m_{jj} - m_T plane.

2107 in Z_0 values than the one measured. Using toy Monte Carlo with the ggF signal strength fixed to unity
2108 and considering only statistical uncertainties, this probability is computed to be 79%, indicating good
2109 agreement between the analyses. This result represents the first observation of the vector boson fusion
2110 production of a Higgs boson.

*The feeling is less like an ending than just another
starting point.*

Chuck Palahniuk

6

2111

2112

Combined Run I $H \rightarrow WW^* \rightarrow \ell\nu\ell\nu$

2113

results

2114

6.1 INTRODUCTION

2115 In the final statistical analysis of $H \rightarrow WW^* \rightarrow \ell\nu\ell\nu$, the dedicated gluon-gluon fusion and vector
2116 boson fusion sensitive signal regions are all combined into a single fit to determine the main parameters
2117 of interest, the Higgs signal strength μ and mass m_H . Therefore, while the specific requirements applied
2118 for the VBF sensitive analysis are discussed in chapter 5, the final measurement of these parameters can
2119 only be discussed in combination with the results of the ggF dedicated analysis. For example, because
2120 ggF Higgs production is considered a background in the VBF analysis, the ggF dedicated signal regions
2121 can actually constrain the normalization of this background in the VBF dedicated region.

2122 This chapter presents the combined interpretation of results in the $H \rightarrow WW^* \rightarrow \ell\nu\ell\nu$ analysis

SR category i				Fit var.	
n_j , flavor	$\otimes m_{\ell\ell}$	$\otimes p_T^{\ell 2}$	$\otimes \ell_2$		
$n_j = 0$	$e\mu$	$\otimes [10, 30, 55]$	$\otimes [10, 15, 20, \infty]$	$\otimes [e, \mu]$	m_T
	$ee/\mu\mu$	$\otimes [12, 55]$	$\otimes [10, \infty]$		m_T
$n_j = 1$	$e\mu$	$\otimes [10, 30, 55]$	$\otimes [10, 15, 20, \infty]$	$\otimes [e, \mu]$	m_T
	$ee/\mu\mu$	$\otimes [12, 55]$	$\otimes [10, \infty]$		m_T
$n_j \geq 2$ ggF	$e\mu$	$\otimes [10, 55]$	$\otimes [10, \infty]$		m_T
$n_j \geq 2$ VBF	$e\mu$	$\otimes [10, 50]$	$\otimes [10, \infty]$		O_{BDT}
	$ee/\mu\mu$	$\otimes [12, 50]$	$\otimes [10, \infty]$		O_{BDT}

Table 6.1: All signal regions definitions input into final statistical fit [61].

for gluon fusion and vector boson fusion Higgs production. First, the results of the dedicated gluon fusion search are presented. Then, a comparison of the individual production mode signal strengths (μ_{ggF} and μ_{VBF} and a measurement of the combined signal strength (μ) are shown. Subsequently, the measured values of the Higgs couplings to fermions and vector bosons is presented. Finally, the cross section measurement for ggF and VBF production are shown.

6.2 RESULTS OF DEDICATION GLUON FUSION $H \rightarrow WW^* \rightarrow \ell\nu\ell\nu$ SEARCH

The details of the dedicated gluon fusion $H \rightarrow WW^* \rightarrow \ell\nu\ell\nu$ search are not discussed in this thesis and instead left to more comprehensive sources [61]. However, a brief summary of the results are essential for describing the results of the full analysis and interpreting the results of the dedicated VBF search in this broader context.

Table 6.1 shows the individual signal regions that were input into the final statistical fit. The ggF dedicated bins use m_T as their discriminating variable and are separated into bins of p_T of the subleading lepton as well. The VBF dedicated bin uses the O_{BDT} distribution as its final discriminant.

Table 6.2 shows the yields in the various signal regions in both data and expected signal and back-

2137 grounds. The yields for signal and background are all scaled according to the final normalizations calcu-
2138 lated in the fit.

	N_{obs}	N_{bkg}	N_{ggF}	N_{VBF}
$n_j = 0$	3750	3430 ± 90	300 ± 50	8 ± 4
$n_j = 1$	1596	1470 ± 40	102 ± 26	17 ± 5
$n_j \geq 2, \text{ggF } e\mu$	1017	960 ± 40	37 ± 11	13 ± 1.4
$n_j \geq 2, \text{VBF}$	130	99 ± 9	7.7 ± 2.6	21 ± 3

Table 6.2: Post-fit yields in the different ggF and VBF dedicated signal regions [61].

2139 Figure 6.1 shows the final post-fit m_T distribution in the $n_j \leq 1$ regions. The data are very consistent with the hypothesis of ggF Higgs production. These yields are used as input, along with the VBF results

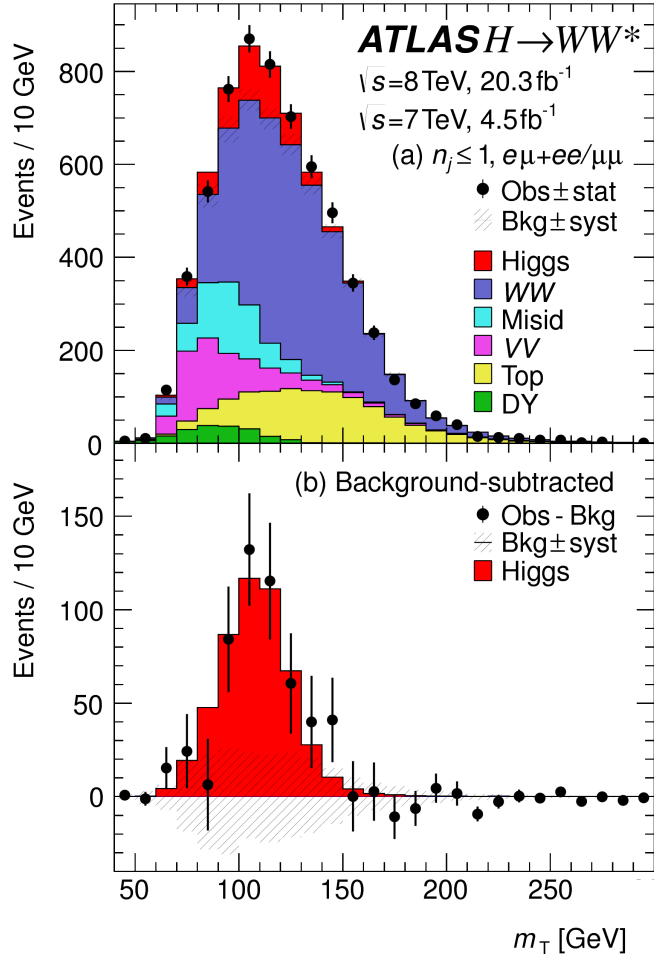


Figure 6.1: Post-fit m_T distribution in the $n_j \leq 1$ regions [61].

2140

2141 in chapter 5, for the physical interpretation of results presented in subsequent sections.

2142 **6.3 SIGNAL STRENGTH MEASUREMENTS IN ggF AND VBF PRODUCTION**

2143 When all of the signal regions are combined in the fit, there can be a combined measurement of the sig-
 2144 nal strength as well as the individual ggF and VBF signal strengths. The combined signal strength is the
 2145 ratio of the sum of the gluon fusion and VBF cross sections to the theory prediction, or a signal strength
 2146 for the total Higgs production cross section that this analysis is sensitive to. The final measured com-
 2147 bined signal strength μ is measured shown in equation 6.1.

$$\begin{aligned} \mu &= 1.09 \quad {}^{+0.16}_{-0.15} \text{ (stat.)} \quad {}^{+0.08}_{-0.07} \left(\text{expt syst} \right) \quad {}^{+0.15}_{-0.12} \left(\text{theo syst} \right) \quad \pm 0.03 \left(\text{lumi syst} \right) \\ &= 1.09 \quad {}^{+0.16}_{-0.15} \text{ (stat)} \quad {}^{+0.17}_{-0.14} \text{ (syst)} \\ &= 1.09 \quad {}^{+0.23}_{-0.21}. \end{aligned} \tag{6.1}$$

2148 Figure 6.2 gives the best fit signal strength $\hat{\mu}$ as a function of the hypothesized Higgs mass. The value
 2149 at 125.36 GeV corresponds to the μ quoted in equation 6.1. This value of the Higgs mass is used because
 2150 it is the most precise mass measurement from ATLAS, a result of the combined $\gamma\gamma$ and ZZ mass mea-
 2151 surements [89].

2152 As explained in chapter 3, a probability p_0 can be computed using the test statistic q_0 to quantify the
 2153 probability that the background could fluctuate to produce an excess at least as large as the one observed
 2154 in the data. The local p_0 value is shown in figure 6.3 as a function of m_H . The minimum p_0 value is
 2155 at $m_H = 130$ GeV and corresponds to a significance of 6.1σ . The curve is relatively flat and the sig-
 2156 nificance is the same at 125.36 GeV within the quoted precision. The expected significance for a signal
 2157 with strength $\mu = 1.0$ is 5.8σ . This represents the first discovery level significance measurement in the
 2158 $H \rightarrow WW^* \rightarrow \ell\nu\ell\nu$ analysis.

2159 All the results presented so far in this section have been for the combined gluon fusion and VBF pro-
 2160 duction modes. However, each signal strength can be calculated separately in the likelihood as well.
 2161 There are two ways to do this. First, the likelihood can be parameterized in terms of a single parameter,

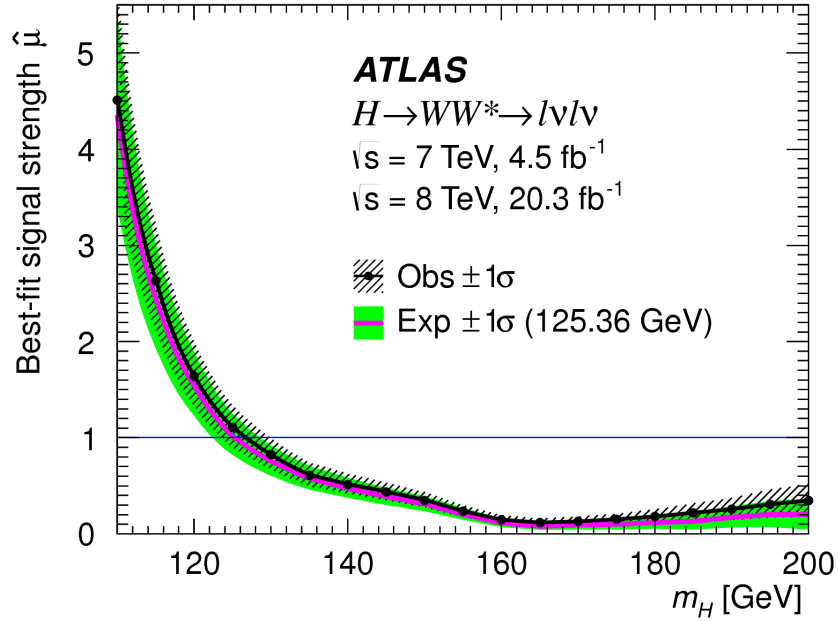


Figure 6.2: Best fit signal strength $\hat{\mu}$ as a function of hypothesized m_H [61].

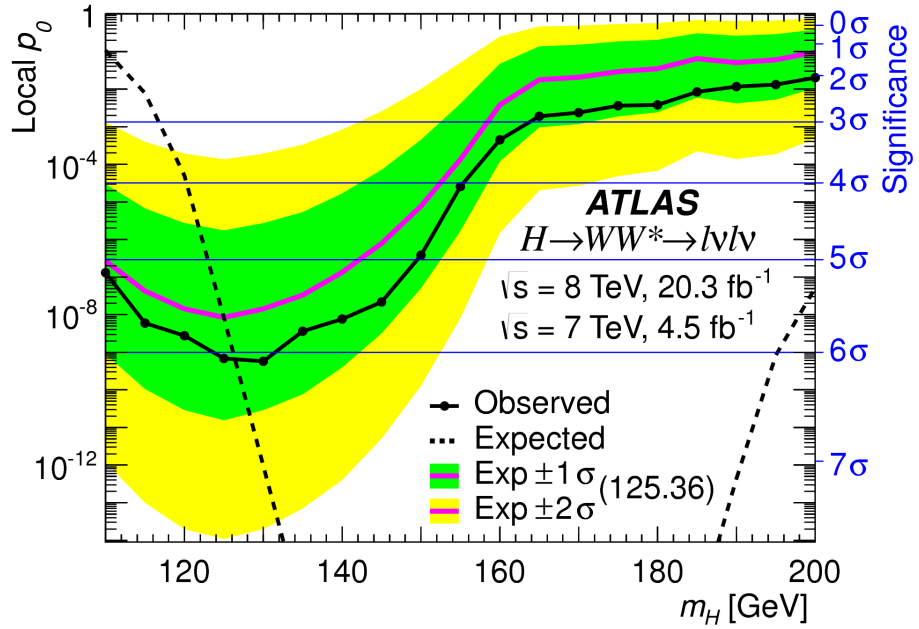


Figure 6.3: Local p_0 as a function of m_H [61].

the ratio of the VBF and gluon fusion signal strengths. With this method, the significance of the VBF observation can be evaluated. Figure 6.4 shows the likelihood as a function of the ratio $\mu_{\text{VBF}}/\mu_{\text{ggF}}$.

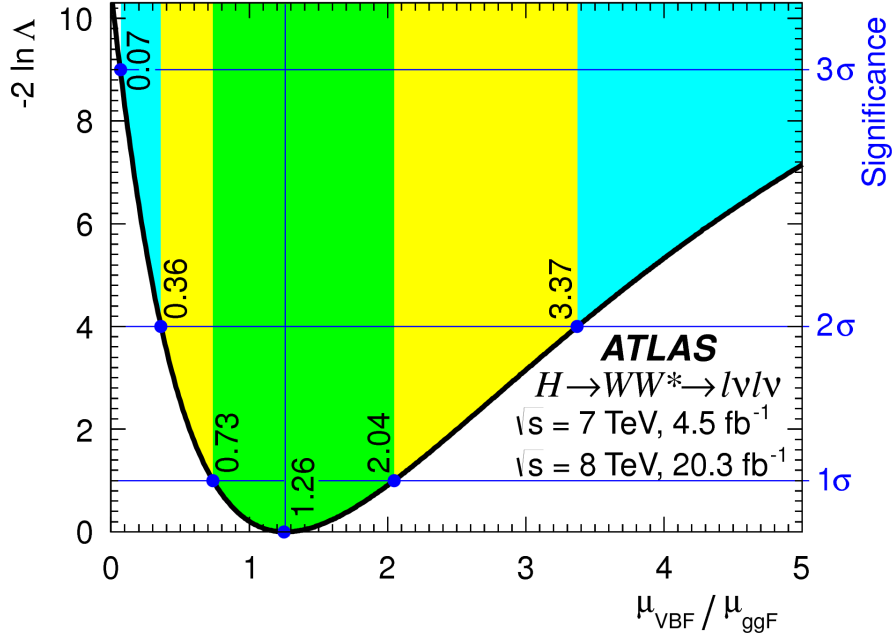


Figure 6.4: Likelihood as a function of $\mu_{\text{VBF}} / \mu_{\text{ggF}}$ [61].

2164 The best fit value of the ratio of signal strengths is shown in equation 6.2. Within the quoted uncer-
 2165 tainties, it is consistent with a ratio of unity.

$$\frac{\mu_{\text{VBF}}}{\mu_{\text{ggF}}} = 1.26^{+0.61}_{-0.45} (\text{stat.})^{+0.50}_{-0.26} (\text{syst.}) = 1.26^{+0.79}_{-0.53} \quad (6.2)$$

2166 The null hypothesis for VBF production corresponds to a ratio of $\mu_{\text{VBF}} / \mu_{\text{ggF}} = 0$. The likelihood in
 2167 figure 6.4 gives a significance of 3.2σ at $\mu_{\text{VBF}} / \mu_{\text{ggF}} = 0$, as quoted in chapter 5.

2168 In addition to the ratio of signal strengths, each signal strength can be varied independently in the
 2169 likelihood as well. Figure 6.5 shows the two dimensional likelihood scan in the $\mu_{\text{ggF}}-\mu_{\text{VBF}}$ plane. The
 2170 best fit values of the two signal strengths are shown in equation 6.3. Both are consistent with unity
 2171 within their uncertainties.

$$\begin{aligned} \mu_{\text{ggF}} &= 1.02 \pm 0.19^{+0.22}_{-0.18} = 1.02^{+0.29}_{-0.26} \\ \mu_{\text{VBF}} &= 1.27 \pm 0.40^{+0.44}_{-0.21} = 1.27^{+0.53}_{-0.45}. \end{aligned} \quad (6.3)$$

(stat.) (syst.)

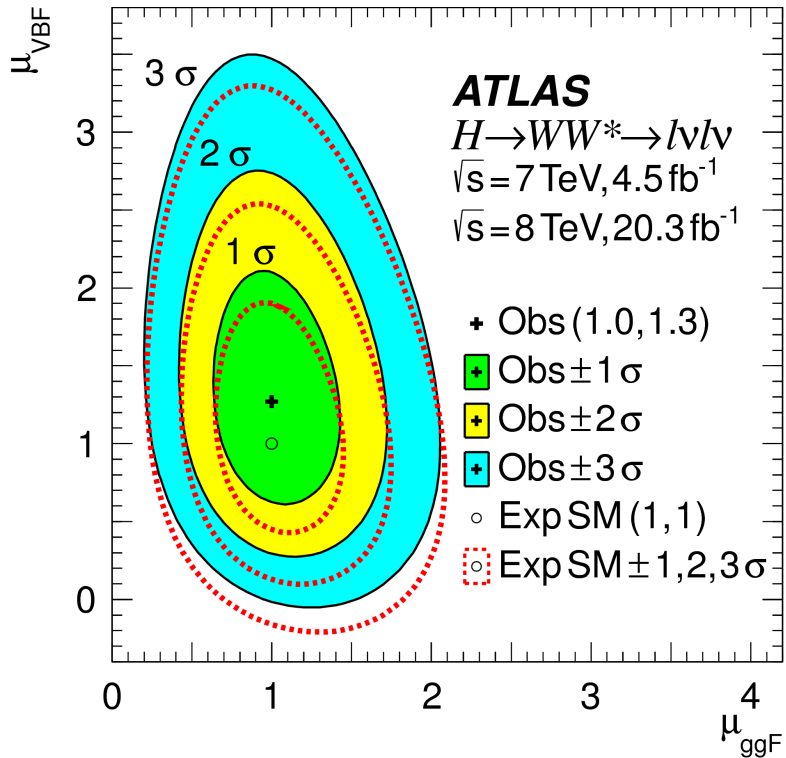


Figure 6.5: Likelihood scan as a function of μ_{VBF} and μ_{ggF} [61].

2172 6.4 MEASUREMENT OF HIGGS COUPLINGS TO VECTOR BOSONS AND FERMIONS

2173 Similar to the parameterization of signal strength, the couplings of the Higgs to fermions and bosons can
 2174 also be parameterized. The parameter of interest in this case is κ , or the ratio of the measured coupling
 2175 to the standard model expectation. Both the fermion and boson couplings have these so-called scale fac-
 2176 tors, κ_F for fermions and κ_V for bosons. Gluon fusion production is sensitive to the fermion couplings
 2177 through the top quark loops in its production, while VBF production is sensitive to the vector boson
 2178 couplings in its production. Both modes are sensitive to the vector boson couplings in their decays. The
 2179 signal strengths will have dependence on the coupling scale factors as described in equation 6.4 [18].

$$\begin{aligned}\mu_{\text{ggF}} &\propto \frac{\kappa_F^2 \cdot \kappa_V^2}{(\mathcal{B}_{H \rightarrow f\bar{f}} + \mathcal{B}_{H \rightarrow gg}) \kappa_F^2 + (\mathcal{B}_{H \rightarrow VV}) \kappa_V^2} \\ \mu_{\text{VBF}} &\propto \frac{\kappa_V^4}{(\mathcal{B}_{H \rightarrow f\bar{f}} + \mathcal{B}_{H \rightarrow gg}) \kappa_F^2 + (\mathcal{B}_{H \rightarrow VV}) \kappa_V^2}.\end{aligned}\quad (6.4)$$

2180 Figure 6.6 shows the two-dimensional likelihood scan of κ_F and κ_V . The best-fit values are given in
 2181 equation 6.5. The best-fit values are consistent with unity within their uncertainties.

$$\begin{aligned} \kappa_F &= 0.93 & +0.24 & +0.21 & = 0.93 & +0.32 \\ \kappa_V &= 1.04 & +0.07 & +0.07 & = 1.04 & \pm 0.11. \end{aligned} \quad (6.5)$$

(stat.) (syst.)

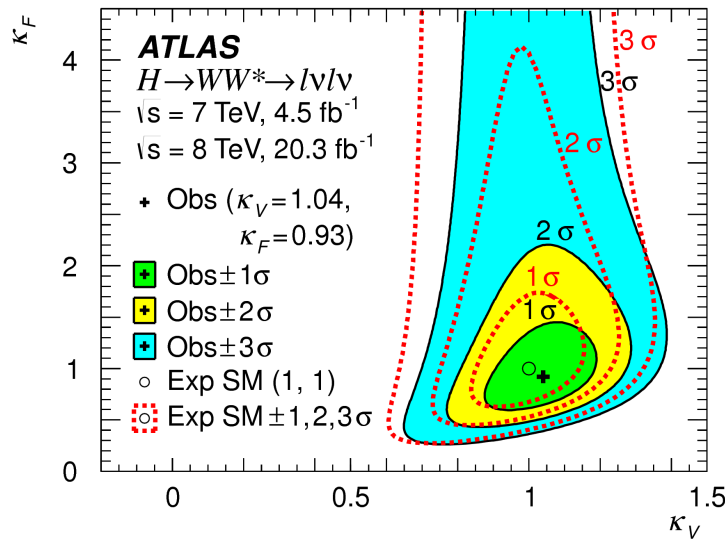


Figure 6.6: Likelihood scan as a function of κ_F and κ_V [61].

2182

2183 6.5 HIGGS PRODUCTION CROSS SECTION MEASUREMENT

2184 Another measurement that comes naturally from the signal strength numbers quoted earlier is the pro-
 2185 duction cross section and 7 and 8 TeV for both gluon fusion and VBF production. The general equa-
 2186 tion for calculating the cross section is given in equation 6.6.

$$\begin{aligned} (\sigma \cdot \mathcal{B}_{H \rightarrow WW^*})_{\text{obs}} &= \frac{(N_{\text{sig}})_{\text{obs}}}{\mathcal{A} \cdot \mathcal{C} \cdot \mathcal{B}_{WW \rightarrow \ell\nu\ell\nu}} \cdot \frac{1}{\int L dt} \\ &= \hat{\mu} \cdot (\sigma \cdot \mathcal{B}_{H \rightarrow WW^*})_{\text{exp}} \end{aligned} \quad (6.6)$$

2187 $(N_{\text{sig}})_{\text{obs}}$ is the number of events observed in data. \mathcal{A} is the geometric and kinematic acceptance of the
 2188 detector, while \mathcal{C} is the efficiency of the signal region selection for events that are reconstructed in the
 2189 detector. The branching ratio of a WW system to leptons must also be divided out. The production
 2190 cross section depends on the center of mass energy and the production mode desired (gluon fusion or
 2191 VBF), and so three separate cross section measurements are quoted in equation 6.7.

$$\begin{aligned}
 \sigma_{\text{ggf}}^{\text{7TeV}} \cdot \mathcal{B}_{H \rightarrow WW^*} &= 2.0 \pm 1.7 \begin{array}{l} +1.2 \\ -1.1 \end{array} = 2.0 \begin{array}{l} +2.1 \\ -2.0 \end{array} \text{ pb} \\
 \sigma_{\text{ggf}}^{\text{8TeV}} \cdot \mathcal{B}_{H \rightarrow WW^*} &= 4.6 \pm 0.9 \begin{array}{l} +0.8 \\ -0.7 \end{array} = 4.6 \begin{array}{l} +1.2 \\ -1.1 \end{array} \text{ pb} \\
 \sigma_{\text{vbf}}^{\text{8TeV}} \cdot \mathcal{B}_{H \rightarrow WW^*} &= 0.51 \begin{array}{l} +0.17 \\ -0.15 \end{array} \begin{array}{l} +0.13 \\ -0.08 \end{array} = 0.51 \begin{array}{l} +0.22 \\ -0.17 \end{array} \text{ pb.}
 \end{aligned} \tag{6.7}$$

(stat.) (syst.)

2192 The predicted cross section values for gluon fusion are 3.3 ± 0.4 pb at 7 TeV and 4.2 ± 0.5 pb at 8 TeV,
 2193 consistent with the measured values within their uncertainties. For vector boson fusion, the predicted
 2194 cross section is 0.35 ± 0.02 pb, again consistent with the measured value.

2195 6.6 CONCLUSION

2196 The combined analysis of the gluon fusion and vector boson fusion processes in $H \rightarrow WW^* \rightarrow \ell\nu\ell\nu$
 2197 in the 7 and 8 TeV datasets has yielded the first discovery level significance for Higgs production in this
 2198 decay channel. Additionally, precise measurements of the couplings to vector bosons and fermions are
 2199 given. Finally, signal strengths and cross sections for each production mode are measured. Figure 6.7
 2200 shows the $H \rightarrow WW^* \rightarrow \ell\nu\ell\nu$ measurements in comparison with other Higgs decay channels in
 2201 ATLAS. The measurement of signal strength from this channel remains the most sensitive in both the
 2202 gluon fusion and VBF production modes for the Run 1 dataset.

ATLAS

Individual analysis

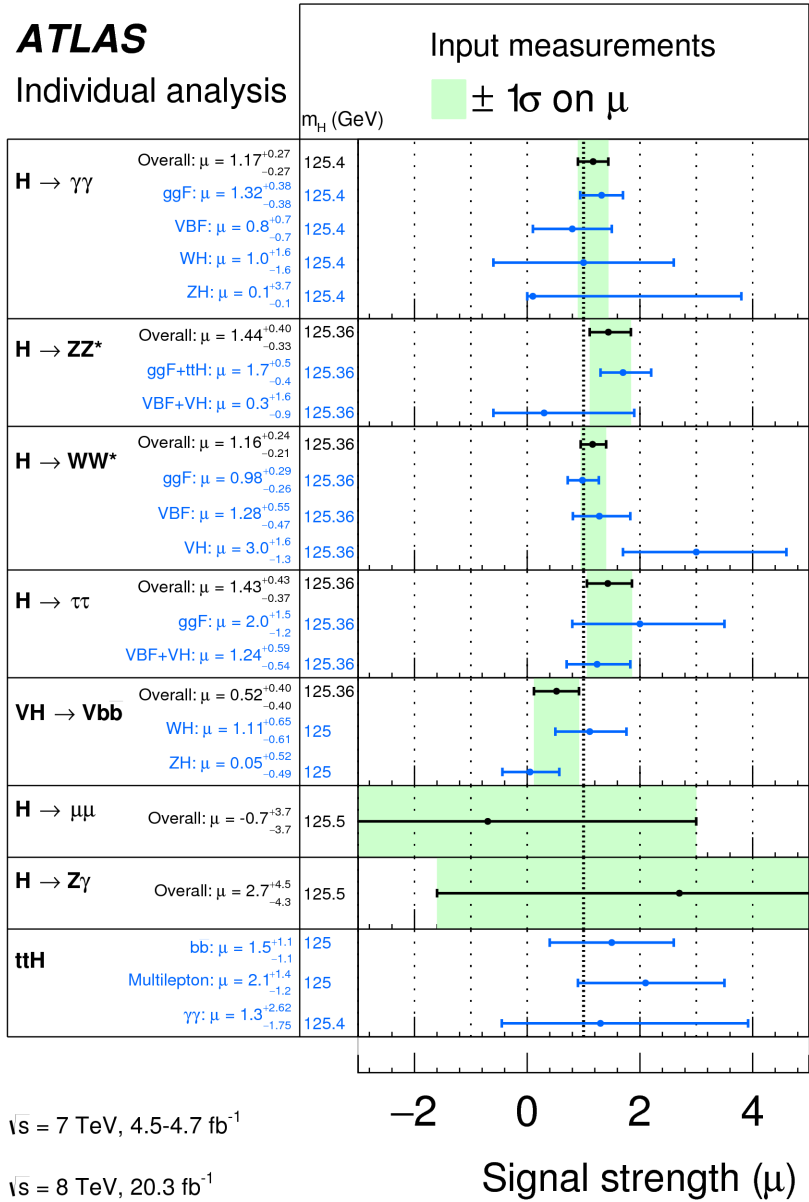


Figure 6.7: Comparison of signal strength measurements in different Higgs decay channels on ATLAS [90].

2203

Part III

2204

Search for Higgs pair production in the

2205

$HH \rightarrow b\bar{b}b\bar{b}$ channel in LHC Run 2 at $\sqrt{s} =$

2206

13 TeV

Passion is in all great searches and is necessary to all creative endeavors.

W. Eugene Smith

7

2207

2208 Search for Higgs pair production in boosted 2209 $b\bar{b}b\bar{b}$ final states

2210 7.1 INTRODUCTION

2211 After the discovery of the Higgs boson in the ATLAS Run 1 dataset and the subsequent measurements
2212 of its properties, the Higgs transformed into a potential tool in searches for physics beyond the Stan-
2213 dard Model. The pair production cross section of the Higgs can be enhanced through BSM physics.
2214 Studying di-Higgs production also probes the Higgs self-coupling, shedding light on the structure
2215 of the Higgs potential. This chapter presents a search for resonant production of a Higgs pair in the
2216 $X \rightarrow HH \rightarrow b\bar{b}b\bar{b}$ final state in 3.2 fb^{-1} of data collected at $\sqrt{s} = 13 \text{ TeV}$. In particular, this
2217 chapter focuses on a search for this final state in the regime where m_X is large ($\gtrsim 1 \text{ TeV}$) and the Higgs
2218 bosons in the decay are significantly boosted. A tailored selection for this boosted selection, using novel

2219 techniques in jet substructure and b -tagging, is discussed. Then, the data-driven background estimate is
 2220 presented. Finally, the results of the search are shown. The signal models used as benchmarks are a spin-
 2221 2 Randall Sundrum graviton (RSG) and a narrow width spin-0 resonance. These models are described
 2222 in more detail in Chapter 1. Limits on signal models are reserved for the next chapter where the results of
 2223 this chapter are combined with the results of a separate selection dedicated to the lower m_X regime.

2224 7.2 MOTIVATION

2225 With the center of mass energy increase from $\sqrt{s} = 8 \text{ TeV}$ to $\sqrt{s} = 13 \text{ TeV}$, the LHC and ATLAS
 2226 are able to probe new resonances at higher mass scales than previously accessible in Run 1. This is a
 2227 powerful motivator for searching for a new resonance in the early 13 TeV data. Figure 7.1 shows the
 2228 ratios of parton luminosities between 8 and 13 TeV for different resonance masses. For a resonance of
 2229 $M_X = 2 \text{ TeV}$, the cross section at $\sqrt{s} = 13 \text{ TeV}$ is roughly a factor of 10 larger than at $\sqrt{s} = 8 \text{ TeV}$.

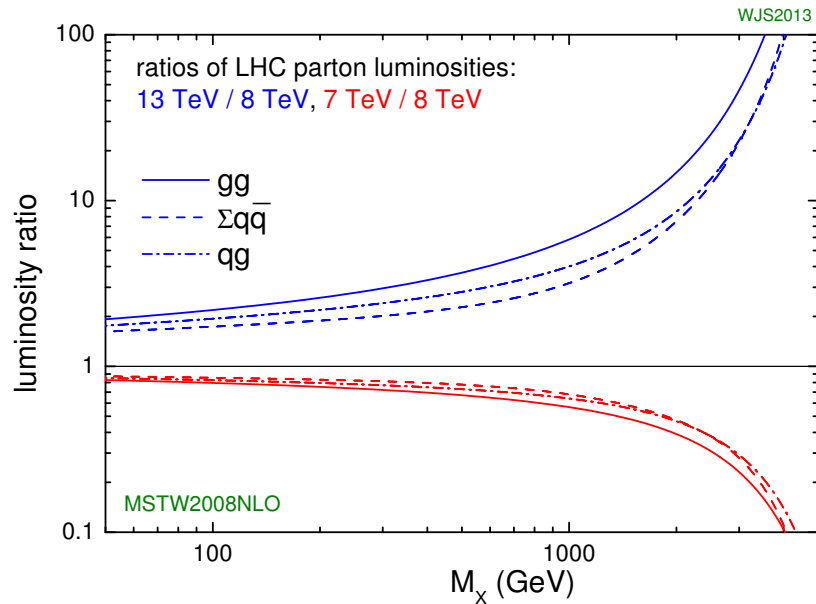


Figure 7.1: Parton luminosity ratios as a function of resonance mass M_X for 13/8 TeV and 7/8 TeV [91].

2230 Higgs pair production offers a vast array of unprobed regions of phase space where searches for BSM
 2231 physics can be made. Chapter 1 discusses some possibilities for both resonant and non-resonant enhance-

ment of the di-Higgs production cross section. Given the increased mass reach of the LHC in Run 2, it is particularly important to focus on resonant searches at high m_X . One consideration when conducting a search in the HH final state is which decay modes of the Higgs to consider. Figure 7.2 shows the branching ratio of the HH final state for different combinations of decays of each individual Higgs. As the largest branching ratio for the 125 GeV Higgs is $H \rightarrow b\bar{b}$, the $HH \rightarrow b\bar{b}b\bar{b}$ branching ratio is also the largest at 33%.

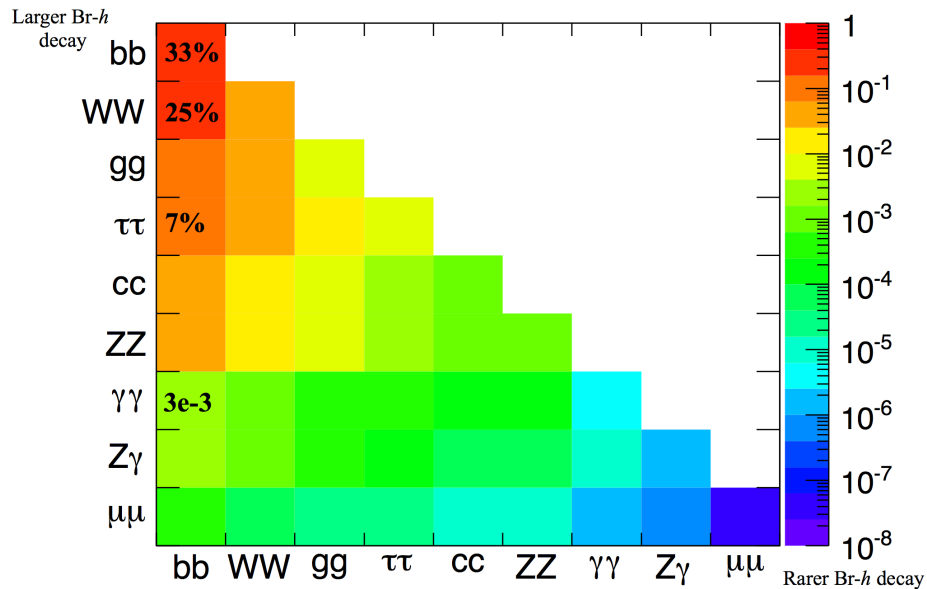


Figure 7.2: Summary of HH branching ratios [92].

At high m_X , the Higgs bosons resulting from the decay of a heavy resonance will have large p_T^* . The ΔR between the decay products of the Higgs is inversely proportional to the Higgs p_T , as shown in equation 7.1.

$$\Delta R \approx \frac{2m}{p_T} \quad (7.1)$$

Figure 7.3 shows the minimum ΔR between truth level B decay vertices in simulation samples for Randall-Sundrum gravitons of different masses. The figure shows that as the mass of the graviton increases, the ΔR distribution between the b quarks in the Higgs decay tends to shift to lower values. Because of this effect, it is necessary to tailor a selection to target these merged b -jets.

*In the limit that $m_H \ell \ell m_X$, the Higgs p_T is roughly $m_X/2$.

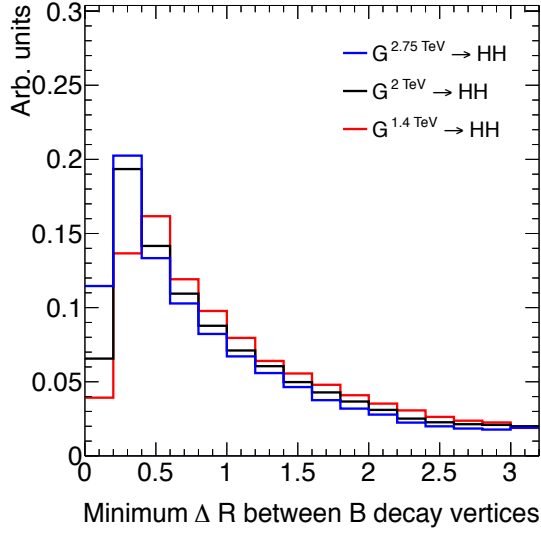


Figure 7.3: Minimum ΔR between B decay vertices for different RSG masses in a $G_{KK}^* \rightarrow HH \rightarrow 4b$ sample with $c = 1$

2245 7.3 DATA AND SIMULATION SAMPLES

2246 7.3.1 SIGNAL MODELS

2247 While the resonance search is by its nature generic (as it is a simple search for a peak in the $4b$ invariant
 2248 mass spectrum), there are two signal models that the selection requirements have been optimized for.
 2249 The first is Randall-Sundrum (RSG) model, where a tower of massive spin-2 Kaluza-Klein gravitons
 2250 is predicted. The second is a heavy narrow spin-0 resonance, the so-called “heavy Higgs”. This type of
 2251 resonance arises, for example, in the two Higgs doublet model (2HDM). More details about the physics
 2252 of these models and their motivation is given in chapter 1.

2253 Signal graviton (G_{KK}^*) events are generated at leading order (LO) with **MADGRAPH5 v2.2.2** [93].
 2254 The PDF set used is the **NNPDF2.3 LO** set [94]. For modeling parton shower and hadronization in jets,
 2255 **PYTHIA 8.186** is used with the A14 tune [73, 95]. The free parameters in the RSG model are the graviton mass and the coupling constant $c \equiv k/\bar{M}_{\text{Pl}}$ [†]. Both the production cross section and width of the graviton are proportional to c^2 . Samples are generated at both $c = 1$ and $c = 2$ for a variety of mass

[†] k is the curvature constant for the warped extra dimension and \bar{M}_{Pl} is the Planck mass divided by 8π

2258 points between 300 GeV and 3 TeV.

2259 The second signal sample is a heavy spin-0 resonance H with a fixed width of $\Gamma_H = 1$ GeV. This
2260 is generated with **MADGRAPH5** and uses the **CT10** PDF set [76]. The parton shower and hadronization
2261 are handled by **HERWIG ++** with the **CTEQ6L1** PDF set and the **UEEE5** event tune [77, 96, 97]. Because
2262 the width and branching ratios depend on 2HDM parameters, each mass point generated with this fixed
2263 width corresponds to a different point in the 2HDM parameter phase space. Mass points are generated
2264 between 300 GeV and 1 TeV as with the RSG signal samples.

2265 7.3.2 BACKGROUND SAMPLES

2266 While the dominant **QCD** multijet background is estimated with a fully data-driven method, the sub-
2267 dominant backgrounds $t\bar{t}$ and Z +jets are modeled with some input from simulation.

2268 $t\bar{t}$ events are simulated at next-to-leading order (NLO) with the **POWHEG-BOX** version 1 generator us-
2269 ing the **CT10** PDF set [98]. The parton shower, hadronization, and underlying event are simulated with
2270 **PYTHIA 6.428** with the **CTEQ6L1** PDF set [72]. The Perugia 2012 tune is used [99]. NNLO QCD cor-
2271 rections to the cross sections are computed in **Top++ 2.0** [100]. The top quark mass is set to 172.5 GeV.
2272 The shapes of distributions in $t\bar{t}$ are taken from MC while the normalization is taken from data.

2273 Finally, the Z +jets background is simulated with **PYTHIA 8.186** and the **NNPDF2.3** LO PDF set. This
2274 background is negligible compared to the others and is taken fully from MC.

2275 7.3.3 DATA SAMPLE AND TRIGGER

2276 This analysis is done on 3.2 fb^{-1} of data taken in 2015 at $\sqrt{s} = 13$ TeV. The details of the machine
2277 conditions during this time can be found in Chapter 2. Only data which was taken during stable beam
2278 conditions with all detectors functioning is used. Events must pass a trigger which requires a single
2279 360 GeV large radius ($R = 1.0$) jet to be reconstructed in the HLT. Figure 7.4 shows the trigger effi-
2280 ciency for various trigger options as a function of graviton mass. Above $m_G > 1$ TeV, the single large
2281 radius jet trigger is 99% efficient for events passing the signal selection.

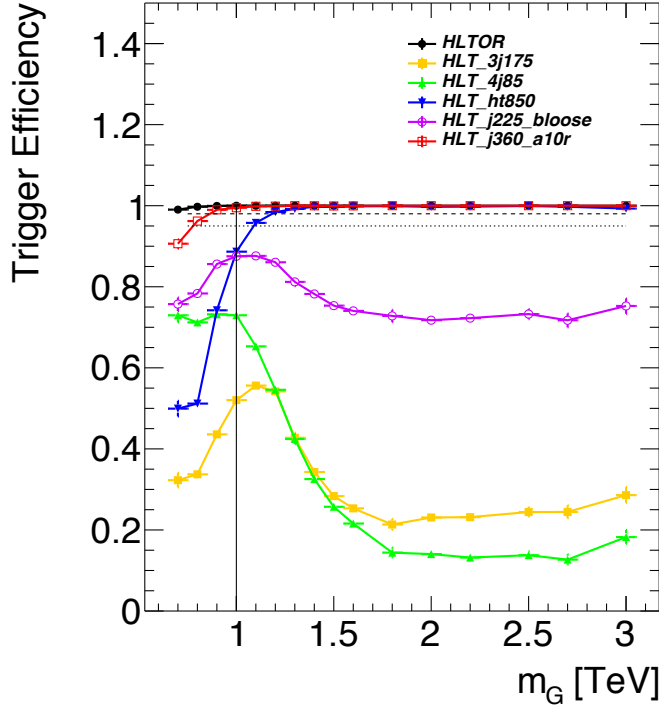


Figure 7.4: Trigger efficiency for events passing all signal region selections as a function of mass in $G_{KK}^* \rightarrow HH \rightarrow 4b$ samples with $c = 1$ [101]. In the trigger names, “ j ” refers to a jet or jets. “ht” refers to H_T , the scalar sum of transverse momenta in the event. “bloose” refers to a loose b -tagging requirement applied to the jet. “a10r” refers to anti- k_T jets with $R = 1.0$. The numbers at the end are the thresholds on the given quantity in GeV.

2282 7.4 EVENT RECONSTRUCTION AND OBJECT SELECTION

2283 The boosted selection first begins by defining a unique set of objects that can be exploited to increase
 2284 signal efficiency in the kinematic regime where the final state b -jets are very merged.

2285 7.4.1 LARGE RADIUS ($R = 1.0$) JETS

2286 The first step towards reconstructing the final state is to define objects that can be used to measure the
 2287 kinematics of the Higgs bosons. In the boosted selection anti- k_T jets with a radius parameter of 1.0
 2288 are used. These jets are much larger in angular size than the typical $R = 0.4$ jets and are intended to
 2289 encompass both jets resulting from the Higgs decay[‡]. The jets are built from clusters in the calorimeter

[‡]This is in contrast to the resolved selection, which uses two $R = 0.4$ anti- k_T jets for each Higgs

2290 calibrated with local calibration weighting [56].

2291 Because of the large extent of these jets, great care must be taken to remove potential contributions of
2292 calorimeter clusters from pile-up. This is done using a technique called jet trimming [102]. With trim-
2293 ming, the constituents of the large radius jet are re-clustered with a smaller radius with the k_T algorithm.
2294 Then, these so-called subjets are removed from the larger jet if $p_T^{\text{subjet}}/p_T^{\text{jet}} < f_{\text{cut}}$. In this analysis, the
2295 subjet radius is $R = 0.2$ and $f_{\text{cut}} = 0.05$. Trimming has been shown to improve the mass resolution
2296 of large radius jets. Figure 7.5 shows the effect of trimming on the large radius jet mass (M_J). Because
2297 the large radius jet fully contains the higgs decay products, its invariant mass should correspond to the
2298 125 GeV mass of the Higgs. The trimming algorithm brings the jet mass much closer to the expected
2299 Higgs mass and improves the mass resolution.

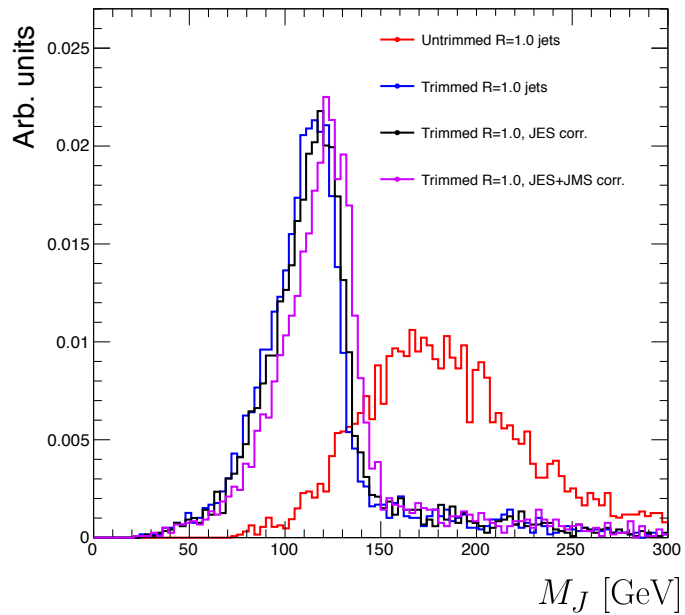


Figure 7.5: Comparison of untrimmed and trimmed jet masses for large radius jets in a RSG sample with $m_{G_{KK}^*} = 1$ TeV. JES (JMS) refers to the standard jet energy (mass) scale calibration for ATLAS [56].

2300 The large radius jets are required to satisfy $250 < p_T < 1500$ GeV. They must also be within
2301 $|\eta| < 2.0$ in order to ensure that the full jet is within the inner detector tracking volume. Finally, they
2302 are required to have $M_J > 50$ GeV. The upper p_T cut and lower threshold on mass are applied to
2303 correspond to the kinematic range where uncertainties are available in ATLAS calibrations [103, 104].

2304 7.4.2 TRACK JETS AND b -TAGGING

2305 Because the b -jets from boosted Higgs decays are so close together (as illustrated in figure 7.3), narrow ra-
2306 dius jets are required to fully resolve both b -jets. The minimum radius feasible for jets based on calorime-
2307 ter deposits is determined by the calorimeter granularity. However, because b -tagging relies on informa-
2308 tion from the inner detector, it is possible to define another type of jet that can have a smaller radius and
2309 better b -tagging resolution. These jets are called “track jets” [104, 105].

2310 Track jets are formed by applying the usual anti- k_T clustering algorithm to tracks that are required
2311 to be consistent with the primary vertex. After the jet axis has been determined using these tracks, a sec-
2312 ond step of track association is also performed to add tracks that can be useful for b -tagging [105]. In this
2313 analysis, the tracks are clustered with a radius parameter of $R = 0.2$. This radius has been shown to
2314 give good performance in boosted Higgs tagging [104, 105]. Figure 7.6 shows a comparison among dif-
2315 ferent track jet radii of the efficiency for reconstructing two b -jets from each Higgs in a RSG sample as a
function of mass. Track jets with radius of 0.2 give the best performance, especially at high mass. In this

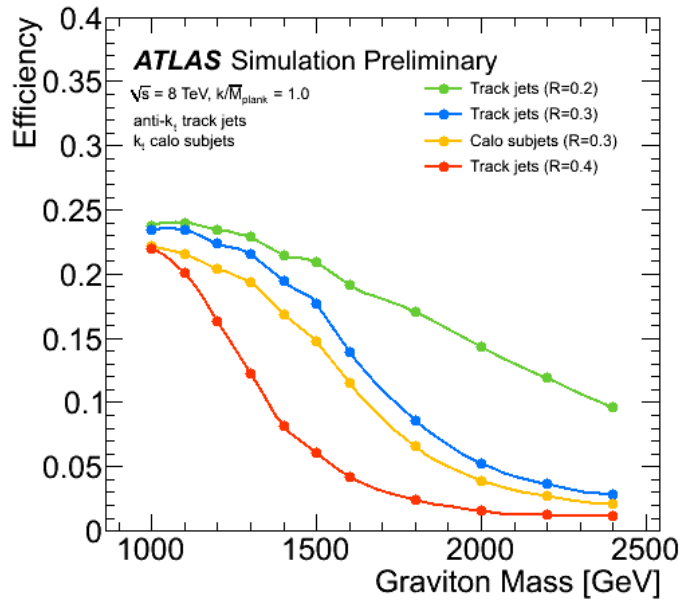


Figure 7.6: Efficiency of finding two b -jets from each Higgs in an RSG event using calorimeter jets with $R = 0.3$ or different track jet radii [105]

2317 analysis, track jets are required to have $p_T > 10 \text{ GeV}$ and $|\eta| < 2.5$. They must also have at least two
2318 tracks.

2319 **7.4.3 MUONS**

2320 Muons are used in this study to correct the four-momenta of calorimeter jets by accounting for semi-
2321 leptonic b decays. The muons used are combined ID and MS muons which must satisfy tight identifica-
2322 tion requirements [52]. The muons must have $p_T > 4 \text{ GeV}$ and $|\eta| < 2.5$. Table 7.1 summarizes the
2323 object requirements described in this section.

	R	p_T	$ \eta $	M
Calorimeter jets	1.0	$250 < p_T < 1500 \text{ GeV}$	< 2.0	$> 50 \text{ GeV}$
Track jets	0.2	$> 10 \text{ GeV}$	< 2.5	-
Muons	-	4 GeV	< 2.5	-

Table 7.1: Summary of requirements on objects used in the $X \rightarrow HH \rightarrow b\bar{b}b\bar{b}$ search

2324 **7.5 EVENT SELECTION**

2325 The first requirement in the boosted selection is for ≥ 2 large radius jets satisfying the selections outlined
2326 above. The two highest momentum large-R jets in the event are referred to as “Higgs candidates”. The
2327 leading jet is required to have $p_T > 350 \text{ GeV}$.

2328 Track jets satisfying the object selections are matched to Higgs candidate jets via ghost association [106].
2329 Each Higgs candidate must have at least 2 track jets associated with it. These basic requirements are illus-
2330 trated in figure 7.7

2331 The QCD multijet background produces less central jets than high mass resonances, so there is an ad-
2332 ditional requirement that the two Higgs candidates be close together in η . The large-R jets are required
2333 to satisfy $|\Delta\eta(JJ)| < 1.7$.

2334 The final set of requirements ensures that the Higgs candidates are consistent with expected proper-
2335 ties of the 125.0 GeV Higgs. First, a variable (X_{hh}) is defined to measure the consistency of both of the

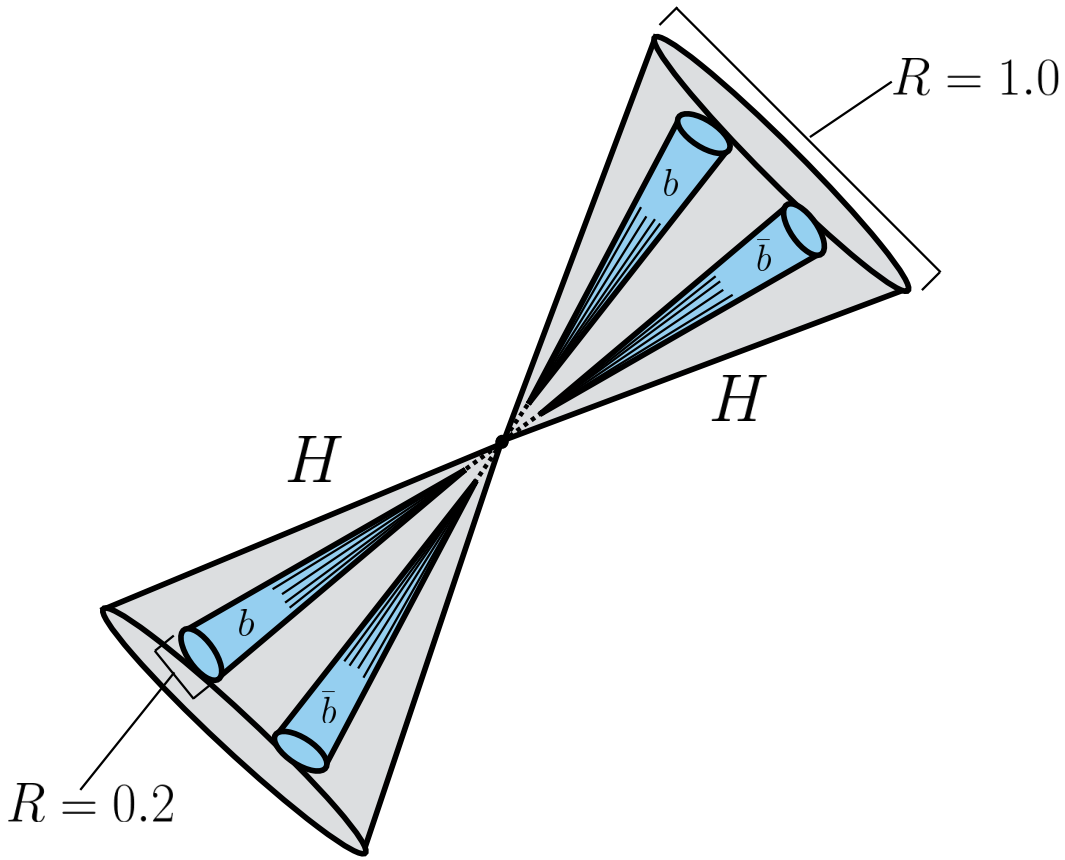


Figure 7.7: Illustration of the boosted selection requirements on Higgs candidates. Each large-radius calorimeter jet (Higgs candidate) must contain two track jets

²³³⁶ Higgs candidate jets with the SM Higgs mass. This is shown in equation 7.2.

$$X_{hh} = \sqrt{\left(\frac{M_J^{\text{lead}} - 124 \text{ GeV}}{0.1 M_J^{\text{lead}}}\right)^2 + \left(\frac{M_J^{\text{sublead}} - 115 \text{ GeV}}{0.1 M_J^{\text{sublead}}}\right)^2} \quad (7.2)$$

²³³⁷ The mass values in the X_{hh} formula are optimized to maximize signal efficiency. The sub-leading jet
²³³⁸ typically has a lower mass due to semi-leptonic b decays and final state radiation. X_{hh} effectively acts as
²³³⁹ a χ^2 measurement of the consistency of the two Higgs candidate masses with the signal hypothesis. The
²³⁴⁰ denominators of each term ($0.1 M$) give the uncertainty on the mass measurement for the large radius
²³⁴¹ jets. Events are required to satisfy $X_{hh} < 1.6$.

²³⁴² The last requirement applied is on the number of b -tagged track jets. There are two signal regions de-

fined. The first requires exactly four b -tagged track jets, two in each Higgs candidate (known as the $4b$ signal region). At high resonance masses, this requirement is inefficient, so an additional signal region requiring only three b -tagged track jets is also defined (known as the $3b$ signal region). While this has a larger background it is also more efficient for high resonance masses. For both signal regions, threshold on MV₂ score is chosen such that the algorithm is 77% efficiency in finding true b -jets[§]. Different working points were tested and this was found to be optimal. Appendix A has more details on this optimization.

Before making the requirement on X_{hh} , the masses of the Higgs candidates are corrected for semi-leptonic b decays using muons with the criteria outlined in the previous section. Any muons within a $\Delta R < 0.2$ of a b -tagged track jet have their four-momenta added to the four-momentum of the Higgs candidate. This correction does not affect the pre-selection requirements but does affect the X_{hh} requirement and the final invariant mass distribution used.

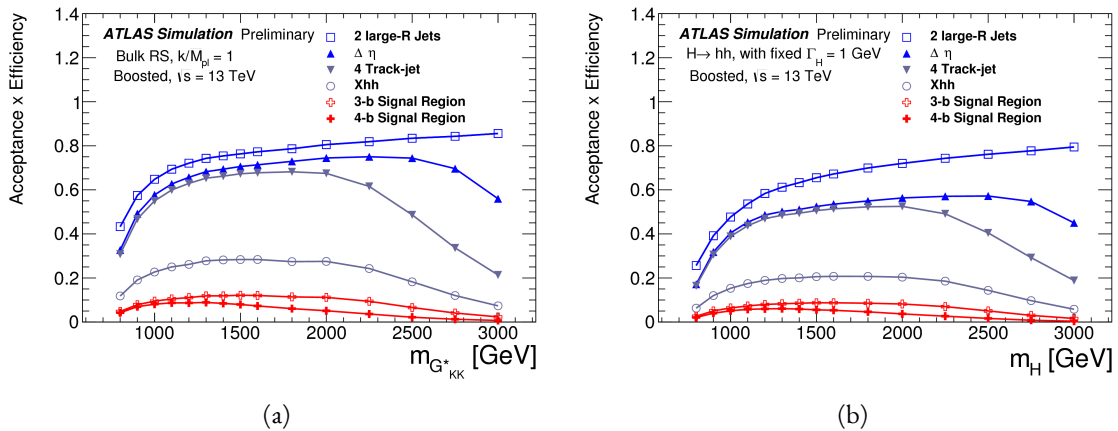


Figure 7.8: Acceptance \times efficiency as a function of mass for (a) RSG and (b) narrow heavy scalar signal models [107].

Figure 7.8 shows the product of acceptance and efficiency as a function of mass for both the RSG and narrow heavy scalar resonance signal models. After $m_X > 1$ TeV, the efficiency of the $4b$ requirement begins to decline. After $m_X > 2$ TeV, the efficiency of requiring two track jets in each Higgs candidate begins to decline as well. Both of these behaviors illustrate the difficulty of resolving the merged decay

[§]The specific MV₂ algorithm chosen is MV_{2c20}, where the fraction of charm events used in the training is 20%

2359 products at high mass. More details on the degradation of the b -tagging efficiency at high masses are
2360 shown in appendix B.

2361 Figure 7.9 shows a more detailed comparison of the signal efficiency in the $3b$ vs $4b$ signal regions for
2362 the RSG model. The efficiencies shown here are relative to all prior selection requirements.

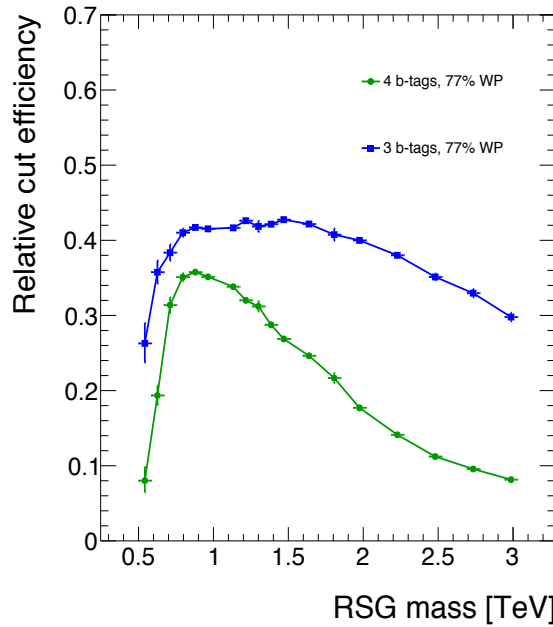


Figure 7.9: Efficiency of requiring 3 or 4 b -tagged track jets vs. RSG mass. The efficiency quoted is relative to the previous selection requirements (rather than an absolute efficiency).

2363 The final discriminating variable used in the boosted analysis is M_{2J} , the invariant mass of the two
2364 Higgs candidates. In order to improve the mass resolution, the four-momenta of each Higgs candidate
2365 are scaled by m_h/M_J . The effect of this correction is small in the boosted analysis but is done for consistency
2366 with the resolved selection.

2367 Table 7.2 shows the effect of the selection requirements on signal and background simulations as well
2368 as data.

2369 7.6 DATA-DRIVEN BACKGROUND ESTIMATION

2370 The largest background to this final state is QCD multijet production, constituting 80-90% of the total
2371 background. Because of the difficulties in modeling higher order QCD processes, this background is

Selection	Data	$m_{G_{KK}^*} = 1\text{TeV}$	$m_{G_{KK}^*} = 2\text{TeV}$	$t\bar{t}$	$Z + \text{jets}$
$N(\text{fiducial large-R jets}) \geq 2$	2202396	23.3	0.48	32345.2	4255.7
leading large-R jet $p_T > 350\text{ GeV}$	1873741	22.9	0.48	26511.7	3649.9
Both large-R jet $m > 50\text{ GeV}$	1854625	21.2	0.47	24369.8	3575.8
Both large-R jet $p_T < 1500\text{ GeV}$	1853601	21.2	0.46	24346.5	3572.9
$ \Delta\eta(JJ) < 1.7$	1435273	20.8	0.44	20751.0	3265.8
≥ 2 track-jets per large-R jet	1224727	19.8	0.40	18234.5	2692.6
$3 b\text{-tags}, X_{hh} < 1.6$	316	3.4	0.067	46.7	2.0
$4 b\text{-tags}, X_{hh} < 1.6$	20	2.9	0.030	1.4	0.0

Table 7.2: Effect of boosted selection on data, RSG signal models, $t\bar{t}$, and $Z + \text{jets}$. The numbers from simulation are normalized with the MC generator cross section and do not take into account the data driven estimates described in section 7.6 [108].

estimated with a fully data-driven method. The only other non-negligible background is $t\bar{t}$, constituting the other 10-20%. Due to the presence of $t\bar{t}$ in the sideband region where the QCD background will be estimated, the normalization of the QCD and $t\bar{t}$ backgrounds are simultaneously estimated.

7.6.1 MASS REGION DEFINITIONS

The first step in the data-driven background estimate is to define a sideband mass region where the background normalization can be derived. Additionally, a control region is defined where the background estimate can be validated. The control (CR) and sideband (SB) regions are defined using a radial distance in the two-dimensional large-R jet mass plane, R_{hh} , which is defined in equation 7.3.

$$R_{hh} = \sqrt{(M_J^{\text{lead}} - 124\text{ GeV})^2 + (M_J^{\text{sublead}} - 115\text{ GeV})^2} \quad (7.3)$$

Events in the sideband region are required to fail the signal region $X_{hh} < 1.6$ requirement and have $R_{hh} > 35.8\text{ GeV}$. The control region consists of those events which are not in the signal or sideband regions. Figure 7.10 shows the definition of the signal, control, and sideband mass regions. Table 7.3 summarizes the mass region selections for the three different regions used in the analysis.

[¶]The $Z + \text{jets}$ background is a sub-percent level contribution

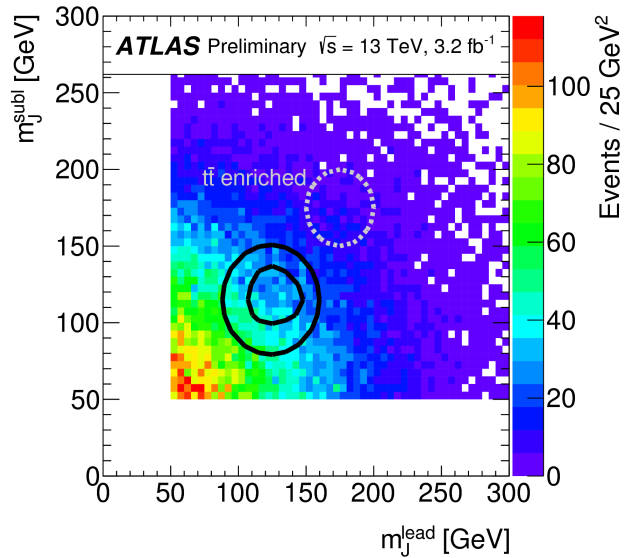


Figure 7.10: M_j^{sublead} vs. M_j^{lead} in a 2 b -tag data sample. The signal region is defined by the inner black contour ($X_{hh} < 1.6$) and the sideband region is defined by the outer contour ($R_{hh} > 35.8 \text{ GeV}$). The region between the black contours is the control region. The mass region which is enriched in $t\bar{t}$ background is also shown for illustration. [107]

Region	Requirement	Notes
Signal Region (SR)	$X_{hh} < 1.6$	-
Control Region (CR)	$R_{hh} < 35.8 \text{ GeV}$ and $X_{hh} > 1.6$	Used for validation of background estimates
Sideband Region (SB)	$R_{hh} > 35.8 \text{ GeV}$	Used to derive background normalization

Table 7.3: Mass region definitions used for background estimation

2384 7.6.2 BACKGROUND ESTIMATION

2385 The method for estimating the background in this analysis is similar to the ABCD method presented in
 2386 Chapter 5. In this case, the two handles used to define different regions for the estimate are the number
 2387 of b -tagged track jets and the mass regions. A region requiring exactly two b -tagged track jets in one large-
 2388 R jet (referred to as the 2-tag or $2b$ region) is defined for use in the background estimate. The number of
 2389 expected background events in the $3b$ and $4b$ signal regions is then given by equation 7.4.

$$N_{\text{bkg}}^{3(4)-\text{tag},\text{SR}} = \mu_{\text{Multijet}} N_{\text{Multijet}}^{2-\text{tag},\text{SR}} + \beta_{t\bar{t}} N_{t\bar{t}}^{3(4)-\text{tag},\text{SR}} + N_{Z+\text{jets}}^{3(4)-\text{tag},\text{SR}} \quad (7.4)$$

2390 In this equation, $N_{\text{bkg}}^{3(4)-\text{tag}}$ is the expected number of background events in the $3b$ or $4b$ signal regions.
 2391 $N_{\text{Multijet}}^{2-\text{tag}}$ is the number of multijet events in the 2-tag region. $N_{t\bar{t}}^{3(4)-\text{tag}}$ is the number of $t\bar{t}$ events
 2392 predicted in the MC for the $3b$ or $4b$ signal region, and the variable is similarly defined for the $Z+\text{jets}$
 2393 background. The $\beta_{t\bar{t}}$ parameter is a scale factor used to correct the normalization of the $t\bar{t}$ estimate in
 2394 the signal region. μ_{Multijet} is an extrapolation factor that is derived in the sideband region and used to
 2395 estimate the ratio of 2-tag events to 3(4)-tag events in the signal region. It is defined in equation 7.5.

$$\mu_{\text{Multijet}} = \frac{N_{\text{Multijet}}^{3(4)-\text{tag},\text{SB}}}{N_{\text{Multijet}}^{2-\text{tag},\text{SB}}} = \frac{N_{\text{data}}^{3(4)-\text{tag},\text{SB}} - \beta_{t\bar{t}} N_{t\bar{t}}^{3(4)-\text{tag},\text{SB}} - N_{Z+\text{jets}}^{3(4)-\text{tag},\text{SB}}}{N_{\text{data}}^{2-\text{tag},\text{SB}} - \beta_{t\bar{t}} N_{t\bar{t}}^{2-\text{tag},\text{SB}} - N_{Z+\text{jets}}^{2-\text{tag},\text{SB}}} \quad (7.5)$$

2396 The $t\bar{t}$ scale factor ($\beta_{t\bar{t}}$) and the QCD multijet extrapolation factor (μ_{Multijet}) are estimated together in
 2397 a simultaneous fit in the sideband region. Then, the number of events in the 2-tag signal region is used,
 2398 along with the $t\bar{t}$ estimate in the $3b$ and $4b$ signal regions and μ_{Multijet} , to estimate the total number of
 2399 background events in the two final signal regions. The shape of the final discriminant M_{2J} is also taken
 2400 from the 2-tag signal region where there are more statistics. This method is illustrated graphically in
 2401 figure 7.II.

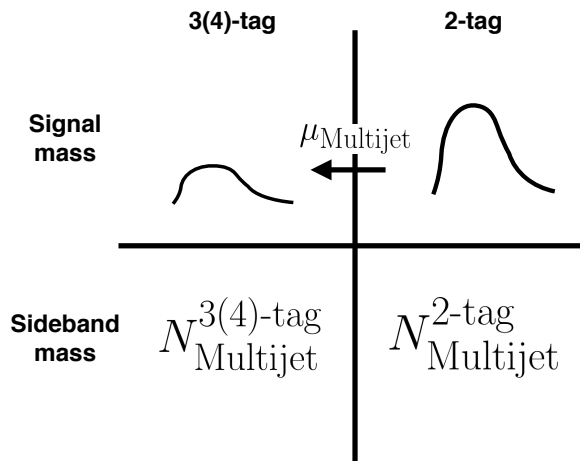


Figure 7.II: An illustration of the data-driven background estimation technique for the boosted analysis

2402 In the $3b$ region, the fit yields values of $\mu_{\text{Multijet}} = 0.160 \pm 0.03$ and $\beta_{t\bar{t}} = 1.02 \pm 0.09$. In the $4b$
 2403 region, the fit gives $\mu_{\text{Multijet}} = 0.0091 \pm 0.0007$ and $\beta_{t\bar{t}} = 0.82 \pm 0.39$. The uncertainties quoted

are statistical only. The larger uncertainties in the $4b$ values indicate the lower statistics available in that region.

Figure 7.12 shows the distributions of data and background estimates in the $3b$ and $4b$ sideband regions after the background fit has been done. The normalizations are constrained from the fit to match that of the data, but good modeling of the shape of the mass of the leading large-R jet is seen as well. The shapes of the kinematic distributions in the $4b$ region are taken from the $3b$ region due to the better MC statistics in that region.

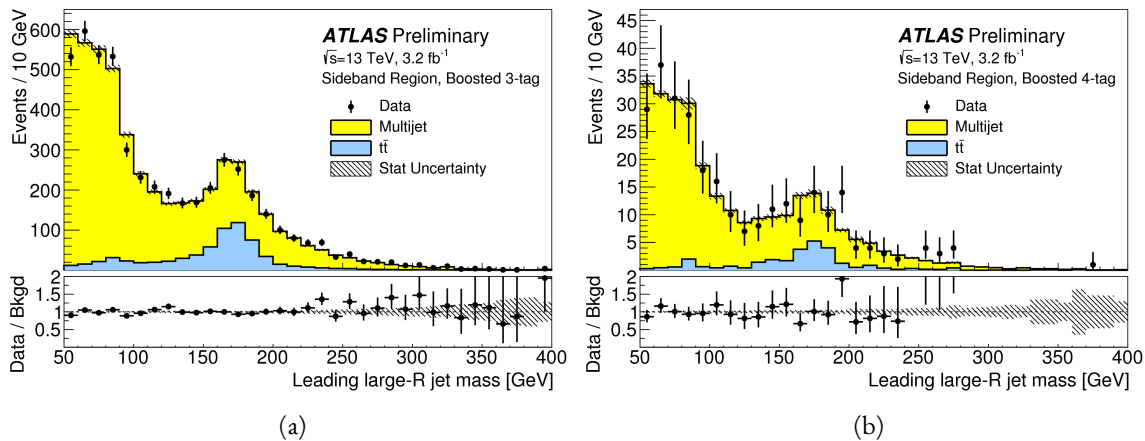


Figure 7.12: Leading large- R jet mass in the $3b$ (a) and $4b$ (b) sideband regions. The multijet and $t\bar{t}$ backgrounds are estimated using the data-driven methods described above. Because their normalizations are derived in the sideband region, the total background normalization is constrained by default to match the normalization of the data [107].

2411 7.6.3 BACKGROUND SHAPE FIT

As mentioned in the previous section, the background shape in the 3-tag and 4-tag signal regions is taken from the 2-tag signal mass region. Due to the limited statistics available, the background shapes are additionally smoothed after being extrapolated to the 3-tag and 4-tag signal regions. Only the data in the range $900 < M_{2J} < 2000$ GeV is included in the fit due to the limited statistics available above 2 TeV. Both the $t\bar{t}$ and QCD multijet background are independently fit with an exponential shape, $y = e^{ax+b}$. Other shapes are considered and used for the systematic uncertainties. Table 7.4 shows the fit values for the parameters. Because both the 3b and 4b QCD shapes come from the 2-tag region, the slopes derived

²⁴¹⁹ are very similar.

	a	b
QCD (4b)	0.00545 ± 0.00021	5.44 ± 0.24
$t\bar{t}$ (4b)	0.00746 ± 0.00021	4.88 ± 0.36
QCD (3b)	0.00545 ± 0.00021	8.30 ± 0.24
$t\bar{t}$ (3b)	0.00746 ± 0.00021	8.58 ± 0.36

Table 7.4: Parameters derived for exponential fit to background M_{2J} shape in the 3b and 4b signal regions [108]

²⁴²⁰ 7.6.4 VALIDATION OF BACKGROUND ESTIMATE

²⁴²¹ The background estimate can be validated by using the method to estimate the number of events in the
²⁴²² control mass region rather than the signal mass region. Figure 7.13 shows the M_{2J} distribution in the 3b
²⁴²³ and 4b control regions, comparing data and background estimates. In both cases, both the background
²⁴²⁴ shape and normalization are consistent with the data, indicating good agreement. The ratio of data to
²⁴²⁵ the background estimates is also fit to a line in the figure to test for any shape difference. The slope of the
²⁴²⁶ line is within 1σ (from the fit uncertainties) of flat, further indicating that the data is consistent with the
²⁴²⁷ background estimate in the control region.

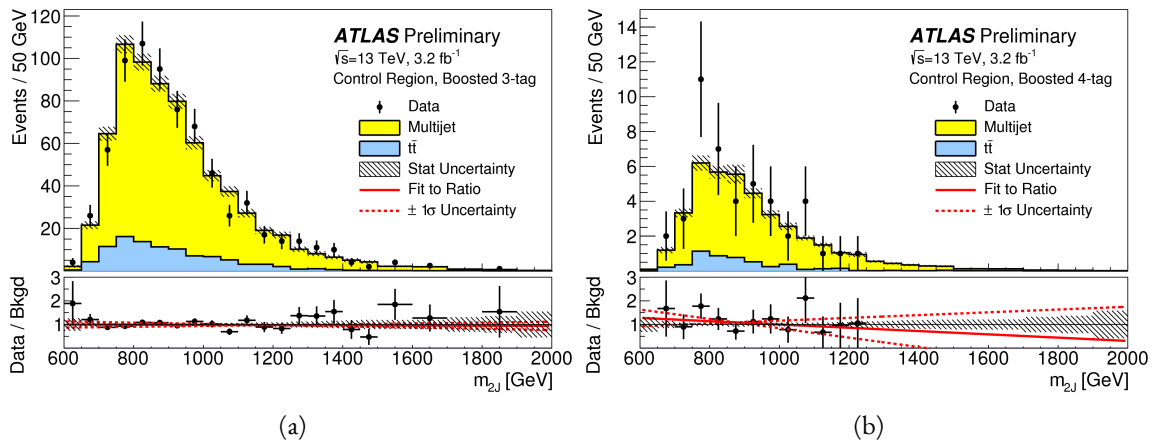


Figure 7.13: Di-jet invariant mass (M_{2J}) in the 3b (a) and 4b (b) control regions. The multijet and $t\bar{t}$ backgrounds are estimated using the data-driven methods described above [107].

²⁴²⁸ Table 7.5 shows the yields in data and background estimates in the 3-tag and 4-tag sideband and con-
²⁴²⁹ trol regions. Again, here, it can be seen that the total number of predicted background events from the

2430 data driven method is consistent with the number of data events in the region.

Sample (3-tag)	Sideband Region	Control Region
Multijet	4328 ± 27	607 ± 10
$t\bar{t}$	683.5 ± 8.1	99.6 ± 3.1
$Z+jets$	31.8 ± 3.7	7.7 ± 1.8
Total	5043 ± 28	715 ± 11
Data	5043	724
Sample (4-tag)	Sideband Region	Control Region
Multijet	247.4 ± 1.5	34.7 ± 0.6
$t\bar{t}$	28.4 ± 1.5	5.1 ± 0.7
$Z+jets$	3.4 ± 1.2	0.6 ± 0.5
Total	279.2 ± 2.5	40.3 ± 1.0
Data	279	45

Table 7.5: The number of events in data and predicted background events in the boosted 3-tag and 4-tag sideband and control regions. The uncertainties shown are statistical only. [107]

2431 **7.7 SYSTEMATIC UNCERTAINTIES**

2432 The systematic uncertainties in this analysis can be divided into two broad categories. The first type is
2433 uncertainties associated with the modeling of the signal processes. The second type of uncertainty is
2434 associated with both the shape and normalization of the background prediction.

2435 **7.7.1 SIGNAL MODELING UNCERTAINTIES**

2436 The signal modeling uncertainty has three main components: theoretical uncertainty on the acceptance,
2437 experimental uncertainties on the large-R jets, and experimental uncertainties on the track jets related to
2438 b -tagging. In this analysis the experimental uncertainties are the most significant.

2439 The first uncertainty on signal modeling is the theoretical uncertainty on the acceptance. As explained
2440 in section 5.6.1, there are four components to this uncertainty. The first is related to missing higher order
2441 terms from the matrix element calculations which is estimated by varying the QCD renormalization and

2442 factorization scales. The second is uncertainty due to the PDF set used. The third is a generator uncer-
2443 tainty which is estimated by modifying the generator used to model the underlying event and hadroniza-
2444 tion. Finally, there is an uncertainty associated with the modeling of the initial state and final state radia-
2445 tion (ISR/FSR). The total theoretical uncertainty on the signal yield is 3%, and this is dominated by the
2446 ISR/FSR modeling.

2447 There are uncertainties on the large-R jets in both the jet energy scale (JES) and jet energy resolution
2448 (JER) as well as the jet mass scale (JMS) and jet mass resolution (JMR). These are evaluated using $\sqrt{s} =$
2449 8 TeV data from Run 1 of ATLAS and extrapolated to the Run 2 beam and detector conditions using
2450 MC[¶]. The details of these uncertainties can be found in reference [109].

2451 Uncertainties on the track jets are related to the b -tagging efficiency. The total uncertainty on the sig-
2452 nal yield due to b -tagging is evaluated by propagating variations of the b -tagging efficiency through the
2453 boosted selection requirements. The uncertainties are calculated jet-by-jet and parameterized as a func-
2454 tion of b -jet p_T and η [88]. For high p_T b -jets (with $p_T > 300$ GeV), the uncertainties are extrapolated
2455 using MC simulation from the lower p_T b -jets [110].

2456 Table 7.6 shows the systematic uncertainties on the signal normalization for models with $m_{G_{KK}^*} =$
2457 1.5 TeV and both $c = 1$ and $c = 2$ as well as a narrow width heavy scalar. The dominant uncertainty
2458 comes from b -tagging and this uncertainty is larger in the 4-tag region than the 3-tag region.

2459 7.7.2 BACKGROUND UNCERTAINTIES

2460 Uncertainties on the QCD multijet background normalization and shape are estimated using the control
2461 mass region. As shown previously, the background predictions in the control region match with the
2462 data yields within the statistical uncertainty in both the 3-tag and 4-tag control regions. As an additional
2463 protection, the statistical uncertainty on the background prediction in the control region is assigned as a
2464 systematic uncertainty on the normalization of the QCD background.

2465 Additional robustness tests are done by varying the definition of the control mass region and the b -
2466 tagging requirements used to define the 2-tag sample. In all cases, the effect of the variations is found to

¶The uncertainties are correspondingly larger due to the uncertainty of this extrapolation.

Source	Background	G_{KK}^*		H
		$c = 1$	$c = 2$	
Luminosity	-	5.0	5.0	5.0
3-tag				
JER	< 1	< 1	< 1	< 1
JES	2	< 1	< 1	< 1
JMR	1	12	12	11
JMS	5	14	13	17
b -tagging	1	23	22	23
Theoretical	-	3	3	3
Multijet Normalization	3	-	-	-
Statistical	2	1	1	1
Total	7	31	30	33
4-tag				
JER	< 1	< 1	< 1	< 1
JES	< 1	< 1	< 1	< 1
JMR	4	12	13	13
JMS	5	13	13	14
b -tagging	2	36	36	36
Theoretical	-	3	3	3
Multijet Normalization	14	-	-	-
Statistical	3	1	1	1
Total	15	42	42	43

Table 7.6: Summary of systematic uncertainties in the total background and signal event yields (expressed in %) in the boosted 3-tag and 4-tag signal regions. Systematic uncertainties on the signal normalization are shown for models with $m_{G_{\text{KK}}^*} = 1.5$ TeV and both $c = 1$ and $c = 2$ as well as a narrow width heavy scalar.

2467 be within the statistical uncertainties on the background normalization in the control region.

2468 Shape uncertainties on the background are evaluated using two techniques. First, as shown in figure 7.13, the ratio between the data and background prediction is fit with a linear function. The uncertainties on the slope of this fit are assigned as shape uncertainties. An additional uncertainty is assigned by using alternate power law fit functions for the smoothing of the background shape. Table 7.7 shows the alternate shapes used. The largest difference between the nominal fit function and the alternates, taking into account the 1σ uncertainty band on each fit as well, is taken as a shape uncertainty.

Functional Form
$f_1(x) = p_0(1-x)^{p_1}x^{p_2}$
$f_2(x) = p_0(1-x)^{p_1}e^{p_2 x^2}$
$f_3(x) = p_0(1-x)^{p_1}x^{p_2}x$
$f_4(x) = p_0(1-x)^{p_1}x^{p_2}\ln x$
$f_5(x) = p_0(1-x)^{p_1}(1+x)^{p_2}x$
$f_6(x) = p_0(1-x)^{p_1}(1+x)^{p_2}\ln x$
$f_7(x) = \frac{p_0}{x}(1-x)^{p_1-p_2}\ln x$
$f_8(x) = \frac{p_0}{x^2}(1-x)^{p_1-p_2}\ln x$

Table 7.7: Alternate fit functions used to model the M_{JJ} distribution in the QCD multijet background. In the equations, $x = M_{JJ}/\sqrt{s}$.

2474 The uncertainties on the $t\bar{t}$ background are obtained by propagating the various experimental varia-
 2475 tions (JES, JER, JMS, JMR, b -tagging) through the analysis selection requirements. Table 7.6 summarizes
 2476 the background uncertainties in the 3-tag and 4-tag regions.

2477 7.8 RESULTS

2478 Table 7.8 shows the observed yields in the 3-tag and 4-tag signal regions for the boosted analysis com-
 2479 pared to the predicted number of background events. In the 3-tag region, 316 events are observed with
 2480 a predicted background of 285 ± 19 . In the 4-tag region, 20 events are observed with a predicted back-
 2481 ground of 14.6 ± 2.4 . Figure 7.14 shows the M_{JJ} distribution in the 3-tag and 4-tag regions. There are
 2482 some small excesses in the data, in particular in the 3-tag region around $M_{JJ} \approx 900$ GeV and in the
 2483 region of $1.6 < M_{JJ} < 2.0$ TeV. The significance of these excesses will be evaluated in the next chapter
 2484 in the statistical combination with the resolved results.

Sample	Signal Region (3-tag)	Signal Region (4-tag)
Multijet	235 ± 14	13.5 ± 2.4
$t\bar{t}$	48 ± 22	1.2 ± 1.0
$Z+jets$	2.0 ± 2.2	-
Total	285 ± 19	14.6 ± 2.4
Data	316	20
G_{KK}^* (1000 GeV), $c = 1$	3.4 ± 0.9	2.9 ± 1.1

Table 7.8: Observed yields in the 3-tag and 4-tag signal regions for the boosted analysis compared to the predicted number of background events Errors correspond to the total uncertainties in the predicted event yields. The yields for a graviton with $m_{G_{KK}^*} = 1$ TeV and $c = 1$ are also shown. [107]

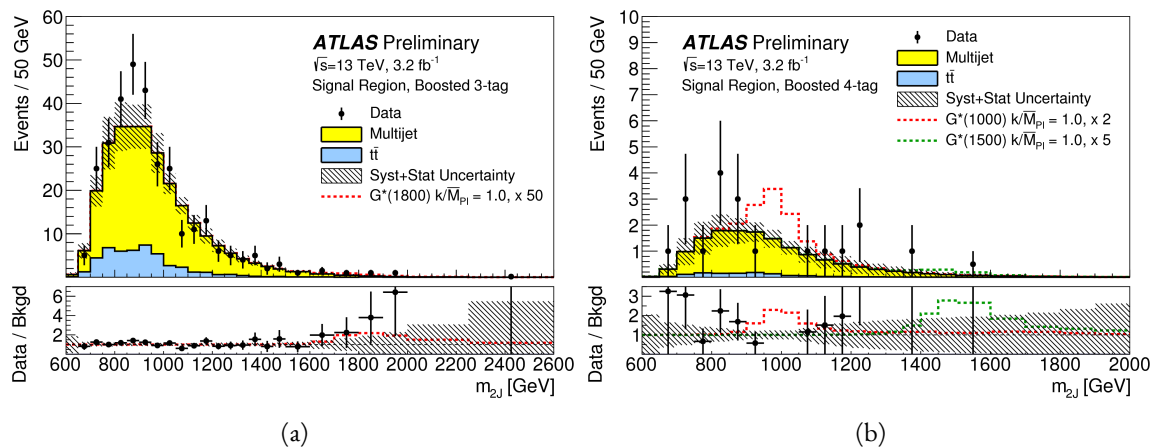


Figure 7.14: Di-jet invariant mass (M_{2J}) in the 3b (a) and 4b (b) signal regions. The multijet and $t\bar{t}$ backgrounds are estimated using the data-driven methods described above. In the 3b region, a graviton signal with $m_{G_{KK}^*} = 1.8$ TeV and $c = 1$ is overlaid, with the cross section multiplied by a factor of 50 so that the signal is visible. In the 4b region, signals with $m_{G_{KK}^*} = 1.0$ TeV and $m_{G_{KK}^*} = 1.5$ TeV are overlaid, both with $c = 1$ and the yields multiplied by factors of 2 and 5 respectively [107].

*There is no real ending. It's just the place where you stop
the story.*

Frank Herbert

8

2485

2486

Combined limits from boosted and resolved searches

2487

2488

8.1 INTRODUCTION

2489 In order to cover the full mass range of possible resonances decaying to di-Higgs final states, two distinct
2490 tailored selections were produced. The resolved selection is more sensitive in the mass range of $400 < m_X < 1100$ GeV while the boosted selection is more sensitive to masses in the range $1100 < m_X <$
2491 3000 GeV. Chapter 7 presents the details of the boosted selection and results. In setting limits on spin-2
2492 Randall-Sundrum graviton (RSG) and narrow width heavy scalar (H) models, the results of the boosted
2493 selection are combined with the results of the resolved selection to cover the full mass range.
2494

2495 This chapter presents limits on signal models resulting from the $X \rightarrow HH \rightarrow b\bar{b}b\bar{b}$ search in both
2496 the resolved and boosted selections. It first presents a brief overview of the resolved results that go into

2497 the limit setting. Then, an overview of the statistical methods used for the search and limit setting is
2498 given. Finally, limits on the RSG and heavy scalar models are presented.

2499 **8.2 RESOLVED RESULTS**

2500 The details of the resolved selection will not be presented here and can be found in reference [107]. In
2501 basic terms, the selection searches for four $R = 0.4$ b-tagged calorimeter jets (where each pair of jets is
2502 one Higgs candidate). This is distinct from the boosted methodology which searches for merged decay
2503 products. The backgrounds to the resolved selection are the same as those presented in Chapter 7 for the
2504 boosted analysis.

2505 Table 8.1 shows the results for data yields and expected background in the resolved signal region. Fig-
2506 ure 8.1 shows the M_{2J} distribution in the resolved signal region. The total number of events is consis-
2507 tent with the prediction and no significant excess is seen. One event in the boosted 4-tag signal is shared
2508 with the resolved signal region and has a mass of 852 GeV.

Sample	Signal Region Yield
Multijet	43.3 ± 2.3
$t\bar{t}$	4.3 ± 3.0
$Z + \text{jets}$	-
Total	47.6 ± 3.8
Data	46
SM hh	0.25 ± 0.07
$G_{\text{KK}}^*(800 \text{ GeV}), c = 1$	5.7 ± 1.5

Table 8.1: Observed yields in the resolve selection 4-tag signal region compared to the predicted number of back-ground events Errors correspond to the total uncertainties in the predicted event yields. The yields for a graviton with $m_{G_{\text{KK}}^*} = 800$ GeV and $c = 1$ are also shown. [107]

2509 **8.3 SEARCH TECHNIQUE AND RESULTS**

2510 The statistical technique used for the search in this analysis is the same as that used in the $H \rightarrow WW^*$
2511 analysis presented in section 3.6.2. The test statistic q_0 is used to define the p -values which measure the

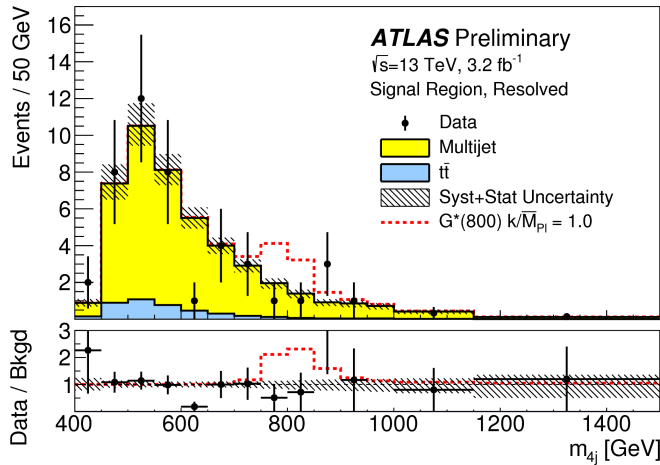


Figure 8.1: Di-jet invariant mass (M_{2J}) in the resolved signal region. A graviton signal with $m_{G_{KK}^*} = 800$ GeV and $c = 1$ is overlaid. [107].

2512 compatibility of the data with the background-only hypothesis corresponding to a signal strength $\mu =$
 2513 0.

2514 Local p_0 values are computed to quantify the probability that the background could produce a fluc-
 2515 tuation greater than or equal to the one observed in the data. In the resolved analysis, no significant ex-
 2516 cesses are observed. The largest discrepancy with respect to the background only hypothesis occurs near
 2517 a resonance mass of 900 GeV and is found to be less than 2σ in significance.

2518 In the boosted selection, the largest local excess is a broad excess in the $3b$ signal region that begins
 2519 near $M_{2J} \approx 1.7$ GeV. Assuming a G_{KK}^* with this mass and $c = 1.0$, the local significance of this excess
 2520 is 2.0σ .

2521 **8.4 LIMIT SETTING**

2522 In the absence of any significant excess observed in the data, limits on different signal models can be set.
 2523 This section describes the limit setting procedure and presents combined results of the resolved and
 2524 boosted analyses.

2525 8.4.1 LIMIT SETTING PROCEDURE

2526 The procedure used for setting exclusion limits in this analysis is the CL_s method [11]. The first step in
 2527 setting the limits is to define a test statistic which will be used. For limit setting, the test statistic is shown
 2528 in equation 8.1.

$$\widetilde{q}_\mu = \begin{cases} -2 \ln \frac{L(\mu, \hat{\theta}(\mu))}{L(0, \hat{\theta}(0))} & \hat{\mu} < 0 \\ -2 \ln \frac{L(\mu, \hat{\theta}(\mu))}{L(\hat{\mu}, \hat{\theta})} & 0 \leq \hat{\mu} < \mu \\ 0 & \hat{\mu} > \mu \end{cases} \quad (8.1)$$

2529 In the above equation, μ is the value of the signal strength under test, $\hat{\mu}$ is the best fit μ , $\hat{\theta}$ is the
 2530 best fit value of the nuisance parameters, $\hat{\theta}$ is the best fit value of the nuisance parameters under the fixed
 2531 μ value, and L is the Poisson likelihood of the data (as described in section 3.6.2).

2532 The test statistic \widetilde{q}_μ is constructed to protect against two interesting corner cases when setting the
 2533 upper limit on the cross section. First, it protects against negative signal strengths μ which are unphys-
 2534 ical. Second, it does not count excesses in the data larger than those expected by a signal strength μ as
 2535 evidence against the μ hypothesis.

2536 The CL_s statistic is constructed by taking a ratio of two probabilities. CL_{s+b} is the probability that
 2537 the signal+background hypothesis would produce a value of the test statistic that is less than or equal
 2538 to the observed value*. CL_b is the probability that the background only hypothesis will pro-
 2539 duce a value of the test statistics less than or equal to the observed. The CL_s statistic is then the ratio
 2540 $\text{CL}_{s+b}/\text{CL}_b$. A 95% upper limit on the cross section is set at the value of μ that makes the CL_s statistic
 2541 less than 5%.

2542 In practice, the limits are computed numerically within an asymptotic approximation for the distri-
 2543 bution of the test statistic \widetilde{q}_μ . The details of this approximation can be found in reference [63].

2544 The resolved and boosted analyses are combined using a very simple procedure rather than a full sta-
 2545 tistical combination. For each mass point tested, the limit which gives the most stringent constraint is
 2546 used. This means that for mass points below 1.1 TeV the resolved signal region is used, while at and

*Lower values of \widetilde{q}_μ mean better compatibility

2547 above this point the combination of the orthogonal $3b$ and $4b$ boosted signal regions is used.

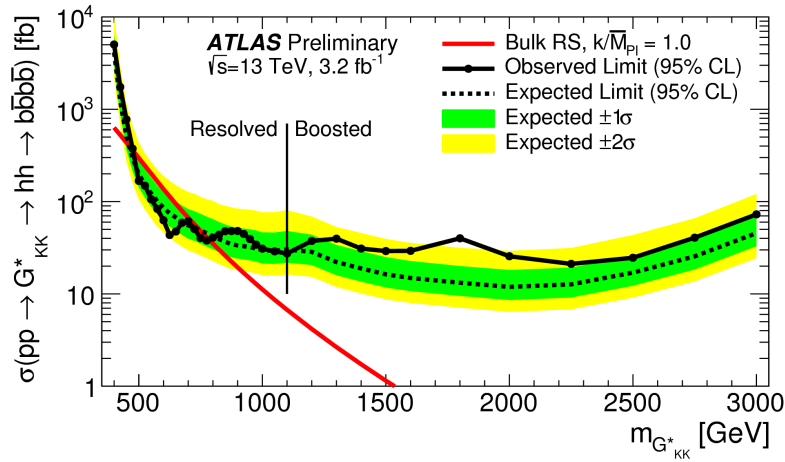
2548 **8.4.2 LIMIT SETTING RESULTS**

2549 Figure 8.2 shows the combined 95% upper bounds as a function of mass for three different models:

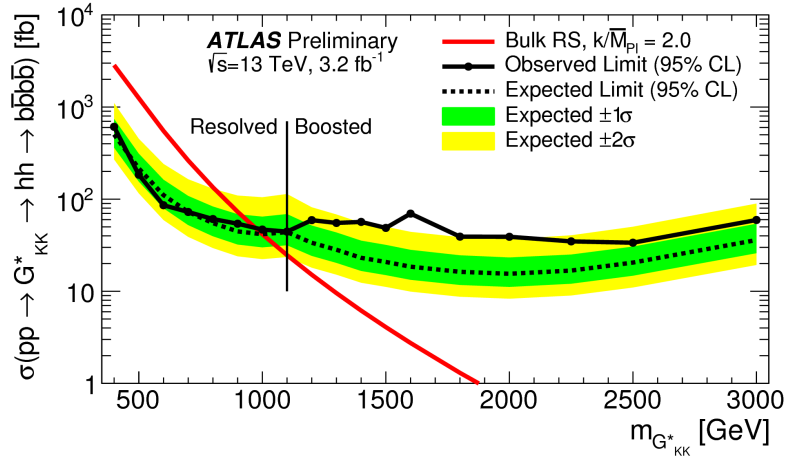
2550 G_{KK}^* with $c = 1$, G_{KK}^* with $c = 2$, and a narrow heavy scalar H .

2551 The cross section of $\sigma(pp \rightarrow G_{\text{KK}}^* \rightarrow hh \rightarrow b\bar{b}b\bar{b})$ with $c = 1$ is constrained to be less than 70 fb
2552 for masses in the range $600 < m_{G_{\text{KK}}^*} < 3000$ GeV. For the RSG model with $c = 2$, cross sections
2553 limits between 40 fb and 200 fb are set for the mass range of $500 < m_{G_{\text{KK}}^*} < 3000$ GeV. Masses in
2554 the range of $475 < m_{G_{\text{KK}}^*} < 785$ GeV are excluded with $c = 1$ (with an exclusion of the range 465
2555 to 745 GeV expected). Masses less than 980 GeV are excluded with $c = 2$ (with an exclusion for masses
2556 less than 1 TeV expected).

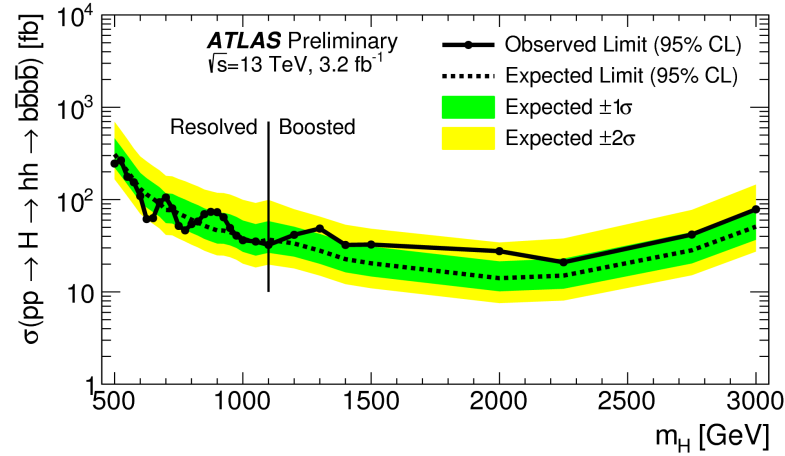
2557 In the heavy Higgs model, the cross section upper limits for $\sigma(pp \rightarrow H \rightarrow hh \rightarrow b\bar{b}b\bar{b})$ ranges from
2558 30 to 300 fb in the mass range of $500 < m_H < 3000$ GeV. The resolved analysis can also set an upper
2559 limit on the Standard Model di-Higgs production cross section discussed in chapter 3. The upper limit
2560 on $\sigma(pp \rightarrow hh \rightarrow b\bar{b}b\bar{b})$ in the Standard Model is constrained to be less than 1.22 pb.



(a) Bulk RS, $c = 1$



(b) Bulk RS, $c = 2$



(c) Spin-0 narrow-width H boson

Figure 8.2: Expected and observed upper limit as a function of mass for G^*_{KK} in the RSG model with (a) $c = 1$ and (b) $c = 2$, as well as (c) H with fixed $\Gamma_H = 1$ GeV, at the 95% confidence level in the CL_s method. [107]

2561

Part IV

2562

Looking ahead

9

2563

2564

Conclusion

2565 After being sought for many years at different collider experiments, the Higgs boson was discovered by
2566 the ATLAS and CMS experiments in 2012, confirming the leading theory for the source of electroweak
2567 symmetry breaking and filling in the last missing piece of the Standard Model. After its discovery, mea-
2568 surements of the particle's detailed properties and searches for new particles decaying to Higgs final states
2569 were both extremely important in constraining physics beyond the Standard Model. This dissertation
2570 presented this evolution through two results: the observation and measurement of the Higgs boson in
2571 the $H \rightarrow WW^* \rightarrow \ell\nu\ell\nu$ channel at $\sqrt{s} = 7$ TeV and $\sqrt{s} = 8$ TeV and a search for Higgs pair
2572 production in the $HH \rightarrow b\bar{b}b\bar{b}$ channel at $\sqrt{s} = 13$ TeV with the ATLAS detector in pp collisions at
2573 the Large Hadron Collider.

2574 In the $H \rightarrow WW^* \rightarrow \ell\nu\ell\nu$, results from both the discovery of the Higgs boson and the full
2575 ATLAS Run 1 dataset were presented. The Higgs boson was discovered with a 6.1σ significance in a
2576 combination of the $H \rightarrow \gamma\gamma$, $H \rightarrow ZZ4\ell$, $H \rightarrow WW^* \rightarrow \ell\nu\ell\nu$ with 4.2 fb^{-1} at $\sqrt{s} = 7$ TeV

and 5.2 fb^{-1} at $\sqrt{s} = 8 \text{ TeV}$. With the full 20.3 fb^{-1} at $\sqrt{s} = 8 \text{ TeV}$ and 4.2 fb^{-1} at $\sqrt{s} = 7 \text{ TeV}$, ATLAS achieved discovery level significance in the $H \rightarrow WW^*$ channel alone and obtained the first observation of vector boson fusion production in that channel. The combined signal strength is measured to be $\mu = 1.09^{+0.23}_{-0.21}$. The total observed significance of the $H \rightarrow WW^*$ process is observed to be 6.1σ (with 5.8σ expected). Advanced methods for background reduction and estimation, particularly in same-flavor lepton final states, are shown. The VBF signal strength is measured to be $\mu_{\text{VBF}} = 1.27^{+0.53}_{-0.45}$ with an observed significance of 3.2σ (with 2.7σ expected).

These results required many novel innovations. The increase of pileup interactions in the higher instantaneous luminosity LHC conditions of 2012 led to a degradation of missing transverse momentum resolution. As a result, the prominent $Z/\gamma^* + \text{jets}$ background of the same flavor $H \rightarrow WW^* \rightarrow \ell\nu\ell\nu$ final states increased greatly. New variables, including a track-based missing transverse momentum and a measurement of the balance between the dilepton system and recoiling jets, allowed for significant reduction of this background. In the VBF channel, selections were optimized to exploit the unique VBF final state topology. Incorporating these variables into a boosted decision tree technique allowed the analysis to exceed the 3σ observation threshold.

After the end of Run 1, the results of Higgs measurements from ATLAS were combined with those from CMS to produce the most precise measurements of the Higgs boson so far [112]. Figure 9.1 shows the combination of ATLAS and CMS data for the Higgs signal strength in and coupling measurements. In the signal strength measurements of gluon fusion and vector boson fusion, the $H \rightarrow WW^*$ channel provides the tightest constraints. Additionally, the Higgs coupling to W bosons is the most precisely measured with a relative uncertainty of 10%.

With the discovery of the Higgs firmly established and its properties measured, a natural next step was to search for new physics with Higgs final states. At $\sqrt{s} = 13 \text{ TeV}$, a search for Higgs pair production in the $b\bar{b}b\bar{b}$ final state with 3.2 fb^{-1} was conducted. A signal region optimized for the boosted final states arising from high mass resonances was constructed. This signal region utilized large-radius calorimeter jets and b -tagging with small radius track jets to maximize the signal acceptance. No significant excesses were observed, and upper limits on cross sections are placed for spin-2 Randall Sun-

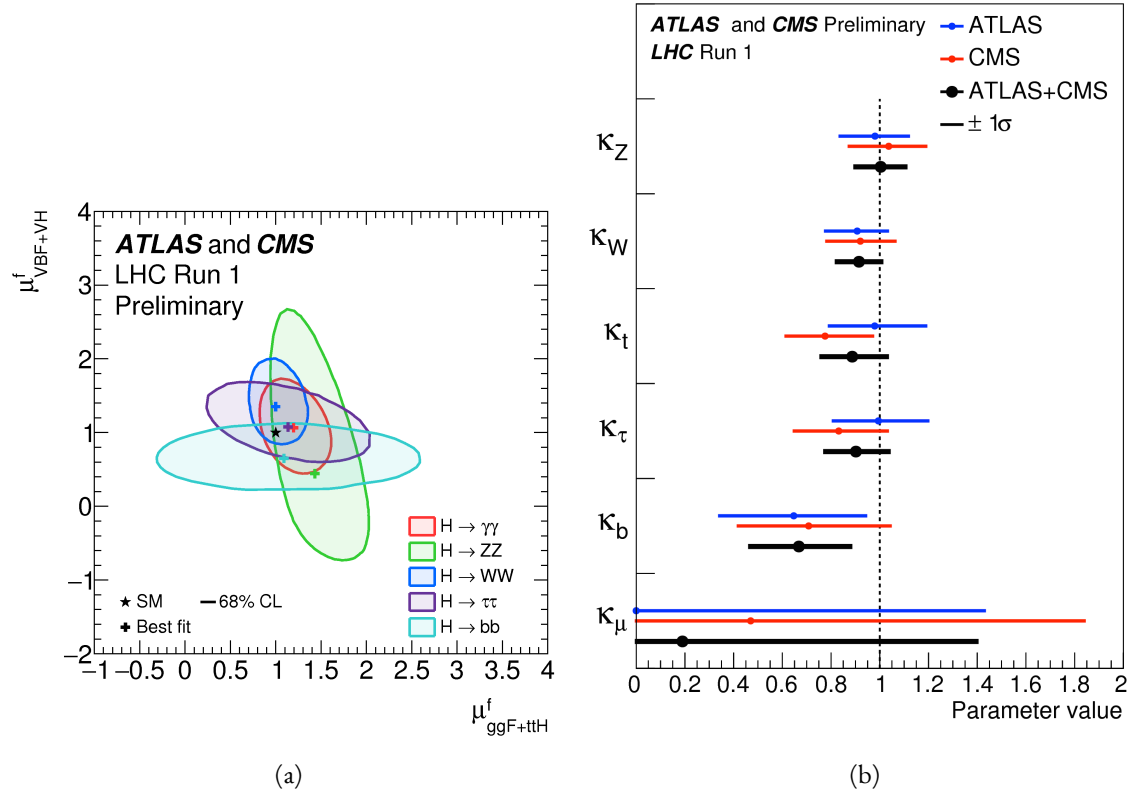


Figure 9.1: Combined ATLAS and CMS measurements in Run 1 for (a) Higgs signal strength in gluon fusion and VBF and (b) Higgs couplings normalized to their SM predictions

drum gravitons (RSG) and narrow spin-0 resonances. The increase in center of mass energy in Run 2 allowed this analysis to extend upper limits up to 3 TeV, while previous results from ATLAS in Run 1 only quotes limits up to 2 TeV. The cross section of $\sigma(pp \rightarrow G_{KK}^* \rightarrow hh \rightarrow b\bar{b}b\bar{b})$ with $k/\bar{M}_{\text{Pl}} = 1$ is constrained to be less than 70 fb for masses in the range $600 < m_{G_{KK}^*} < 3000$ GeV. For the RSG model with $k/\bar{M}_{\text{Pl}} = 2$, cross sections limits between 40 fb and 200 fb are set for the mass range of $500 < m_{G_{KK}^*} < 3000$ GeV. The cross section upper limits for $\sigma(pp \rightarrow H \rightarrow hh \rightarrow b\bar{b}b\bar{b})$ ranges from 30 to 300 fb in the mass range of $500 < m_H < 3000$ GeV.

While there has been a rigorous program of measurements and searches involving the Higgs, there is still much room for improvement at the High Luminosity LHC (HL-LHC) and beyond. The measured signal strength for VBF production in $H \rightarrow WW^*$ still has a relative error at the level of 40%, largely dominated by statistical uncertainty. Projections for the HL-LHC show that the uncertainty on the VBF signal strength can be reduced to approximately 15% with 3000 fb^{-1} [113, 114]. This uncertainty

2616 also assumes that theoretical uncertainties on the signal, which would be the largest contribution in this
 2617 dataset, remain as they are now. Improvements in the theoretical understanding of the Higgs signal
 2618 would also reduce the signal strength uncertainty dramatically. Such precision measurements allow for
 2619 measurements of the Higgs coupling to vector bosons precise to the few percent level, therefore giving
 2620 much power to constrain or discover new physics.

2621 The prospects for detection of resonant di-Higgs production at the HL-LHC are also quite promising.
 2622 Figure 9.2 shows projections for the discovery significance of RSG signals at the HL-LHC in the
 2623 $X \rightarrow HH \rightarrow b\bar{b}b\bar{b}$ search [114]. In all detector budget scenarios, a 1.5 TeV resonance is above or near
 2624 5σ significance, while a 2 TeV resonance is between 4-5 σ except for the lowest budget.

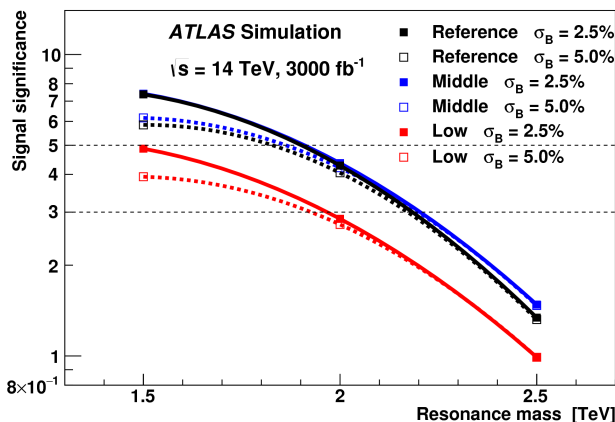


Figure 9.2: Discovery significance for RSG models at the HL-LHC in three different budget scenarios [114].
 Systematic uncertainties on the background prediction (σ_B) of 2.5% and 5.0% are both tested.

2625 The Higgs will continue to be an incredibly powerful tool in the understanding of nature at the HL-
 2626 LHC and beyond. Through both precision measurements and searches, the nature of electroweak sym-
 2627 metry breaking will be better understood and the potential for the discovery of physics beyond the Stan-
 2628 dard Model has never been greater.

A

2629

2630

Optimization of b -tagging working point in

2631

$X \rightarrow HH \rightarrow b\bar{b}b\bar{b}$ search

2632 To the $3b$ and $4b$ signal regions in the boosted $X \rightarrow HH \rightarrow b\bar{b}b\bar{b}$ search, the MV₂ algorithm with a
2633 20% fraction of charm events in training is used (MV_{2c20}). Once the algorithm is selected, an efficiency
2634 working point must also be chosen. This working point defines the efficiency with which true b -jets
2635 are tagged and also fixes the overall background rejection of the algorithm. Higher efficiency working
2636 points accept more true b -jets but also allow for more background. Five different working points (70%,
2637 77%, 80%, 85%, 90%) are tested. With each working point, the full data driven background estimation
2638 method is run to quantify the amount of background that will be present in the final signal region. The
2639 significance is quantified using the median discovery significance for signal and background with Poisson

2640 errors, given in equation A.1 [115].

$$Z = \sqrt{2 \left((s + b) \ln \left(1 + \frac{s}{b} \right) - s \right)} \quad (\text{A.1})$$

2641 Note that in the limit where s is much smaller than b , this equation reduces to the more well known
 2642 s/\sqrt{b} .

2643 Figure A.1 shows the estimated significance as a function of signal mass in RSG $c = 1$ models for
 2644 the $3b$ and $4b$ signal regions. The 77% working point gives the best performance over a wide range of
 2645 masses in the $4b$ signal region. As this is the region which contributes the most to the total discovery
 2646 significance, the 77% efficiency working point is chosen for the analysis.

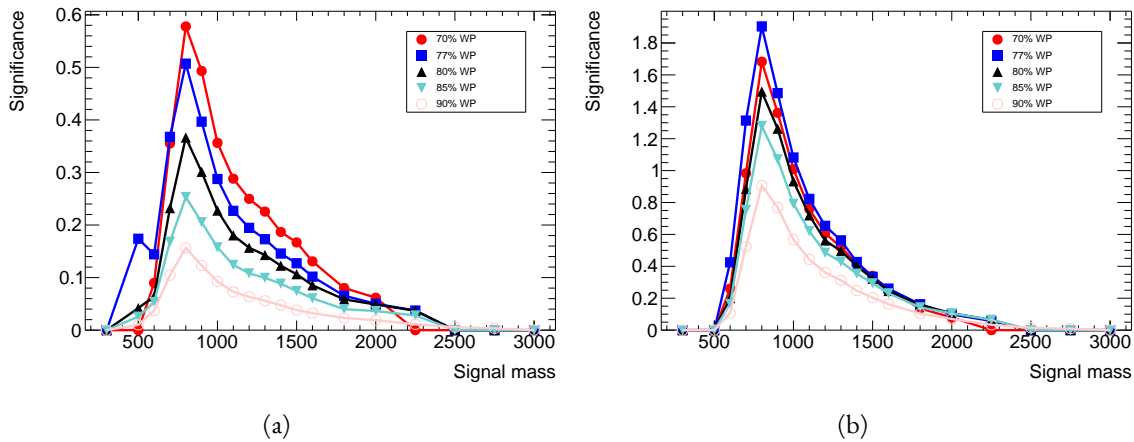


Figure A.1: Estimated significance as a function of signal mass for RSG $c = 1$ models in the $3b$ (a) and $4b$ (b) regions for different b -tagging efficiency working points

B

2647

2648

b-tagging performance at high p_T

2649 One of the limiting factors of the signal acceptance in the *FourB full* search at high resonance masses is
2650 the degradation of the *b*-tagging efficiency for high p_T jets. This appendix presents a study of the under-
2651 lying causes of this degradation.

2652 B.I MV₂ ALGORITHM OVERVIEW

2653 The MV₂ algorithm is a boosted decision tree incorporating twenty-four input variables constructed
2654 from three lower level input algorithms: IPxD, SVI, and JetFitter. IPxD uses the two and three dimen-
2655 sional impact parameter information of tracks in the jet to construct templates for light, charm, and bot-
2656 tom quarks and compute likelihood ratios. SVI is a secondary vertex reconstruction algorithm. JetFitter
2657 attempts to fit to the full decay chain of the *B* hadron, looking for multiple decay vertices aligned along a
2658 single axis. Figure B.I summarizes the inputs to MV₂.

IP2D and IP3D (6 inputs)	SV1 (8 inputs)	JetFitter (8 inputs)
$\log(p_b/p_u)$	Mass	Mass
$\log(p_b/p_c)$	Energy fraction	Energy fraction
$\log(p_c/p_u)$	# tracks at vertex	# vertices
	# 2 track vertices	# tracks at vertex
	Lxy	# 1 track vertices
	L3d	# 2 track vertices
	3D significance	3D significance
	ΔR	ΔR
Kinematics (2 inputs)		
	p_T	
	η	

Figure B.1: Summary of the inputs to the MV2 b -tagging algorithm

2659 **B.2 CHANGES IN MV2 SCORE AT HIGH p_T**

2660 The degradation of b -tagging at high p_T was studied in particular in the context of RSG models at high
 2661 mass. Figure B.2 shows the p_T of the leading track jet inside of the leading calorimeter jet in RSG events.
 2662 At high $m_{G_K^*}$, the p_T spectrum of track jets is much harder than at lower masses due to the increased
 2663 Higgs p_T .

2664 Figure B.3 shows the MV2c2o algorithm score for the leading and subleading track jets inside of the
 2665 leading calorimeter jet. In both cases, it can be seen that at higher RSG masses the MV2 score shifts to-
 2666 wards more background like (negative) values. Additionally, this effect is more pronounced in the lead-
 2667 ing track jet than the subleading.

2668 To understand what is causing this change in the MV2c2o score, the same comparisons can be made
 2669 for the input variables of MV2c2o. The focus in these comparisons will be on the leading track jet as
 2670 this is the one seen to have the largest difference in MV2 score. Figure B.4 shows the log likelihood ratio
 2671 $\log(p_b/p_u)$ from the IP3D (three dimensional impact parameter) algorithm. At higher masses, the IP3D
 2672 likelihood ratio distribution does become more background-like.

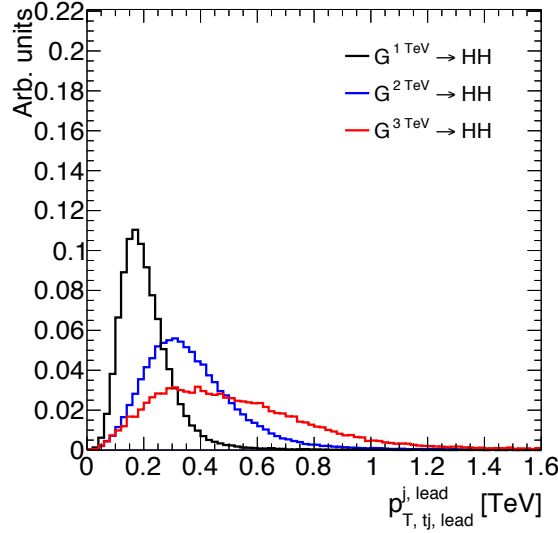


Figure B.2: p_T of the leading track jet in the leading calorimeter jet for different signal masses in RSG $c = 1$ models

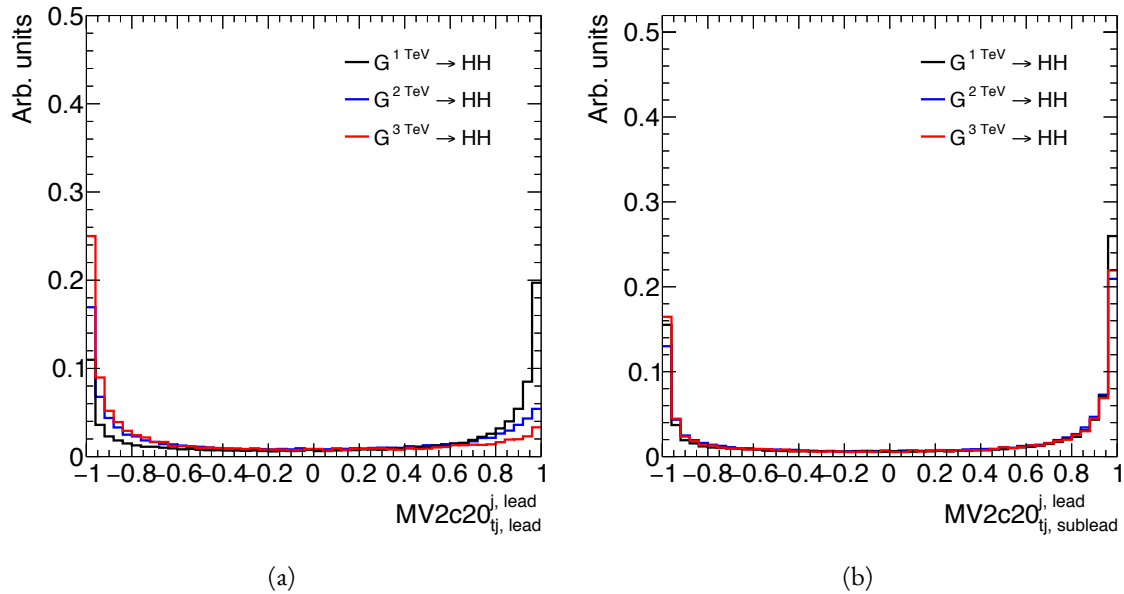


Figure B.3: MV2c20 score for the leading track jet (a) and subleading track jet (b) of the leading calorimeter jet for different signal masses in RSG $c = 1$ models

Figure B.5 shows the mass and number of tracks at the secondary vertex computed by the SV1 algorithm. When there is no secondary vertex found, the algorithm assigns a default negative value for these quantities. Both of these distributions show that there is a significantly larger fraction of jets where no secondary vertex is found in the high mass samples compared to the $m_{G_{KK}^*} = 1$ TeV sample. The SV1

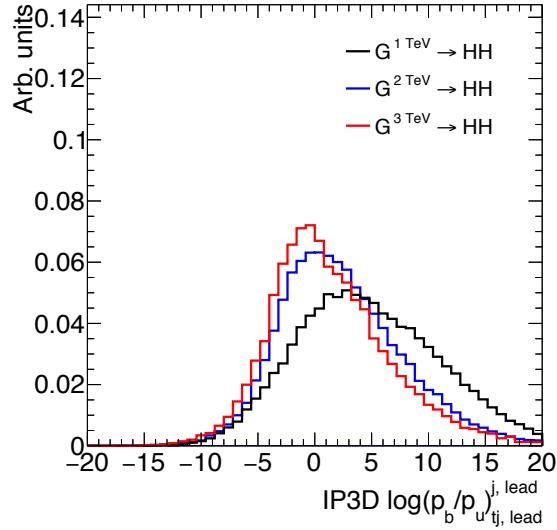


Figure B.4: IP3D log-likehood ratio ($\log(p_b/p_u)$) of the leading track jet in the leading calorimeter jet for different signal masses in RSG $c = 1$ models

algorithm's inability to find a secondary vertex could be an important factor in the overall MV₂ score shift, as this eliminates eight of the input variables that would normally contribute information to the algorithm.

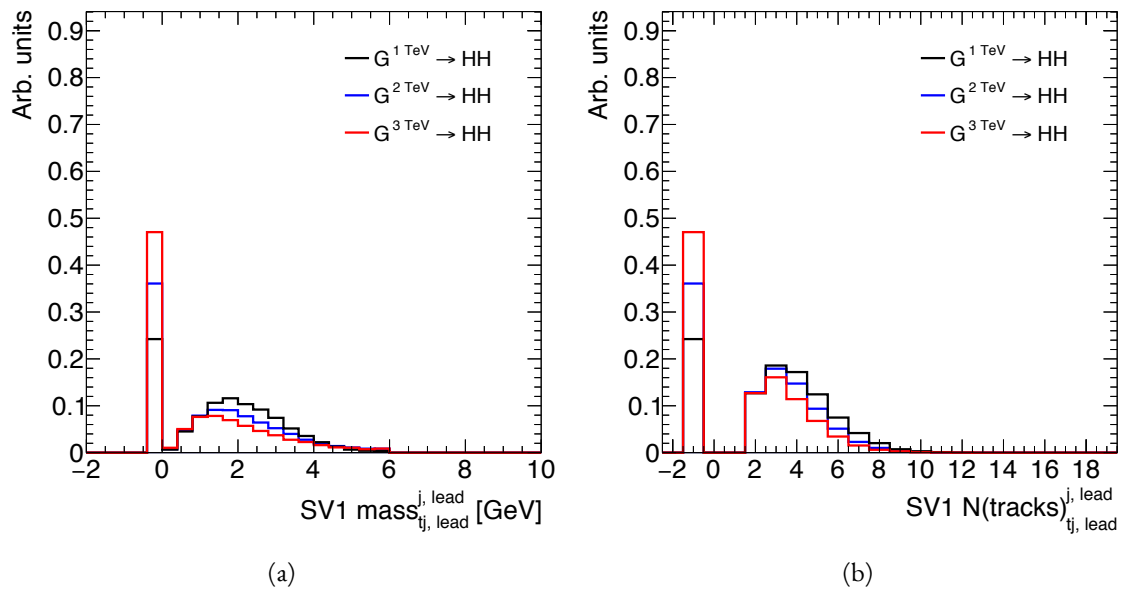


Figure B.5: Mass (a) and number of tracks (b) for the secondary vertices computed with the SV1 algorithm. When no secondary vertex is found, the quantities are assigned to default negative values.

2680 Figure B.6 shows the same quantities for the JetFitter algorithm. In this case, there is also a change in
 2681 the fraction of jets which have their secondary vertices successfully reconstructed, but this change is not
 2682 as drastic as that seen in SVI. There is also an increase in the number of jets which have high values of
 2683 mass.

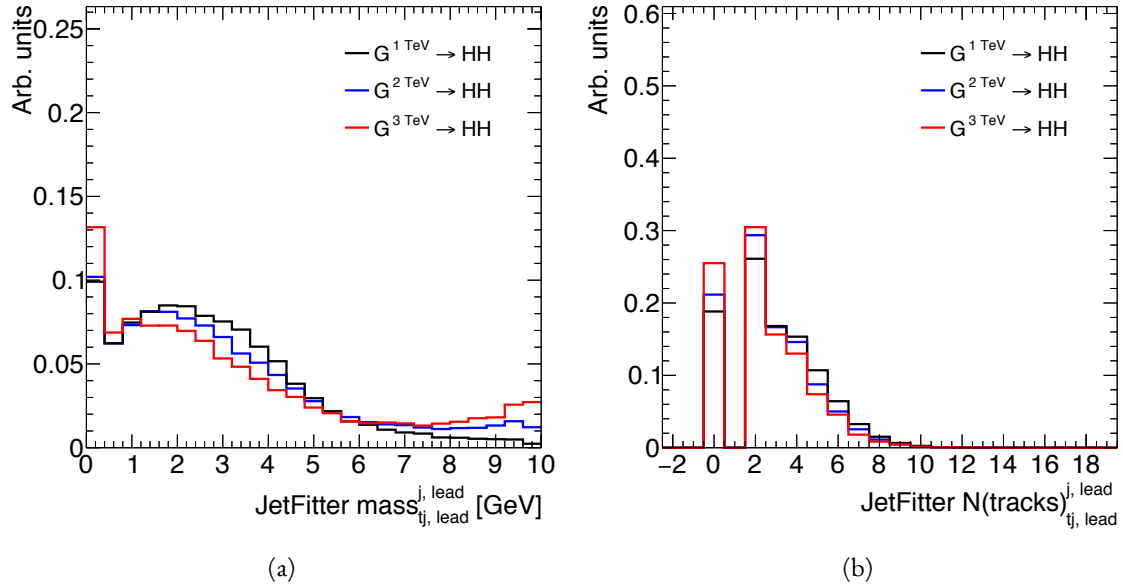


Figure B.6: Mass (a) and number of tracks (b) for vertices computed with the JetFitter algorithm. When no vertices are found, the quantities are assigned to default negative values.

2684 B.3 TAGGING EFFICIENCY BY INDIVIDUAL JET

2685 In the last section, the largest changes in MV₂ score were seen for the leading track jet inside the leading
 2686 calorimeter jet. To confirm that the overall 4*b* tagging efficiency is indeed degrading because of degra-
 2687 dation of the leading track jet efficiency, the tagging efficiency for each individual jet as a function of mass
 2688 can be compared. This is shown in figure B.7. The figure shows that the leading jet tagging efficiency
 2689 in both calorimeter jets degrades heavily, while the sub-lead jet tagging efficiency remains relatively con-
 2690 stant.

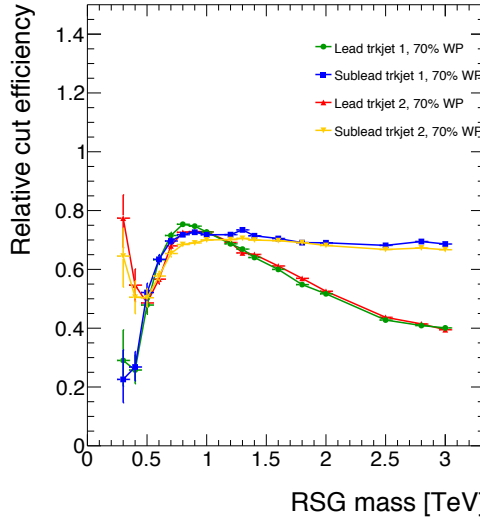


Figure B.7: MV₂c20 b -tagging efficiency for each of the four track jets in the boosted 4 b selection as a function of RSG mass for $c = 1$ models.

2691 **B.4 EFFECT OF MULTIPLE b -QUARKS INSIDE ONE JET**

2692 One hypothesis for why the efficiency of b -tagging the leading track jet degrades is that at high masses,
2693 the b quarks get close enough together that both of them are inside of the leading track jet. Because MV₂
2694 is not tuned for tagging multiple b quarks inside one jet, the tagging efficiency could degrade. Figure B.8
2695 shows MV₂ scores and SV₁ mass for cases where there are two b quarks at truth level within the radius
2696 of the leading track jet compared to cases where there is only one true b^* . This figure suggests that the
2697 presence of two b -quarks inside the leading jet is not the cause of the degradation in efficiency. There is a
2698 change in the shape of the MV₂ score distribution, but it is not nearly as pronounced as that seen in B.3
2699 at higher masses. Additionally, the fraction of jets with no secondary vertex found is nearly identical in
2700 the track jets with two truth b -quarks.

*When two truth b quarks are required in the leading jet, the subleading jet is required to have zero. When one is required for the leading, one is also required for the subleading.

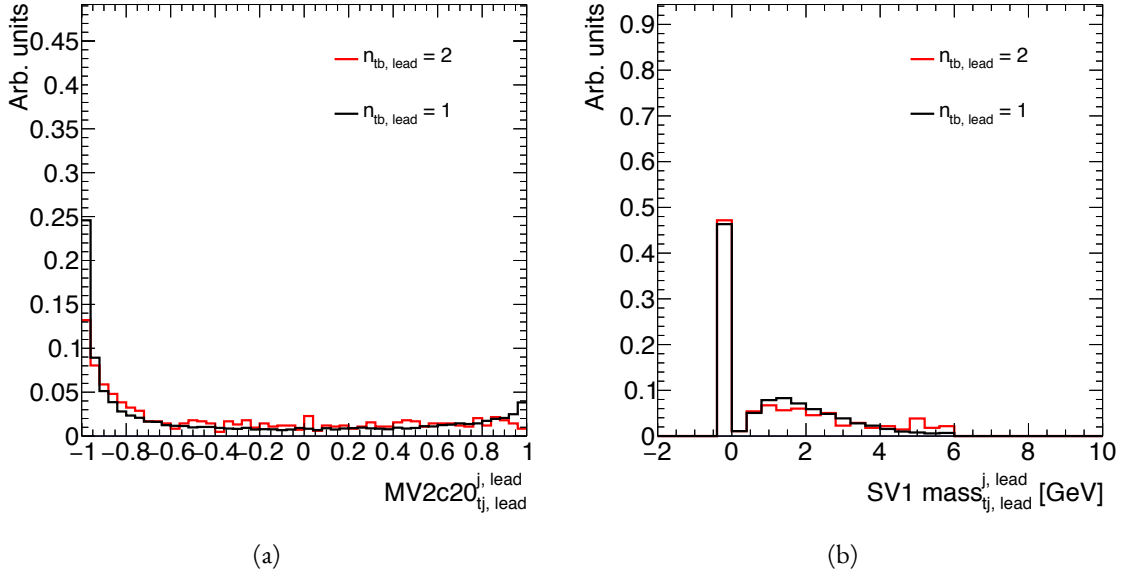


Figure B.8: MV2c20 score (a) and SV1 mass (b) for leading track jets with two truth b quarks ($n_{tb, \text{lead}} = 2$) compared to those with only one truth b ($n_{tb, \text{lead}} = 1$).

2701 B.5 CHANGES IN TRACK QUALITY AT HIGH p_T

2702 Another hypothesis for the degradation of the b -tagging efficiency is a decrease in track quality for high
 2703 p_T b jets. One way to check the overall quality of the tracking inside the jet is to investigate quantities
 2704 related to the leading track inside of the track jet. Figure B.9 shows the fit χ^2/n_{DOF} and number of hits
 2705 in the pixel detector for the leading track of the leading track jet. In both cases, the figure shows that in
 2706 higher mass samples, the quality of the leading track inside of the track jet degrades substantially. The
 2707 fit quality is lessened and the tracks have less hits in the pixel detector. This is likely due to the fact that
 2708 at higher p_T , the B -hadron will sometimes live long enough to miss the IBL and first pixel layer, thus
 2709 decreasing the number of hits on the track.

2710 To check whether this is the cause for the shift in the MV2 score and the higher difficulty in recon-
 2711 structing secondary vertices, jets whose leading track have at least four pixel hits are compared with those
 2712 whose tracks have less than four pixel hits. The results for the MV2 score and SV1 mass are shown in fig-
 2713 ure B.10. Track jets where the leading track does not have at least four pixel hits are more likely to not
 2714 have a secondary vertex reconstructed. Additionally, their MV2c20 score is shifted more significantly to

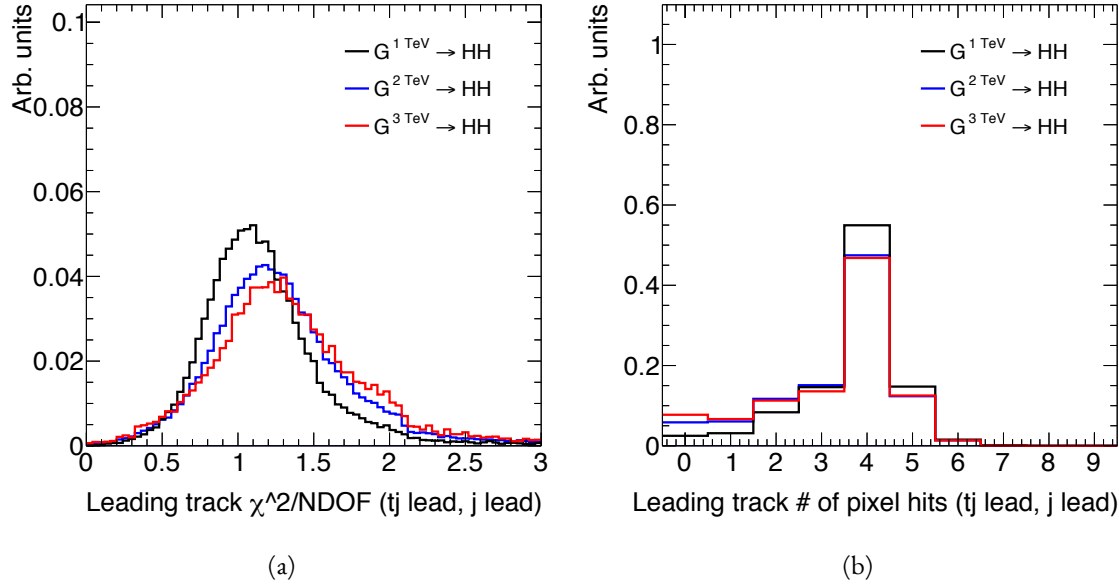


Figure B.9: Track fit χ^2/n_{DOF} (a) and number of pixel detector hits (b) for the leading track of the leading track jet in different mass RSG $c = 1$ samples

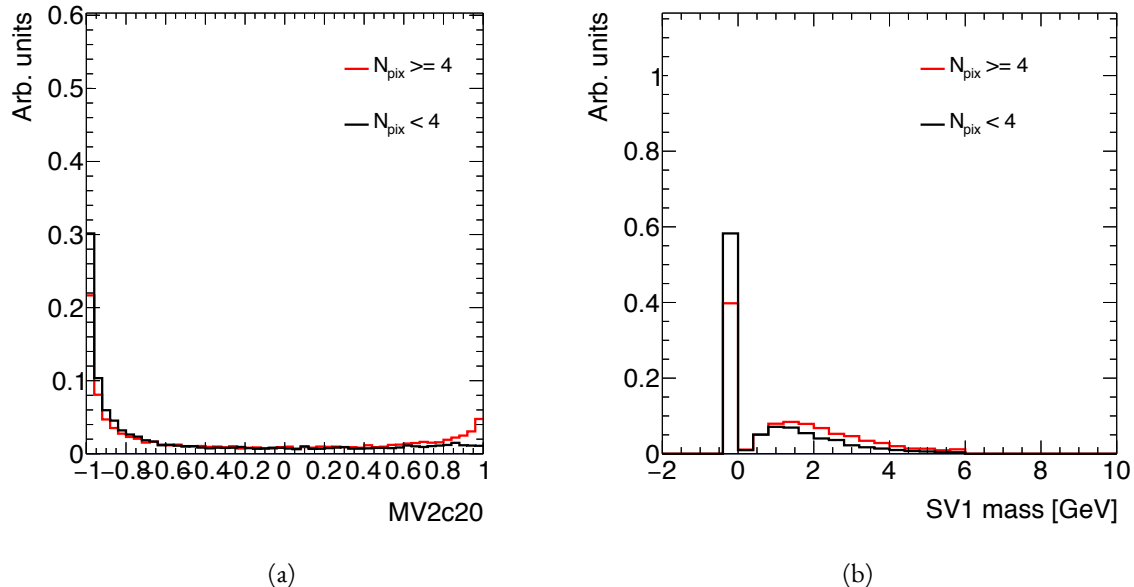


Figure B.10: MV2c20 score (a) and SV1 mass (b) for leading track jets whose leading track jet has at least four pixel hits ($N_{\text{pix}} \geq 4$) compared to those which do not ($N_{\text{pix}} < 4$).

²⁷¹⁵ background-like values. This seems to confirm the hypothesis that degrading track quality is responsible
²⁷¹⁶ for the lowered b -tagging efficiency at high p_{T} .

References

2717

- 2718 [1] Georges Aad et al. Observation of a new particle in the search for the Standard Model Higgs
2719 boson with the ATLAS detector at the LHC. *Phys. Lett.*, B716:1–29, 2012. doi: 10.1016/j.physletb.
2720 2012.08.020.
- 2721 [2] Serguei Chatrchyan et al. Observation of a new boson at a mass of 125 GeV with the CMS experi-
2722 ment at the LHC. *Phys. Lett.*, B716:30–61, 2012. doi: 10.1016/j.physletb.2012.08.021.
- 2723 [3] David Griffiths. *Introduction to elementary particles*. 2008.
- 2724 [4] F. Halzen and Alan D. Martin. *QUARKS AND LEPTONS: AN INTRODUCTORY*
2725 *COURSE IN MODERN PARTICLE PHYSICS*. 1984. ISBN 0471887412, 9780471887416.
- 2726 [5] Christopher G. Tully. *Elementary particle physics in a nutshell*. 2011.
- 2727 [6] K. A. Olive et al. Review of Particle Physics. *Chin. Phys.*, C38:090001, 2014. doi: 10.1088/
2728 1674-1137/38/9/090001.
- 2729 [7] Matthew D. Schwartz. *Quantum Field Theory and the Standard Model*. Cambridge University
2730 Press, 2014. ISBN 1107034736, 9781107034730. URL <http://www.cambridge.org/us/academic/subjects/physics/theoretical-physics-and-mathematical-physics/quantum-field-theory-and-standard-model>.
- 2731 [8] S. Dawson. Introduction to electroweak symmetry breaking. In *High energy physics and cos-
2732 mology. Proceedings, Summer School, Trieste, Italy, June 29-July 17, 1998*, pages 1–83, 1998. URL
2733 <http://alice.cern.ch/format/showfull?sysnb=0301862>.
- 2734 [9] S. L. Glashow. Partial Symmetries of Weak Interactions. *Nucl. Phys.*, 22:579–588, 1961. doi:
2735 10.1016/0029-5582(61)90469-2.
- 2736 [10] Steven Weinberg. A Model of Leptons. *Phys. Rev. Lett.*, 19:1264–1266, 1967. doi: 10.1103/
2737 PhysRevLett.19.1264.
- 2738 [11] A. Salam. *Elementary Particle Theory*. Almqvist and Wiksell, Stockholm, 1968.
- 2739 [12] J. Iliopoulos S.L. Glashow and L. Maiani. *D2:1285*, 1970.
- 2740 [13] R. Keith Ellis, W. James Stirling, and B. R. Webber. QCD and collider physics. *Camb. Monogr.
2741 Part. Phys. Nucl. Phys. Cosmol.*, 8:1–435, 1996.

- 2744 [14] P. W. Higgs. Broken symmetries and the masses of gauge bosons. *13*:508, 1964.
- 2745 [15] P. W. Higgs. Spontaneous symmetry breakdown without massless bosons. *145*:1156, 1966.
- 2746 [16] F. Englert and R. Brout. Broken symmetry and the mass of gauge vector mesons. *13*:321, 1964.
- 2747 [17] G. S. Guralnik, C. R. Hagen, and T. W. .B. Kibble. Global conservation laws and massless parti-
2748 cles. *Phys. Rev. Lett.*, *13*:585, 1964. doi: [10.1103/PhysRevLett.13.585](https://doi.org/10.1103/PhysRevLett.13.585).
- 2749 [18] LHC Higgs Cross Section Working Group, S. Heinemeyer, C. Mariotti, G. Passarino, and
2750 R. Tanaka (Eds.). Handbook of LHC Higgs Cross Sections: 3, Higgs Properties. 2013.
- 2751 [19] J. Baglio, A. Djouadi, R. Gröber, M. M. Mühlleitner, J. Quevillon, and M. Spira. The mea-
2752 surement of the Higgs self-coupling at the LHC: theoretical status. *JHEP*, *04*:151, 2013. doi:
2753 [10.1007/JHEP04\(2013\)151](https://doi.org/10.1007/JHEP04(2013)151).
- 2754 [20] Matthew J. Dolan, Christoph Englert, and Michael Spannowsky. New Physics in LHC Higgs
2755 boson pair production. *Phys. Rev.*, *D87*(5):055002, 2013. doi: [10.1103/PhysRevD.87.055002](https://doi.org/10.1103/PhysRevD.87.055002).
- 2756 [21] Roberto Contino, Margherita Ghezzi, Mauro Moretti, Giuliano Panico, Fulvio Piccinini, and
2757 Andrea Wulzer. Anomalous Couplings in Double Higgs Production. *JHEP*, *08*:154, 2012. doi:
2758 [10.1007/JHEP08\(2012\)154](https://doi.org/10.1007/JHEP08(2012)154).
- 2759 [22] R. Grober and M. Mühlleitner. Composite Higgs Boson Pair Production at the LHC. *JHEP*, *06*:
2760 020, 2011. doi: [10.1007/JHEP06\(2011\)020](https://doi.org/10.1007/JHEP06(2011)020).
- 2761 [23] Lisa Randall and Raman Sundrum. A Large mass hierarchy from a small extra dimension. *Phys.*
2762 *Rev. Lett.*, *83*:3370–3373, 1999. doi: [10.1103/PhysRevLett.83.3370](https://doi.org/10.1103/PhysRevLett.83.3370).
- 2763 [24] Kaustubh Agashe, Hooman Davoudiasl, Gilad Perez, and Amarjit Soni. Warped Gravitons at the
2764 LHC and Beyond. *Phys. Rev.*, *D76*:036006, 2007. doi: [10.1103/PhysRevD.76.036006](https://doi.org/10.1103/PhysRevD.76.036006).
- 2765 [25] A. Liam Fitzpatrick, Jared Kaplan, Lisa Randall, and Lian-Tao Wang. Searching for the Kaluza-
2766 Klein Graviton in Bulk RS Models. *JHEP*, *09*:013, 2007. doi: [10.1088/1126-6708/2007/09/013](https://doi.org/10.1088/1126-6708/2007/09/013).
- 2767 [26] Julien Baglio, Otto Eberhardt, Ulrich Nierste, and Martin Wiebusch. Benchmarks for Higgs Pair
2768 Production and Heavy Higgs boson Searches in the Two-Higgs-Doublet Model of Type II. *Phys.*
2769 *Rev.*, *D90*(1):015008, 2014. doi: [10.1103/PhysRevD.90.015008](https://doi.org/10.1103/PhysRevD.90.015008).
- 2770 [27] G. C. Branco, P. M. Ferreira, L. Lavoura, M. N. Rebelo, Marc Sher, and Joao P. Silva. Theory
2771 and phenomenology of two-Higgs-doublet models. *Phys. Rept.*, *516*:1–102, 2012. doi: [10.1016/j.physrep.2012.02.002](https://doi.org/10.1016/j.physrep.2012.02.002).
- 2773 [28] Howard E. Haber and Oscar Stål. New LHC benchmarks for the \mathcal{CP} -conserving two-Higgs-
2774 doublet model. *Eur. Phys. J.*, *C75*(10):491, 2015. doi: [10.1140/epjc/s10052-015-3697-x](https://doi.org/10.1140/epjc/s10052-015-3697-x).

- 2775 [29] Jose M. No and Michael Ramsey-Musolf. Probing the Higgs Portal at the LHC Through Resonant di-Higgs Production. *Phys. Rev.*, D89(9):095031, 2014. doi: 10.1103/PhysRevD.89.095031.
- 2776
- 2777 [30] Johan Alwall, Michel Herquet, Fabio Maltoni, Olivier Mattelaer, and Tim Stelzer. MadGraph 5: Going Beyond. *JHEP*, 1106:128, 2011. doi: 10.1007/JHEP06(2011)128.
- 2778
- 2779 [31] Lyndon R Evans and Philip Bryant. LHC Machine. *J. Instrum.*, 3:S08001. 164 p, 2008. URL <https://cds.cern.ch/record/1129806>. This report is an abridged version of the LHC Design Report (CERN-2004-003).
- 2780
- 2781
- 2782 [32] ATLAS Collaboration. The ATLAS experiment at the CERN Large Hadron Collider. *JINST*, 3:S08003, 2008. doi: 10.1088/1748-0221/3/08/S08003.
- 2783
- 2784 [33] CMS Collaboration. The cms experiment at the cern lhc. *Journal of Instrumentation*, 3(08):S08004, 2008. URL <http://stacks.iop.org/1748-0221/3/i=08/a=S08004>.
- 2785
- 2786 [34] LHCb Collaoration. The LHCb Detector at the LHC. *JINST*, 3:S08005, 2008. doi: 10.1088/1748-0221/3/08/S08005.
- 2787
- 2788 [35] ALICE Collaboration. The alice experiment at the cern lhc. *Journal of Instrumentation*, 3(08):S08002, 2008. URL <http://stacks.iop.org/1748-0221/3/i=08/a=S08002>.
- 2789
- 2790 [36] Lyndon Evans. The Large Hadron Collider. In Holstein, BR and Haxton, WC and Jawahery, A, editor, *ANNUAL REVIEW OF NUCLEAR AND PARTICLE SCIENCE, VOL 61*, volume 61 of *Annual Review of Nuclear and Particle Science*, pages 435–466. 2011. doi: {10.1146/annurev-nucl-102010-130438}.
- 2791
- 2792
- 2793
- 2794 [37] ATLAS Collaboration. Luminosity Determination in pp Collisions at $\sqrt{s} = 7$ TeV Using the ATLAS Detector at the LHC. *Eur. Phys. J.*, C 71:1630, 2011. doi: 10.1140/epjc/s10052-011-1630-5.
- 2795
- 2796 [38] Mike Lamont for the LHC team. The First Years of LHC Operation for Luminosity Production. International Particle Accelerator Conference, 2013. URL https://accelconf.web.cern.ch/accelconf/IPAC2013/talks/moyab101_talk.pdf.
- 2797
- 2798
- 2799 [39] Paul Collier for the LHC team. LHC Machine Status. CERN Resource Review Board, 2015. URL <https://cds.cern.ch/record/2063924/files/CERN-RRB-2015-119.PDF>.
- 2800
- 2801 [40] Track Reconstruction Performance of the ATLAS Inner Detector at $\sqrt{s} = 13$ TeV. Technical Report ATL-PHYS-PUB-2015-018, CERN, Geneva, Jul 2015. URL <http://cds.cern.ch/record/2037683>.
- 2802
- 2803

- 2804 [41] M Capeans, G Darbo, K Einsweiller, M Elsing, T Flick, M Garcia-Sciveres, C Gemme, H Perneg-
2805 ger, O Rohne, and R Vuillermet. ATLAS Insertable B-Layer Technical Design Report. Tech-
2806 nical Report CERN-LHCC-2010-013, ATLAS-TDR-19, CERN, Geneva, Sep 2010. URL
2807 <https://cds.cern.ch/record/1291633>.
- 2808 [42] ATLAS Collaboration. ATLAS Trigger Operations Public Results. 2015. URL <https://twiki.cern.ch/twiki/bin/view/AtlasPublic/TriggerOperationPublicResults>.
- 2810 [43] ATLAS Collaboration. ATLAS Luminosity Public Results, Run 1. 2012. URL <https://twiki.cern.ch/twiki/bin/view/AtlasPublic/LuminosityPublicResults>.
- 2812 [44] ATLAS Collaboration. ATLAS Luminosity Public Results, Run 2. 2015. URL <https://twiki.cern.ch/twiki/bin/view/AtlasPublic/LuminosityPublicResultsRun2>.
- 2814 [45] T Kawamoto, S Vlachos, L Pontecorvo, J Dubbert, G Mikenberg, P Iengo, C Dallapiccola,
2815 C Amelung, L Levinson, R Richter, and D Lellouch. New Small Wheel Technical Design Re-
2816 port. Technical Report CERN-LHCC-2013-006, ATLAS-TDR-020, CERN, Geneva, Jun 2013.
2817 URL <https://cds.cern.ch/record/1552862>. ATLAS New Small Wheel Technical Design
2818 Report.
- 2819 [46] Y. Giomataris, Ph. Rebours, J.P. Robert, and G. Charpak. Micromegas: a high-granularity
2820 position-sensitive gaseous detector for high particle-flux environments. *Nuclear Instruments
2821 and Methods in Physics Research Section A: Accelerators, Spectrometers, Detectors and As-
2822 sociated Equipment*, 376(1):29 – 35, 1996. ISSN 0168-9002. doi: [http://dx.doi.org/10.1016/0168-9002\(96\)00175-1](http://dx.doi.org/10.1016/0168-9002(96)00175-1). URL <http://www.sciencedirect.com/science/article/pii/0168900296001751>.
- 2825 [47] T. Alexopoulos, J. Burnens, R. de Oliveira, G. Glonti, O. Pizzirusso, V. Polychronakos,
2826 G. Sekhniaidze, G. Tsipolitis, and J. Wotschack. A spark-resistant bulk-micromegas chamber for
2827 high-rate applications. *Nuclear Instruments and Methods in Physics Research Section A: Acceler-
2828 ators, Spectrometers, Detectors and Associated Equipment*, 640(1):110 – 118, 2011. ISSN 0168-9002.
2829 doi: <http://dx.doi.org/10.1016/j.nima.2011.03.025>. URL <http://www.sciencedirect.com/science/article/pii/S0168900211005869>.
- 2831 [48] Joao Pequenao and Paul Schaffner. An computer generated image representing how ATLAS
2832 detects particles. Jan 2013. URL <https://cds.cern.ch/record/1505342>.
- 2833 [49] Improved electron reconstruction in ATLAS using the Gaussian Sum Filter-based model for
2834 bremsstrahlung. Technical Report ATLAS-CONF-2012-047, CERN, Geneva, May 2012. URL
2835 <https://cds.cern.ch/record/1449796>.

- 2836 [50] Electron efficiency measurements with the ATLAS detector using the 2012 LHC proton-proton
2837 collision data. Technical Report ATLAS-CONF-2014-032, CERN, Geneva, Jun 2014. URL
2838 <https://cds.cern.ch/record/1706245>.
- 2839 [51] Georges Aad et al. Electron and photon energy calibration with the ATLAS detector using LHC
2840 Run 1 data. *Eur. Phys. J.*, C74(10):3071, 2014. doi: 10.1140/epjc/s10052-014-3071-4.
- 2841 [52] Georges Aad et al. Measurement of the muon reconstruction performance of the ATLAS detec-
2842 tor using 2011 and 2012 LHC proton–proton collision data. *Eur. Phys. J.*, C74(11):3130, 2014. doi:
2843 10.1140/epjc/s10052-014-3130-x.
- 2844 [53] W Lampl, S Laplace, D Lelas, P Loch, H Ma, S Menke, S Rajagopalan, D Rousseau, S Snyder,
2845 and G Unal. Calorimeter Clustering Algorithms: Description and Performance. Technical
2846 Report ATL-LARG-PUB-2008-002. ATL-COM-LARG-2008-003, CERN, Geneva, Apr 2008.
2847 URL <https://cds.cern.ch/record/1099735>.
- 2848 [54] Georges Aad et al. Topological cell clustering in the ATLAS calorimeters and its performance in
2849 LHC Run 1. 2016.
- 2850 [55] Matteo Cacciari, Gavin P. Salam, and Gregory Soyez. The Anti-k(t) jet clustering algorithm.
2851 *JHEP*, 04:063, 2008. doi: 10.1088/1126-6708/2008/04/063.
- 2852 [56] Monte Carlo Calibration and Combination of In-situ Measurements of Jet Energy Scale, Jet En-
2853 ergy Resolution and Jet Mass in ATLAS. Technical Report ATLAS-CONF-2015-037, CERN,
2854 Geneva, Aug 2015. URL <http://cds.cern.ch/record/2044941>.
- 2855 [57] Georges Aad et al. Performance of *b*-Jet Identification in the ATLAS Experiment. 2015.
- 2856 [58] Expected performance of the ATLAS *b*-tagging algorithms in Run-2. Technical Report ATL-
2857 PHYS-PUB-2015-022, CERN, Geneva, Jul 2015. URL <http://cds.cern.ch/record/2037697>.
- 2858
- 2859 [59] Georges Aad et al. Performance of Missing Transverse Momentum Reconstruction in Proton-
2860 Proton Collisions at 7 TeV with ATLAS. *Eur. Phys. J.*, C72:1844, 2012. doi: 10.1140/epjc/
2861 s10052-011-1844-6.
- 2862 [60] Performance of Missing Transverse Momentum Reconstruction in ATLAS studied in Proton-
2863 Proton Collisions recorded in 2012 at 8 TeV. Technical Report ATLAS-CONF-2013-082, CERN,
2864 Geneva, Aug 2013. URL <http://cds.cern.ch/record/1570993>.
- 2865 [61] ATLAS Collaboration. Observation and measurement of Higgs boson decays to WW* with the
2866 ATLAS detector. *Phys. Rev. D*, 92(012006), 2015.

- 2867 [62] Aaron James Armbruster. Discovery of a Higgs Boson with the ATLAS detector. 2013. CERN-
 2868 THESIS-2013-047.
- 2869 [63] G. Cowan, K. Cranmer, E. Gross, and O. Vitells. Asymptotic formulae for likelihood-based tests
 2870 of new physics. *Eur. Phys. J., C* 71:1554, 2011. doi: 10.1140/epjc/s10052-011-1554-0.
- 2871 [64] ATLAS Collaboration. Limits on the production of the Standard Model Higgs Boson in pp
 2872 collisions at $\sqrt{s} = 7$ TeV with the ATLAS detector. *Eur. Phys. J., C* 71:1728, 2011. doi: 10.1140/
 2873 epjc/s10052-011-1728-9.
- 2874 [65] ATLAS Collaboration. Performance of the ATLAS muon trigger in pp collisions at $\sqrt{s} = 8$
 2875 TeV. *Eur. Phys. J. C*, (arXiv:1408.3179. CERN-PH-EP-2014-154):75. 19 p, Aug 2014. URL <https://cds.cern.ch/record/1749694>.
- 2877 [66] ATLAS collaboration. Electron trigger performance in 2012 ATLAS data, 2015. ATLAS-COM-
 2878 DAQ-2015-091.
- 2879 [67] Paolo Nason. A new method for combining NLO QCD with shower Monte Carlo algorithms.
 2880 *JHEP*, 11:040, 2004.
- 2881 [68] B. P. Kersevan and E. Richter-Was. The Monte Carlo event generator AcerMC version 2.0 with
 2882 interfaces to PYTHIA 6.2 and HERWIG 6.5. 2004.
- 2883 [69] Nikolas Kauer and Giampiero Passarino. Inadequacy of zero-width approximation for a light
 2884 Higgs boson signal. 2012.
- 2885 [70] T. Gleisberg, Stefan Hoeche, F. Krauss, M. Schonherr, S. Schumann, et al. Event generation with
 2886 SHERPA 1.1. *JHEP*, 0902:007, 2009. doi: 10.1088/1126-6708/2009/02/007.
- 2887 [71] Michelangelo L. Mangano et al. ALPGEN, a generator for hard multiparton processes in
 2888 hadronic collisions. *JHEP*, 0307:001, 2003. doi: 10.1088/1126-6708/2003/07/001.
- 2889 [72] Torbjorn Sjostrand, Stephen Mrenna, and Peter Z. Skands. PYTHIA 6.4 Physics and Manual.
 2890 *JHEP*, 0605:026, 2006. doi: 10.1088/1126-6708/2006/05/026.
- 2891 [73] Torbjorn Sjostrand, Stephen Mrenna, and Peter Z. Skands. A Brief Introduction to PYTHIA 8.1.
 2892 *Comput.Phys.Commun.*, 178:852–867, 2008. doi: 10.1016/j.cpc.2008.01.036.
- 2893 [74] G. Corcella et al. HERWIG 6: An event generator for hadron emission reactions with interfering
 2894 gluons (including super-symmetric processes). *JHEP*, 01:010, 2001. doi: 10.1088/1126-6708/2001/
 2895 01/010.
- 2896 [75] J. M. Butterworth, Jeffrey R. Forshaw, and M. H. Seymour. Multiparton interactions in photo-
 2897 production at HERA. *Z. Phys., C* 72:637, 1996. doi: 10.1007/s002880050286.

- 2898 [76] Jun Gao, Marco Guzzi, Joey Huston, Hung-Liang Lai, Zhao Li, et al. The CT10 NNLO Global
 2899 Analysis of QCD. *Phys. Rev.*, D89:033009, 2014. doi: 10.1103/PhysRevD.89.033009.
- 2900 [77] P. M. Nadolsky. Implications of CTEQ global analysis for collider observables. *Phys. Rev.*, D 78:
 2901 013004, 2008. doi: 10.1103/PhysRevD.78.013004.
- 2902 [78] A. Sherstnev and R. S. Thorne. Parton distributions for the LHC. *Eur. Phys. J.*, C 55:553, 2009.
 2903 doi: 10.1140/epjc/s10052-008-0610-x.
- 2904 [79] S. Agostinelli et al. GEANT4, a simulation toolkit. *Nucl. Instrum. Meth.*, A 506:250, 2003. doi:
 2905 10.1016/S0168-9002(03)01368-8.
- 2906 [80] R.K. Ellis, I. Hinchliffe, M. Soldate, and J.J. Van Der Bij. Higgs decay to $\tau+\tau$ -a possible signature
 2907 of intermediate mass higgs bosons at high energy hadron colliders. *Nuclear Physics B*, 297(2):
 2908 221 – 243, 1988. ISSN 0550-3213. doi: [http://dx.doi.org/10.1016/0550-3213\(88\)90019-3](http://dx.doi.org/10.1016/0550-3213(88)90019-3). URL
 2909 <http://www.sciencedirect.com/science/article/pii/0550321388900193>.
- 2910 [81] Eilam Gross and Ofer Vitells. Transverse mass observables for charged Higgs boson searches at
 2911 hadron colliders. *Phys. Rev.*, D81:055010, 2010. doi: 10.1103/PhysRevD.81.055010.
- 2912 [82] J. R. Andersen et al. Les Houches 2013: Physics at TeV Colliders: Standard Model Working
 2913 Group Report. 2014.
- 2914 [83] I. Stewart and F. Tackmann. Theory uncertainties for Higgs mass and other searches using jet
 2915 bins. *Phys. Rev.*, D 85:034011, 2012. doi: 10.1103/PhysRevD.85.034011.
- 2916 [84] ATLAS Collaboration. Luminosity Determination in pp Collisions at $\sqrt{s} = 7$ TeV Using the
 2917 ATLAS Detector at the LHC. *Eur. Phys. J.*, C 71:1630, 2011. doi: 10.1140/epjc/s10052-011-1630-5.
- 2918 [85] Jet energy scale and its systematic uncertainty in proton-proton collisions at $\sqrt{s} = 7$ tev with
 2919 atlas 2011 data. *ATLAS-CONF-2013-004*, 2013.
- 2920 [86] Calibrating the b -tag efficiency and mistag rate in 35 pb^{-1} of data with the atlas detector.
 2921 *ATLAS-CONF-2011-089*, 2011.
- 2922 [87] ATLAS Collaboration. Measurement of the b -tag Efficiency in a Sample of Jets Containing
 2923 Muons with 5 fb^{-1} of Data from the ATLAS Detector. *ATLAS-CONF-2012-043*, 2012. URL
 2924 <http://cdsweb.cern.ch/record/1435197>.
- 2925 [88] ATLAS Collaboration. Calibration of b -tagging using dileptonic top pair events in a combinatorial
 2926 likelihood approach with the ATLAS experiment. (ATLAS-CONF-2014-004), 2014. URL
 2927 <http://cds.cern.ch/record/1664335>.

- 2928 [89] Georges Aad et al. Measurement of the Higgs boson mass from the $H \rightarrow \gamma\gamma$ and $H \rightarrow ZZ^* \rightarrow$
 2929 4ℓ channels with the ATLAS detector using 25 fb^{-1} of pp collision data. *Phys. Rev.*, D90(5):
 2930 052004, 2014. doi: 10.1103/PhysRevD.90.052004.
- 2931 [90] Georges Aad et al. Measurements of the Higgs boson production and decay rates and coupling
 2932 strengths using pp collision data at $\sqrt{s} = 7$ and 8 TeV in the ATLAS experiment. *Eur. Phys. J.*,
 2933 C76(1):6, 2016. doi: 10.1140/epjc/s10052-015-3769-y.
- 2934 [91] W.J. Stirling. $7/8$ and $13/8$ TeV LHC luminosity ratios. 2013. URL http://www.hep.physics.ac.uk/~wstirlin/plots/lhclumi7813_2013_v0.pdf.
- 2935 [92] J Alison. Experimental Studies of hh. Oct 2014. URL <http://cds.cern.ch/record/1952581>.
- 2936 [93] J. Alwall et al. The automated computation of tree-level and next-to-leading order differential
 2937 cross sections, and their matching to parton shower simulations. *JHEP*, 07:079, 2014.
- 2940 [94] Richard D. Ball et al. Parton distributions with LHC data. *Nucl. Phys. B*, 867:244, 2013.
- 2941 [95] ATLAS Collaboration. ATLAS Run 1 Pythia8 tunes. (ATL-PHYS-PUB-2014-021), Nov 2014.
 2942 URL <https://cds.cern.ch/record/1966419>.
- 2943 [96] M. Bahr et al. Herwig++ Physics and Manual. *Eur. Phys. J. C*, 58:639–707, 2008. doi: 10.1140/
 2944 epjc/s10052-008-0798-9.
- 2945 [97] Stefan Gieseke, Christian Rohr, and Andrzej Siodmok. Colour reconnections in Herwig++. *Eur.*
 2946 *Phys. J. C*, 72:2225, 2012. doi: 10.1140/epjc/s10052-012-2225-5.
- 2947 [98] Simone Alioli, Paolo Nason, Carlo Oleari, and Emanuele Re. A general framework for imple-
 2948 menting NLO calculations in shower Monte Carlo programs: the POWHEG BOX. *JHEP*, 06:
 2949 043, 2010.
- 2950 [99] Peter Zeiler Skands. Tuning Monte Carlo Generators: The Perugia Tunes. *Phys. Rev. D*, 82:
 2951 074018, 2010. doi: 10.1103/PhysRevD.82.074018.
- 2952 [100] Michal Czakon and Alexander Mitov. Top++: A Program for the Calculation of the Top-Pair
 2953 Cross-Section at Hadron Colliders. 2011.
- 2954 [101] Baojia (Tony) Tong. Private communication.
- 2955 [102] D. Krohn, J. Thaler, and L.-T. Wang. Jet Trimming. *JHEP*, 02:084, 2010. doi: 10.1007/
 2956 JHEP02(2010)084.
- 2957 [103] ATLAS Collaboration. Identification of Boosted, Hadronically Decaying W Bosons and Com-
 2958 parisons with ATLAS Data Taken at $\sqrt{s} = 8$ TeV. 2015.

- 2959 [104] Expected Performance of Boosted Higgs ($\rightarrow b\bar{b}$) Boson Identification with the ATLAS Detector
 2960 at $\sqrt{s} = 13$ TeV. Technical Report ATL-PHYS-PUB-2015-035, CERN, Geneva, Aug 2015. URL
 2961 <https://cds.cern.ch/record/2042155>.
- 2962 [105] Flavor Tagging with Track Jets in Boosted Topologies with the ATLAS Detector. Technical
 2963 Report ATL-PHYS-PUB-2014-013, CERN, Geneva, Aug 2014. URL [https://cds.cern.ch/](https://cds.cern.ch/record/1750681)
 2964 [record/1750681](https://cds.cern.ch/record/1750681).
- 2965 [106] Matteo Cacciari and Gavin P. Salam. Pileup subtraction using jet areas. *Phys. Lett. B*, 659:119,
 2966 2008. doi: [10.1016/j.physletb.2007.09.077](https://doi.org/10.1016/j.physletb.2007.09.077).
- 2967 [107] Search for pair production of Higgs bosons in the $b\bar{b}b\bar{b}$ final state using proton-proton collisions
 2968 at $\sqrt{s} = 13$ TeV with the ATLAS detector. Technical Report ATLAS-CONF-2016-017, CERN,
 2969 Geneva, Mar 2016. URL <https://cds.cern.ch/record/2141006>.
- 2970 [108] Qi Zeng. Private communication.
- 2971 [109] ATLAS Collaboration. Identification of boosted, hadronically-decaying W and Z bosons in
 2972 $\sqrt{s} = 13$ TeV Monte Carlo Simulations for ATLAS. (ATL-PHYS-PUB-2015-033), Aug 2015.
 2973 URL <https://cds.cern.ch/record/2041461>.
- 2974 [110] ATLAS Collaboration. Performance of b -Jet Identification in the ATLAS Experiment. 2015.
- 2975 [111] Alexander L. Read. Presentation of search results: The CL(s) technique. *J. Phys. G*, 28:2693,
 2976 2002. doi: [10.1088/0954-3899/28/10/313](https://doi.org/10.1088/0954-3899/28/10/313).
- 2977 [112] Measurements of the Higgs boson production and decay rates and constraints on its couplings
 2978 from a combined ATLAS and CMS analysis of the LHC pp collision data at $\sqrt{s} = 7$ and 8 TeV.
 2979 Technical Report ATLAS-CONF-2015-044, CERN, Geneva, Sep 2015. URL <http://cds.cern.ch/record/2052552>.
- 2981 [113] Projections for measurements of Higgs boson signal strengths and coupling parameters with the
 2982 ATLAS detector at a HL-LHC. Technical Report ATL-PHYS-PUB-2014-016, CERN, Geneva,
 2983 Oct 2014. URL <http://cds.cern.ch/record/1956710>.
- 2984 [114] ATLAS Phase-II Upgrade Scoping Document. Technical Report CERN-LHCC-2015-020.
 2985 LHCC-G-166, CERN, Geneva, Sep 2015. URL <http://cds.cern.ch/record/2055248>.
- 2986 [115] Glen Cowan, Eilam Gross. Discovery significance with statistical uncertainty in the background
 2987 estimate. 2008. URL <http://www.pp.rhul.ac.uk/~cowan/stat/notes/SigCalcNote.pdf>.



THIS THESIS WAS TYPESET using L^AT_EX, originally developed by Leslie Lamport and based on Donald Knuth's T_EX.

The body text is set in 11 point Egenolff-Berner Garamond, a revival of Claude Garamont's humanist typeface. The above illustration, *Science Experiment 02*, was created by Ben Schlitter and released under CC BY-NC-ND 3.0. A template that can be used to format a PhD dissertation with this look & feel has been released under the permissive AGPL license, and can be found online at github.com/asm-products/Dissertate or from its lead author, Jordan Suchow, at suchow@post.harvard.edu.